

**INTERNATIONAL RESEARCH IN
SCIENCE AND MATHEMATICS**

December 2022

EDITOR

PROF. DR. FİLİZ ÖZBAŞ GERÇEKER

PROF. DR. HASAN AKGÜL

ASSOC.PROF.DR. HAYRİ BABA

 **SERÜVEN**
YAYINEVİ

Genel Yayın Yönetmeni / Editor in Chief • C. Cansın Selin Temana

Kapak & İç Tasarım / Cover & Interior Design • Serüven Yayınevi

Birinci Basım / First Edition • © Aralık 2022

ISBN • 978-625-6399-22-8

© copyright

Bu kitabın yayın hakkı Serüven Yayınevi'ne aittir.

Kaynak gösterilmeden alıntı yapılamaz, izin almadan hiçbir yolla

çoğaltılamaz. The right to publish this book belongs to Serüven

Publishing. Citation can not be shown without the source, reproduced in

any way without permission.

Serüven Yayınevi / Serüven Publishing

Türkiye Adres / Turkey Address: Yalı Mahallesi İstikbal Caddesi No:6

Güzelbahçe / İZMİR

Telefon / Phone: 05437675765

web: www.seruyenyayinevi.com

e-mail: seruyenyayinevi@gmail.com

Baskı & Cilt / Printing & Volume

Sertifika / Certificate No: 47083

International Research in Science and Mathematics

December 2022

Editors

Prof. Dr. Filiz ÖZBAŞ GERÇEKER

Prof. Dr. Hasan AKGÜL

Doç. Dr. Hayri BABA

CONTENTS

Chapter 1

OPTIMAL CONTROL THEORY FOR FISHERY MANAGEMENT*

Mahir DEMİR..... 1

Chapter 2

EFFECTS OF THE IN-PLANE APPLIED FIELD AND THE OUT-OF-PLANE ANISOTROPY ON THE DOMAIN STRUCTURE IN ULTRATHIN FILMS

Bengü KAPLAN..... 17

Chapter 3

STATISTICAL POWER ANALYSIS BASED ON ONE SAMPLE T-TEST WITH JAMOVI

Tuğba Söküt Açar27

SECTION 4

STORAGE OF LIQUID CHEMICALS USED FOR EXPERIMENTS AT BANAZ VOCATIONAL SCHOOL

Melek GOKMEN KARAKAYA.....47

Chapter 5

PALLADIUM(II) SCHIFF BASE CHELATES: SYNTHESIS, CHARACTERIZATION AND ANTIBACTERIAL STUDIES

Hülya AVCI OZBEK 69

Deniz DEMİR ATLI69

Chapter 6

RECYCLING A SCRAPPED MAGNETIC STIRRER/HEATER USING AN ARDUINO MICROCONTROLLER

Zafer GÜLTEKİN 83

Nuray ALTINÖLÇEK GÜLTEKİN2..... 83

Chapter 7

ORGANIC SUBSTANCES AFFECTING GROWTH AND DEVELOPMENT IN PLANTS (PLANT GROWTH REGULATORS, PHOTOHORMONES)

Kadriye URUÇ PARLAK.....93

Chapter 8

ENTROPY-BASED VOLATILITY FORECASTING FOR SARS- COV-2 PANDEMIC DATA OF TURKEY

Mine DOĞAN..... 105

Ayşe METİN KARAKAŞ 105

Chapter 9

BDELLOVIBRIO AND LIKE ORGANISMS (BALOS): BRIEFLY LIFE

Dilek ŞEKER..... 121

Chapter 10

PLANE SYMMETRIC SCALAR FIELD IN LYRA THEORY

Doğukan TAŞER..... 143

Sertaç Serkan DOĞRU 143

Chapter 11

CHARGE CARRIER RECOMBINATION KINETICS AND LIFETIME MEASUREMENTS IN A-SI:H P-I-N SOLAR CELLS WITH CR BACK CONTACT

Bengü KAPLAN..... 159

Chapter 12

USE OF DIFFERENTIAL SCANNING CALORIMETRY IN MODEL MEMBRANE RESEARCH

Sevgi Türker Kaya 179

Chapter 13

USING MACHINE LEARNING ALGORITHMS IN THE
CLASSIFICATION OF PRICES ON MOBILE PHONES

Serpil AYDIN.....201

Chapter 14

RECENT STUDIES ON THE ANTIMICROBIAL AND
ANTICANCER ACTIVITIES OF HYDRAZIDE-HYDRAZONES

Belma HASDEMİR215

“

Chapter 1

OPTIMAL CONTROL THEORY FOR FISHERY MANAGEMENT*

*Mahir DEMİR*¹

”

¹ Assistant Prof. Mahir Demir, Department of Mathematics, Giresun University, Giresun, Turkey. ORCID ID: 0000-0002-9670-5210.

* The main parts of this chapter is produced from my dissertation (Adviser: Prof. Suzanne Lenhart) cited as M. Demir, Optimal Control Strategies in Ecosystem-Based Fishery Models, Ph.D dissertation, University of Tennessee in Knoxville, 2019. Available from: https://trace.tennessee.edu/utk_grad-diss/5421.

1. Introduction

Fish populations are an important part of marine ecosystems, and any violation of fish populations is directly affecting marine ecosystems and their resilience. Since fish populations are a vital source of food for the human population worldwide, their harvesting strategies are very important for both sustainable fisheries and resilient ecosystems. Therefore, sustainable harvesting strategies are essential for both fish stocks and the ecosystem they are in. Unfortunately, due to wrong strategies in the management of fisheries, many fish stocks have been suffering from overfishing.

Overfishing is one of the biggest threats to sustainable fisheries and marine ecosystems, most fisheries have been overexploited or have already collapsed worldwide. There are many reasons for overfishing, and major ones are (1) illegal and unregulated fishing, (2) lack of sustainable harvesting strategies, (3) its economic value and increasing demand for food, (4) having no governmental rule, law, or strategy for open access fisheries, and so on. Due to such reasons, fish are harvested more than they can replenish their size by natural reproduction.

In the chapter, I will focus on sustainable harvesting strategies to address at least one of the problems causing overfishing. There has been some work investigating different techniques for sustainable harvesting, such as seasonal fishery (Charles [2011]; Ben-Hasan et al. [2019]; Kvamsdal et al. [2019]). In seasonal fishery, fishing is forbidden in reproduction periods of fish populations. Thus, fish populations are harvested after the reproduction periods. This strategy not only lets fish populations replenish their size and reproduce more fish for the next fishing season, but also reduces the cost of fishing. No-take marine reserves (protected areas) are another strategy for sustainable harvesting (Revenga and Badalamenti [2008]; Garcia et al., [2014]; Öztürk et al., [2017]). In this strategy, protected areas serve as a source of new individuals for fish stocks and compensate for the overfishing occurring outside of protected areas. Another strategy for sustainable fishery is ecosystem-based fishery management (Pikitch et al. [2004]; Fletcher et al. [2010]; Fulton et al. [2014]). In this strategy, the food web of target fish plays the main role in the fate of target fish for sustainable harvesting.

Having these three most known techniques in mind for a sustainable fishery, I will focus on a more complete and general technique for sustainable fisheries, which is using optimal control theory together with food chain models. This technique not only offers optimal and the most profitable harvesting strategies for fish stocks but also helps to investigate

the effect of fishery on ecosystems. In many cases, no-take marine reserve areas are natural results of the optimal control application in fishery management (Neubert [2003]; Joshi et al. [2009]; Moberg et al. [2015]; Kelly Jr et al. [2019]). The optimal control technique is also able to capture seasonal harvesting if it is the optimal strategy (Demir and Lenhart [2021]). Thus, with this technique, we can capture more appropriate optimal strategies for any fishery. Besides these, including food chains in the optimal control technique gives us more complete optimal strategies since we also consider food chains in the ecosystem. Aquatic ecosystems are very complex in terms of predator-prey relationships and such relationships should be taken into consideration in a harvesting strategy (Grishin et al. [2007]).

Thus, this new technique, using optimal control tools with a food chain modeling framework is more general since it considers the other three techniques. In the next sections, I will first introduce optimal control theory and then discuss the benefits of using optimal control theory together with the food chain modeling framework.

2. Definition of Optimal Control Theory

Optimal Control Theory (OCT) is a modern approach to control dynamic systems, and it has been commonly used in many areas including robotics, aircraft, bioengineering, economics, and control of biological and ecological systems. OCT helps to control and manipulate a dynamical system to maximize or minimize a desired goal by changing the behavior of the dynamical system. In the chapter, OCT will be applied to ordinary differential equations and partial differential equations. Therefore, I will introduce OCT on ODEs and PDEs in this section, and then discuss the benefits of using OCT in the next section.

2.1 Optimal Control for ODE Systems

Application of OCT with ODE systems developed by Lev Semenovic Pontryagin, and his work resulted in Pontryagin's Maximum Principle, for the optimal control of finite-dimensional problems. As an illustration of Pontryagin's Maximum Principle, the following problem is considered (Pontryagin et al. [1986]). Given a piecewise continuous control function $h(t)$, there is an associated continuous and piecewise differentiable state $x(t)$, defined on $[t_0, t_1]$, a finite time interval, that solves

$$\frac{dx}{dt} = g(t, x(t), h(t)) \quad (\text{state equation})$$

with the initial condition, $x(t_0) = x_0$. The main goal is to find the control, h^* that maximizes the objective functional:

$$J(h^*) = \max_h J(h) = \max_h \int_{t_0}^{t_1} f(t, x(t), h(t)) dt. \quad (2.1)$$

If the control, $h^*(t)$ is an optimal for the system in Eq. 2.1 together with its corresponding state, $x^*(t)$, then it is necessary that there exists a differentiable adjoint function, λ and for all $t \in [t_0, t_1]$, $\lambda(t) \neq 0$ and satisfies the following condition for all controls (Pontryagin et al. [1986]):

$$H(t, x^*(t), h(t), \lambda(t)) \leq H(t, x^*(t), h^*(t), \lambda(t)),$$

where H is called as Hamiltonian and defined as follow

$$H(t, x(t), h(t), \lambda(t)) = f(t, x(t), h(t)) + \lambda g(t, x(t), h(t)),$$

and $\lambda(t)$ satisfies the following conditions

$$\frac{d\lambda}{dt} = -\frac{\partial H}{\partial x} \text{ (adjoint equation) and } \lambda(t_1) = 0 \text{ (transversality condition).}$$

2.2 Optimal Control for PDE Systems

The theory of optimal control for PDEs was developed by Lions [1971]. Although some similarities exist with Pontryagin's Maximum Principle generalized for ODEs, there is no straightforward generalization of Pontryagin's Maximum Principle to PDEs. See the book by Li and Yong [1995] for some applicable cases of Maximum Principles for PDEs. To obtain optimality systems for PDEs, the following steps are considered for an optimal control problem with a PDE (Lenhart and Workman [2007] and Hackbusch [1978]):

1. Build up a PDE in a weak solution space with a control in a specified set and an objective functional and provide the existence of an optimal control.
2. Derive the necessary conditions as follows, need to differentiate the maps: h (control) $\rightarrow J(h)$ (Objective functional) as well as h (control) $\rightarrow x(h)$ (state) in the following weak convergence sense,

$$\frac{x(h+\varepsilon l) - x(h)}{\varepsilon} \xrightarrow{\text{weak}} \psi \quad \text{as } \varepsilon \rightarrow 0$$

where for all $h \in A$ (Admissible class for control variables) and $l \in L^\infty$ such that $(h + \varepsilon l) \in A$, and we call ψ as the “sensitivity” function.

3. The “sensitivity” function is the directional derivative of the control-to-state map. The sensitivity function solves a PDE, which is the linearized version of the state PDE.

4. By using the operator associated with the sensitivity PDE, obtain the adjoint operator associated with the adjoint PDE together with boundary conditions and transversality conditions.

5. Then, differentiate the objective functional $J(h)$ with respect to the control, h at the optimal control.

6. Finally, use the adjoint PDE and the sensitivity PDE in this derivative of J to obtain the explicit characterization of optimal control.

3. Applications of Optimal Control Theory for Sustainable Fishery

In this section, optimal control theory is applied to ODEs or PDEs. I first discussed that marine protected areas and seasonal fisheries are natural results of optimal control, and then roughly went through how to obtain an optimality system for a food chain model and discussed the benefits of using food chain models in optimal control applications. Note that in this study, I present and discuss some of my previous works and some other works done related to sustainable fisheries and then discuss these techniques used in these studies and then showed that food chain modeling frameworks coupled with optimal control theory is the more complete and general one.

3.1 Marine Protected Areas and Optimal Control

In this subsection, I will re-visit the works done by Neubert [2003] and H.R. Joshi et al. [2008]. These studies investigate marine reserve areas at equilibrium to come up with sustainable optimal policies and derive the yield-maximizing spatial harvesting strategy in a spatially explicit model in which no reserves are imposed. Let’s start with the work proposed by Neubert [2003]. The fishery model used in this study is given as

$$\frac{\partial N}{\partial T} = rN \left(1 - \frac{N}{K}\right) + D \frac{\partial^2 N}{\partial X^2} - qE(X)N \quad (3.1)$$

with boundary condition $N(0, T) = N(L, T) = 0$ for $0 < X < L$. Where $N(X, T)$ is the population density of the fish stock at location X and time T . Considering the fish stock at equilibrium that implies $\partial N / \partial T = 0$, then Eq. 3.1 can be rewritten as

$$D \frac{\partial^2 N}{\partial X^2} = -rN \left(1 - \frac{N}{K} \right) + qE(X)N \quad (3.2)$$

with $N(0) = N(L) = 0$.

The equilibrium yield is then given by the integral

$$Y[N(X), E(X)] = \int_0^L qE(X)N(X)dX \quad \text{with } 0 \leq E(X) \leq E_{max}.$$

Neubert first reduced the second-order ordinary differential equation (ODE) given in Eq. 3.1 to a system of first-order differential equations and then applied Pontryagin's Maximum Principle (Neubert [2003]). After that he obtained adjoint equations and the characterized optimal control, $E(X)$. Since this optimal control is obtained in the dynamical system at equilibrium, the optimal harvesting strategy also will be sustainable if the equilibrium point is stable. He investigated solutions of the optimal control problem for different lengths of a habitat. When the given fish density was low, then most of the habitat was reserved as no-take marine reserve areas and a small portion of coastal areas are considered as harvesting areas. When a fish density is large enough but still it is below $\frac{1}{2}$ of its maximum density at a larger habitat, then the harvesting areas are larger in coastal areas, but optimal control theory still offers no-take marine reserve areas in the center of the habitat.

Let's visit another work done by H.R. Joshi et al. [2008]. This study is an extension of Neubert [2003] by including advection. The assumption of equilibrium is relaxed and replaced with maximizing the present value of yield over a finite time horizon. Since this new fishery model is a system of PDEs with advection and diffusion, there is no full generalization of Pontryagin's maximum principle for the control of partial differential equation (PDE) systems. Therefore, they need to prove the existence of an optimal control and develop the necessary conditions for optimality from scratch (see H.R. Joshi et al. [2008]). I will not cover the process of obtaining the optimality system since it is out of the scope of the study, authors simply follow the steps given in subsection 2.2, instead, I will focus on some results of the study.

Rather than investigating the effect of habitat length as considered in Neubert [2003], authors in H.R. Joshi et al. [2008]) investigated the effect of the time horizon on the optimal harvest rates and showed that no-take marine reserve areas (marine protected areas) are a natural result of optimal control, especially for a long-term fishery.

Thus, the results of these both studies show that marine protected areas are natural results of optimal controls, and the characterized optimal controls not only provide marine protected areas but also offer a sustainable harvesting policy since analyses are made at equilibrium or for a long term.

3.2 Optimal Control applied to a Food Chain Model

Now, I will focus on another valuable benefit of optimal control when applied to food chain models. There are many studies for harvesting fish stocks using a single equation (Hilborn [1992]; Skern-Mauritzen [2016]), which ignores the dynamics of ecosystems by excluding predator-prey relations and their effects on fisheries. Using a single equation may not represent the biological system well enough for modeling sustainable fishery management (Lauck et al. [1998]; Gwaltney et al. [2004]). Therefore, food chain models that are included the interaction of key species become an increasingly useful method for sustainable fisheries (Chaudhuri and Ray [1996]; Kar and Chaudhuri [2004], Hoekstra and Van den Bergh [2005]).

In this subsection, I will share some results of my published work (Demir and Lenhart [2020]). This study investigates the benefits of using a food chain model in fishery management, by comparing the results of the food chain model with a single species model. We first introduced the models and obtained their optimality systems that are consisting of state equations, adjoint equations, and the characterization of optimal control. After that, we made a stability analysis for the equilibrium point that all the species co-exist and obtained an upper bound for sustainable harvesting.

Food chain model:

A food chain model is utilized with three trophic levels, which are the key species representing the general behavior of a food web in the Black Sea. A , P , and Z stand for the Black Sea anchovy, jellyfish, and zooplankton biomasses, respectively. For a given control, h , the corresponding state variables, $A(h)$, $P(h)$, and $Z(h)$ satisfy the state system given below:

$$\begin{aligned}
\frac{dA}{dt} &= r_1 A \left(1 - \frac{A}{K_1}\right) + m_0 AZ - m_1 PA - hA, \\
\frac{dP}{dt} &= r_2 P \left(1 - \frac{P}{K_2}\right) + m_2 PZ + m_3 PZ - m_6 P, \\
\frac{dZ}{dt} &= r_3 Z \left(1 - \frac{Z}{K_3}\right) + m_4 AZ - m_5 PZ
\end{aligned} \tag{3.3}$$

with the initial conditions:

$$A(0) = A_0, P(0) = P_0, \text{ and } Z(0) = Z_0, \tag{3.4}$$

where all the coefficients and initial conditions are positive and bounded (for details, see Demir and Lenhart [2020]). The coefficients $m_0, m_1, m_2, m_3, m_4, m_5,$ and m_6 denote interaction terms between the species. The Black Sea anchovy harvest term, $h(t)A(t)$, is proportional to the anchovy biomass and the harvest rate, $h(t)$, which represents the amount of anchovy biomass taken from the system at time t . The objective functional for systems (3.3) and (3.4) is

$$\begin{aligned}
J(h) &= \int_0^T e^{-\alpha t} (phA - (\mu_1 + \mu_2 h)h) dt \\
&= \int_{\Omega} e^{-\alpha t} (phA - \mu_1 h - \mu_2 h^2) dt,
\end{aligned} \tag{3.5}$$

where Ω is the union of time intervals as $\Omega = \cup_{i=1}^n [a_i, b_i]$ with n denoting the number of years, the interval $[a_i, b_i]$ represents the fishery season in year $i = 1, 2, \dots, n$. Thus, we have seasonal fishery on the set $[0, T]$, and the control, h , is zero on the set $[0, T] \setminus \Omega$. $J(h)$ is the discounted net profit value of the Black Sea anchovy fishing, h is the harvest rate (the control variable), and $e^{-\alpha t}$ denotes the discount rate with interest rate α . The term $e^{-\alpha t} phA$ represents the revenue of the fishery with price p , and the term $e^{-\alpha t} (\mu_1 + \mu_2 h)h$ represents the cost of the fishery. This cost term is nonlinear in h , but the coefficient μ_2 is taken small enough to have a small effect on numerical calculations.

Next, we state our necessary conditions for optimal control using Pontryagin's Maximum Principle (Pontryagin et al. [1967]) and see the proof of the optimality system (Demir [2019]). The optimality system

consists of the state system, the adjoint system, and the characterization of the optimal control, h^* , is given in the following form:

State System:

$$\frac{dA}{dt} = r_1 A \left(1 - \frac{A}{K_1}\right) + m_0 AZ - m_1 PA - hA,$$

$$\frac{dP}{dt} = r_2 P \left(1 - \frac{P}{K_2}\right) + m_2 PZ + m_3 PZ - m_6 P,$$

$$\frac{dZ}{dt} = r_3 Z \left(1 - \frac{Z}{K_3}\right) + m_4 AZ - m_5 P$$

Adjoint System:

$$\frac{d\lambda_A}{dt} = -(e^{-\alpha t} h + \lambda_A \left[r_1 - \frac{2r_1}{K_1} A^* + m_0 Z^* - m_1 P^* - h \right] + m_2 \lambda_P P^* - m_4 \lambda_Z Z^*)$$

$$\frac{d\lambda_P}{dt} = -(-m_1 \lambda_A A^* + \lambda_P \left[r_2 - \frac{2r_2}{K_2} P^* + m_2 A^* + m_3 Z^* - m_6 \right] - m_5 \lambda_Z Z^*)$$

$$\frac{d\lambda_Z}{dt} = -(-m_0 \lambda_A A^* + m_3 \lambda_P P^* + \lambda_Z \left[r_3 - \frac{2r_3}{K_3} Z^* - m_4 A^* - m_5 P^* \right])$$

Characterization of the optimal control, h^* on $[0, T]$:

$$h^*(t) = \min \left\{ M, \max \left\{ 0, \frac{A^*(1 - e^{-\alpha t} \lambda_A^*) - \mu_1}{2\mu_2} \right\} \right\}$$

together with the initial conditions:

$$A^*(0) = A_0, P^*(0) = P_0, \text{ and } Z^*(0) = Z_0,$$

and the transversality conditions at the final time:

$$\lambda_A(T) = 0, \lambda_P(T) = 0, \text{ and } \lambda_Z(T) = 0.$$

Our optimality system consists of the state system, the adjoint system, and the characterization of the optimal control, h^* . Since the adjoint system is linear in λ_A , λ_P , and λ_Z with bounded coefficients, the solutions are bounded for all $t \in [0, T]$. Therefore, solutions of our optimality system are bounded for all $t \in [0, T]$. Such bounds give the existence and uniqueness of the optimality system for sufficiently small final time T together with bounded coefficients, initial conditions, and transversality conditions (Fister et al. [1998]), which implies the uniqueness of the optimal control.

Single Species Model:

Let's now present the single-species model. For a given control h , the corresponding state variables, $A(h)$, satisfies the following state equation:

$$\frac{dA}{dt} = rA \left(1 - \frac{A}{K}\right) - hA, \quad (3.6)$$

with initial condition $A(0) = A_0$. Thus, the optimal control problem for the single species model becomes

$$J(h) = \int_{\Omega} e^{-\alpha t} (p h A - \mu_1 h - \mu_2 h^2) dt$$

subject to Eq. 3.6. After that optimal control of models are obtained for the single species model and food chain model and applied for 5 years to contrast model results. This comparison shows that the single species model estimates higher biomass for anchovy as compared with that in the food chain model (see Figure 1). This is due to ignoring interactions between species in the single-species model. Note that we obtained Figure 1 by applying harvesting strategies and then obtained these dynamics. In this way, we can see the estimate of fish stocks for the long term after applying any harvesting strategy.

This study indicated that the single-species model overestimates the landing by 15% and the net profit by 18%. If decision-makers of this fisher used the outcomes of the single-species model for the management of the Black Sea anchovy, then they would take out more fish from the system depending on the optimal harvesting strategy in the single-species model, which could result in more stress on the anchovy stock and even might cause a collapse of this anchovy fishery. Thus, managers who use a simplistic modeling framework may end up falling short of their projected harvest and profit levels. This study also shows that we can track the effect

of the fishery by investigating the predicted dynamic of a targeted fishery for the long term as we did in Figure 1.

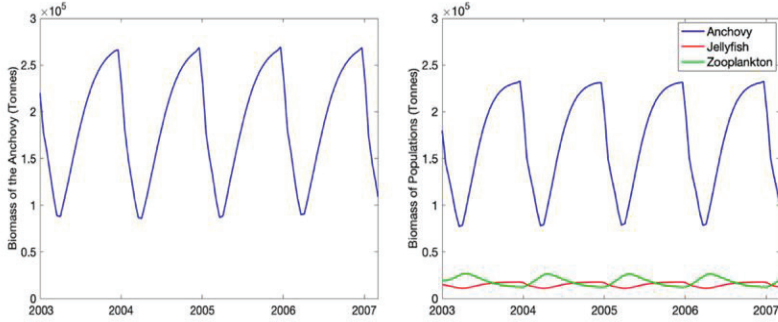


Figure 1. Left plot: Biomass of the Black Sea anchovy obtained from the single-species model. Right plot: Biomass of the Black Sea anchovy obtained from the food chain model (Demir and Lenhart [2020]).

3.3 Seasonal Fishery and Optimal Control

The seasonal fishery is one of the well-known strategies in fishery management and it has a direct impact on the sustainability of a fishery. For example, if fish are being harvested during their reproduction seasons, stocks could diminish and become less productive for upcoming seasons.

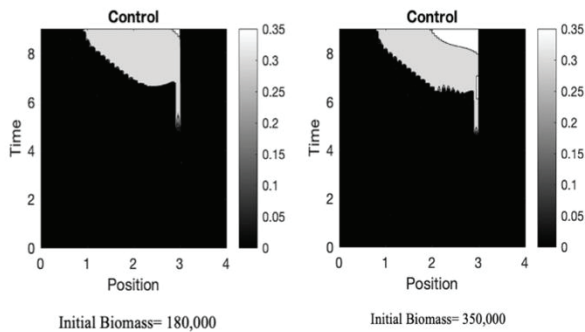


Figure 2. Optimal harvesting rate applied for 9 months with different initials of fish stock. In black areas harvesting is zero and in white areas harvesting is not zero (Demir and Lenhart [2021]).

Therefore, fishing is forbidden in the reproduction periods of fish populations in seasonal fisheries. This strategy not only lets fish populations replenish their size and reproduce more fish for upcoming

fishing seasons, but also reduces the cost of the fishery. Optimal control theory can also capture such seasonality and the times when fish are at peak harvest and most abundant. I will revisit one of my recent works (Demir and Lenhart [2021]). In this study, the ODE system (Demir and Lenhart [2020]) is extended to a PDE system by including advection (from left to right) and diffusion to be able to capture spatial features of the Black Sea anchovy. As we investigate spatial features of the anchovy fishery, we also showed that seasonality is a natural result of optimal control (see Figures 2 and 3). As it can be seen from Figures 2 and 3, the characterized optimal control for this fishery does not suggest any harvesting from month 1 to month 6 and then starts harvesting the fish stock in the last 3 months. This result indicates how valuable optimal control theory is for sustainable fisheries.

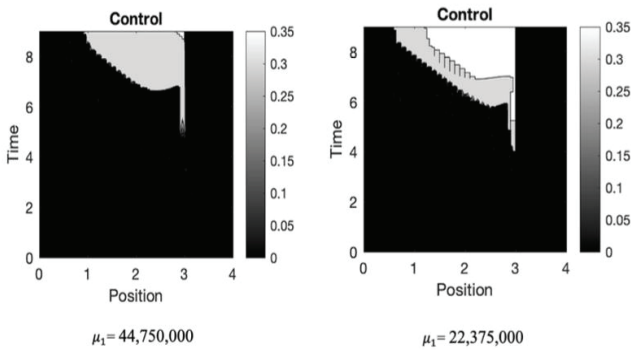


Figure 3. Optimal harvesting rate applied for 9 months with different costs of harvesting. In black areas harvesting is zero and in white areas harvesting is not zero (Demir and Lenhart [2021]).

4. Conclusion

In this chapter, we see that optimal control theory (1) offers sustainable and optimal harvesting strategies, (2) captures marine protected areas and seasonal fisheries if these cases are optimal, (3) provides the maximum profit and landing via objective functionals, (4) can provide maximum sustainable harvesting strategies at (coexistence) equilibrium, (5) can be coupled with food chain models for more realistic, accurate and trackable harvesting strategies.

REFERENCES

- Ben-Hasan, A., Walters, C., & Sumaila, R. (2019). Effects of Management on the Profitability of Seasonal Fisheries. *Frontiers in Marine Science*. 310. 10.3389/fmars.2019.00310.
- Chaudhuri, K. S., & Ray, S. S. (1996) On the combined harvesting of a prey predator system, *Biol. Syst.*, 4, 373–389.
- Charles, A. (2011). Optimal Fisheries Investment: Comparative Dynamics for a Deterministic Seasonal Fishery. *Canadian Journal of Fisheries and Aquatic Sciences*. 40. 2069-2079. 10.1139/f83-240
- Demir, M. (2019). Optimal Control Strategies in Ecosystem-Based Fishery Models, Ph.D dissertation, University of Tennessee in Knoxville. Available from: https://trace.tennessee.edu/utk_graddiss/5421.
- Demir, M., & Lenhart, S. (2020) Optimal sustainable fishery management of the Black Sea anchovy with food chain modeling framework, *Nat. Resour. Model.*, 33 (2020), 29pp.
- Demir, M., & Lenhart, S. (2021), A Spatial Food Chain Model for the Black Sea Anchovy, and its Optimal Fishery, *Discrete and Continuous Dynamical Systems Series B*, 26(1): 155-171.
- Fister, K., Lenhart, S., & McNally, S. (1998). Optimizing chemotherapy in an HIV model. *Electronic Journal of Differential Equations*, 32, 1–12.
- Fletcher, W. J., Shaw, J., Metcalf, S. J., & Gaughan, D. J. (2010). An ecosystem based fisheries management framework: The efficient, regional-level planning tool for management agencies, *Marine Policy*, 34, 1226–1238.
- Fulton, E. A., Smith, A. D. M., Smith, D. C., & Johnson, P. (2014) An integrated approach is needed for ecosystem-based fisheries management: Insights from ecosystem-level management strategy evaluation, *PLoS One*, 9.
- Garcia, S., Henichart, L., Boncoeur, J., Alban, F., & Monbrison, D. (2013). Marine protected areas in fisheries management.
- Grishin, A., Daskalov, G., Shlyakhov, V., & Mihneva, V. (2007). Influence of gelatinous zoo-plankton on fish stocks in the Black Sea: Analysis of biological time-series, *Marine Ecological J.*, 6, 5–24.

- Gwaltney, C. R., Styczynski, M. P., & Stadtherr, M. A. (2004). Reliable computation of equilibrium states and bifurcations in food chain models, *Comput. Chemical Engrg.*, 28, 1981–1996.
- Hackbusch, W. (1978). A numerical method for solving parabolic equations with opposite orientations. *Computing*, 20(3). 6, 9, 10, 36
- Hilborn, R., Walters, & Walters, C. J. (1992). *Quantitative Fisheries Stock Assessment: Choice, Dynamics and Uncertainty*, Springer.
- Hoekstra, J., & Van den Bergh, J. C. J. M. (2005); Harvesting and conservation in a predator-prey system, *J. Econom. Dynam. Control*, 29, 1097–1120.
- Joshi, H. R., Herrera, G. E., Lenhart, S., & Neubert, M.G. (2009) Optimal dynamic harvest of a mobile renewable resource, *Nat. Resour. Model.*, 22, 322–343.
- Kar, T. K. & Chaudhuri, K. S. (2004). Harvesting in a two-prey one-predator fishery: A bioeconomic model, *ANZIAM J.*, 45, 443–456.
- Kelly Jr, M. R., Neubert, M. G., & Lenhart, S. (2019). Marine reserves and optimal dynamic harvesting when fishing damages habitat, *Theoretical Ecology*, 12, 131–144.
- Kvamsdal, S., Maroto, J., Moran, M., & Sandal, L. (2019). Bioeconomic modeling of seasonal fisheries [August 2019]. *European Journal of Operational Research*. 281. 10.1016/j.ejor.2019.08.031.
- Lauck T., Clark, C. W., Mangel, M., & Munro, G. R., Implementing the precautionary principle in fisheries management through marine reserves, *Ecological Appl.*, 8 (1998), S72–S78
- Lenhart, S., & Workman, J. T. (2007). *Optimal Control Applied to Biological Models*. Chapman and Hall/CRC, Boca Raton. 5, 6, 10, 36
- Lions, J. L. (1971). *Optimal control of systems governed by partial differential equations*. Springer-Verlag, Berlin, New York. 6
- Li, X., & Yong, J. (1995). *Optimal Control Theory for Infinite Dimensional Systems*. Birkhauser, Boston. 6
- Moberg, E. A., Shyu, E., Herrera, G. E., Lenhart, S., Lou, Y., & Neubert, M. G. (2015). On the bioeconomics of marine reserves when dispersal evolves, *Nat. Resour. Model.*, 28, 456–474.
- Neubert, M. G. (2003) Marine reserves and optimal harvesting, *Ecology Lett.*, 6, 843–849.

- Öztürk, B., Fach, B., Keskin, Ç., Arkin, S., Topaloğlu, B., & Öztürk, A. (2017). Prospects for Marine Protected Areas in the Turkish Black Sea: A Network Perspective. 10.1002/9781119075806.ch13.
- Pikitch, E. K., Santora, C., Babcock, E. A., Bakun, A. & Bonfil, R., et al. (2004). Ecosystem-based fishery management, *Science*, 305, 346–347.
- Pontryagin, L. S., Boltyanskii, V. G., Gamkrelidze, R. V., & Mishchenko, E. F. (1967). *The mathematical theory of optimal processes*. New York: Wiley.
- Pontryagin, L. S., Boltyanskii, V. G., Gamkrelidze, R. V., and Mishchenko, E. F., *The Mathematical Theory of Optimal Processes*, Vol 4, Gordon and Breach Science Publishers, 1986.
- Revenge, S., & Badalamenti, F. (2008). Management of Marine Protected Areas for fisheries in the Mediterranean.
- Skern-Mauritzen, M., Ottersen, G., Handegard, N. O., Huse, G., & Dingsor, G. E., et al. (2016) Ecosystem processes are rarely included in tactical fisheries management, *Fish and Fisheries*, 17, 165–175.

“

Chapter 2

**EFFECTS OF THE IN-PLANE APPLIED
FIELD AND THE OUT-OF-PLANE
ANISOTROPY ON THE DOMAIN
STRUCTURE IN ULTRATHIN FILMS**

Bengü KAPLAN¹

”

¹ Prof. Dr., University of Mersin, Physics Division, Department of Mathematics and Science Education, iftlikky Campus, 33343 Mersin, Turkey.
bkaplan@mersin.edu.tr Orcid ID: 0000-0002-1334-6137

1. Introduction

Magnetism in amorphous RE-TM (Rare Earth-Transition Metals) thin films have been widely investigated due to their macroscopic physical properties such as remarkable structural, mechanical and thermal characteristics which arise from the intrinsic of the material. RE-TM alloys usually present perpendicular magnetic anisotropy and, when they are prepared in the form of thin films, they show periodic magnetic domain above a certain critical thickness, with lateral dimensions in the range of a few hundred nanometers [1-4]. Several methods were used to determine the first- and second-order anisotropy constants which successfully applied on intermetallic crystals[5] and magnetic thin films [6].

Recently, Alvarez-Prado et al. [7] have determined the anisotropy contributions in the second-order approximation in amorphous Nd-Co thin films by micromagnetic simulations so that these films exhibit stripe shaped periodic magnetic domains with local out-of-plane magnetization components due to their perpendicular magnetic anisotropy. They have observed that the first- and second-order anisotropy constants, K_1 and K_2 respectively, must be used to properly describe the variation of the stripe domains with the in-plane applied field. Their method shows that an accurate description of magnetic anisotropy in Nd-Co amorphous films requires including the second-order anisotropy constant, K_2 , despite being one order of magnitude smaller than K_1 . The second-order anisotropy K_2 plays a crucial role in the magnetic behaviour, resulting in magnetization of ultrathin magnetic films [8]. Theoretical models should take into account especially by considering the role of finite-size walls [9].

It is of interest to look at the magnetostatic solution for the total energy of the stripe pattern for well-separated walls in in-plane applied magnetic field, H , by considering anisotropies in the second-order approximation. In the present study, we would like, however, to consider the magnetization process and also compare the results with experimental observations at low and room temperatures.

2. Calculations and discussion

In this study the film is taken as an infinite slab parallel to the $x - y$ plane with thickness L along the z coordinate. We assume a stripe configuration of walls which is the equilibrium configuration for the continuum model [10,11]. We consider only the situation in which the domain walls are sufficiently widely separated for the interactions between walls to be neglected. The dipolar energy depends on the value of the perpendicular magnetization in the film. The average perpendicular magnetization will

vanish over the region of the wall and this effect causes strong changes in the dipolar energy. Since our theory is valid only for well-separated walls in which ω represents the domain wall width, we use the continuum model to calculate the dipolar energy throughout. The quantity ω is not constant and depends on film parameters, in particular, on the film thickness L , as well. Given a regular array of stripe pattern and assuming that the finite wall width, ω , is important when compared with the stripe period in which the exchange energy would be important. Within these assumptions, the total energy of the system is written as [12, 13]:

$$U_t = \{U_d + U_e + U_{a1}\} \sin^2\theta + U_{a2} \sin^4\theta - (U_{a1} + U_{a2}) + U_o - U_z \quad (1)$$

where θ is the angle between magnetization and normal to the film plane. The first term of the curly brackets, which denotes the magnetostatic energy, is found by expanding the magnetic potential in a Fourier series and matching to the boundary conditions as explained in a previous work [11]. For wider domain walls the magnetostatic energy per unit area is written as:

$$U_d = (2\pi M_o^2 a_o) n_l \left[\left(1 - \frac{4\xi}{\pi^2}\right) - \frac{2}{\pi} \mathcal{N}(\xi)(ka_o)n_l \right] \quad (2)$$

where M_o is the saturation magnetization, a_o is the lattice spacing, n_l is the number of atomic layers, ξ is defined as ω/D , $k = 1/D$, $\mathcal{N}(\xi) = 2P + \ln(\frac{1}{\xi})$, and the value of P is obtained from the finite series [11] and is $P \cong 0.635$. The second term of the curly brackets in Eq. 1 is the exchange energy per unit area in the wall and is given by [10]

$$U_e = \frac{\pi^2}{2\xi} \frac{A}{a_o} (ka_o)^2 n_l \quad (3)$$

where $A = 2JS^2/a_o$, and $2JS^2$ is the interaction energy between the nearest neighbours. The third term of the curly brackets in Eq. 1 is the anisotropy energy per unit area in the wall which is written as [10,13]

$$U_{a1} = -\frac{K_s^1}{2} \left(1 - \frac{4\xi}{\pi^2}\right) n_l \quad (4)$$

where $K_s^1 = K_1 a_o$ represents the first-order anisotropy energy per unit of area. In Eq. 1, U_{a2} represents the second-order anisotropy energy per unit of area which is written as similar to Eq. 4 above in which K_s^2 indicates the

second-order anisotropy energy per unit of area. In Eq. 1, U_o is anisotropy energy independent of the angle and is usually ignored. The last term in Eq. (1) corresponds to the Zeeman energy. We first define a normalized energy, $E = \frac{U_t}{E_o}$ where $E_o = 2\pi M_o^2 a_o$, and $n_l = \frac{L}{a_o}$, $R = \frac{A}{a_o E_o}$, $f_1 = \frac{K_s^1}{2E_o}$, $f_2 = \frac{K_s^2}{2E_o}$, $f_3 = f_1 + f_2$ and therefore the expression for E is given by

$$E = n_l \left[\left\{ (1 - f_1) \left(1 - \frac{4\xi}{\pi^2} \right) - \frac{2}{\pi} \mathcal{N}(\xi) (ka_o) n_l + \frac{\pi^2 R}{2\xi} (ka_o)^2 \right\} \sin^2 \theta - f_2 \left(1 - \frac{4\xi}{\pi^2} \right) \sin^4 \theta + f_3 \left(1 - \frac{4\xi}{\pi^2} \right) - h \sin \theta \cos \left(\frac{\pi}{4} - \varphi \right) \right] \quad (5)$$

By minimizing of Eq. 5 with respect to (ka_o) and θ we obtain Eqs. 6 and 7 respectively in the following:

$$(ka_o) = \frac{2\xi \mathcal{N}(\xi) n_l}{\pi^3 R} \quad (6)$$

and

$$\frac{h}{2} \cos \left(\frac{\pi}{4} - \varphi \right) = \left\{ (1 - f_1) \left(1 - \frac{4\xi}{\pi^2} \right) - \frac{2\xi \mathcal{N}^2(\xi) n_l^2}{\pi^4 R} \right\} \sin(\theta) - 2f_2 \left(1 - \frac{4\xi}{\pi^2} \right) \sin^3(\theta) \quad (7)$$

where $h = \frac{H}{2\pi M_o}$. Equation 6 shows that the actual values of D and ω depend on R , and therefore on the way of dealing with the exchange energy. The surface anisotropy constants exhibit different behaviours with film thickness, with the first-order presenting the usual inverse of ferromagnetic layer thickness. Besides this inverse of thickness behaviour, the second order also comes up with a constant value[14].

Alvarez-Prado et al. [7] experimentally showed that the amorphous Nd-Co thin films exhibit stripe shaped periodic magnetic domain with local out-of-plane magnetization components due to their perpendicular magnetic anisotropy. They observed that the first and second anisotropy constants must be used to properly describe the variation of the stripe domains with the in-plane applied magnetic field. The saturation fields are much higher at 10 K than at 300 K. The values they used are: $L = 100 \text{ nm}$, $M_S = 1.06 \times 10^6 \text{ A/m}$, $K_1 = 8.7 \times 10^5 \text{ J/m}^3$ and $K_2 = 3.4 \times 10^5 \text{ J/m}^3$ at 10 K and also, the exchange stiffness constant $A = 0.7 \times 10^{-11} \text{ J/m}$ for all temperatures.

Further, inserting Eq. 6 into Eq. 5, we write the normalized minimum free energy which is given by

$$E_{min} = n_l \left[\left\{ (1 - f_1) \left(1 - \frac{4\xi}{\pi^2} \right) - \frac{2\xi \mathcal{N}^2(\xi) n_l^2}{\pi^4 R} \right\} \sin^2 \theta - f_2 \left(1 - \frac{4\xi}{\pi^2} \right) \sin^4 \theta + f_3 \left(1 - \frac{4\xi}{\pi^2} \right) - h \sin \theta \cos \left(\frac{\pi}{4} - \varphi \right) \right] \quad (8)$$

At equilibrium $\theta = \pi/2$ as before and for $\varphi = \pi/4$. Using these equilibrium conditions, the Eq. 7 is written as:

$$\frac{h}{2} = (1 - f_{eff}) \left(1 - \frac{4\xi}{\pi^2} \right) - \frac{2\xi \mathcal{N}^2(\xi) n_l^2}{\pi^4 R} \quad (9)$$

where $f_{eff} = f_1 + 2f_2$ [7] which is the effective uniaxial anisotropy constant.

Figures 1(a) and (b) show the $y = \sin \theta$ vs. $H/4\pi M_o$ with the field applied parallel to the film plane using Eq. 7 in which $\varphi = \pi/4$. It can be seen that these curves show clear hysteresis which are given for some values of ξ . The experimental data of Ref. [7] are $f_1 = 0.96$, $f_2 = 0.38$ at $T=300 \text{ K}$ and also $f_1 = 0.62$, $f_2 = 0.24$ at $T=10 \text{ K}$ respectively.

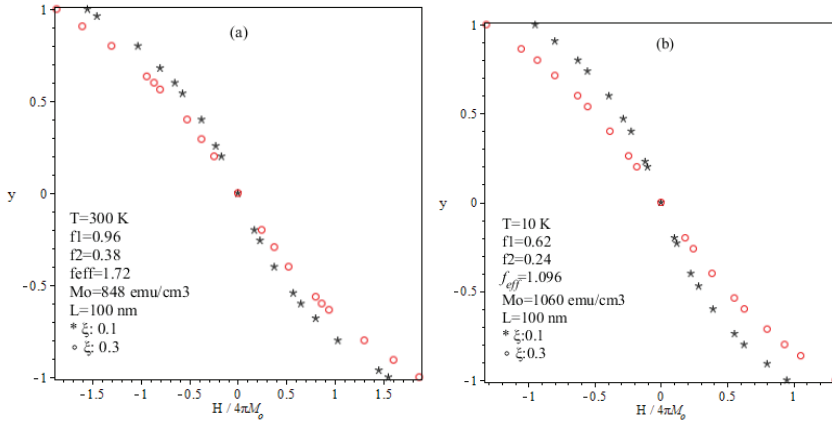


Fig. 1 Hysteresis curves for some values of ξ at 300 K (a) and 10 K (b)

Although it is not shown here, we have found $R \cong 3400$ for different values of ξ which varies in the interval 10^{-1} -1.

Parts of (a) and (b) in Figures 2 also show the magnetization curves for some values of ξ at 300K and 10 K respectively. The magnetization curves are not straight line in general, as would be expected from classical continuum theory but show characteristic deviations.

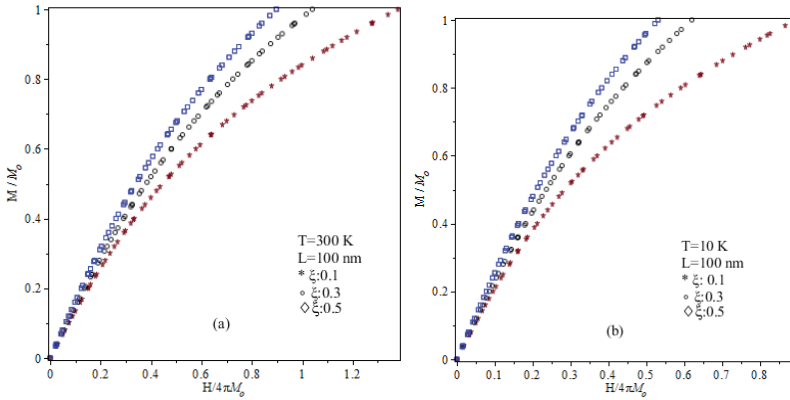


Fig. 2 Magnetization process for the stripe domain structure with different parameter of ξ at 300 K (a) and 10 K (b).

Saturation occurs in a field smaller than $4\pi M_0$, which is in agreement with the Ref. [7]. For large ξ , the film can be magnetized easily, because the normalized saturation field is small. With decreasing ξ , the normalized

saturation field increases, corresponding to the fact that the energy difference between the saturation state and the demagnetized state becomes smaller for the smaller value of ξ . In the linear model, when ξ tends to 1, it corresponds to a nonvanishing domain but as the domain width varies very rapidly in this region, and the contribution of the walls to the total energy soon becomes very high.

Figures 3(a) and (b) show the expected value of D/a_o vs. $H/4\pi M_o$ for a range of values of the second order anisotropy energy at 300 K and 10 K respectively that as ξ varies in the interval 10^{-1} -1. The widths D of the domains with magnetization parallel of the applied field increases very rapidly near saturation whereas the reversed domains decreases only slowly upon magnetization. The theoretical curve is obtained with the parameter values $f_{eff} = 1.72$ at 300 K and 1.09 at 10 K respectively.

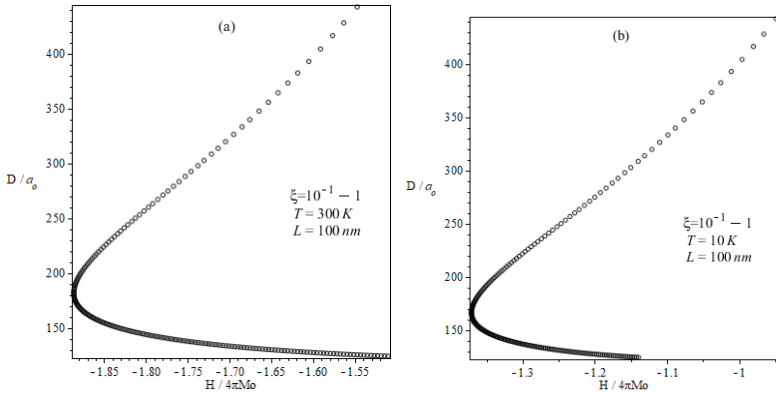


Fig. 3 Field dependent stripe domain period at 300 K (a) and 10 K (b), defined in units of the lattice constants a_o .

Figures 4(a) and (b) show the domain wall width ω/a_o vs. $H/4\pi M_o$ for a range of the second order anisotropy energy at 300 K and 10 K respectively that as ξ varies in the interval 10^{-1} -1. The width ω of the domain walls with magnetization parallel of the applied field increases very rapidly near saturation whereas the reversed domain walls decreases only slowly upon magnetization.

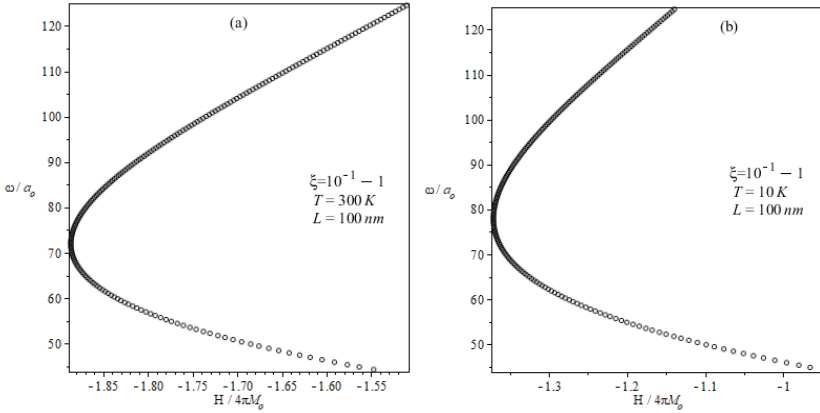


Fig. 4 Field dependent domain wall period at 300 K (a) and 10 K (b), defined in units of the lattice constants a_0 .

3. Conclusions

In conclusion, we calculated the total energy of the magnetized film including the magnetostatic energy, anisotropy energies in the second-order approximation, and the exchange energy in parallel applied magnetic field by using a continuum model. We found that the total energy depends on anisotropy constants, crystallographic orientation and film thickness. We have also deduced a good expression for the width of the domain pattern and the domain wall width. The numerical calculations indicated that the magnetization process has characteristic deviations. Our results show that different anisotropies can be considered in thin films in order to manipulate the stripe domain size and domain-wall size and also magnetization process. The calculated magnetization curves were compared with the experimental data for amorphous Nd-Co thin films and good coincidence was obtained between both curves.

REFERENCES

- [1] Ge, Y., Heczko, O., Södenberg, O., Lindroos, V. K., *J. Appl. Phys.* 96 (2004) 2159.
- [2] Ge, Y., et al. *Mater. Sci. Eng. A* 436-440 (2006) 961.
- [3] Ullakko, K., Huang, J. K., Kantner, C., Kokorin, V. V., O'Handly, R. C., *Appl. Phys. Lett.* 69 (1996) 1966.
- [4] Chernenko, V. A., L'vov, V. A., Golub, V., Aseguinolaza, I. R., Barandiaran, J. M., *Phys. Rev. B* 84 (2011) 054450.
- [5] Gerstein, G., et al. *Funct. Mater. Lett.* 10 (4) (2017) 1750044.
- [6] Rames, M., Heczko, O., Sozinov, A., Ullakko, K., Straka, L., *Scripta Materialia* 142 (2018) 61.
- [7] Alvarez-Prado, L. M., et al. *J. Magn. Magn. Mater.* 456 (2018) 251.
- [8] Yang, G., et al. *Applied Surface Science* 353 (2015) 489.
- [9] Donzelli, O., Bassani, B., Spizzo, F., Palmeri, D., *J. Magn. Magn. Mater.* 320 (2008) e261.
- [10] Yafet, Y. and Gyorgy, E. M., *Phys. Rev. B* 38 (1988) 9145.
- [11] Kaplan, B. and Gehring, G. A., *J. Magn. Magn. Mater.* 128 (1993) 111.
- [12] Nakagawa, S., et al. *Journal de Physique, Colloque C8, Supplement au n° 12,* (1988) Tome 49.
- [13] Kaplan, B., *J. Magn. Magn. Mater.* 288 (2005) 178.
- [14] Oliveira, A. B., et al. *J. Magn. Magn. Mater.* 469 (2019) 64-68.

“

Chapter 3

**STATISTICAL POWER ANALYSIS BASED
ON ONE SAMPLE T-TEST WITH JAMOVI**

Tuğba SÖKÜT AÇAR¹

”

¹ Assist. Prof. Dr. Tuğba Söküt Açar, Çanakkale Onsekiz Mart University, Faculty of Sciences, De-partment of Statistics, t.sokut@comu.edu.tr, ORCID:0000-0002-4444-1671

1. Introduction

Statistical science refers to all the procedures that operate from the moment a research problem is determined. Population and sample are two basic concepts of statistics. After the framework of the problem, that is, the main mass is determined, the researcher can describe the population and its parameters if can make a full count. However, if difficulties (time, space, material, etc.) are encountered in reaching the population, the researcher should choose a sample over the population. There are both probabilistic and non-probabilistic sampling methods for sampling. A sample size of n to be selected from a population of N units is obtained in as many different ways as n combinations of N . And it should not be forgotten that the researcher works with only one of these combinations and makes inferences based on this sample. For this reason, it can never be worked with 100% confidence when making inferences. How many observations/subjects/units capable of representing the population should be taken as the sample size? With what probabilities will the sample represent the population? Can the risk taken in the decision process be calculated in advance? The answer to these questions lies in statistical power analysis. Power analysis is carried out through the following concepts.

Sample Size

If the researcher will conduct the study with the sampling method, how many observations should be determined as the sample size? With another question form, how many sample size increases the ability to represent the population parameter? In most studies, the sample size is determined by standard calculations (see, Noordzij et al. (2010), Zhong (2009)). These calculations are based on specific formulas, and the important thing here is the selection of numbers to insert the formula. These choices should not be the values that the researcher gives to arbitrariness. When making a decision, a minimum sample size should be determined for it to be a test with high power in determining the difference, which is suitable for the design of the study. Determining the sample size based on statistical power is extremely important for the quality of the study. Choosing the right sample size is not a matter of preference, but a crucial element of the analysis (Fox et al., 2009).

Null & Alternative Hypotheses

The hypothesis is the proposition whose population parameters are relevant, and this hypothesis is either true or untrue. On the other hand, the researcher either rejects or cannot reject the hypothesis put forward. Therefore, the hypothesis is constructed in such a way as to choose between two hypotheses that also represent the opposite thought. The first of these,

the null hypothesis expressed by H_0 , states that a population parameter (mean, correlation, variance, etc.) is equal to a default value or zero. An alternative hypothesis expressed by H_1 is a hypothesis that states that a population parameter is different from the default value, i.e. it is established as opposed to the sample in the null hypothesis. An alternative hypothesis is a proposition that is believed to be true or tried to be proven true. Which of these two hypotheses is adopted depends on the numerical value obtained from the sample. If the alternative hypothesis is constructed as less than or greater, a one-tailed test is performed; if it is constructed as not equal, a two-tailed test is performed.

Type I and Type II errors, Power

While forming the hypothesis, the researcher has to decide without knowing the real situation. As a result of the hypothesis test performed based on the sample statistics, the researcher has to either reject the hypothesis or not be able to reject it. There are four possible situations in such a scenario:

| | | Reality | |
|------------------------|-------------------------|--------------------|---------------------|
| | | H_0 True | H_0 False |
| Hypothesis Test Result | H_0 can't be rejected | Correct decision | False decision (II) |
| | H_0 rejected | False decision (I) | Correct decision |

The probabilities of occurrence of the four possible situations are different from each other. There are two false decision cases (I and II). Case I represents the rejection of the H_0 hypothesis as a result of hypothesis testing when H_0 is actually true. It is called α error or Type I error in the literature and is expressed mathematically as $P(H_0 \text{ Rejected} | H_0 \text{ true}) = \alpha$. It is accepted as 5% in research and package programs unless otherwise considered or defined in the program. The literal meaning of this is to accept a 5% probability of accepting a value that is actually true in the long run as false in the long run. While H_0 is actually true, the probability of not rejecting H_0 is $(1 - \alpha)$ as a result of hypothesis testing, that is, it indicates a correct decision. $100(1 - \alpha)$ refers to the level of confidence that the study is conducted, for example, to conduct a study with 95% confidence. Another false decision is case II which means that when H_0 is actually false, the test result is the inability to reject H_0 . This false decision is called β error, that is, Type II error in the literature, and it is mathematically represented by $(P(H_0 \text{ not rejected} | H_0 \text{ false}) = \beta)$. It is generally set at 20%, which means that the propensity to make a Type II error, in the long run, is 20%. In reality, rejecting the test result H_0 when H_0 is false is a

correct decision and is denoted by $(1 - \beta)$. In other words, it is the probability of successfully identifying an existing effect. $100(1 - \beta)$ gives the power of the test. When it has sufficient statistical power, the study is too much Type II error becomes sensitive enough to avoid making. $(1 - \beta)$ is especially prominent in research in medicine and psychology, and in general, studies are carried out with at least 80% power.

Effect Size

It is an important outcome of quantitative research, but there are few guidelines describing how researchers can determine which effect sizes are significant (Anvari and Lakens, 2021). Effect size calculations first started with Cohen (1969) (Goulet-Pelletier and Cousineau, 2018). Effect size is the statistical value that shows the deviation level of the statistics obtained from the sample from the parameter value defined in the null hypothesis (Vacha-Haasse ve Thompson, 2004). That is, it expresses the size of the phenomenon related to the research problem (Bartlett and Charles, 2022). The effect size obtained depending on the null and alternative hypothesis is calculated in two types: non-standardized and standardized. Unstandardized effect size is easy to use where the units of measure are the same, but in many applications, the units of measure can be inconsistent (Baguley, 2009). Standardization of effect size is often carried out for sample size calculation and power analysis because effect size, population distributions, and units vary between research (Kang, 2021). The standardized mean difference known as Cohen's d is one of the most common ways to measure effect size (Hedges et. al., 2012). Since the statistical power will be examined through one sample t-test in this chapter, the formula to be used for Cohen's d is as follows

$$\delta = \text{Cohens } d = \frac{\mu_o - \mu_a}{\sigma} \quad (1)$$

Here μ_o denotes the true value of the population, μ_a denotes the claimed value and σ denotes the population standard deviation. If the population variance σ^2 is unknown, the unbiased estimator sample variance $s^2 = \frac{\sum_{i=1}^n (x_i - \bar{x})^2}{n-1}$ is used. Undoubtedly, there are alternative effect size calculations to Cohen's d (see, Hedges (1983), Algina et al., (2005), Cahan and Gamliel (2011)). A study may be defined as under-reported if the effect size you are trying to detect is smaller than the effect size your study is capable of detecting (Bartlett and Charles, 2022). How much of an effect size would make the study to be conducted meaningful? There are several ways to answer this question. If similar studies have been done before, the effect size of that study is used, that is, it is an inductive method. As another, they can use widely accepted conventions to represent large, medium, or influence (Murphy et al., 2014).

Let's for the one-sample t-test, the error types, decision rule, effect size, and power take over an example.

Example: Assume that the number of borrowed books a student borrows in a year in the central library of a university is normally distributed with 12 standard deviations. The librarian wants to test the following hypothesis by choosing a sample of 50 students and taking the probability of making a Type I error of 0.1, 0.05, and 0.01, respectively:

$$H_0: \mu = 15$$

$$H_1: \mu > 15.$$

While obtaining the test statistics in the test of the hypothesis, it is obtained through the sample statistics. Since the aim of the research is to the average number of books borrowed, the sample statistic is \bar{x} .

The greater the value of \bar{x} is greater than 15, the more likely the librarian will reject the H_0 hypothesis and adopt the H_1 hypothesis. Now, let the decision rules be created for three possible different α errors. In other words, whatever value \bar{x} takes in the sample statistic, the probability that the H_0 hypothesis will be rejected is determined. Suppose the probability of rejection is $\alpha = 0.01$ when H_0 is actually true. Since the alternative hypothesis is $H_1: \mu > 15$, the rejection area will be the area of 0.01 on the right side of the curve. The z-score corresponding to this probability is obtained as $z_{\alpha=0.01} = 2.3263$.

Thus, the rejection region can be written as $2.3263 \leq \frac{\bar{x}-15}{\frac{12}{\sqrt{50}}}$. Using this

inequality, the decision rule is determined as follows: if $\bar{x} \geq 18.9479$, the true $H_0: \mu = 15$ hypothesis will be rejected with a probability of 1%. So, how does the decision rule change if it sets $\alpha = 0.05$? $1.6449 \leq \frac{\bar{x}-15}{\frac{12}{\sqrt{50}}}$ where 1.6449 comes from $z_{\alpha=0.05} = 1.6449$. The interpretation of

this inequality is: If $\bar{x} \geq 17.7915$, the true $H_0: \mu = 15$ hypothesis will be rejected with 5% probability. Finally, let's increase our probability of making the Type I error (α) to 0.1, that is, let's assume the confidence level of the study as 90%. In this case, since: $z_{\alpha=0.10} = 1.216$, the decision rule changes as follows $1.2816 \leq \frac{\bar{x}-15}{\frac{12}{\sqrt{50}}}$. If $\bar{x} \geq 17.1749$, the true $H_0: \mu = 15$

hypothesis will be rejected with a 10% probability. Three different Type I errors created three different decision rules. As the probability of making a Type I error increases, the critical value in the decision rule decreases. This scenario shows that before applying the sample, the researcher who

determined a Type I error can determine in advance at which value of the sample statistic will be rejected H_0 and for which value will not be rejected.

If H_0 is actually false, let's deal with the probability of not rejecting H_0 as a result of hypothesis testing, namely beta error. Since the alternative hypothesis of the research is one-tailed, if $H_0: \mu = 15$ is actually false, $H_1: \mu > 15$ is true in reality and an infinite value can be written to confirm this. For example, let's take $\mu = 20$ and deal with the case where H_0 cannot be rejected. Since β occurs when H_0 cannot be rejected, and it cannot be rejected if $\bar{x} < 18.9479$ for $\alpha = 0.01$, β probability can be written as

$$\begin{aligned}\beta &= P(\bar{x} < 18.9479) = P\left(z < \frac{18.94749 - 20}{\frac{12}{\sqrt{50}}}\right) \\ &= P(z < -0.620) = 0.2676.\end{aligned}\quad (2)$$

Hence the power $(1 - \beta)$ in such a design is obtained as 0.7324.

Now let's calculate what would be the β probability for $\mu = 20$ if the researcher had accepted the probability of making a Type 1 error as 0.05 before making the design. For $\alpha = 0.05$, H_0 cannot be rejected when $\bar{x} < 17.7915$. This leads to the following calculation of the β probability

$$\begin{aligned}\beta &= P(\bar{x} < 17.7915) = P\left(z < \frac{17.7915 - 20}{\frac{12}{\sqrt{50}}}\right) = P(z < -1.3014) = \\ &0.0966.\end{aligned}\quad (3)$$

In such a design, the power would be 0.9034. Finally, let's calculate the probability of the β that the researcher would make if $\alpha = 0.01$ at $\mu = 20$. Since H_0 could not be rejected for $\bar{x} < 17.1749$ for $\alpha=0.10$, this probability is equivalent to

$$\begin{aligned}\beta &= P(\bar{x} < 17.1749) = P\left(z < \frac{17.1749 - 20}{\frac{12}{\sqrt{50}}}\right) \\ &= P(z < -1.6647) = 0.0481.\end{aligned}\quad (4)$$

The power in such a design is 0.9519. Similar methods can be used to determine the β probability and power for each potential value of μ to validate $H_1: \mu > 15$.

The visualization of the decision rules is given in Figure 1. The red dashed straight line in the figures, that is, cv values indicate the critical values of the decision rule.

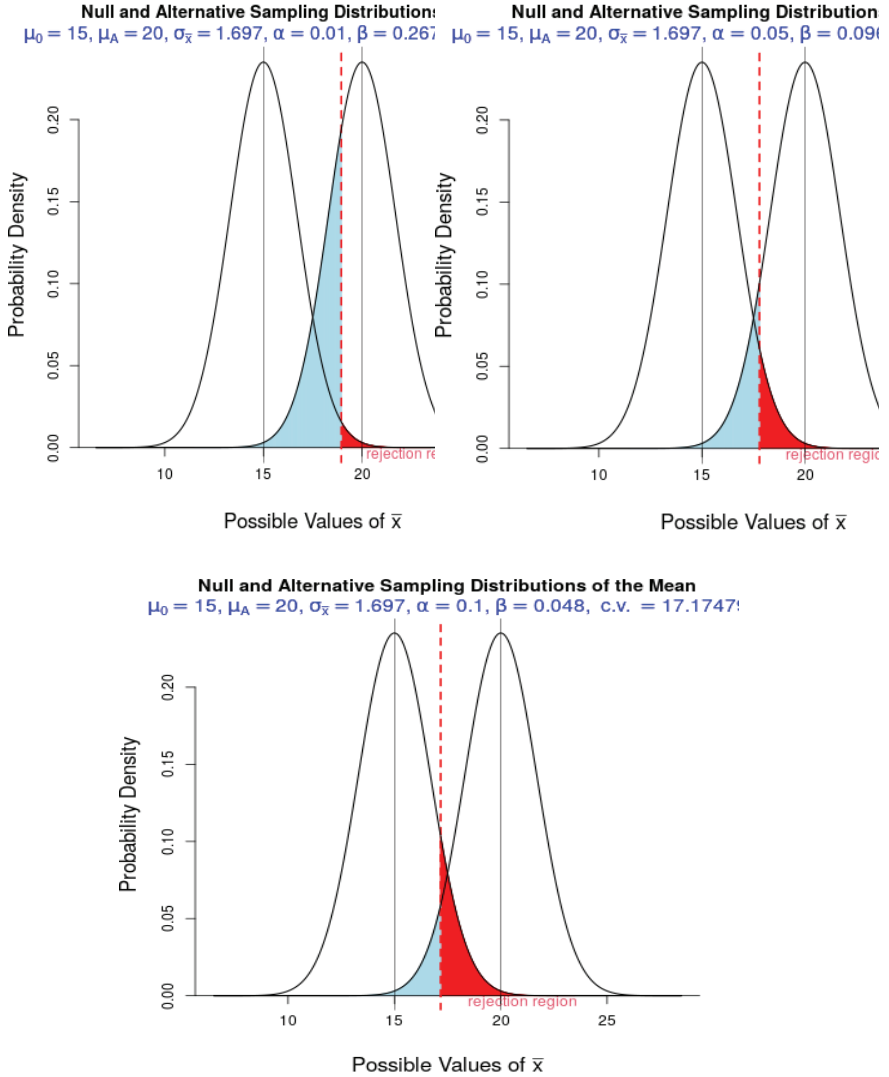


Figure 1. Power analysis visuals at different Type 1 error rates for sample data based on standard normal distribution

Noted that, in the calculations performed on the example, it was assumed that the population parameter $\sigma=12$. For this reason, the test statistic is built on the standard normal distribution and the critical value is based on the z-scores. However, in applications where the population standard deviation is not known, s estimator, which is an unbiased sample statistic, is used. In testing the hypothesis of one sample mean, if the variable is normally distributed but the standard deviation is unknown due to the population variance, the test statistic is built on the Student t distribution and the t score at

the relevant significance level with $n-1$ degrees of freedom is used. The statistical power analysis in Jamovi is based on t-tests.

2. JAMOVI

A modern program called Jamovi has been created using the R programming language. In addition to being free software, it can be used as a cloud directly on the browser or run by installing it on a computer, having a drop-down menu feature, analysis menus and outputs appearing in the same interface and simultaneous results provide a great convenience in analysis and reporting. It is a program whose first version was published in 2019 and is constantly updated by converting the coding logic over R into drop-down menus. To open Jamovi in your browser visit the page <https://cloud.jamovi.org/> or to download the latest version (2.3.18 as of the date of writing of the book) visit the page <https://www.jamovi.org/download.html>. The interface of the program when it was first installed is introduced in Figure 2.

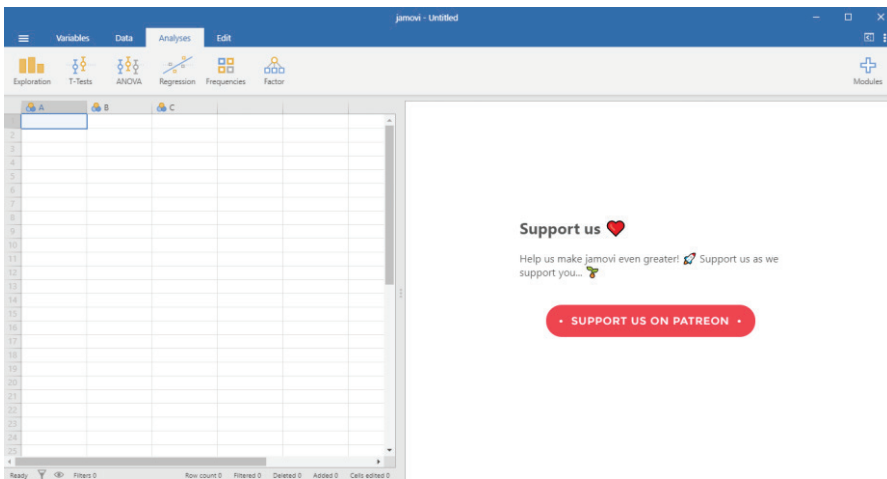


Figure 2. Jamovi interface

As can be seen in Figure 2, the program interface is quite simple and includes a few basic analysis menus. Also, power analysis is not defined in this section. Jamovi library is selected from the modules section in the upper right corner of the interface and jpower is installed from there (Figure 3).

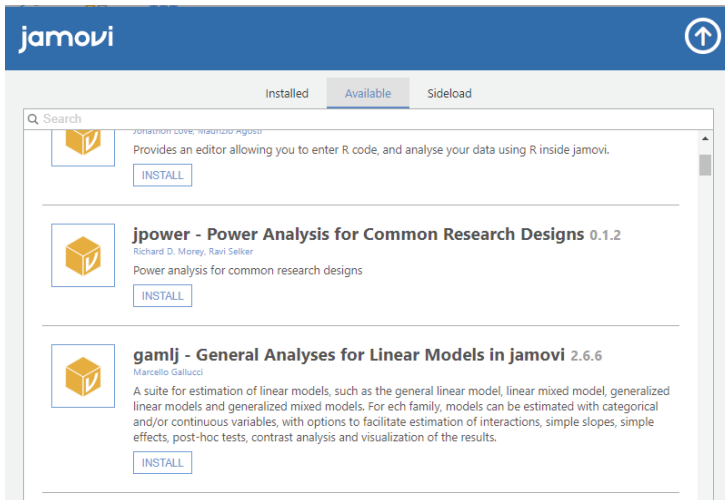


Figure 3. Uploading power analysis to Jamovi

In Jamovi, power analysis is limited to independent samples t-test, paired-samples t-test, and one sample t-test. There are three different purposes in statistical power analysis with Jamovi. The sample size (N), power, and effect size in the calculate tab are selected which is suitable for the purpose. If the aim is to determine the power, the minimally-interesting effect size (δ), sample size (n), and Type I error rate (α), and whether it is one-tail or two-tails in the alternative hypothesis are entered by the researcher. The analysis result is given on the right screen of the interface simultaneously.

Let's apply the example that was examined theoretically in the first chapter with Jamovi. In this example since the purpose is to determine the power, values are entered as in Figure 4.

The screenshot shows the 'One Sample T-Test' window. The 'Calculate' dropdown is set to 'Power'. The input fields are: Minimally-interesting effect size (δ) = 0.417, Minimum desired power = 0.9, N = 50, α (type I error rate) = 0.01, and Tails = one-tailed (consistent). Under 'Plots', all four options are checked: Power contour plot, Power curve by effect size, Power curve by N, and Power demonstration. Under 'Additional Options', 'Explanatory text' is checked.

Figure 4. Assigning values in power analysis

For this example, the sample size is $n = 50$, the effect size is $\delta = \left| \frac{15-20}{12} \right| = 0.417$, $\alpha = 0.01$ and since $H_1: \mu > 15$ the hypothesis is one-tailed (Fig. 4).

Table 1 gives the power value calculated with the information entered by the researcher.

Table 1. A Priori Power Analysis

| Power | User Defined | | |
|-------|--------------|-------------|----------|
| | N | Effect Size | α |
| 0.706 | 50 | 0.417 | 0.0100 |

A design with a sample size of 50 can detect effect sizes of $\delta \geq 0.417$ with a probability of at least 0.706, assuming a one-sided criterion for detection that allows for a maximum Type I error rate of $\alpha = 0.01$ (Table 1).

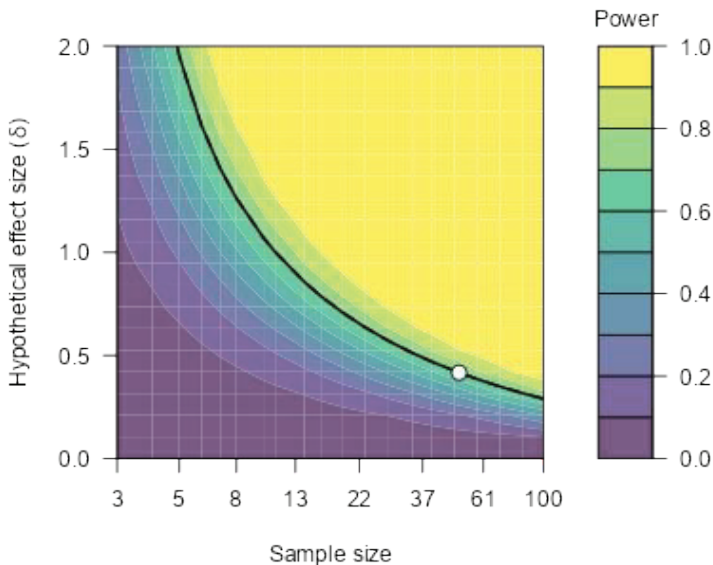
Table 2 shows the interpretation of effect size according to the inputs in Figure 3.

Table 2. Power by Effect Size

| True effect size | Power to detect | Description |
|---------------------|-----------------|------------------------|
| $0 < d = 0.338$ | $\leq 50\%$ | Likely miss |
| $0.338 < d = 0.461$ | 50% – 80% | Good chance of missing |
| $0.461 < d = 0.578$ | 80% – 95% | Probably detect |
| $d = 0.578$ | $\geq 95\%$ | Almost surely detect |

If the minimally-interesting effect size can be increased to 0.578 when other inputs are kept constant, then it is clearly seen that the power of the test will exceed 95% (Table 2). And also, effect sizes smaller than $\delta=0.338$ are definitely missed (power less than 50%).

The power contour is presented in Figure 5. With a power contour, researchers can quickly see what type of effect sizes can be reliably detected at which sample widths.

**Figure 5.** Power Contour

The solid black curve in Figure 5 shows the sample size/effect size combinations with a power of 0.705. The dot indicates the design and effect size

specified. Considering the scale to the right of Figure 5, it is clear that smaller effect sizes become reliably detectable as the sample size increases. In Figure 6, the graph of the power curve according to the effect size is presented.

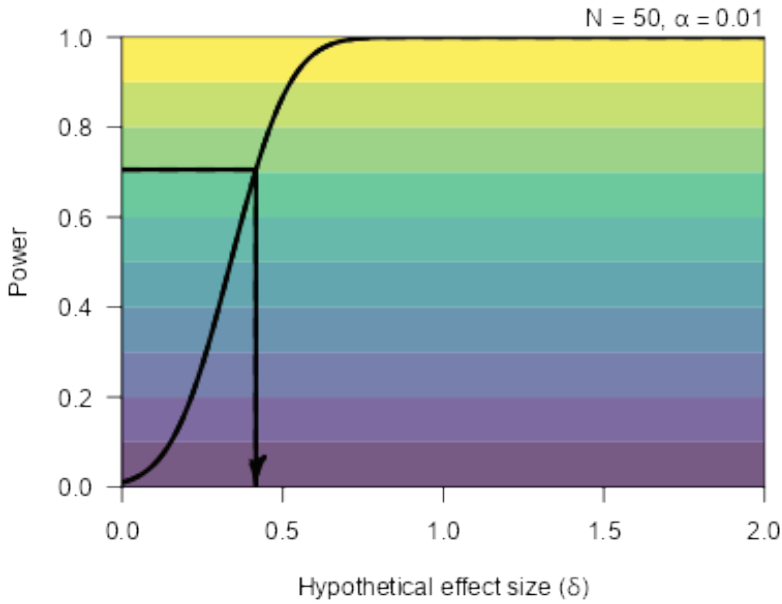


Figure 6. Power Curve by Effect Size

Figure 6 shows that the test and design would have a power of at least 0.706 to effect sizes of $\delta > 0.417$ if the sample size is 50. It is clear that the power of the test decreases as the effect size approaches zero.

Figure 7 is a graph showing the power of the test according to the sample size when the effect size and probability of making a Type I error are held constant in the research design.

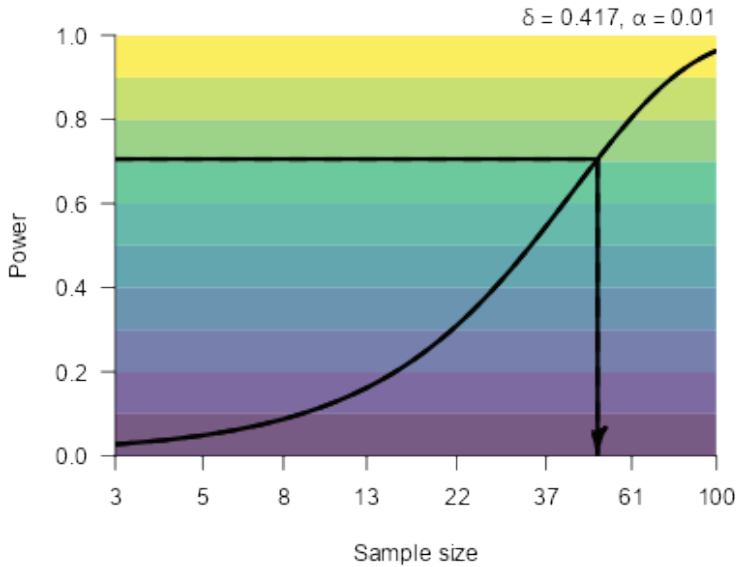


Figure 7. Power Curve by N

Figure 7 shows that for the test and design to have sufficient sensitivity (power > 0.706) to detect $\delta \neq 0$, a sample size of at least 50 is needed when the effect size is 0.417 or greater. In addition, it is clear that the power of the test increases as the number of samples increases. Figure 8 is a graph that visualizes Type I error, Type II error, and power probabilities together.

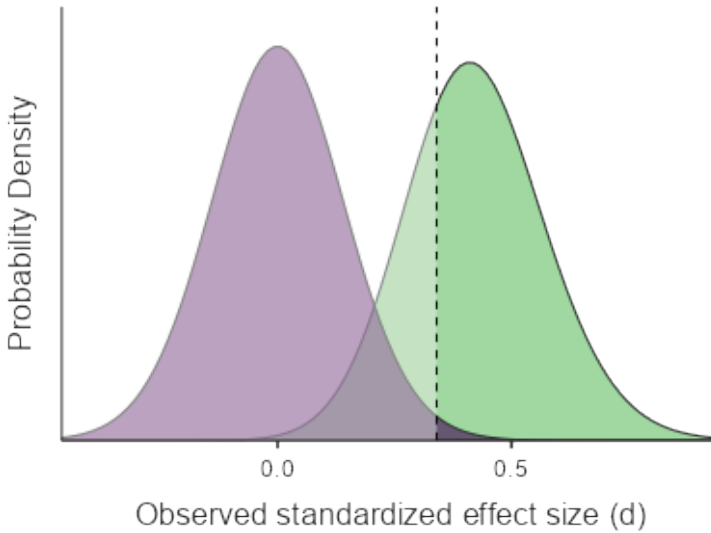


Figure 8. Power Demonstration

The curve on the left represents the distribution where the effect size is 0, that is, the H_0 hypothesis is actually true, while the curve on the right represents the distribution where the effect size is 0.417, that is, the H_1 hypothesis is actually true. The vertical line shows the value in the decision rule calculated for $\alpha=0.01$, that is, the critical value. The light purple area in the left distribution shows the probability of $1-\alpha=0.99$. In other words, it is the probability of not rejecting H_0 as a result of hypothesis testing when H_0 is actually true. The small dark purple area in the left distribution shows the probability of $\alpha=0.01$. In other words, it is the probability of rejecting H_0 as a result of hypothesis testing when H_0 is actually true.

Type II error, β , shows in the distribution on the right since it deals with the case where H_0 is actually false. And in this distribution, the area to the left of the critical value line gives the probability of making the Type II, that is, $\beta = 0.294$. The area to the right of the critical value line in the second distribution gives the probability $(1 - \beta) = 0.706$ that H_0 is rejected as a result of hypothesis testing when H_0 is actually false.

If the aim was to determine the sample size with statistical power analysis in Jamovi, the results would be as in Figure 9.



Figure 9. Calculating sample size with values defined in a one-tailed hypothesis test in jpower

The inputs and outputs in Figure 9 confirm that if the minimum desired power was determined to be 0.80, a sample of 61 units would have to be selected for an effect size of 0.417 when a one-way test was performed with an alpha error of 0.01.

If the aim was to determine the effect size with statistical power analysis in Jamovi, the results would be as in Figure 10.



Figure 10. Calculating effect size with values defined in a one-tailed hypothesis test in jpower

In a one-tailed test performed with a probability of Type I error of 0.01 in a sample of 50 units, the effect size would have to be 0.461 to perform the analysis with a minimum power of 80% (Fig. 10).

If the aim was to determine the power for a two-tailed hypothesis test with statistical power analysis in Jamovi, the results would be as in Figure 11.

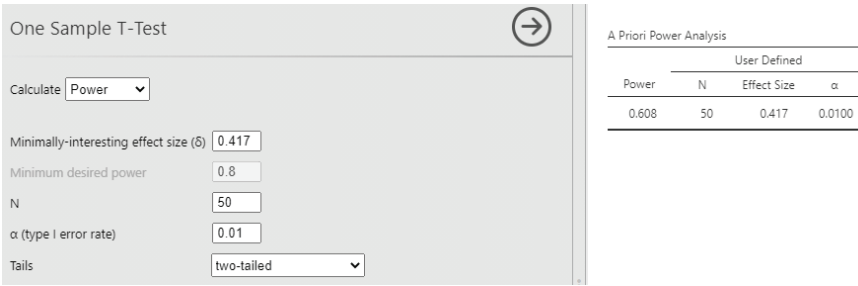


Figure 11. Calculating power with values defined in a two-tailed hypothesis test in jpower

If a two-tailed hypothesis test were performed (that is $H_1: \mu \neq 15$), the power of the test would be 0.608 for $\alpha=0.01$ probability of Type 1 error, a sample size of 50 units, and effect size of 0.417 (Fig. 11). Comparing Table 1 to Fig. 11, it is seen that the two-tailed test has less power than the one-tailed test.

If the aim was to determine the sample size for a two-tailed hypothesis test with statistical power analysis in Jamovi, the results would be as in Figure 12.

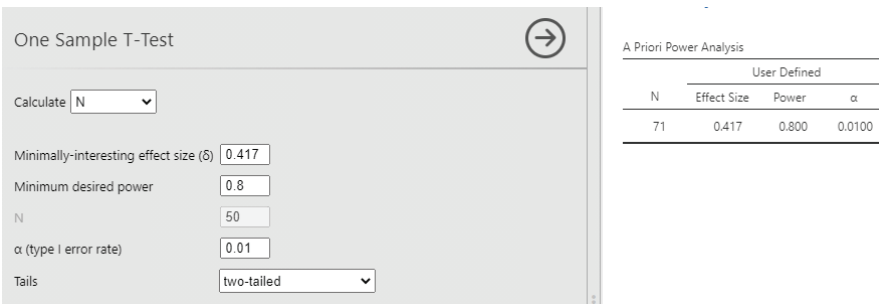


Figure 12. Calculating sample size with values defined in a two-tailed hypothesis test in jpower

A sample size of 71 is required to increase the power of the test to 0.80 at the same effect size (Fig. 12).

Finally, if the aim is to determine the effect size with jpower in the two-tailed hypothesis test, the inputs and outputs will be as in Figure 13.

One Sample T-Test

Calculate: **Effect size**

Minimally-interesting effect size (δ): 0.5

Minimum desired power: 0.8

N: 50

α (type I error rate): 0.01

Tails: two-tailed

A Priori Power Analysis

| Effect Size | User Defined | | |
|-------------|--------------|-------|----------|
| | N | Power | α |
| 0.500 | 50 | 0.800 | 0.0100 |

Figure 13. Calculating effect size with values defined in a two-tailed hypothesis test in jpower

Figure 13 shows that, in a two-tailed hypothesis test for $\alpha = 0,01$, $n = 50$ the effect size should be 0.50 in order to reach a minimum power of 0.80.

Conclusion

In statistics, hypothesis testing is the process by which a population parameter assumption is put to the test. A hypothesis is either true or not true and when we perform a hypothesis test, we either accept or reject the null, H_0 , hypothesis. In fact, the researcher creates a decision rule under uncertainty. This uncertainty presents as a Type I error (falsely rejecting the null hypothesis) and a Type II error (accepting the null hypothesis as false). Acceptable sizes of Type I and Type II errors are predetermined and are important for sample size, effect size, and power analysis calculations. While the research design is designed, the error concepts are not considered much, but the probability of error types is set as the values accepted by the researcher. We must design a pattern that minimizes both types of errors in hypothesis testing. Identifying the beta bug may seem a bit more complicated than identifying the alpha bug. Statistical power is calculated by checking all error probabilities with Jamovile. Jamovi provides the researcher with the opportunity to perform analysis by determining the sample size, effect size, and power most suitable for his design. It should not be forgotten that it is impossible to control research that is not designed properly. For this reason, all investigations should be done before doing research.

REFERENCES

- Algina, J., Keselman, H. J., & Penfield, R. D. (2005). An alternative to Cohen's standardized mean difference effect size: a robust parameter and confidence interval in the two independent groups case. *Psychological methods*, 10(3), 317.
- Anvari, F., & Lakens, D. (2021). Using anchor-based methods to determine the smallest effect size of interest. *Journal of Experimental Social Psychology*, 96, 104159.
- Baguley, T. (2009). Standardized or simple effect size: What should be reported? *British journal of psychology*, 100(3), 603-617.
- Bartlett, J. E., & Charles, S. J. (2022). Power to the People: A Beginner's Tutorial to Power Analysis using jamovi. *Meta-Psychology*, 6.
- Cahan, S., & Gamliel, E. (2011). Cohen's d vs Alternative Standardized Mean Group Difference Measures. *Practical Assessment, Research, and Evaluation*, 16(1), 10.
- Cohen, J. (1969). *Statistical Power Analysis for the Behavioral Sciences*. New York: Academic Press.
- Fox, N., Hunn, A., & Mathers, N. (2009). Sampling and sample size calculation. East Midlands/Yorkshire: the National Institutes for Health Research. Research Design Service for the East Midlands/Yorkshire & the Humber.
- Goulet-Pelletier, J. C., & Cousineau, D. (2018). A review of effect sizes and their confidence intervals, Part I: The Cohen's d family. *The Quantitative Methods for Psychology*, 14(4), 242-265.
- Hedges, L. V. (1983). A random effects model for effect sizes. *Psychological bulletin*, 93(2), 388.
- Hedges, L. V., Pustejovsky, J. E., & Shadish, W. R. (2012). A standardized mean difference effect size for single case designs. *Research Synthesis Methods*, 3(3), 224-239.
- Kang, H. (2021). Sample size determination and power analysis using the G* Power software. *Journal of educational evaluation for health professions*, 18.
- Murphy, K. R., Myers, B., & Wolach, A. (2014). *Statistical power analysis: A simple and general model for traditional and modern hypothesis tests*. Routledge.
- Noordzij, M., Tripepi, G., Dekker, F. W., Zoccali, C., Tanck, M. W., & Jager, K. J. (2010). Sample size calculations: basic principles and common pitfalls. *Nephrology dialysis transplantation*, 25(5), 1388-1393.

- R Core Team (2021). *R: A Language and environment for statistical computing*. (Version 4.1) [Computer software]. Retrieved from HYPERLINK "<https://cran.r-project.org>" \t "_blank" <https://cran.r-project.org>. (R packages retrieved from MRAN snapshot 2022-01-01).
- The jamovi project (2022). *jamovi*. (Version 2.3) [Computer Software]. Retrieved from HYPERLINK "<https://www.jamovi.org>" \t "_blank" <https://www.jamovi.org>.
- Vacha-Haase, T., & Thompson, B. (2004). How to estimate and interpret various effect sizes. *Journal of counseling psychology*, 51(4), 473.
- Zhong, B. (2009). How to calculate sample size in randomized controlled trial?. *Journal of thoracic disease*, 1(1), 51.

“

SECTION 4

**STORAGE OF LIQUID CHEMICALS
USED FOR EXPERIMENTS AT BANAZ
VOCATIONAL SCHOOL**

Melek GOKMEN KARAKAYA¹

”

¹ *University of Usak, Banaz Vocational School 64500 Banaz USAK, TURKEY.*
melek.karakaya@usak.edu.tr

INTRODUCTION

Safety is the essential principle in the laboratory studies. Accuracy and precision and finalization experiment in the laboratory without causing an accident are main targets. However, it must be kept in mind could encounter with any bad incident at any moment by accident. Assessments for safe operation should be made and some measures to secure work before starting the laboratory work should be taken. Before starting the experiment; the physical conditions of the laboratory, materials and chemicals that will be used should be evaluated.

A list of chemical substances to be used in the test laboratory should be performed and properties of substances (Physical hazards, hazard for human health, and environment hazard) should be investigated and measures taken according to current Commission Regulation (EU) 2017/542 of 22 March 2017 (Commission Regulation (EU) 2017/542).

Global Harmonized System of Classification and Labelling of Chemicals (GHS) is used around the world. GHS provides convenience in taxation and custom union. GHS has standardized hazard-testing criteria, universal warning pictograms, and harmonized safety data sheets. United Nations' GHS into EU law as the Classification and Labelling of Chemicals (CLP) Regulation that take place under European Chemical Agency (ECHA) Legislations. In Turkey, according to the topic the Regulation published December 10, 2020 dated and 31330 numbered Official Newspaper, Republic of Turkey, Regulation Amending the Regulation on Classification, Labeling and Packaging of Substances and Mixtures (T.C. Resmi Gazete, 2020). Prior to this Amending Regulation published December 11, 2013 dated and 28848-numbered Official Newspaper, Regulation on Classification, Labeling and Packaging of Substances and Mixtures was in effect (T.C. Resmi Gazete, 2013). This Regulation was prepared on the basis of 4 laws, 4 decrees and 1 statute that entered into force in Turkey between 1930 and 2011 and parallel with the provisions of **Regulation (EC) No 1272/2008 of the European Parliament and of the Council of 16 December 2008 on classification, labelling and packaging of substances and mixtures, amending and repealing Directives 67/548/EEC and 1999/45/EC, and amending Regulation (EC) No 1907/2006.**

Commission Regulation (EU) 2017/542 of 22 March 2017 (Commission Regulation (EU) 2017/542) amending Regulation (EC) No 1272/2008 (**Regulation (EC) No 1272/2008**) of the European Parliament and of the Council on classification, labelling and packaging of substances and mixtures by adding an Annex on harmonised information relating

to emergency health response. Labelling according Regulation (EC) No 1272/2008 had been prepared based on the Environmental Law No. 2872 dated 9/8/1983; Decree-Law on the Organization and Duties of the Ministry of Environment and Urbanization dated 29/6/2011 and numbered 644; Decree-Law on the Organization and Duties of the Ministry of Health and its Affiliates, dated 11/10/2011 and numbered 663; Public Health Law No. 1593 dated 24/4/1930; Decree-Law on the Organization and Duties of the Ministry of Customs and Trade, dated 3/6/2011 and numbered 640; Decree-Law on the Organization and Duties of the Ministry of Food, Agriculture and Livestock, dated 3/6/2011 and numbered 639; Veterinary Services, Plant Health, Food and Feed Law dated 11/6/2010 and numbered 5996; Law on the Preparation and Implementation of the Technical Legislation Regarding the Products dated 29/6/2001 and numbered 4703; Regulation on the Procedures and Principles of Production, Import, Transport, Storage, Storage, Sale, Use, Disposal, Inspection of Explosive Substances Excluded from Monopoly, Hunting Equipment and the like, which was put into effect with the Decision of the Council of Ministers dated 14/8/1987 and numbered 87/12028.

Commission Regulation (EU) 2017/542 incorporates the classification criteria and labelling rules agreed at the UN GHS. CLP introduced European hazard symbols (pictograms), Risk and Safety Statements for labelling.

The regulation aims to protect workers, consumers and the environment by labelling that reflects a particular chemical's possible hazards. Importers and downstream users placing such products on the market should provide specific product information to the Ministry of Health. Importers and downstream users placing such products on the market should provide specific product information to the poison centers in EU and in Turkey T.C. Ministry of Health, General Directorate of Public Health, Department of Administrative and Financial Affairs, to the National Poison Information Center in Turkey.

The unique formula identifier (UFI, 16-digit code) will appear on product labels as a new identification element from 2020. By 2025, the UFI will become mandatory on the label of all products classified for health or physical hazards. The submitter shall create a unique formula identifier, herein after UFI, by electronic means made available by the Agency. The UFI is a unique alphanumeric code that unambiguously links the submitted information on the composition of a mixture or a group of mixtures to a specific mixture or group of mixtures.

The first comprehensive studies dealing with the classification, labeling, Packaging and storage of dangerous chemicals published

in 1967, which was Dangerous Substances Directive (67/548/EEC) (Council Directive 67/548/EEC, 1967) **and this** Directive applied only to pure substances, not preparations, and developed in 1999 with Dangerous Preparations Directive (1999/45/EC) (Directive 1999/45/EC). **CLP Regulation replaced this** Regulation (EC) No 1272/2008 (**Regulation (EC) No 1272/2008**). CLP regulation came into force in January 2009 (Chemical Glossary, 2009). Then Commission Regulation (EU) 2017/542 of 22 March 2017 (Commission Regulation (EU) 2017/542) **has** amending Regulation (EC) No 1272/2008 (**Regulation (EC) No 1272/2008**).

It is a regulation in all EU Member States, including the UK. The regulation requires companies to appropriately classify, label and package substance before placing them on the market. This is a way of protecting handlers, consumers and the environment. Because it warns them of dangers and precautions to take when handling a particular package that may present a hazard. The CLP Regulation adopts the United Nations' Globally Harmonized System on the classification and labeling of chemicals (GHS), and is legally binding, as it is currently voluntary rather than a law. CLP is expected to facilitate global trade and the harmonized communication of hazard information of chemicals and it incorporates the classification criteria and labeling rules agreed at UN level GHS. However, CLP introduces new classification criteria, European hazard symbols, Risk, and Safety Statements.

This Regulation should ensure a high level of protection of human health and the environment as well as the free movement of chemical substances, mixtures and certain specific articles, while enhancing competitiveness and innovation. A high level of human health and environmental protection should be ensured in the approximation of legislation on the criteria for classification and labelling of substances and mixtures, with the goal of achieving sustainable development.

Classification, Labelling and Packaging regulation had to propose until 1 December 2010 “provisional classifications” for substances, which had been used for the labelling of pure substances since that date. The deadline for classifying mixtures was 31 May 2015. The deadline for re-labelling and re-packaging of products already on the market was 1 June 2017 (European Chemicals Agency, Labels, 2017).

Republic Of Turkey Ministry of Environment, Urbanization and Climate Change is the competent authority in the application of regulations for classification, Labeling and packaging in Turkey.

The objective of this Regulation should be to determine which properties of substances and mixtures, and should lead to a classification as hazardous, in order for the hazards of substances and mixtures to be

properly identified and communicated. Such properties should include physical hazards as well as hazards to human health and to the environment, including hazards to the ozone layer.

PURPOSE

This study aimed at the safe storage of liquid chemicals, which are found Banaz Vocational School of Chemistry and Chemical Process Technology Department, Chemistry Laboratory, according to the CLP regulation for the best practice on experiments and create a chemical inventory.

This study includes the current liquid chemicals, which are found in the Banaz Vocational School Laboratory. Label information of these chemicals have been found from the list in Annex section third Table 3.2. pages from 996 to 1630 (T.C. Resmi Gazete, 2020). These chemicals were grouped according to hazard class (Physical hazards (flammable, explosive, oxidizing potential), hazard for human health, and environment hazard). Chemicals are divided into groups and placed individually in ventilated chemical locker. Hazard symbols and chemical list was pasted on the chemical locker.

METHOD

The safe storage of hazardous chemicals is an essential part of protection an environmental, health, and safety program. The material safety data sheet [MSDS] for the substance must be referred to in order to determine safe storage conditions and any incompatibilities. Materials of compatible or incompatible were separated then stored appropriate storage lockers. Pictograms dealing with stored chemicals in were adhered on the lockers.

FINDINGS

For Principles of Safe Storage, firstly chemical inventory was created and all hazardous chemical containers were appropriately and clearly labeled with hazard category for the benefit of current users (students and academic staff), emergency personnel, and future users. Secondly materials were separated and stored according to their chemical family or hazard classification. Finally segregated chemicals were placed chemical lockers.

In Banaz Vocational School chemistry laboratory hazard classes for liquid chemicals consist of flammable, oxidizing, corrosive acid, corrosive base, toxic, health hazard (exclamation mark), serious health hazard, environmental hazard liquid chemical classes. Some chemicals situated there are incompatible each other. Accidentally contact between incompat-

tible chemicals can result in a fire, an explosion, the formation of highly toxic and/or flammable substances, or other potentially harmful reactions: Oxidizers mixed with flammable solvents can cause a fire. Acids mixed with metal dust can produce flammable hydrogen gas. For example, if nitric acid (an oxidizing acid) and zinc powder (a combustible metal) were stored together and an accidentally broke their containers, the chemicals could mix and react with violence explosive.

In this study, each chemical family was separated from all other chemical families and stored safely by an approved chemical storage locker. Each hazard class was being kept in a locker separately or on a shelf segregated from other hazard classes. Incompatible chemicals within the same hazard class were also being separated from one another. For example, hydrochloride acid is incompatible with organic acids (such as acetic acid) and they were stored separately. Flammable liquids were stored in appropriate flammable storage lockers. In this locker, we did not store anything without flammable or combustible liquids.

Generally, in safety storage chemicals; acids are separated from bases; in acid groups, organic acids are separated mineral acids. Oxidizers are kept away other chemicals, especially flammables, combustibles, and toxic materials. Corrosives are kept away from substances that they may react with and release corrosive, toxic or flammable vapors. Some chemicals concern one hazard class, where as many chemicals belong to more than one chemical family or hazard class. In such cases, all storage rules must be strictly observed. For example, acetic acid is both a corrosive acid and a flammable liquid. It must be stored away from corrosive bases, such as sodium hydroxide, and from oxidizing acids, such as nitric acid. For more specific information, labels can be obtained from material safety data sheets (MSDSs) from the manufacturer. MSDSs provide information on chemical compatibility and incompatibility.

Common incompatible chemicals do not store in close proximity to each other. In a fire, earthquake, or another accidently spill, they could mix and react violently and/ or release poisonous gas.

According to the chemical inventory belong to this chemistry laboratory; Acetic acid does not store incompatible chemicals, which are nitric acid, ethylene glycol. Acetone does not store with concentrated sulfuric and nitric acid mixtures. Aniline does not store with nitric acid and hydrogen peroxide. Bromine does not store with ammonia. Hydrogen Peroxide does not store with flammable liquids or combustible materials and aniline. Nitric Acid does not store with acetic acids, aniline, flammable material. Sulfuric acid does not store with chlorates, perchlorates, per-

manganates, which are solid because of this these chemicals were stored another locker in this chemistry laboratory.

Storage areas were labeled according to the type of chemical family or hazard classification found there.

Doorways, exits, aisles are kept clear. Storage areas are kept well lit and appropriately ventilated. Ignition sources are eliminated such as open flames, heat sources, or direct sunlight. Fire extinguishers and emergency equipment are kept handy in good working state. Leaks or spills are controlled by confining chemical storage areas. Chemicals were not stored under the sink lest chemicals should be got wet from water.

A lot of chemicals have multiple hazard classifications. Consequently, several storage guidelines according to MSDS are used to determine how to store a hazardous chemical safely. For example, acetic acid is a corrosive acid and also a combustible liquid. For this reason, one hazard class chemicals, if they are compatible, are stored with together. For example some of Flammables and Combustibles Characteristic Chemicals are stored together. These chemicals are easily ignited and may present a serious fire and explosion hazard. Flammable (pyrophoric) liquids have a flashpoint below 23°C and at or below 93°C (1910.106 - Flammable liquids).

Table I shows Hazard Class Pictograms, Hazard Class Code and Hazard Class according to The Classification, Labelling and Packaging (CLP) (Commission Regulation (EU) 2017/542). Regulation purpose is to ensure a high level of protection of health and the environment, as well as the free movement of substances, mixtures and articles.










| <i>Table I Hazard Class pictogram, Hazard Class Code and Hazard Class according to Commission Regulation (EU) 2017/542 and T.C. Resmi Gazete 2020</i> | | |
|---|------------------------------------|--|
| Hazard Class Pictograms | Hazard Class Code and Hazard Class | What does it mean? |
| | GHS02: Flammable | Extremely flammable gas Flammable gas. Extremely flammable aerosol Flammable aerosol Highly flammable liquid and vapor Flammable liquid and vapor Flammable solid |
| | GHS03: Oxidizing | May cause or intensify fire; oxidizer. May cause fire or explosion; strong oxidizer |
| | GHS05: Corrosive | May be corrosive to metals Causes severe skin burns and eye damage |
| | GHS06: Toxic | Fatal if swallowed Fatal in contact with skin Fatal if inhaled Toxic: if swallowed Toxic in contact with skin Toxic if inhaled |
| | GHS07: Health Hazard | May cause respiratory irritation May cause drowsiness or dizziness May cause an allergic skin reaction Causes serious eye irritation Causes skin irritation Harmful if swallowed Harmful in contact with skin Harmful if inhaled Harms public health and the environment by destroying ozone in the upper atmosphere |












| <i>Table I Hazard Class Pictograms, Hazard Class Code and Hazard Class according to Commission Regulation (EU) 2017/542 and T.C. Resmi Gazete 2020</i> | | |
|--|------------------------------------|--------------------|
| Hazard Class Pictograms | Hazard Class Code and Hazard Class | What does it mean? |
| | | |




| | | |
|--|------------------------------|---|
| | GHS08: Serious Health Hazard | May be fatal if swallowed and enters airways Causes damage to organs May cause damage to organs May damage fertility or the unborn child Suspected of damaging fertility or the unborn child May cause cancer Suspected of causing cancer May cause genetic defects Suspected of causing genetic defects May cause allergy or asthma symptoms or breathing difficulties if inhaled |
| | GHS09: Environmental Hazard | Very toxic to aquatic life with long lasting effects Toxic to aquatic life with long lasting effects |

Flammable Liquids in Banaz Vocational Scholl Chemistry laboratory were listed on the table II. Chemicals: alcohols (methanol, ethanol, 2-metilpropan-2-ol, 2-propanol, anisole, 3-methylanisole), esters (ethyl acetate), ethers (diethyl ether, methyl phenyl ether (anisole), ethyl phenyl ether, tetrahydrofuran), ketones (acetone, ethyl methyl ketone), acid (acetic acid glacial %100 pure), other flammable liquids (toluene, n- hexane, acetonitrile, N,N-dimethyl formamide, propargyl bromide, benzene.).

Table II: Flammable Liquid Chemical Material List. Hazard Class according to and T.C. Resmi Gazete 2020









| FLAMMABLE LIQUID CHEMICAL LIST | | Hazard Class Code and Hazard Class | Hazard Class Pictograms |
|--------------------------------|-------------------------------|--|---|
| 1 | 2-metilpropan-2-ol | GHS02: Flammable, GHS08: Serious Health Hazard |   |
| 2 | 2-propanol | GHS02: Flammable GHS07: Health Hazard GHS08: Serious Health Hazard |    |
| 3 | 3-methylanisole | GHS02: Flammable GHS07: Health Hazard |   |
| 4 | Acetic acid glacial %100 pure | GHS02: Flammable GHS05: Corrosive |   |














| Table II: Flammable Liquid Chemical Material List. Hazard Class according to Commission Regulation (EU) 2017/542 and T.C. Resmi Gazete 2020 | | |
|---|---|--|
| FLAMMABLE LIQUID CHEMICAL LIST | Hazard Class Code and Hazard Class | Hazard Class Pictograms |
| 5 Acetone | GHS02: Flammable, GHS07: Health Hazard |  |
| 6 Acetonitrile | GHS02: Flammable, GHS07: Health Hazard |  |
| 7 Anisole | GHS02: Flammable, GHS07: Health Hazard |  |
| 8 Benzene | GHS02: Flammable GHS08: Serious Health Hazard GHS07: Health Hazard |  |
| 9 Diethyl ether | GHS07: Health Hazard GHS02: Flammable |  |
| 10 Ethanol | GHS02: Flammable GHS07: Health Hazard |  |
| 11 Ethyl acetate | GHS02: Flammable GHS07: Health Hazard |  |
| 12 Ethyl methyl ketone | GHS02: Flammable GHS07: Health Hazard |  |
| 13 Methanol | GHS02: Flammable, GHS06: Toxic GHS08: Serious Health Hazard |  |
| 14 n- Hexane | GHS02: Flammable GHS08: Serious Health Hazard GHS07: Health Hazard GHS09: Environmental Hazard |  |
| 15 N,N- Dimethylformamide | GHS02: Flammable GHS08: Serious Health Hazard GHS07: Health Hazard |  |
| 16 Phenetole; Ethoxybenzene; Ethyl phenyl ether | GHS02: Flammable | |

| <i>Table II: Flammable Liquid Chemical Material List. Hazard Class according to Commission Regulation (EU) 2017/542 and T.C. Resmi Gazete 2020</i> | | | |
|--|---|--|--|
| FLAMMABLE LIQUID CHEMICAL LIST | | Hazard Class Code and Hazard Class | Hazard Class Pictograms |
| 17 | Propargyl bromide, 80 wt% solution in toluene | GHS02: Flammable, GHS06: Toxic GHS05: Corrosive, GHS08: Serious Health Hazard |  |
| 18 | Tetrahydrofuran | GHS02: Flammable GHS07: Health Hazard GHS08: Serious Health Hazard |  |
| 19 | Toluene | GHS02: Flammable GHS07: Health Hazard GHS08: Serious Health Hazard |  |

Flammable liquid in this chemistry laboratory is acetic acid which can be stored with other organic acids.



Corrosive Characteristic liquid materials in this chemistry laboratory were listed on table III; which are Strong acids and bases can destroy human tissue and corrode metals. Acids and bases are incompatible with one another and may react with many other hazard classes. Therefore, they were stored together with taken special precautions. In this group chemicals in Banaz Vocational School Chemistry Laboratory were organic acids (acetic acid, formic acid), inorganic oxidizing acids (nitric acid, hydrogen peroxide solution 35%), inorganic non-oxidizing acids (hydrochloric acid 37%, hydrofluoric acid, *o*-phosphoric acid, sulfuric acid, basic solution (ammonia solution 25 %,) and other corrosive characteristic liquid materials (aniline, bromine, diethanolamine, diphenyl ether, formaldehyde solution % 37 stabilized, thionyl chloride,).









| <i>Table III: Corrosive Liquid Chemical List. Hazard Class according to Commission Regulation (EU) 2017/542 and T.C. Resmi Gazete 2020</i> | | |
|--|--|---|
| CORROSIVE LIQUID CHEMICAL LIST | Hazard Class Code and Hazard Class | Hazard Class Pictograms |
| 1 | Acetic acid glacial %100 pure GHS02: Flammable GHS05: Corrosive |  |
| 2 | Ammonia solution 25 % GHS05: Corrosive GHS07: Health Hazard GHS09: Environmental Hazard |  |
| 3 | Aniline GHS06: Toxic GHS08: Serious Health Hazard GHS05: Corrosive GHS09: Environmental Hazard |  |
| <i>Table III: Corrosive Liquid Chemical List. Hazard Class according to Commission Regulation (EU) 2017/542 and T.C. Resmi Gazete 2020</i> | | |
| CORROSIVE LIQUID CHEMICAL LIST | Hazard Class Code and Hazard Class | Hazard Class Pictograms |
| 4 | Bromine GHS06: Toxic GHS05: Corrosive GHS09: Environmental Hazard |  |
| 5 | Diethanolamine GHS05: Corrosive GHS08: Serious Health Hazard GHS07: Health Hazard |  |
| 6 | Diphenyl ether GHS05: Corrosive |  |
| 7 | Formaldehyde solution %37 stabilized GHS06: Toxic GHS08: Serious Health Hazard GHS05: Corrosive |  |
| 8 | Formic acid GHS05: Corrosive GHS06: Toxic GHS02: Flammable |  |

| | | | |
|----|---|--|---|
| 9 | Hydrochloric acid 37 % | GHS05: Corrosive GHS07: Health Hazard |   |
| 10 | Hydrofluoric acid | GHS06: Toxic GHS05: Corrosive |   |
| 11 | Hydrogen peroxide solution 35% | GHS05: Corrosive GHS07: Health Hazard GHS03: Oxidizing |    |
| 12 | Nitric acid extra pure 63 % | GHS03: Oxidizing GHS05: Corrosive |   |
| 13 | <i>o</i> -Phosphoric acid solution 85 % | GHS05: Corrosive |  |
| 14 | Sulfuric acid 98 % | GHS05: Corrosive |  |
| 15 | Thionyl chloride | GHS05: Corrosive GHS06: Toxic |   |

Storage Precautions for Corrosive acids and bases; they were separated from each other according to they are acid or base and inorganic oxidizing acids (e.g., nitric acid) and organic acids (e.g., acetic acid). Corrosives were stored on lower shelves, at least below eye level and in compatible secondary containers. Aniline, ammonia solution 25 %, diethanolamine and diphenyl ether were stored together but bromine was stored different place from ammonia solution 25 % because of their incompatibles. Acidic corrosive materials and basic corrosive materials storage different place.



Toxic Characteristic liquid chemicals in Banaz Vocational School Chemistry Laboratory were listed Table IV; Overexposure to toxic chemicals can cause damage to organs.

| <i>Table IV: Toxic Liquid Chemical List. Hazard Class according to Commission Regulation (EU) 2017/542 and T.C. Resmi Gazete 2020</i> | | | |
|---|----------|--|---|
| TOXIC LIQUID CHEMICAL LIST | | Hazard Class Code and Hazard Class | Hazard Class Pictograms |
| 1 | Methanol | GHS02: Flammable GHS06: Toxic GHS08: Serious Health Hazard |   |

| | | | |
|---|---|---|--|
| 2 | Aniline | GHS06: Toxic GHS08: Serious Health Hazard GHS05: Corrosive GHS09: Environmental Hazard |  |
| 3 | Bromine | GHS06: Toxic GHS05: Corrosive GHS09: Environmental Hazard |  |
| 4 | Chloroform | GHS06: Toxic GHS08: Serious Health Hazard |  |
| 5 | Formaldehyde solution %37 stabilized | GHS06: Toxic GHS08: Serious Health Hazard GHS05: Corrosive |  |
| 6 | Formic acid | GHS05: Corrosive GHS06: Toxic GHS02: Flammable |  |
| 7 | Hydrofluoric acid | GHS06: Toxic GHS05: Corrosive |  |
| 8 | Propargyl bromide, 80 wt% solution in toluene | GHS02: Flammable GHS06: Toxic GHS05: Corrosive GHS08: Serious Health Hazard |  |
| 9 | Thionyl chloride | GHS05: Corrosive GHS06: Toxic |  |

Methanol can be stored with flammable chemicals with some precautions. Propargyl bromide 80 wt% solution in toluene is kept refrigerated in this chemistry laboratory. Aniline, bromine, formaldehyde solution 37 % stabilized, formic acid, hydrofluoric acid, thionyl chloride and chloroform are classified in this group. Storage precautions for toxics; toxics were separated from other hazard classes and stored in a cool, well-ventilated area, away from light and heat. Containers were tightly sealed to minimize exposure to personnel and contamination of other chemicals.

Oxidizer characteristic liquid chemicals are shown in Table V. Oxidizers are a fire hazard. They will readily decompose under certain conditions to yield oxygen or react to promote or initiate the combustion of flammable or combustible materials.

| <i>Table V: Oxidizing Liquid Chemical List. Hazard Class according to Commission Regulation (EU) 2017/542 and T.C. Resmi Gazete 2020</i> | | | |
|--|--------------------------------|--|--|
| OXIDIZING LIQUID CHEMICAL LIST | | Hazard Class Code and Hazard Class | Hazard Class Pictograms |
| 1 | Hydrogen peroxide solution 35% | GHS05: Corrosive GHS07: Health Hazard GHS03: Oxidizing |  |
| 2 | Nitric acid extra pure 63 % | GHS03: Oxidizing GHS05: Corrosive |  |

These group liquids were hydrogen peroxide, nitric acid and non-laboratory chemicals (used as a bleaching agent sodium hypochlorite) in this laboratory.

Storage precautions for oxidizer chemicals; oxidizers were discreet from flammable and combustible materials (paper, wood) and segregated oxidizers from formic acid as a reducing agents. Inorganic oxidizers were separated from organic peroxides. Oxidizer Chemicals were stored in a cool, dry place and not stored under sink. Nitric acid and hydrogen peroxide and other oxidizers must not be stored on wooden shelves because a leak of their bottle could start a fire.
















Peroxide forming characteristic chemicals in this chemistry laboratory, over a period of time, diethyl ether and tetrahydrofuran can form peroxides that may explode when the cap is removed or when they are concentrated during laboratory activities. It is important to note the date on the bottle when the chemical arrived in the laboratory and opened.

Liquid Chemical List, which have no pictogram are listed Table VI. For 3-Bromoanisol, Buffer Solution pH10,0 Carbonate buffer, Buffer Solution pH 4,00, Buffer Solution pH 7,00 and glycerol according to CLP Classification - Regulation (EC) No 1272/2008 physical hazards based on available data, the classification criteria are not met. Health hazards based on available data, the classification criteria are not met. Environmental hazards based on available data, the classification criteria are not met.





These chemicals are harmful to aquatic life with long lasting effects. Because of this avoid release these chemicals to the environment.

| <i>Table VI: Liquid Chemical List, which have no pictogram. Hazard Class according to Commission Regulation (EU) 2017/542 and T.C. Resmi Gazete 2020</i> | | | |
|--|---|---|-------------------------|
| LIQUID CHEMICAL LIST | | Hazard Class Code and Hazard Class | Hazard Class Pictograms |
| 1 | 3-Bromoanisol | This mixture does not meet the criteria for classification. | not required |
| 2 | Buffer Solution pH10,0 Carbonate buffer | This mixture does not meet the criteria for classification. | not required |
| 3 | Buffer Solution pH 4,00 | This mixture does not meet the criteria for classification. | not required |
| Table VI: Liquid Chemical List, which have no pictogram. Hazard Class according to Commission Regulation (EU) 2017/542 and T.C. Resmi Gazete 2020 | | | |
| LIQUID CHEMICAL LIST | | Hazard Class Code and Hazard Class | Hazard Class Pictograms |
| 4 | Buffer Solution pH 7,00 | This mixture does not meet the criteria for classification. | not required |
| 5 | Glycerol; glycerin | This mixture does not meet the criteria for classification. | not required |

Liquid Chemicals with a serious health hazard pictogram were listed in Table VII. The health hazard pictogram indicates a product contains chemicals that may cause health effects in humans, including cancer, gene mutation, reproductive health effects, respiratory sensitivity, aspiration toxicity, and organ toxicity. A carcinogen agent (cancer-causing agent) with respiratory, reproductive or organ toxicity that causes damage over time. Liquid serious health hazard chemicals in Banaz Vocational school Chemistry Laboratory include: 1,2-Diphenylhydrazine, 2-metilpropan-2-ol, 2-propanol, aniline, benzene, chloroform, dichloromethane, diethanolamine, ethylene glycol, formaldehyde solution %37 stabilized, methanol, n-hexane, N,N-dimethylformamide, paraffin oil, phenolpht-halein, propargyl bromide, 80 wt% solution in toluene, tetrahydrofuran, toluene.

| <i>Table VII: Liquid Serious Health Hazard Chemical List. Hazard Class according to Commission Regulation (EU) 2017/542 and T.C. Resmi Gazete 2020</i> | | | |
|--|-----------------------|---|--|
| SERIOUS HEALTH HAZARD LIQUID CHEMICAL LIST | | Hazard Class Code and Hazard Class | Hazard Class Pictograms |
| 1 | 1,2-Diphenylhydrazine | GHS07: Health Hazard GHS08: Serious Health Hazard |   |
| 2 | 2-metilpropan-2-ol | GHS02: Flammable GHS08: Serious Health Hazard |   |
| 3 | 2-propanol | GHS02: Flammable GHS07: Health Hazard GHS08: Serious Health Hazard |    |
| 4 | Aniline | GHS06: Toxic GHS08: Serious Health Hazard GHS05: Corrosive GHS09: Environmental Hazard |     |
| 5 | Benzene | GHS02: Flammable GHS08: Serious Health Hazard GHS07: Health Hazard |   |
| 6 | Chloroform | GHS06: Toxic GHS08: Serious Health Hazard |   |

| <i>Table VII: Liquid Serious Health Hazard Chemical List. Hazard Class according to Commission Regulation (EU) 2017/542</i> | | | |
|---|--------------------------------------|---|-------------------------|
| SERIOUS HEALTH HAZARD LIQUID CHEMICAL LIST | | Hazard Class Code and Hazard Class | Hazard Class Pictograms |
| 7 | Dichloromethane | GHS08: Serious Health Hazard GHS07: Health Hazard | |
| 8 | Diethanolamine | GHS05: Corrosive GHS08: Serious Health Hazard GHS07: Health Hazard | |
| 9 | Ethylene glycol | GHS08: Serious Health Hazard GHS07: Health Hazard | |
| 10 | Formaldehyde solution %37 stabilized | GHS06: Toxic GHS08: Serious Health Hazard GHS05: Corrosive | |
| 11 | Methanol | GHS02: Flammable GHS06: Toxic GHS08: Serious Health Hazard | |
| 12 | n- Hexane | GHS02: Flammable GHS08: Serious Health Hazard GHS07: Health Hazard GHS09: Environmental Hazard | |
| 13 | N,N-Dimethylformamide | GHS02: Flammable GHS08: Serious Health Hazard GHS07: Health Hazard | |
| 14 | Paraffin oil | GHS08: Serious Health Hazard | |

| | | | |
|----|---|--|--|
| 15 | Phenolphthalein | GHS08: Serious Health Hazard |  |
| 16 | Propargyl bromide, 80 wt% solution in toluene | GHS02: Flammable GHS06: Toxic GHS05: Corrosive |  |
| 17 | Tetrahydrofuran | GHS02: Flammable GHS07: Health Hazard GHS08: Serious Health Hazard |  |
| 18 | Toluene | GHS02: Flammable GHS07: Health Hazard GHS08: Serious Health Hazard |  |

RESULT AND CONCLUSION

In the Banaz vocational school chemistry laboratory, liquid chemical inventory was created and classified according to MSDS forms by this study for secure work place. Label information and pictograms of these chemicals had been found from the list in Annex section third Table 3.2. pages from 996 to 1630, which is belong to the Regulation published December 10, 2020 dated and 31330 numbered Official Newspaper, Republic of Turkey, the Classification, Labeling and Packaging of substances and mixtures (T.C. Resmi Gazete, 2020) and MSDS forms. These chemicals were grouped according to hazard class (Physical hazards (flammable, explosive, oxidizing potential), hazard for human health, and environment hazard). Chemicals separated into groups were placed individually in ventilated chemical lockers for approved storage. Hazard symbols and chemical list were pasted on the locker. Its shelves were raised from the manufacturer firm to prevent containers from falling in case of an earthquake. Shelves were located away from direct sun, flame and heat sources. Containers were not protruded over shelf edges. Large bottles were stored no higher than 2 feet from the floor. Corrosives were stored on lower shelves.

REFERENCES

- Regulation (EC) No 1272/2008 of the European Parliament and of the Council of 16 December 2008 on classification, labelling and packaging of substances and mixtures, amending and repealing Directives 67/548/EEC and 1999/45/EC, and amending Regulation (EC) No 1907/2006 (Text with EEA relevance)** Reached from <https://www.legislation.gov.uk/eur/2008/1272/article/20/2020-12-31#> Retread 21.12.2022
- Directive 1999/45/EC of the European Parliament and of the Council of 31 May 1999 concerning the approximation of laws, regulations and administrative provisions of the Member States relating to the classification, packaging and labelling of dangerous preparations. *OJEC* L200, 20.7.1999, pp. 1–68.
- Reached from <https://eur-lex.europa.eu/legal-content/EN/TXT/PDF/?uri=CELEX:31999L0045&from=EN> Retrieved 21.12.2022
- Regulation (EC) No 1907/2006 of the European Parliament and of the Council of 18 December 2006 concerning the Registration, Evaluation, Authorisation and Restriction of Chemicals (REACH), establishing a European Chemicals Agency. *OJEC* L396, 30.12.2006, pp. 1–849. Reached from <https://eur-lex.europa.eu/legal-content/EN/TXT/PDF/?uri=CELEX:02006R1907-20140410&from=EN> Retrieved 21.12.2022
- Chemical Glossary: CLP Regulation. (2009). Paragraph 10, reagent.co.uk (Reached from <https://www.reagent.co.uk/chemical-glossary/> Retrieved 21.12.2022
- T.C. Resmi Gazete (2013). Maddelerin ve Karışımların Sınıflandırılması, Etiketlenmesi ve Ambalajlanması Hakkında Yönetmelik (No 28848). Printed 11 December 2013. (reached from <https://www.resmigazete.gov.tr/eskiler/2013/12/20131211M1-1.htm>) Retrieved 21.12.2022
- T.C. Resmi Gazete (2020). Maddelerin Ve Karışımların Sınıflandırılması, Etiketlenmesi Ve Ambalajlanması Hakkında Yönetmelikte Değişiklik Yapılmasına Dair Yönetmelik (No 31330). 10 Aralık 2020. (Reached from <https://www.resmigazete.gov.tr/eskiler/2020/12/20201210M1-1.htm>) Retrieved 21.12.2022
- 1910.106 - Flammable liquids. | Occupational Safety and Health Administration". (Reached from www.osha.gov. Retrieved 21.12.2022
- Council Directive 67/548/EEC of 27 June 1967 on the approximation of laws, regulations and administrative provisions relating to the classification, packaging and labeling of dangerous substances. Reached from <https://eur-lex.europa.eu/legal-content/EN/TXT/PDF/?uri=CELEX:31967L0548&from=EN> Retread 21.12.2022
- Commission Regulation (EU) 2017/542 of 22 March 2017 amending Regulation (EC) No 1272/2008 of the European Parliament and of the Council on classification, labelling and packaging of substances and mixtures by add-

ing an Annex on harmonised information relating to emergency health response (Text with EEA relevance). Reached from <https://www.legislation.gov.uk/eur/2017/542/body/2020-12-31#> Retread 21.12.2022

Labels – make sure you're legal after 1 June 2017, European Chemicals Agency (Reached from <https://www.en.nvc.nl/news/item/clp-etiketten-overgangs-regeling-loopt-af-op-1-juni-2017/>) Retread 21.12.2022

“

Chapter 5

PALLADIUM(II) SCHIFF BASE CHELATES: SYNTHESIS, CHARACTERIZATION AND ANTIBACTERIAL STUDIES

Hülya AVCI OZBEK¹

Deniz DEMİR ATLI²

”

1 Dr., Manisa Celal Bayar University, Faculty of Science and Letters, Department of Chemistry, 45140 Yunusemre-Manisa, TURKEY, <https://orcid.org/0000-0003-1508-2558>. E-mail: hulya.avci@cbu.edu.tr

2 Doç. Dr., Manisa Celal Bayar University, Faculty of Science and Letters, Department of Chemistry, 45140 Yunusemre-Manisa, TURKEY, <https://orcid.org/0000-0001-8442-4916>. E-mail: deniz.demir@cbu.edu.tr

Introduction

Schiff bases (Figure 1) are regarded as imines with $R^1R^2C=NR^3$ general formula where R^1 , R^2 and R^3 are linear or cyclic alkyl and/or aryl group ($R^3 =$ but not hydrogen). They are important class of organic compounds. The synthesis of these compounds takes place by condensation reaction of an aldehyde/ketone compound with a primary amine under specific conditions. As a result of this reaction, only water is formed as a by-product. Nitrogen atom of azomethine group play a key role for the chemical and biological properties (Kumar et al., 2019). Schiff bases have been used species in the development of transition metal chemistry thanks to their fascinating structural flexibility.

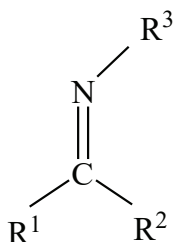


Figure 1. Schiff base

Schiff bases and their metal complexes have been of significance in homogeneous and heterogeneous catalysis. They have been employed as active catalysts in ethylene polymerization, Suzuki-Miyaura, Sonogashira and Heck coupling reactions. Also, these compounds have got attention in medicinal and biological applications by virtue of their antibacterial, antifungal and anticancer activities (Avcı Özbek et al., 2021; Kordestani et al., 2021; Arabi et al. 2022; Jain et al. 2022; Prabhu Kumar et al., 2022, Sedighipoor et al., 2018; Puzarı et al., 2021; Nagalakshmi et al., 2022, Turan et al., 2022).

The Schiff Bases (*N*-[1-(3-aminopropyl)imidazole]salicylaldimine (**HL₁**) and *N*-[1-(3-aminopropyl)imidazole]-3,5-di-*tert*-butylsalicylaldimine (**HL₂**) are known compounds. Some reports interested these compounds are as follows: Preparation of the Schiff base **HL₂** and Cu(II) complex and electrochemical investigations of the complex were reported (Tas et al., 2004). The Schiff base **HL₁** and its metal chelates (zinc(II), copper(II) and silver) prepared and biological activity studies were executed (McGinley et al., 2013). Anti-corrosive tendency of **HL₁** were investigated in a study (Satpati et al., 2022). In different studies, some metal

chelates were prepared and antimicrobial activity surveys were practised (Kalanithi et al., 2012, Qian et al., 2014).

In this study, two neutral palladium (II) chelates of HL₁ and HL₂ Schiff bases with the general formula [PdL(OAc)] were prepared. ¹H NMR, ¹³C NMR, FT-IR, TGA and elemental analysis techniques were utilized for the characterization. In addition, antibacterial activity studies of the complex containing tert-butyl substituent were performed.

Experimental

Synthesis of [Pd(L₁)(OAc)] complex

Pd(OAc)₂ (75 mg, 0.33 mmol) and HL₁ (77 mg, 0.33 mmol) in CH₂Cl₂ (10 mL) was constantly stirred at RT for 24 hours. The resultant yellow colored precipitate was separated by filtration washing the solid with CH₂Cl₂ was established. Yield: 56 mg, 41%. m.p.: 163-165°C. FT-IR (KBr pellets): $\nu = 465$ (m), 595 (m), 616 (m), 650 (m), 686 (m), 753 (m), 825 (m), 913 (m), 1023 (m), 1102 (m), 1130 (m), 1149 (m), 1200 (m), 1314 (m), 1362 (m), 1447 (m), 1539 (m), 1596 (m), 1618 (s), 2923 (m), 3128 (m), 3421 (w) cm⁻¹. Elem. Anal. Calcd. C₁₅H₁₉N₃O₄Pd (411.75 g/mol): C, 43.75, H, 4.65, N, 10.21. found: C, 44.10, H, 4.59, N, 10.01. TGA (loss of H₂O): calcd. 4.38%, found 4.47%; (loss of OAc): calcd. 14.33%, found 14.81%; (loss of OAc): calcd. 25.85%, found 26.10%.

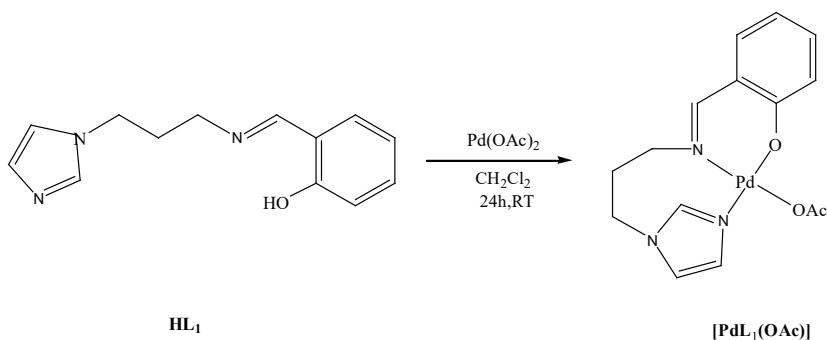
Synthesis of [Pd(L₂)(OAc)] complex

Pd(OAc)₂ (100 mg, 0.45 mmol) was added to HL₂ (152 mg, 0.45 mmol) in CH₂Cl₂ (10 mL) with constant stirring at RT for 24 hours. The solution was concentrated. Orange solids were precipitated by adding of n-pentane (20 mL). The product was filtrated and washed with n-pentane. Yield: 160 mg, 67%. m.p.: 274-275°C. FT-IR (KBr pellets): $\nu = 558$ (m), 655 (m), 688 (m), 745 (m), 779 (m), 836 (m), 916 (m), 960 (m), 1109 (m), 1169 (m), 1198 (m), 1255 (m), 1271 (m), 1311 (m), 1362 (m), 1409 (m), 1434 (m), 1530 (m), 1621 (s), 2868 (m), 2954 (s), 3134 (m), 3422 (w) cm⁻¹. ¹H NMR (400MHz, CDCl₃): $\delta = 1.36$ (s, 9H, Bu^t), 1.47 (s, 9H, Bu^t), 1.96 (s, 3H, Me), 2.5-2.7 (m, 2H, CH₂), 3.87 (t, 2H, CH₂), 4.26 (t, 2H, CH₂), 6.99 (s, 1H, -N=CH-N), 7.45 (d, 2H, -CH=CH-), 7.73 (s, 1H, -N=CH) ppm. ¹³C NMR (101 MHz, CDCl₃): $\delta = 23.57, 29.36, 31.30, 33.81, 36.52, 45.85, 56.92, 118.57, 118.80, 131.14, 136.49, 178.41$ ppm. Elem. Anal. Calcd. C₂₃H₃₅N₃O₄Pd (523.96 g/mol): C, 52.72, H, 6.73, N, 8.02. found: C, 52.74, H, 7.25, N, 8.28. TGA (loss of H₂O): calcd. 3.44%,

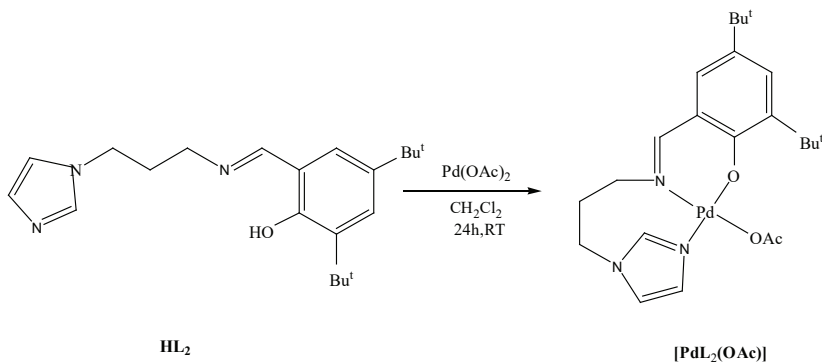
found 3.54%; (loss of OAc): calcd. 11.27%, found 11.49%; %; (loss of OAc): calcd. 20.31%, found 20.57%.

Results and Discussions

The reactions of $\text{Pd}(\text{OAc})_2$ with 1 equivalent HL_1 and HL_2 Schiff bases gave the neutral $[\text{Pd}(\text{L}_1)(\text{OAc})]$ and $[\text{Pd}(\text{L}_2)(\text{OAc})]$ complexes, respectively (Scheme 1 and scheme 2). The compounds are air and moisture stable. Since the yellow coloured $[\text{Pd}(\text{L}_1)(\text{OAc})]$ is not soluble in any solvent, it was characterized by only TGA, elemental analysis and FT-IR methods. The other one is soluble in the solvents such as CH_2Cl_2 and DMSO and insoluble in n-pentane, n-hexane. It was further characterized using NMR analysis.



Scheme 1. Synthesis of $[\text{PdL}_1(\text{OAc})]$ complex



Scheme 2. Synthesis of $[\text{PdL}_2(\text{OAc})]$ complex

FT-IR spectra of the complexes are given in figure 2 and figure 3. Some FT-IR data are summarized in table 1. The ν_{OH} peaks around at 3410-3434 cm^{-1} in the spectra of the HL_1 and HL_2 disappear in the spectra of the chelates. This shows to be deprotonation of the phenolic proton. The decrease in the $\nu_{\text{C=N}}$ values was observed in the FT-IR spectra of the palladium(II) chelates, pointing coordination of imine nitrogen. The stretching frequencies related to Pd-O and Pd-N bonds for the complexes appear in the range of 558–595 and 460-465, respectively. These values are compatible with the literature (Kalanithi et al., 2012; Tas et al., 2004; Tajuddin et al., 2012). NMR data support the expected structure for $[\text{Pd}(\text{L}_2)(\text{OAc})]$. The absence of OH signal in the spectrum of the complex indicates that the phenolic proton has undergone deprotonation.

Table 1. Some FT-IR data

| Compound | FT-IR spectra (cm^{-1}) | | | |
|------------------------------|------------------------------------|-------------------|--------------------|--------------------|
| | $\nu(\text{O-H})$ | $\nu(\text{C=N})$ | $\nu(\text{Pd-O})$ | $\nu(\text{Pd-N})$ |
| HL_1 | 3434 | 1632 | - | - |
| $[\text{PdL}_1(\text{OAc})]$ | - | 1618 | 595 | 465 |
| HL_2 | 3410 | 1626 | - | - |
| $[\text{PdL}_2(\text{OAc})]$ | - | 1621 | 558 | 460 |

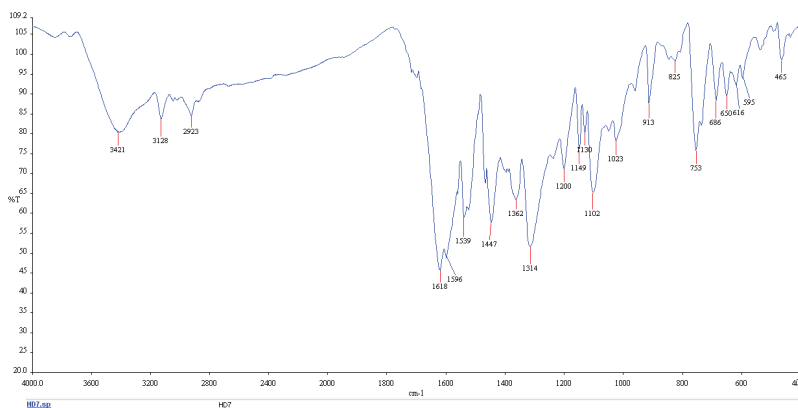


Figure 2. FT-IR spectrum of $[\text{PdL}_1(\text{OAc})]$

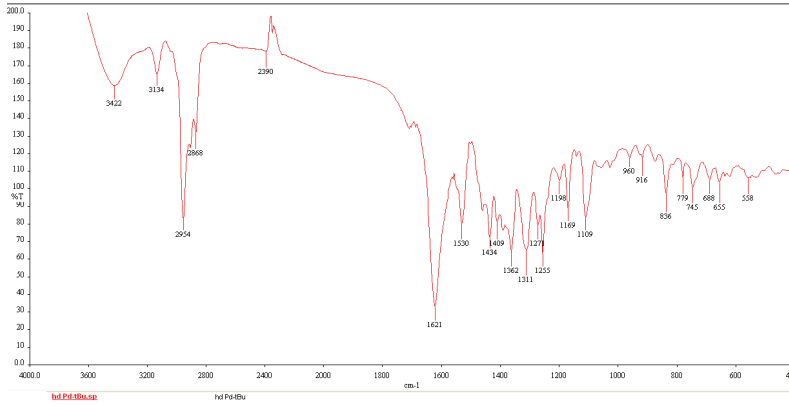


Figure 3. FT-IR spectrum of $[PdL_2(OAc)]$

The TGA curve of $[PdL_1(OAc)]$ has third mass decrease steps (Figure 4). The first weight loss of 1 molecule H_2O (4.47%) in the range of 44-169 °C is ascribed to the deprivation of hydrated water molecule. The second weight loss of 14.81% in the range of 169–262 °C possibly corresponds to the loss of OAc group. The third mass decrease is 26.10% from 262 to 277 °C assigned to the release of Pd. The TGA curve of $[PdL_2(OAc)]$ also has third mass decrease step (Figure 5). The first mass deprivation of 1 molecule H_2O (3.53%) in the range of 77-187 °C is ascribed to the loss of hydrated water molecule. The second weight loss of 11.49% in the range of 187–294 °C possibly corresponds to the loss of OAc group. The third mass decrease is 20.57% from 294 to 304 °C assigned to the release of Pd. The experimental and calculated values are resumed in table 2. These values are compatible with each other.

Table 2. TGA analysis results

| | Compound | |
|-------------------------------|-------------------------------|-------------------------------|
| | [PdL₁(OAc)] | [PdL₂(OAc)] |
| Temperature range (°C) | 44-169 | 77-187 |
| Losses part | H ₂ O | H ₂ O |
| Calculated (%) | 4.38 | 3.44 |
| Experimental (%) | 4.47 | 3.53 |
| Temperature range (°C) | 169-262 | 187-294 |
| Losses part | OAc | OAc |
| Calculated (%) | 14.33 | 11.27 |
| Experimental (%) | 14.81 | 11.49 |
| Temperature range (°C) | 262-277 | 294-304 |
| Losses part | Pd | Pd |
| Calculated (%) | 25.85 | 20.31 |
| Experimental (%) | 26.10 | 20.57 |

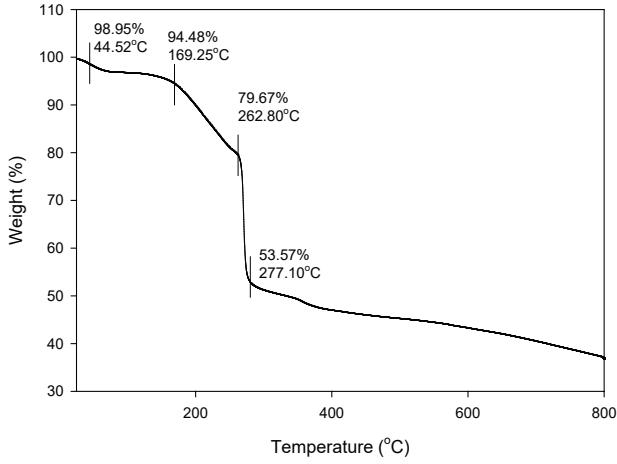


Figure 4. TGA spectrum of $[PdL_1(OAc)]$

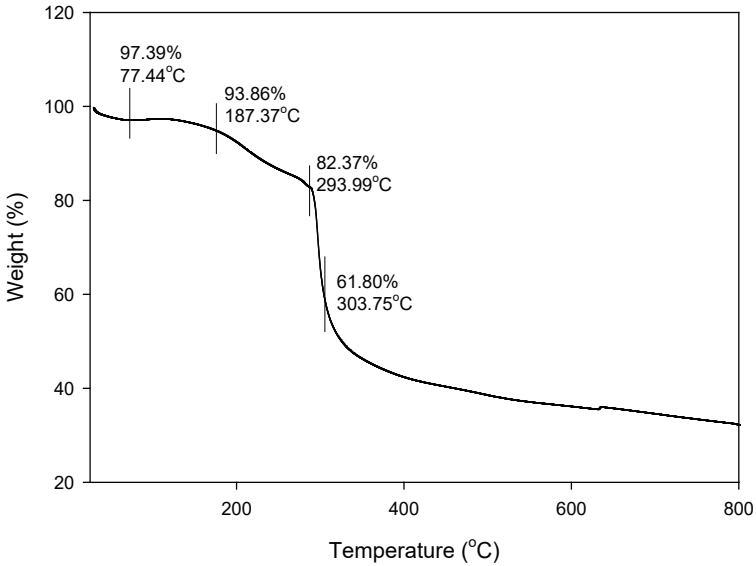


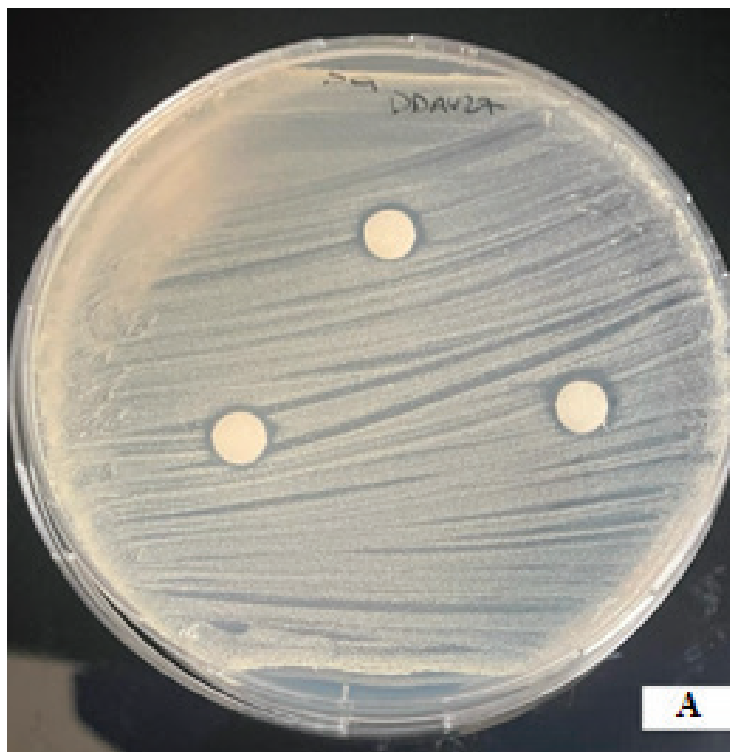
Figure 5. TGA spectrum of $[PdL_2(OAc)]$

The antimicrobial data of HL_2 and $[PdL_2(OAc)]$ against *Staphylococcus aureus* ATCC 25923 and *Escherichia coli* ATCC 25922 are recorded in table 3 and are displayed in the figure 6 and figure 7. It can be concluded that the Schiff base ligand (HL_2) shows low activity against *Escherichia coli* and *Staphylococcus aureus* but $[PdL_2(OAc)]$ compound has

antimicrobial effect against *S. aureus* and *E. coli*. $[\text{PdL}_2(\text{OAc})]$ compound has high antimicrobial activity than ligand. In fact, $[\text{PdL}_2(\text{OAc})]$ has good antimicrobial activity as previously published for some Pd (II) Schiff base complexes (PrabhuKumar et al., 2022).

Table 3. Antimicrobial activity of HL_2 and $[\text{PdL}_2(\text{OAc})]$ against *S. aureus* and *E. coli*

| Compound | Microorganisms (Inhibition zone, mm) | |
|------------------------------|--------------------------------------|----------------|
| | <i>S. aureus</i> | <i>E. coli</i> |
| HL_2 | 7±0 | 7±0 |
| $[\text{PdL}_2(\text{OAc})]$ | 31.6±0.47 | 19±0.82 |



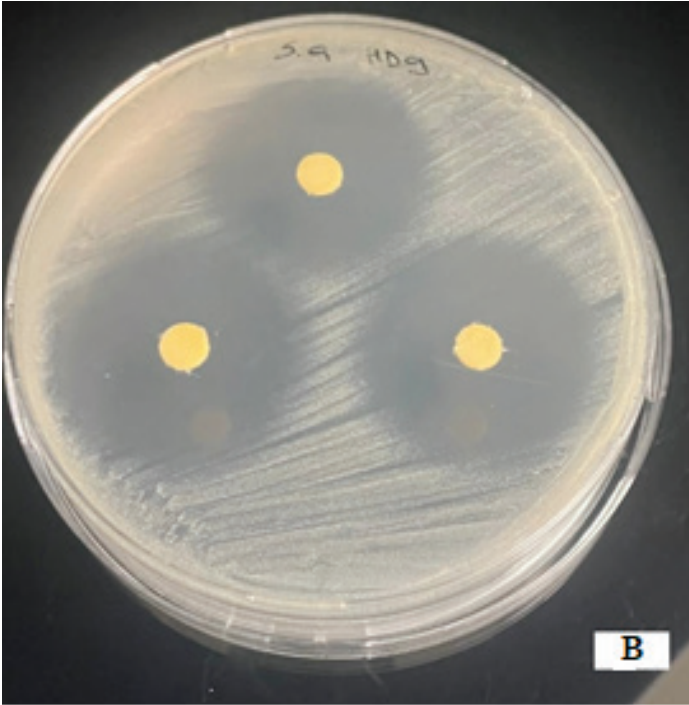
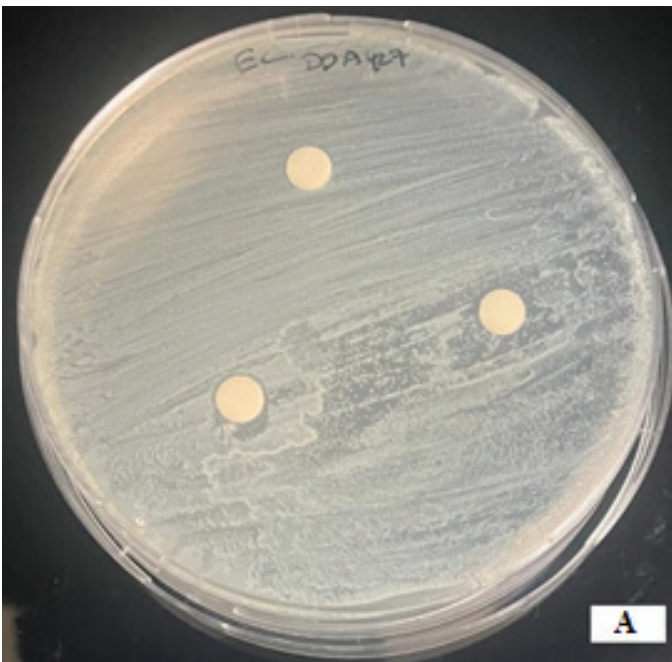


Figure 6. Antibacterial activity results of compounds: **A)** HL₂, **B)** [PdL₂(OAc)] for *Staphylococcus aureus* ATCC 25923



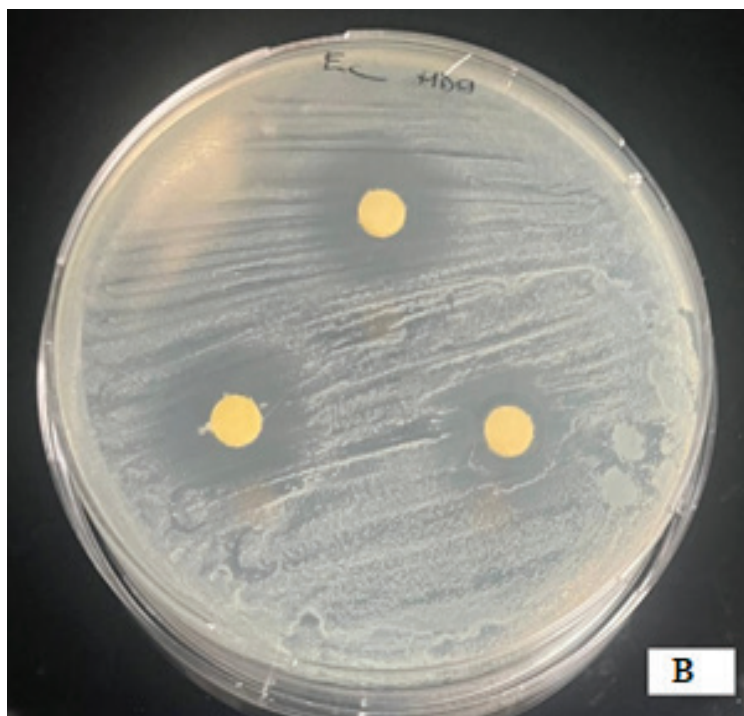


Figure 7. Antibacterial activity results of compounds: **A)** HL_2 **B)** $[PdL_2(OAc)]$ for *Escherichia coli* ATCC 25922

Conclusions

This study reports the preparation and structural elucidation of the new two Pd (II) Schiff bases. Their characterization was achieved using 1H NMR, ^{13}C NMR, FT-IR, TGA and elemental analysis. Moreover $[PdL_2(OAc)]$ compound possesses promising antimicrobial activity against two pathogenic microbes.

REFERENCES

- Arabi, H., Beheshti, M. S., Manteghi, A., (2022), Ethylene Polymerization through Neutral Nickel Complexes Bearing Cyclic Imides, *Advances in Polymer Technology*, 2022, 8788585.
- Avci Özbek, H., Çınar, S., Oskay, M., Aydemir, T., Demirhan, F., (2021), Antimicrobial and SOD-like activities of *N,N'*-Bis(ferrocenylmethylene)ethylenediamine Schiff Base and It's Metal Complexes, *Journal of the Chilean Chemical Society*, 66 (3), 5237-5241.
- Jain, S., Rana, M., Sultana, R., Mehandi, R., Rahisuddin, (2022), Schiff Base Metal Complexes as Antimicrobial and Anticancer Agents, *Polycyclic Aromatic Compounds*.
- Kalanithi, M., Rajarajan, M., Tharmaraj, P., Sheela, C.D., (2012), Spectral, biological screening of metal chelates of chalcone based Schiff bases of *N*-(3-aminopropyl) imidazole, *Spectrochimica Acta Part A: Molecular and Biomolecular Spectroscopy*, 87, 155-162.
- Kordestani, N., Rudbari, H. A., Correia, I., Valente, A., Co`rte-Real, L., Islam, M. K., Micale, N., Braun, J. D., Herbert, D. E., Tumanov, N., Woutersg, J., Enamullah, M., (2021), Heteroleptic enantiopure Pd(II)-complexes derived from halogen-substituted Schiff bases and 2-picolyamine: synthesis, experimental and computational characterization and investigation of the influence of chirality and halogen atoms on the anticancer activity, *New Journal of Chemistry*, 45, 9163-9180.
- Kumar, M., Pallvi, Tuli, H. S., Khare, R., (2019), Synthesis, Characterization and Biological Studies of Novel Schiff Base viz. *Bis*-1,1'- (pyridine-2,6-diyl-dieth-1-yl-1-ylidene) biguanidine and Their Transition Metal Complexes, *Asian Journal of Chemistry*, 31, (4), 799-804.
- McGinley, J., McCann, M., Ni, K., Tallon, T., Kavanagh, K., Devereux, M., Ma, X., McKee, V., (2013), Imidazole Schiff base ligands: Synthesis, coordination complexes and biological activities, *Polyhedron*, 55, 169-178.
- Nagalakshmi, N., Sathya, M., Premkumar, M., Kaleeswaran, D., Venkatachalam, G., Balasubramani, K., (2022), Palladium(II) complexes comprising naphthylamine and biphenylamine based Schiff base ligands: Synthesis, structure and catalytic activity in Suzuki coupling reactions, *Journal of Organometallic Chemistry*, 914, 121220-121226.
- PrabhuKumar, K. M., Satheesh, C. E., RaghavendraKumar, P., Kumar, M. N. S., Lingaraju, K., Suchetan, P. A., Rajanaika, H., (2022), Synthesis, characterization, antibacterial, antifungal and antithrombotic activity studies of new chiral selenated Schiffbases and their Pd complexes, *Journal of Molecular Structure*, 1264, 133172-133182.
- Puzari, A., Gogo, A., Das, P., (2021), An unsymmetrical Schiff-base derived recyclable Pd-catalyst for Suzuki–Miyaura and Sonogashira reactions in aqueous media, *Journal of Chemical Sciences*, 133, 56-63.

- Qian, H.F., Dai, Y., Geng, J., Wang, L., Wang, C., Hua, W., (2014), A flexible multidentate Schiff-base ligand having multifarious coordination modes in its copper(II) and cadmium(II) complexes, *Polyhedron*, 67, 314-320.
- Satpati, S., Suhasaria, A., Ghosal, S., Adhikari, U., Banerjee, P., Dey, S., Sukul, D., (2022), Anti-corrosive propensity of naturally occurring aldehydes and 1-(3-aminopropyl)imidazole condensed Schiff bases: Comparison on the effect of extended conjugation over electron donating substituents, *Journal of Molecular Structure*, 1268, 133684.
- Sedighipoor, M., Kianfar, A. H., Mohammadnezhad, G., Görls, H., Plass, W., (2018), Unsymmetrical palladium(II) N,N,O,O-Schiff base complexes: Efficient catalysts for Suzuki coupling reactions, *Inorganica Chimica Acta*, 476, 20–26.
- Tajuddin, A.M., Bahron, H., Kassim, K., Ibrahim, W.N.W., Yamin, B.M., (2012), Synthesis and characterization of palladium(II) Schiff base complexes and their catalytic activities for Suzuki Coupling reaction, *The Malaysian Journal of Analytical Sciences*, 16(1), 79-87.
- Tas, E., Aslanoğlu, M., Güler, M., Ulusoy, M., (2004), Synthesis, Characterization and Electrochemical Properties of Copper(II) Complexes with Novel Bidentate Salicylaldimines Derived From 3,5-Di-*t*-Butyl-2-Hydroxybenzaldehyde, *Journal of Coordination Chemistry*, 57(7), 583–589.
- Turan, N., Buldurun, K., Bursal, E., Mahmoudi, G., (2022), Pd(II)-Schiff base complexes: Synthesis, characterization, Suzuki–Miyaura and Mizoroki–Heck cross-coupling reactions, enzyme inhibition and antioxidant activities, *Journal of Organometallic Chemistry*, 970-971, 122370-122382.

“

Chapter 6

**RECYCLING A SCRAPPED MAGNETIC
STIRRER/HEATER USING AN ARDUINO
MICROCONTROLLER**

Zafer GÜLTEKİN¹

Nuray ALTINÖLÇEK GÜLTEKİN²

”

¹ Zafer Gültekin, Arş. Gör., Bursa Uludağ Üniversitesi, Fen-Edebiyat Fakültesi, Fizik Bölümü, Katıhal Fiziği A.B.D., ORCID ID: 0000-0001-8026-0379

² Nuray Altınölçek Gültekin, Dr. Öğrt. Üyesi, Bursa Uludağ Üniversitesi, Yenişehir İbrahim Orhan MYO, Gıda İşleme, Gıda Teknolojisi, ORCID ID: 0000-0002-9553-1474

Introduction

Heat transfer is the transfer of energy caused by a temperature difference. Heat transfer always occurs within a medium or between environments, whenever there is a temperature difference. Thermal conductivity is the property which indicates the ability of materials to conduct heat [1]. Since the conductive heat transfer phenomenon takes place in a thermal field with temperature differences, of interest is how thermal conductivity varies with temperature. Thus, the variation of thermal conductivity with temperature for materials is defined $\lambda = \lambda_0 [1 + C(T - T_0)]$ W/(m.K). Here, λ is thermal conductivity at temperature T , λ_0 , thermal conductivity at reference temperature T_0 , C is a constant property of each material [2]. Classical diffusive heat transport is described by Fourier law, which in 1D takes the form $q = -\lambda(dT/dx)$ where q is heat flux, T is temperature, and λ is thermal conductivity. Combined with the energy conservation law, the Fourier law leads to the classical heat conduction equation of the parabolic type, which describes heat conduction as a pure thermal diffusion. This has the unphysical property that if a sudden change of temperature is made at some point on the body, it will be felt instantly everywhere, though with exponentially small amplitudes at distant points. One may say that classical heat conduction theory gives rise to the infinite speed of the propagation of a temperature (thermal) wave [3].

A magnetic stirrer/heater (MKI) based on the thermal conduction principle is one of the most frequently used instruments when preparing solutions in the laboratory. While chemical materials are dissolved in solvents such as pure water, alcohol, acetone, etc., in some cases it is very difficult to dissolve without heating. On the other hand, continuous mixing of the solution is required to obtain a homogeneous mixture. In such cases, MKI comes to our aid. However, although most MKIs used in laboratories give a temperature close to the temperature desired by the user, they cannot give a completely constant temperature. By making continuous measurements with a thermometer, the user can try to control the temperature by touching an ice cube or a wet cloth to the heating plate in cases where the temperature increases too much. However, despite all efforts, the temperature may not be controlled as desired. Undoubtedly, this situation can be both uncomfortable and cause to spend all the time at the beginning of the MKI, especially as the heating time gets longer.

In addition, in many laboratories, such devices are waiting in a corner in a broken way. In this case, either a new device needs to be purchased or the device needs to be repaired. The purchase of a new device may cause

both a decrease in natural resources and an extra burden on the national economy.

To avoid such situations, in this article, a fully software-controlled MKI with an accuracy of about $\pm 3^{\circ}\text{C}$ for the heater was recycled using an Arduino microcontroller.

Two types of software were developed for the device, with Arduino own codes and the Labview program. In the first, the user enters the desired temperature (25-110^oC range) and speed (500-1500 rpm range) values into the system with two separate potentiometers. These values entered by the user are displayed on an LCD (Liquid Crystal Display) screen and the system automatically activates and starts working to keep the temperature and speed constant at the desired value. In addition, if the user wishes, he/she can also introduce the system how long it will work and stop. Thus, the user can take care of his other work without having to wait by the device in any way, saving his/her energy and time as much as possible.

In the second, the user can perform the same operations one by one through the Labview interface. The only difference is that in this section, a graph of solution and plate temperature as a function of time is plotted on the computer screen. If desired, the heating coefficient of the solution can be easily calculated using this graph.

2. Material and Method

2.1. Equipment

An Arduino nano microcontroller was used in the construction of the MKI shown in Fig. 1. The stirrer control of the MKI is provided by the microcontroller controlling a DC (Direct Current) motor via an AO-D4184A 40V N-Channel metal-oxide semiconductor field effect transistor (MOSFET).

The temperature control of the MKI was provided by the microcontroller feeding the resistance of the 1000 W heating plate with AC voltage through a 10 A relay. The microcontroller controls the temperature by collecting data from a 100K NTC thermistor placed tightly under the heating plate and the PT1000 temperature sensor immersed in the solution.

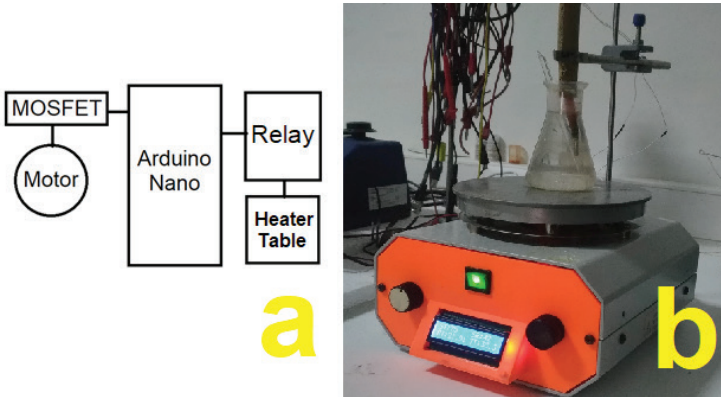


Figure 1 a) Schematic representation of MKI b) MKI device

An NTC (Negative Thermocouple) thermistor was used to measure the table temperature of the MKI. The NTC thermistor is a resistor that varies with temperature and has a negative temperature coefficient. As the temperature rises, the resistance value decreases. The microcontroller does not have a component that can directly measure this resistance value. Instead, it has a voltage reader known as an analog-to-digital converter (ADC). Therefore, a standard voltage divider circuit in Figure 2 was used to measure the resistance value of the NTC.

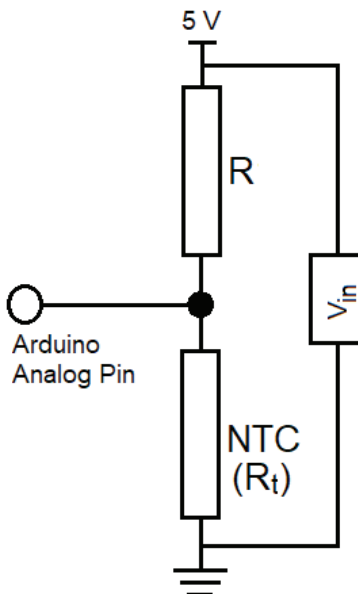


Figure 2 Voltage divider circuit

The voltage divider circuit consists of an NTC thermistor supplied with 5V, connected in series, and a known value resistor (R). To read the analog data from the NTC thermistor, the middle part of the NTC thermistor and the R resistor are connected to the analog pin of the Arduino microcontroller. The thermistor resistance was calculated by converting the analog data read from the NTC thermistor to voltage (V_{out}) and using it in the voltage divider circuit equation given in the expression (1).

$$R_t = R \times [(V_{in}/V_{out})-1] \quad (1)$$

Here, R is the voltage between a known value resistor (10K), R_t , thermistor resistance, V_{in} , supply (5V), V_{out} , thermistor and resistance (R) with the known value. The Steinhart-Hart equation given in [4] is used to convert the calculated resistance to temperature. In [5], there is a ready-made calculation program that gives the coefficients of this equation. In this article, the temperature values were calculated using the equation coefficients obtained from [5].

PT1000 temperature sensor was used to measure the solution temperature. The PT1000 is a linear sensor, which means that with increasing or decreasing temperature, its internal resistance also increases and decreases. This allows the data read from the PT1000 to be processed by the microcontroller without complex mathematical formulas such as the NTC thermistor. Instead of using a voltage divider circuit to measure solution temperature more precisely, PT1000 is connected to an Arduino microcontroller using the Adafruit MAX31865 RTD PT1000 Amplifier module.

2.2. Software

The MKI system, which was designed using an Arduino nano microcontroller, was written in two different programming languages as software. The first is Arduino's firmware, which consists of its own codes, and the second is the system interface (Figure 3), which is controlled via a computer using the Labview program.



Figure 3 Labview interface of the heater/stirrer

The microcontroller starts to control the heating plate and solution temperature at certain intervals after the temperature value is entered into the system. By controlling the data coming from the sensors, the microcontroller tries to keep the temperature constant by turning the relay on/off near the set temperature level. The stirrer part is controlled by a MOSFET. The rotation speed is adjusted by using pulse width modulation (PWM) according to the speed values entered into the system (500-1500 rpm).

3. Result and Discussion

Testing of the stirrer part of the system was performed in previous studies found in [6]. The heater part was tested using water, isopropyl alcohol, methanol and acetone. In Figure 4, the boiling point determination results for these liquids are shown graphically. The tests were carried out at an altitude of approximately 150 m above sea level and are in agreement with the literature results [7].

Figure 5 shows temperature swings around temperatures of 65, 75 and 85 degrees for water. The heater is energized by keeping the relay on until the temperature value entered in the system is reached. After the entered temperature value is reached, the relay is closed and the energy to the heating plate is cut off. As soon as the temperature drops below the entered temperature, the relay is turned on again and the heating plate is re-energized. The temperature is controlled with an accuracy of about ± 3 degrees by forcing the system to oscillate around the temperature value entered in this way. It is noteworthy in the figure that as the temperature rises, the oscillation period around the entered temperature decreases. The

reason for this is that at high temperatures, the heating plate cools faster when the energy is cut off.

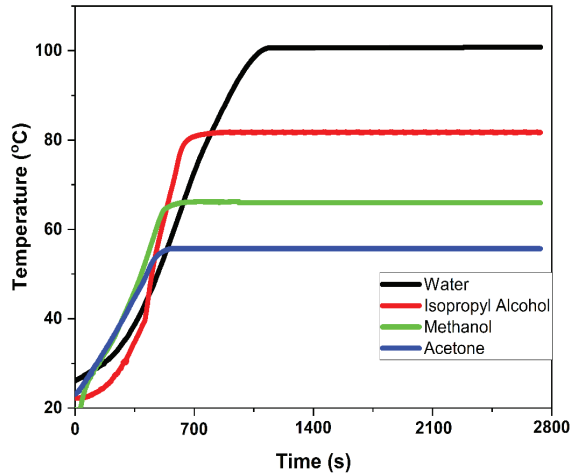


Figure 4 Boiling point determination of liquids

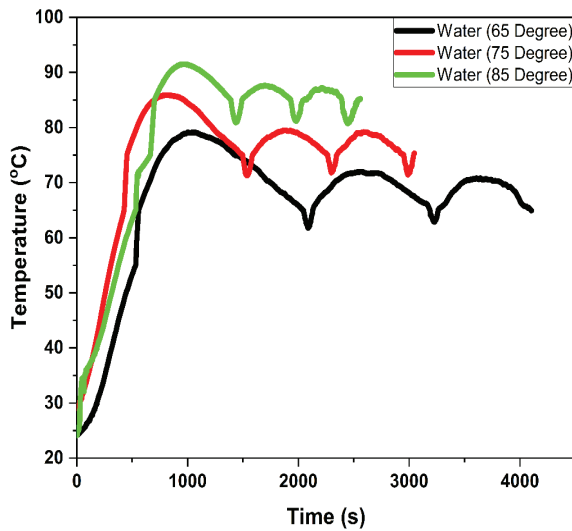


Figure 5 The temperature oscillation of the device around the set temperature

4. Conclusion

A scrapped MKI was recycled using an Arduino microcontroller at a low cost and software controlled. This device was used to determine the boiling points of water, isopropyl alcohol, methanol and acetone and the results were found to be in agreement with the literature results. The device was tested for water at temperatures of 65, 75 and 85 degrees. The results showed that the device can control the temperature value entered into the system with an accuracy of about ± 3 degrees. Also, with this study, it was seen that scrapped devices like this can be easily reused.

Nomenclature

| | |
|-------------|---|
| λ | thermal conductivity |
| λ_0 | thermal conductivity at reference temperature |
| T | temperature |
| T_0 | reference temperature |
| C | a constant property of each material |
| q | heat flux |
| R | the voltage between a known value resistor |
| R_t | thermistor resistance |

REFERENCES:

- Janna W. S. (2000). *Engineering heat transfer, 2nd Ed.* CRC Press LLC, US.
- Flori M., Putan V. & Vilceanu L., (2017). *Using the heat flow plate method for determining thermal conductivity of building materials. IOP Conf. Ser.: Mater. Sci. Eng.*, 163 012018.
- Sobolev S.L. & Dai W., (2022). *Heat Transport on Ultrashort Time and Space Scales in Nanosized Systems: Diffusive or Wave-like?*. *Materials*, 15, 4287.
- Steinhart–Hart Equation [Online]. Available:https://en.wikipedia.org/wiki/Steinhart%E2%80%93Hart_equation. (Accessed June 26, 2022).
- SRS Thermistor Calculator [Online]. Available:<https://www.thinksrs.com/downloads/programs/therm%20calc/ntccalibrator/ntccalculator.html>. (Accessed June 26, 2022).
- Gültekin Z., Alper M., Akay C. & Hacıismailoğlu M.C. (2021). *Design and Construction of Home-Made Spin Coater for OLED Production*. *Int J Electron Device Phys.*, 5:011.
- Liquids and Gases-Boiling Points [Online]. Available:https://www.engineering-toolbox.com/boiling-points-fluids-gases-d_155.html. (Accessed June 26, 2022).

“

Chapter 7

**ORGANIC SUBSTANCES AFFECTING
GROWTH AND DEVELOPMENT
IN PLANTS (PLANT GROWTH
REGULATORS, PHOTOHORMONES)**

Kadriye URUÇ PARLAK¹

”

¹ Doç. Dr. Kadriye URUÇ PARLAK Ağrı İbrahim Çeçen Üniversitesi,
Fen Edebiyat Fakültesi, Moleküler Biyoloji ve Genetik Bölümü, AĞRI
Email: uruckadriye@gmail.com Telf:05077020575 ORCID ID: 0000-
0002-1474-1868

INTRODUCTION

Phytohormones, also known as plant growth regulators, are organic compounds that plants naturally produce and that control growth and development, facilitate intercellular communication, and exert their effects even at extremely low concentrations (Opik et al., 2005; Rademacher, 2015).

Plant growth regulators (PGR) are produced in various locations, including the roots, buds, and leaves. Following interaction with particular receptors, PGR is then delivered to the places that need them (Rademacher, 2015.)

PGR is derived from several fungi and plant organs (Morsünbül et al., 2010). In general, the PGR maintains control over the physiological events that take place in a plant's structure.

The importance of PGR was first understood in the 1930s. The first study in Turkey was about the plant hormone gibberellic acid (GA), which was used to stimulate the production of seedless grapes and increase fruit and cluster size in 1960 (Flasiński and Hąc-Wydro, 2014; Algül et al., 2016). Some studies on plant physiology revealed the effects of PGR on plant growth and development. It was understood that over time, growth-promoting substances and growth-inhibiting substances were synthesized in the plant (Raven et al., 1992; Fishel, 2006). When applying PGR externally to plants, considerations such as selecting the suitable chemical for the job, picking the right application timing, concentration, environmental conditions affecting their absorption, and the plant's physiological state are crucial (Palavan-Ünsal, 1993; Buban, 2000).

In agricultural activities, PGRs are generally used to increase plant biomass, reduce the negative effects of the presence of pollutants in the plant, increase the germination power of seeds, encourage or delay flowering, encourage root-shoot and tuber formation, increase fruit size, increase shelf life of products, and resist extreme climatic conditions. It is preferred to increase resistance, to provide resistance of plants against diseases and pests, and to reduce labor force in harvest by ensuring that the products mature simultaneously (Abid and Asghari, 2006; Hadi et al., 2010; Rademacher, 2015).

Plant growth regulators, known as the classical quintet, are grouped under five groups (auxin, cytokinin, gibberellin, abscisic acid, and ethylene). However, nowadays, in addition to these, plant hormones known as

brassinosteroid, salicylic acid, strigolactone, and jasmonic acid have been discovered. These hormones are classified into three main groups according to the physiological effects they play on the plant and play an active role in the development of the plant (Table 1).

Plant growth regulators have some common features;

1. Synthesis by plant
2. Being portable and causing metabolic changes where it is transported
3. It should be able to show these effects even at very low concentrations.

Among the natural PGRs, ethylene is the most widely used herbal hormone in the world with a rate of 23%, while auxin is in the second place with 20% and Gibberellins is in the third place with 17%.

Table 1. Effects of phytohormones (plant growth regulators) in plants (Williams, 2011)

| Control of the vegetative growth | Control of the reproduction | Stress response |
|---|------------------------------------|------------------------|
| Auxin | Ethylene | Salicylic acid |
| Cytokinin | Abscisic acid | Jasmonic acid |
| Strigolakton | | |
| Gibberellins | | |
| Brassinostereoids | | |

AUXINS

Plant growth regulators with auxin properties are the oldest hormones used in agriculture (Halloran and Kasım, 2002). Auxin is synthesized by all higher plants, and the most abundant auxin form is Indole-3-acetic acid (IAA) (Grunewald et al., 2009). Auxin is the substance that generally causes cell expansion and growth, promoting plant growth by providing cell elongation, tissue development, and root formation. Auxins in meristematic tissues, including leaves, higher buds, and flowers, are transported downstream. Only one hormone, indole-3-acetic acid (IAA), is naturally produced in plants (Grunewald et al., 2009). The chemical makeup of

auxin was clarified, and it was shown that various chemicals with more or less structural similarities to IAA have similar effects on plants. 2011 (Williams). IAA is abundant at the plant's roots and stem ends (Cox et al. 2018). IAA is one of the most useful phytohormones, which promotes plant development under normal conditions and during times of stress. (Kazan 2013).

According to Algül et al. (2016), in addition to IAA, the most prevalent auxins include indole butyric acid (IBA), naphthalene acetic acid (NAA), naphthoxy acetic acid (NOAA), phenoxy acetic acid (FOAA), 2,4-D, phenylacetic acid (FAA), parachlorophenoxy acetic acid (4-CPA), and 2,4,5-trichlor Auxin is a crucial component of plant growth, gravitropism and phototropism, branching, and the development of embryonic patterns. Auxin is a key player in identifying and protecting stem cell differentiation in the root apical meristem and initiating lateral organ creation in the apical meristem of shoots during plant growth.

Some functions of auxins in plants are as follows (Halloran and Kasım, 2002);

- a) Since auxins can be transported in multiple directions or polar, they can be transferred from cell to cell. It effectively accelerates cell division, growth, and development in plants.
- b) It has been found to be effective in cell growth by increasing the cell's osmosis, facilitating the cell's permeability against water, and increasing the synthesis of specific RNA and protein-structured enzymes that increase the flexibility and width of the cell wall.
- c) Ensuring adventitious root development; Success has been achieved in rooting from stem segments, especially after treating the cut surfaces of vegetatively propagated woody plants with IAA.
- d) Obtaining parthenocarpic fruits; In the absence of pollination, flowers and fruits generally do not form. It is possible to obtain parthenocarpic fruits without fertilization by applying auxin (NAA) to some plant species. In most plants of the Solanaceae family, they promote fruit set in unfertilized ovaries.
- e) Prevention of leaf and fruit shedding; In particular, auxin is applied to transport ornamental plants that are desired to remain

evergreen and prevent citrus fruits' shedding before harvest. In addition, auxin (NAA) is applied in fruits such as apples or olives to ensure fruit thinning and to cause the remaining fruits to mature better.

- f) High auxin concentration in plants provides apical dominance during periods of rapid growth in the tips.
- g) It is effective in controlling weeds. Synthetic auxins with 2,4-D are widely used to control weeds in agricultural areas. Compounds with 2,4-D cause disorders in many plant functions, such as phloem transport, absorption, and photosynthesis. (Source and Memis, 1997). Recent studies have prohibited the use of 2,4-D compounds in tomato and eggplant due to the carcinogenic effect.

CYTOKININS

In contrast to other hormones, which are produced in plant tissues, particularly during cell division, quinine is an organic compound in both plants and mammals. The two major categories of cytokinins are (i) synthetic phenylurea derivatives, such as tidiuron (TDZ) and urea, and (ii) naturally occurring adenine derivatives, such as kinetin (KN) and 6-benzyladenine (BA).

The potency of synthetic phenylurea derivatives is greater than that of TDZ adenine derivatives. The most prevalent cytokinins are KN, BA, and zeatin, and they are typically present in immature tissues. According to Durmuş and Kadioğlu (2005), these phytohormones are crucial in protecting plants from biotic stressors, including viruses, bacteria, and fungus and abiotic stressors like cold, drought, heat, and salinity of the soil. Many CN-like compounds have been found in young fruits, running sap, and germinating seeds (Te-chato et al., 2008). Zeatin is a naturally occurring cytokinin that is obtained from canned fruit, coconut endosperm, and cornflakes. There are enough cytokinins in all organs with active cell division. It is specifically produced in root meristems, and the xylem subsequently transports it to the vegetative sections of the plant. Effective cell-division hormones also slow down aging (Algül et al., 2016). Auxins promote the growth of roots, whereas cytokinins promote the growth of shoots. In tissue culture medium, they help with organ creation and growth. According to theory, cytokinins postpone senescence by limiting the development of nuclease and protease in leaves, which prevents protein breakdown

(Williams, 2011). In addition to breaking dormancy, cytokinins speed up the transport of carbohydrates and reduce apex shoot dominance. Additionally, cytokinins are utilized to boost the yield and oil content of oilseeds like peanuts, hasten root induction, develop an effective root system, and prolong the shelf life of fruits (Singh et al, 2021).

STRIGOLACTONES

A variety of plants, including mosses, fungi, and angiosperms, produce the signal molecule strigolactones, which are important for plant development (Foo et al., 2013). It is the branching hormone that was just recently found. Strigolactones are terpene-group plant hormones with an extremely low molecular weight that are involved in how a plant reacts to various biotic and abiotic stimuli. Together with auxin, it has been acknowledged as one of the two hormones that have influenced the development of apical dominance during the past century. (2009) Hayward et al. Strigolactones are produced in the roots and transferred to the apical region of the plant via the xylem, where they are subsequently released to prevent the growth of lateral buds (Ferguson and Beveridge, 2009). The branching-related genes *ramosus*, *max*, and *Dad* are predicted to communicate well when strigolactones are present (Baktır, 2010). Strigolactones simultaneously promote the development of primary roots and root hairs while inhibiting the emergence of lateral roots (Koltai, 2015).

GIBBERELLINS

Gibberellins, like auxins, stimulate growth and development at low levels because they comprise a broad group of tetracyclic diterpenoid carboxylic acid derivatives (Garca-Martnez, 1997). The only class of plant growth regulators that is organized based on chemical structure rather than biological activity is the group of gibberellins. These substances are crucial for many plant growth and development processes, including seed germination, stem lengthening, and leaf formation. In 1926, a Japanese scientist discovered gibberellins in the fungus *Gibberella fujikuroi* and noted that it induces abnormal height growth in rice (Seçer, 1989). Later, this chemical was separated and given the name gibberellic acid (GA3) (Ferguson and Beveridge, 2009). Gibberellic acid is the most prevalent and significant form of gibberellin (Sponsel and Hedden, 2010). By controlling antioxidant metabolism and lowering lipid membrane peroxidation, gibberellic acid increases the absorption of calcium ions and other nutrients that may improve stress tolerance (Siddiqui et al., 2008). Now, it is known that gibberellin exists in 126 different forms. The plants contain

cambium, buds, embryos, roots, young leaves, blooms, and fruits (Baktır, 2010). Cell growth and division are increased by gibberellins, which is their most noticeable effect. Additionally, they work great for breaking dormancy, removing stunting and the need for chilling, and fostering parthenocarpic fruiting and germination (Rao et al., 2002). In order to decrease the number of fruits in the cluster and increase fruit size, GA is realistically utilized in the majority of tables and raisins.

BRASSINOSTEROIDS

Brassinostereoids (BR) was isolated from the pollen of rapeseed (*Brassica napus*) (Grove et al., 1979). The name of the brassinosteroids in the steroid structure comes from the *Brassica* genus of the *Crucifereae* family. Mevalonic acid serves as the beginning point for BR synthesis, despite the fact that this process is not entirely understood. BRs regulate plant growth and development in a variety of ways (Yokata, 1997). Increased vascular differentiation, cell division and expansion, pollen tube development, cellular differentiation, preservation of apical dominance, lateral root growth, flowering, senescence, and stress tolerance can be described as the key effects of BRs on plant development (Savaldi-Goldstein and Chory, 2006; Ashraf et al. al., 2010). When applied topically to some dwarf mutant plants that are unable to manufacture steroids, BR dramatically enhances stem elongation (Baktır, 2010). BRs are employed for a variety of other purposes as well, including improving yield, avoiding fruit drop, promoting germination and root development, and giving resistance to cold, salt stress, and infections (Rao et al., 2002).

ETHYLENE

Unlike other hormones, ethylene (C₂H₄) is an organic molecule gaseous at room temperature and affects the plant physiologically, even in extremely low quantities. All tissues are capable of producing ethylene. A crucial hormone, ethylene, significantly impacts the flavor, color, texture, and structure of horticultural crops. It is called the ripening hormone as well (gas). Every stage of a plant's growth and development can release this hormone. The highest levels of ethylene production occur during wilting in the leaves and flowers (Çetin, 2002). Fruits and vegetables like bananas, citrus fruits, pears, tomatoes, melons, and pineapple mature more quickly and turn yellow due to ethylene emissions in poorly ventilated warehouses. Bananas that have been picked before they are fully ripe are ripened in the same environment as a chemical (carbide) that causes the release of ethylene.

The most important functions of ethylene in the plant under natural conditions are as follows;

- a) To ensure fruit ripening, Under the influence of ethylene, the chlorophyll in the fruit is broken down and turns into pigments, the natural color of the fruit. Starch, organic acids, or fats are converted into sugars during maturation.
- b) It promotes aging.
- c) Ethylene facilitates separation by increasing the activities of enzymes that provide shedding, making it suitable for machine harvesting. It encourages yellowing leaves and easy separation of leaves, flowers, and fruit stems.
- d) It stimulates adventitious root formation.
- e) It is effective in determining the sex of plants. It is especially used to direct the sex in plants where male and female organs are in the same individual. The high use of ethylene causes the male flowers to drop and encourages the formation of females.

ABSCISIC ACID

It is a chemical with a sesquiterpene structure. It naturally opposes growth stimulants, including auxin, gibberellin, and cytokinin (Brewer et al., 2009). It is typically made in the cytoplasm of mesophyll cells and is present in practically all plant tissues, primarily in green leaves, and it is constantly accessible. The roots are not where ABA is generated since they lack chloroplasts. An abrupt rise in endogenous ABA levels is seen in the plant as external stress levels rise, which activates particular signaling pathways and modifies gene expression levels (Brien and Benkova 2013). Thus, it also alters how physiological events are affected. It is normally found in high amounts in dormant seeds and buds and is thought to have a dormancy-maintaining effect (Brewer et al., 2009). However, it is also found in leaves, stems, and fruits. Plants send the ABA they produce in their bodies to regions where there will be leaf fall, and in this way, leaf fall occurs in autumn. ABA promotes the closure of stomata in most plant species. It is known that ABA slows down RNA and protein synthesis and causes stomata closure together with CO₂ in plants under water stress. They prevent growth in storage organs such as seeds in annual plants and buds and tubers in biennial and perennial plants (Kaynak and Ersoy, 1997).

SALICYLIC ACID

Johann Buchner, a German scientist, first extracted salicylic acid (SA) from the willow tree's bark in 1828. (Hayat ve Ahmad 2007). SA is structurally a phenolic chemical from plants. Since SA is an analog of acetylsalicylic acid, it has been manufactured for use in commerce under the name "Aspirin" in Germany. Some scientists have found that SA is useful in promoting plant growth and development (Medina et al., 2017; Belt et al., 2018). SA is often present throughout the entire plant and is delivered by phloem to the necessary locations (Baktır, 2010). By altering roots and photosynthesis in legumes, SA reduces apple ethylene synthesis and increases yield (Hayat et al., 2007). Most importantly, salicylic acid has an important effect on the regulation of multiple responses to abiotic and biotic stress (Baktır, 2010).

JASMONIC ACID

First, methyl jasmonate (MeJA) and jasmonic acid (JA) esters were harvested from jasmine (*Jasminum spp*) plants (Fan et al., 1998). It is a fragrant substance that can be found in flowers and a variety of fruits. These substances boost a plant's resistance to diseases and pests and are produced by various plant organs, including the root, stem, leaves, flowers, and immature fruits (Medina et al., 2017).

REFERENCES

- Algül, B.E., Tekintaş, F.E., and Dalkılıç, G. (2016), Bitki Büyüme Düzenleyicilerinin Kullanımı ve İçsel Hormonların Biyosentezini Arttırıcı Uygulamalar. *Adnan Mend. Üniv. Zir. Fak. Der.*, 13(2), 87-95.
- Ashraf, M., Akram, N.A., Arteca, R.N., Foolad, M.R. (2010), The physiological, biochemical and molecular roles of brassinosteroids and salicylic acid in plant processes and salt tolerance, *Critical Reviews in Plant Sciences*, 29, 162-190.
- Baktır, İ. (2010). Bitki Büyüme Düzenleyicileri Özellikleri ve Kullanımları. Hasad Yayıncılık.
- Belt, K., Huang, S., Thatcher, L.F., Casarotto, H., Singh, K., Aken, O., and Millar, A.H. (2018), Salicylic acid-dependent plant stress signalling via mitochondrial succinate dehydrogenase. *Plant Physiology*, 176(1),1-30.
- Brewer, P.B., Dun, E.A., Ferguson, B.J., Rameau, C., Beveridge, C.A. (2009), Strigolactone Acts Downstream of Auxin to Regulate Bud Outgrowth in *Pea* and *Arabidopsis*. *Plant Physiology*, 150, 482-493.
- Brien, J.A.O., Benkova, E. (2013), Cytokinin cross-talking during biotic and abiotic stress responses. *Front Plant Sci*, 4, 451.
- Buban, T. (2000), The use of benzyladenine in orchard fruit growing:a mini review. *Plant Growth Regulation*, 32, 381-390.
- Cox, C.E., Brandl, M.T., de Moraes, M.H., Gunasekera, S., Teplitski, M. (2018), Production of the Plant Hormone Auxin by *Salmonella* and Its Role in the Interactions with Plants and Animals. *Front. Microbiol.* 8, 1-10.
- Çetin, V. (2002), Meyve ve Sebzelerde Kullanılan Bitki Gelişmeyi Düzenleyiciler. *Gıda ve Yem Bil. Tek. Der.* 12(2), 40-50.
- Durmus, N., Kadioğlu, A. (2005), Reduction of paraquat toxicity in maize leaves by benzyladenine, *Acta Biologica Hungarica*, 56 (1-2), 97-107.
- Fan, X., Matheis, J.B., and Fellman, J.K. (1998), A Role for Jasmonates in Climacteric Fruit Ripening. *Planta*, 204, 444-449.
- Ferguson, B.J., Beveridge, C.A. (2009), Roles for Auxin, Cytokinin, and Strigolactone in Regulating Shoot Branching. *Plant Physiology*, 149, 1929-1944.
- Fishel, F.M. (2006), Plant Growth Regulators, Document PI-139, Pesticide Information Office, Florida Cooperative Extension Service. *Institute of Food and Agricultural Sciences*, University of Florida.
- Flasiński, M., Hąc-Wydro, K. (2014), Natural vs synthetic auxin: Studies on the interactions between plant hormones and biological membrane lipids, *Environmental Research*, 133, 123-134.

- Foo, E., Yoneyama, K., Hugill, C., Quittenden, L.J., Reid, J.B. (2013), Strigolactones: internal and external signals in plant symbioses?. *Plant Signaling & Behavior*, 8(3), e23168.
- García-Martínez, J. (1997), Gibberellin metabolism and control of fruit growth. In: *VIII gibberellin (GA3) in the regulation of enzyme activities and in osmoprotectant accumulation in Brassica juncea L. under salt stress. J. Agron. Crop Sci.*, 194, 214-224.
- Grove, M.D., Spencer, G.F., Rohwedder, W.K., Mandava, N., Worley, J.F., Warthen, Jr., J.D., Steffens, G.L., Flippen-Anderson, J.L., Cook, Jr., J.C. (1979), Brassinolide, a plant growth-promoting steroid isolated from *Brassica napus* pollen. *Nature*, 281, 216–217.
- Grunewald, W., Noorden, G.V., Isterdael, G.V., Beeckman, T., Gheysen, G., Mathesius, U. (2009), Manipulation of auxin transport in plant roots during Rhizobium symbiosis and nematode parasitism. *The Plant Cell*, 21, 2553–2562.
- Hadi, F., Bano, A., Fuller, M. (2010), The improved phytoextraction of lead (Pb) and the growth of maize (*Zea mays* L.): the role of plant growth regulators (GA3 and IAA) and EDTA alone and in combinations. *Chemosphere*, 80, 457-462.
- Halloran, N., Kasım, M.U. (2002), Meyve ve sebzelerde büyüme düzenleyici madde kullanımı ve kalıntı düzeyleri. *Gıda*, 27 (5), 351-359.
- Hayat, S., Ahmad, A. (2007), *Salicylic Acid: A Plant Hormone*, Editors: S. Hayat, A. Ahmad içinde, Springer, Netherlands. <https://doi.org/10.1007/1-4020-5184-0>
- Hayat, S., Ali, B., Ahmad, A. (2007), *Salicylic Acid: Biosynthesis, Metabolism and Physiological Role in Plants*, Editors: S. Hayat, A. Ahmad içinde, *Salicylic Acid: A Plant Hormone*. Springer, Dordrecht.
- Hayward, A., Stirnberg, P., Beveridge, C., Leyser, O. (2009), Interactions Between Auxin and Strigolactone in Shoot Branching Control. *Plant Physiology*, 151, 400–412.
- International Symposium on Plant Bioregulation in Fruit Production*, 463, pp. 39-52.
- Kaynak, L., Ersoy, N. (1997), Bitki büyüme düzenleyicilerinin genel özellikleri ve kullanım alanları. *Akd. Üniv. Zir. Fak. Dergisi*, 10, 223-236.
- Kazan, K. (2013), Auxin and the integration of environmental signals into plant root development. *Ann Bot*, 112, 1655–1665.
- Kazan, K. (2013), Auxin and the integration of environmental signals into plant root development. *Ann. Bot.*, 112, 1655–1665.
- Koltai, H. (2015), Cellular events of strigolactone signalling and their crosstalk with auxin in roots. *Journal of Experimental Botany*, 66(16), 4855-4861.

- Medina, A.M., Appels, F.V.W., van Wees., S.C.M. (2017). Impact of salicylic acid and jasmonic acid-regulated defences on root colonization by *Trichoderma harzianum* T-78. *Plant Signaling & Behavior*, 12:8, e1345404 (4 pages), DOI:10.1080/15592324.2017.1345404
- Morsünbül, T., Solmaz, S.K.A., Üstün, G.E., Yonar, T. (2010), Bitki Gelişim Düzenleyicilerin Çevresel Etkileri ve Çözüm Önerileri. *Uludağ Üniv. Müh. Fak. Der.*, 15(1), 22-32.
- Opik, H., Rolfe, S.A., Willis, A.J., Street, H.E. (2005), *The Physiology of Flowering Plants* (4th ed.). Cambridge University Press. (p. 191.) ISBN 978-0-521-66251-2.
- Rademacher, W. (2015), Plant growth regulators: backgrounds and uses in plant production. *Journal of Plant Growth Regulation*, 34(4), 845-872.
- Rao, R.S.S., Vardhini, B.V., Sujatha, E., Anuradha., S. (2002). Brassinosteroids-A New Class of Phytohormones. *Current Science*, 82(10), 1239-1245.
- Raven, P.H., Evert, R.F., Eichhorn, S.E. (1992), *Regulating growth and development: The plant hormones* (in: *Biology of Plants*) (p 545-571), Worth Publishers, New York, USA.
- Savaldi-Goldstein, S., Chory, J. (2006), Brassinosteroids, Editors: L. Taiz, E. Zeiger içinde, *Plant Physiology, Fourth Edition* (p. 617-634), Sinauer Associates, Sunderland, Massachusetts.
- Seçer, M. (1989). Doğal Büyüme Düzenleyicilerin (Bitkisel Hormonların) Bitkilerdeki Fizyolojik Etkileri ve Bu Alanda Yapılan Araştırmalar. *Derim.*, 6(3), 109-124.
- Siddiqui, M.H., Khan, M.N., Mohammad, F., Khan, M.M.A. (2008), Role of nitrogen and
- Singh, V., Patel, Rajendra., Kumar, Satish., Sahu, M. P., Ahirwal, Arvind. (2021), Plant Growth Regulators and Their Use in Plant Growth and Development, 2 (4), 26-28.
- Sponsel, V.M., Hedden, P. (2004), Gibberellin, biosynthesis and inactivation. Editor: P.J. Davies içinde, *Plant hormones biosynthesis, signal transduction, action!*(p. 63-94), Springer, Dordrecht.
- Te-chato, S., Hilae, A., In-peuy K. (2008), Effects of cytokinin types and concentrations on growth and development of cell suspension culture of oil palm. *Journal of Agricultural Technology*, 4(2), 157-163.
- Williams, M.E. (2011), Introduction to Phytohormones. Teaching Tools in Plant Biology: Lecture Notes. The Plant Cell (online), doi/10.1105/tpc.110.tt0310.
- Yokota, T. (1997), The structure, biosynthesis and function of brassinosteroids. *Trends in Plant Science*, 2 (4), 137-143.

“

Chapter 8

**ENTROPY-BASED VOLATILITY
FORECASTING FOR SARS-COV-2
PANDEMIC DATA OF TURKEY**

Mine DOĞAN¹

Ayşe METİN KARAKAŞ²

”

1 Department of Statistic, Faculty of Sciences, Fırat University, Elazığ, Turkey. mined685@gmail.com **ORCID:** 0000-0002-2745-9909

2 Department of Statistic, Faculty of Art and Sciences, Bitlis Eren University, Bitlis, Turkey. aysekarakas5767@gmail.com 0000-0003-3552-0105

Introduction

As we know that the time-dependent pattern entropy is a technique that detracts to variable binary symbolic structure and modeling emblems in a gliding temporal window. In [1], authors have used this algorithm to simulate the instability of changes in multiple currency rates. In [2], researchers derived the weighted version of the measure and consequently named it Weighted Cumulative Residual Entropy. This technique or an entropy measure has been used in the time series and volatilities of the six financial markets in [3]. In [4], researchers have presented a fresh technique for simulating short-term information entropy to analyze rates of exchange. Also, they have created the short-term information entropy measure, by reducing the changes in rates of exchange to binary symbolic structures. And finally, a few upper and lower limits of the new dynamic measure which they developed are obtained in [5]. In [6], authors proposed a modified the cumulative measure of residual information founded on Tsallis entropy and its dynamic form. They examined the properties of the measure of knowledge which they suggested and defined a new life distribution classes according to this measure. In [7], researchers organized a cumulative Tsallis entropy in past life founded on the quantile mapping. They have received various properties formed on the given measurement and quantity-based reliability criteria. In [8], by using entropy measures depending on the powers of probability, authors proposed some entropy maximization problems to obtain risk-free densities. In [9], some differences and the relationship between the given model structure and its alternative format can be studied. In [10], authors introduced an different measure of the cumulative Tsallis entropy of the degree α and examined its characteristics. In [11], has examined the volatility of bitcoin and Ethereum. In [12], authors examined various entropy techniques for world indices (FTSE 100, ISE 30, SP 500, DAX 30, and NIKKEI 225) in before the starting of coronavirus-19 period (02.01.2019–17.11.2019) and the post-coronavirus-19 duration (18.11.2019–23.11.2020). In this study, a method based on entropy approach is used to investigate the Turkish corona-virus pandemic data sets (daily number of serious patients, daily number of tests performed, daily number of healing patients and daily number of deaths), for the period of 04.04.2020-08.02.2021. For the given data set, we determined the highest volatility by using the entropy technique.

Materials and Methods

Shannon Entropy and Renyi Entropy

Shannon Entropy specifies that a measure of the quantity of information $S(q)$ implicated on the series of incidents of q_1, q_2, \dots, q_N meets to three necessities:

- S should be continuous in the q_i ;
- if all the q_i are equally probably, then S should be a monotonic increasing function of N ,
- S should be additive,

then demonstrate that the S convincing these three necessities is:

$$S(Q) = -\beta \sum_{i=1}^N q_i \ln q_i$$

where β is a positive constant. Since this weight has called as the Shannon entropy. In the applications of information theory, the answer is proposed by the asymptotic equipartition characteristic; there is $U \subseteq S^n$ with,

$$|U| \leq e^{n(S(\rho) + \varepsilon)}$$

such that illustration n times from p , gives an factor of U with probability $> 1 - \varepsilon$, and $\varepsilon \rightarrow 0$ as $n \rightarrow \infty$. Renyi was capacitable to stretch the Shannon entropy to a continuous company of entropy measures;

$$S_t(Q) = -\frac{1}{1-t} \ln \sum_{i=1}^N q_i^t$$

The Renyi entropy goes to become Shannon entropy as $t \rightarrow 1$.

Renyi entropy;

- The scaling factor is traditional: it textures S_t non-negative for all t and ascertains $S_t(u_n) = \log n$, here u_n is the uniform distribution on an n -element set.
- The main common characteristic between the Rényi and Shannon entropy is additivity:

$$S_t(\alpha \times \delta) = S_t(\alpha) + S_t(\delta).$$

- For $t = 1$, acquired Shannon entropy:

$$S_1(\alpha) = \lim_{t \rightarrow 1} S_t(\alpha)$$

$$\frac{d}{dt} \left(\frac{1}{1-t} \log \left(\sum_i \alpha(i)^t \right) \right)_{t=1} = - \sum_i \alpha(i) \log \varepsilon(i).$$

- For $t = \infty$, acquired the min entropy:

$$S_\infty(\alpha) = - \log \max_i \alpha(i) = \log \min_i \frac{1}{\alpha(i)}$$

The Tsallis Entropy

Let φ is positive real-number, then the Tsallis Entropy of order φ of probability measure q defined on finite set X is given by

$$S_\varphi(q) = \begin{cases} \frac{1}{\varphi-1} \left(1 - \sum_{i \in X} q_i^\varphi \right), & \text{if } \varphi \neq 1 \\ - \sum_{i \in X} q_i \ln q_i, & \text{if } \varphi = 1 \end{cases}.$$

Approximate Entropy

(Pincus, 1991); for a given non-negative integer i , and positive integer N with $i \leq N$, a real number (positive) r , and a real numbers sequence $v: = (v(1), v(2), \dots, v(N))$, assume that the distance between two blocks $x(a)$ and $x(b)$, where $x(a) = (v(a), v(a+1), \dots, v(a+i-1))$, be given by $d(x(a), x(b)) = \max_{c=1,2,\dots,i} (|v(a+c-1) - v(b+c-1)|)$.

Then let $C_a^i(r) = (\text{number of } b \leq N - i + 1 \text{ such that } d(x(a), x(b)) \leq r) / (N - i + 1)$. Now,

$$\begin{aligned} \phi^i(r) &= \frac{1}{N - i + 1} \sum_{a=1}^{N-i+1} \log C_a^i(r), \\ \text{ApEn}(i, r, N)(v) &= \phi^i(r) - \phi^{i+1}(r), \quad i \geq 1; \\ \text{ApEn}(0, r, N)(v) &= -\phi^1(r) \end{aligned}$$

$\text{ApEn}(i, r)$ is a group of parameters; proportions are purposed with fixed i and r . Most crucially, nevertheless thematic schematic similarities, $\text{ApEn}(i, r, N)$ is not purposed as a Kolmogorov–Sinai entropy’s approximate value. Pincus and Goldberger, 1994 and Steve Pincus, 2008 given;

$-\text{ApEn}(i, r, N)(v) \approx$ average over a of $\ln[\text{conditional frequency that } |v(b+i) - v(a+i)| \leq r, \text{ given that } |v(b+c) - v(a+c)| \leq r$

for $c = [0, 1, 2, \dots, i - 1]$
with equality (for fixed i and r) in the limit as $N \rightarrow \infty$.

Results

Data Set

We choose the Turkish pandemic datasets of corona between 04.04.2020 to 08.02.2021 (the number of daily seriously ill patients, number of tests, improving the patient number, and the number of deaths). Table 1 summarizes the statistics of the data for Turkey's corona pandemic which we adopted (number of patients per day, number of tests, improving the patient number and, the number of death). Also, various mean-values for the data set in Table 1 are shown and the relative standard deviations are various. Here, the skewness for the data set is positive. The kurtosis of both data sets is greater than 1. The Jarque-Bera (JB) test exemplifies that the mean of the general data set distributions are not normal since the normality of each series distribution is rejected at the 0.05 significance level. Figure 1 shows the quantile plots. Looking at these graphs, it is observed that the series is far from a normal distribution. In Figures 2,3,4 and 5 the daily change graph of the residuals of the series is given. In Figure 6, autocorrelation graphs are given for the data set which we used. The autocorrelation data set shows the correlation between values in different time periods. In other words, the similarity between the observed values is a function of the temporal delay. Here, we examined the autocorrelation graphics of the data set which we determined for Sars-Cov-2, and observed its changes over time as seen in Figures 6(a), 6(b), 6(c), and 6(d). The highest autocorrelation in the series occurs in the number of tests applied per day. This is followed by the number of patients per day, the number of deaths and, the number of recoveries.

Table 1. Descriptive Statistics (period 04.04.2020-08.02.2021)

| | Daily Number of Patients | Daily Number of recovering patients | Daily Number of Performed Test | Daily Number of Deaths Patients |
|-------------|-----------------------------|--|-----------------------------------|------------------------------------|
| Mean | 2113,090 | 4440,845 | 98692,47 | 85,33871 |
| Maximum | 7381,000 | 44514,00 | 208873,0 | 259,0000 |
| Minimum | 618,0000 | 256,0000 | 19664,00 | 14,00000 |
| Std. Dev | 1539,228 | 7013,000 | 56479,24 | 68,83998 |
| Skewness | 1,622981 | 3,157252 | 0,265210 | 0,977141 |
| Kurtosis | 4,824214 | 13,24312 | 1,694008 | 2,914048 |
| Jarque-Bera | 179,0769 | 1870,261 | 25,66491 | 49,42696 |
| Probability | 0.000000 | 0.000000 | 0.000003 | 0.000000 |

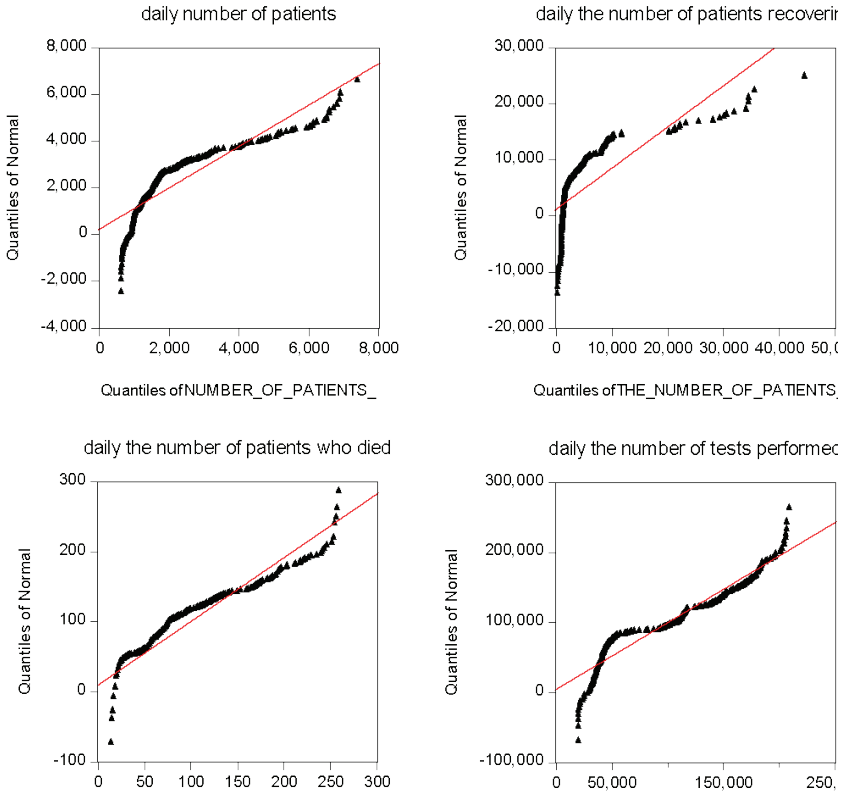
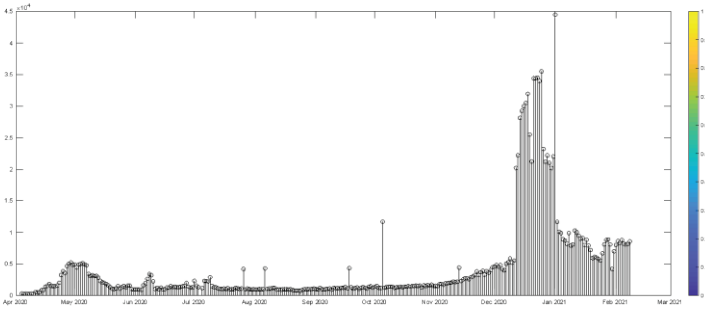


Figure1. Quantiles Graphs of Data sets (period 04.04.2020-02.12.2020)



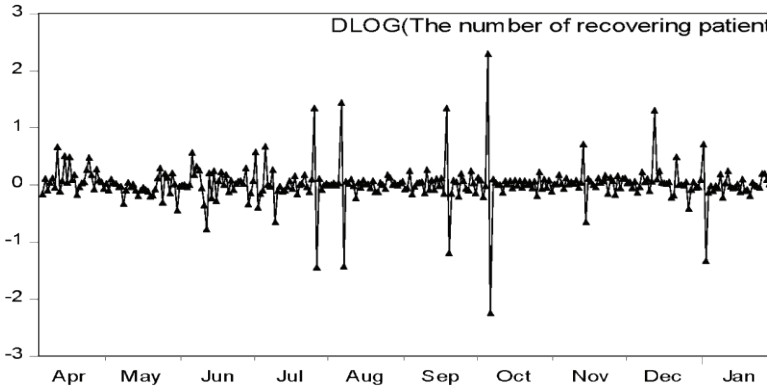


Figure 2. Graph of daily number of recovering patients (period 04.04.2020-08.02.2021)

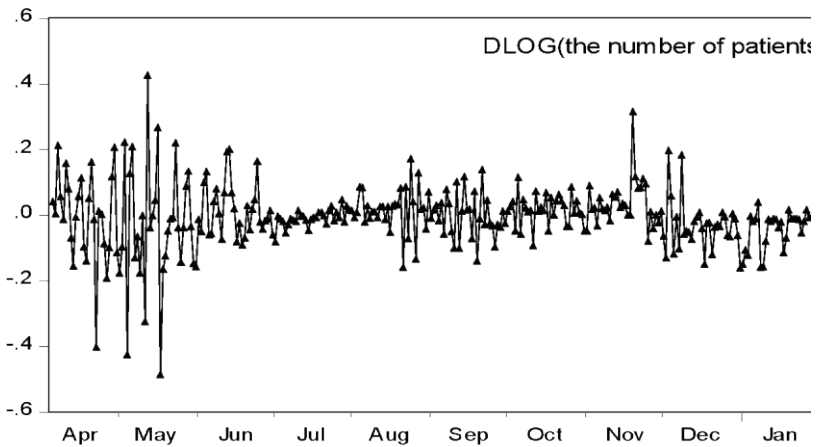
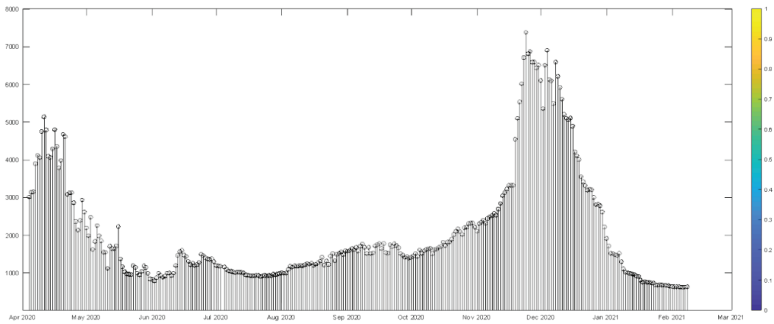


Figure 3. Graph of daily number of patients and residual patients (period 04.04.2020-08.02.2021)

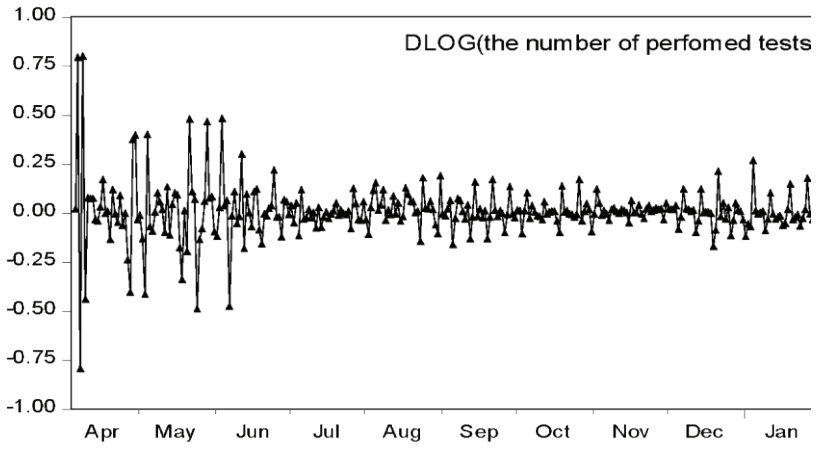
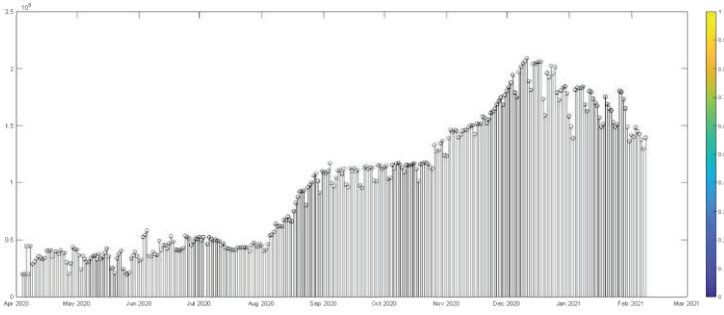
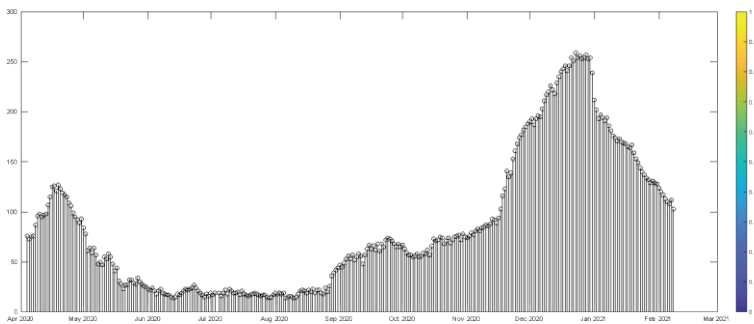


Figure 4. Graph of daily number of tests performed and residual tests performed (period 04.04.2020-08.02.2021)



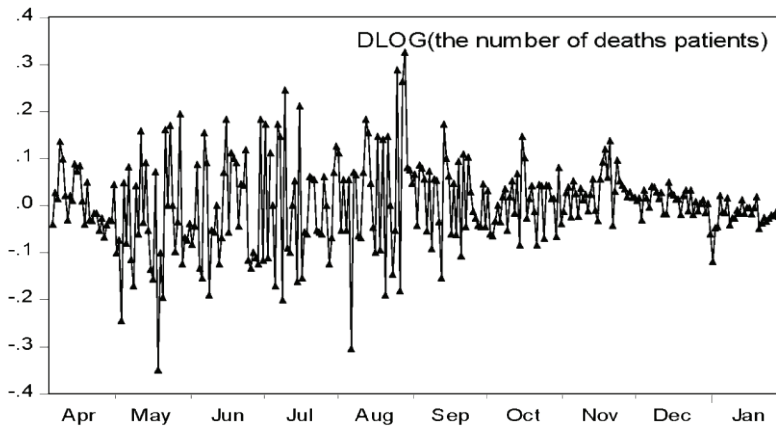
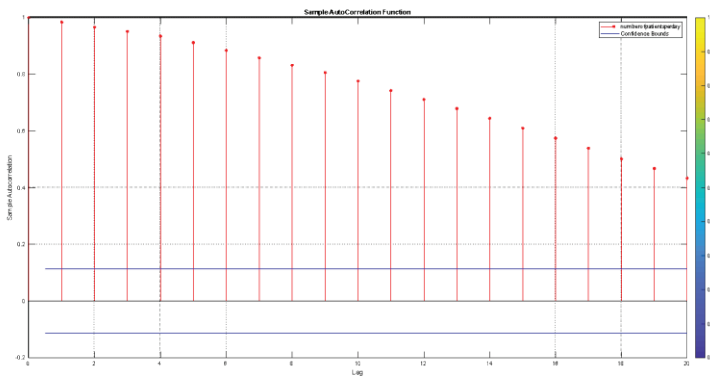
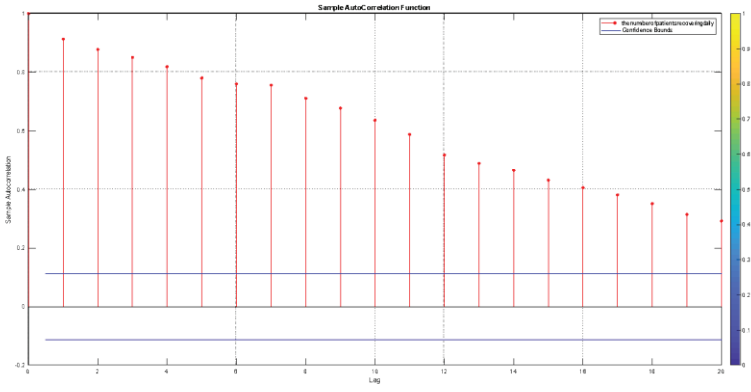


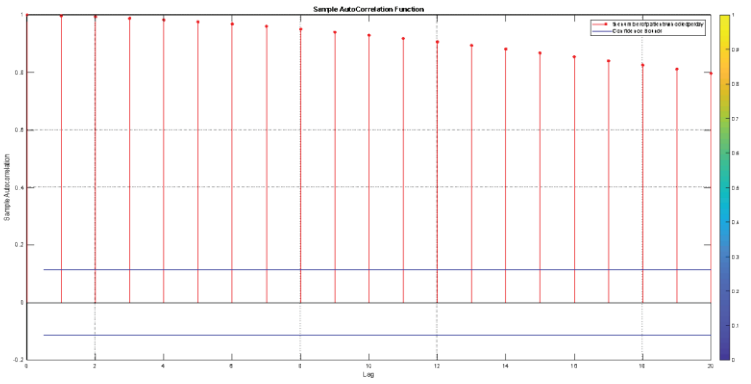
Figure 5. Graph of daily number of deaths patients (period 04.04.2020-08.02.2021)



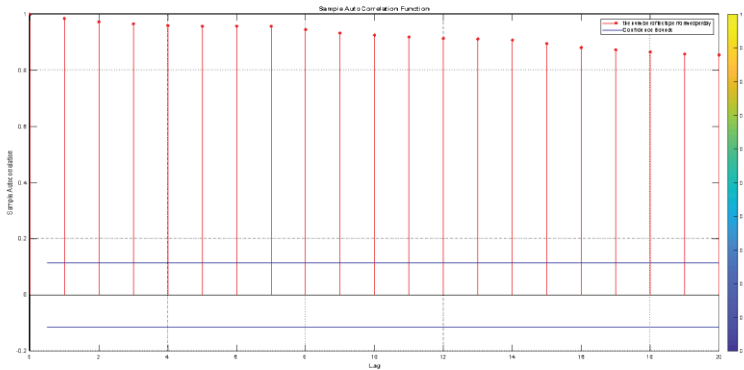
a) The number of daily patient



b) The number of daily recovering patients



c) The number of daily deaths patients



d) The number of daily test performance

Figure 6. Graphs of ACF, Daily the number of patients, daily the number of recovering patients, daily the number of deaths patients and daily the number of test performance, respectively, (period 04.04.2020-08.02.2021)

Entropy Approach

We use the entropy method for the volatility of a daily number of serious patients, the number of tests performed, the number of healing patients and a number of dying patients for Turkey's coronavirus pandemic cases, respectively. Therefore, we estimate Tsallis, Shannon, approximate, and Rényi entropies. In Table 2-5, for Turkey's corona pandemic cases, initially, we obtain various several estimators for the Shannon entropy measure. Subsequently, we acquired the Tsallis entropy for a variety of parameter values and Rényi entropy measures for various parameter values. Eventually, we got approximate entropy. When whole possible cases have an equal probability, the entropy acquires maximum value. From our analysis, volatility doesn't justify difference; this model demonstrates linear and non-linear structures. From the quantitative conclusions, we get that whole entropies are positive so, the characters of our data sets are non-linear. We obtained those data sets (daily serious patients, the number of tests performed, healing number, and a number of dying patients for Turkey's corona pandemic case) series that have a great value of approximate entropy, respectively. In the data series, when we are looking at the daily number of serious patients, the number of tests performed, number of healing patients, and a number of dying patients for Turkey's coronavirus pandemic case volatility in Tables 2-5 and Figures 1-5, we observed that volatility is mostly seen in the number of tests

performed, followed by the number of healing patients, the number of dying patients, respectively. Here we see that the volatility in the number of tests, actually directly affects the number of patients, the number recovered, and the number of deaths. Therefore, it is obvious that the volatility in the number of tests will be prevented by following the rules that the applicants feel sick and change rapidly on a daily basis. It concludes that the corona pandemic of Turkey's cases that the number of tests performed, the data series is higher than the volatility of other data series. For the Shannon entropy forecasters, the corona pandemic of Turkey's cases, it is justified that the number of tests performed in the series has a larger value. In the same way, for the measures of Rényi, and Tsallis entropy, we considered that q and r are close to 1, so we get the Shannon entropy.

Table 2. Daily number of patients (period 04.04.2020-08.02.2021)

| Method | Shannon | | Tsallis | | Renyi | Approximate Entropy |
|----------|----------|-----|------------|----------|----------|---------------------|
| | Value | q | Value | r | Value | Value |
| ML | 4.254406 | 0 | 308.000000 | 0 | 5.733341 | |
| MM | 4.256997 | 0.2 | 72.2809512 | 0.25 | 4.958091 | |
| Jefferys | 4.266721 | 0.4 | 25.3396935 | 0.5 | 4.502874 | |
| Laplace | 4.278458 | 0.6 | 12.0781409 | 1 | 4.254406 | |
| SG | 4.254488 | 0.8 | 6.8221111 | 2 | 4.187699 | 0.1730986 |
| Minimax | 4.273569 | 1 | 4.2544064 | 4 | 4.101606 | |
| CS | 4.264662 | 1.2 | 2.8542310 | 8 | 3.847798 | |
| Shrink | 4.261069 | 1.4 | 2.0368206 | 16 | 3.604435 | |
| | | 1.6 | 1.5329072 | 32 | 3.488179 | |
| | | 1.8 | 1.2064258 | 64 | 3.432811 | |
| | | 2 | 0.9848188 | Infinite | 3.379173 | |

Table 3. Daily number of tests performed (period 04.04.2020-08.02.2021)

| Method | Shannon | | Tsallis | | Renyi | Approximate Entropy |
|----------|----------|-----|------------|----------|----------|---------------------|
| | Value | q | Value | r | Value | Value |
| ML | 5.561127 | 0 | 308.000000 | 0 | 5.733341 | |
| MM | 5.566191 | 0.2 | 117.673882 | 0.25 | 5.684713 | |
| Jefferys | 5.563006 | 0.4 | 47.990271 | 0.5 | 5.639590 | |
| Laplace | 5.564852 | 0.6 | 21.196740 | 1 | 5.561127 | |
| SG | 5.56114 | 0.8 | 10.295455 | 2 | 5.448432 | 0.4046694 |
| Minimax | 5.563245 | 1 | 5.561127 | 4 | 5.329611 | |
| CS | 5.561127 | 1.2 | 3.346980 | 8 | 5.227627 | |
| Shrink | 5.572326 | 1.4 | 2.224053 | 16 | 5.143766 | |
| | | 1.6 | 1.604722 | 32 | 5.080754 | |
| | | 1.8 | 1.234242 | 64 | 5.040571 | |
| | | 2 | 0.995697 | Infinite | 4.985120 | |

Table 4. Daily number of recovering patients (period 04.04.2020-02.12.2020)

| Method | Shannon | | Tsallis | | Renyi | Approximate Entropy |
|----------|----------|-----|-------------|----------|----------|---------------------|
| | Value | q | Value | r | Value | Value |
| ML | 3.900078 | 0 | 308.0000000 | 0 | 5.733341 | |
| MM | 3.904174 | 0.2 | 72.6956620 | 0.25 | 4.950579 | |
| Jefferys | 3.919988 | 0.4 | 24.0181920 | 0.5 | 4.356531 | |
| Laplace | 3.938961 | 0.6 | 10.9258813 | 1 | 3.900078 | |
| SG | 3.90021 | 0.8 | 6.1390795 | 2 | 3.752276 | 0.2620661 |
| Minimax | 3.924905 | 1 | 3.9000776 | 4 | 3.692292 | |
| CS | 3.915211 | 1.2 | 2.6809180 | 8 | 3.632421 | |
| Shrink | 3.906425 | 1.4 | 1.9544545 | 16 | 3.517028 | |
| | | 1.6 | 1.4943439 | 32 | 3.409803 | |
| | | 1.8 | 1.1885148 | 64 | 3.355692 | |
| | | 2 | 0.9765357 | Infinite | 3.303260 | |

Table 5. Daily number of deaths patients (period 04.04.2020-02.12.2020)

| Method | Shannon | | Tsallis | | Renyi | Approximate Entropy |
|----------|----------|-----|-------------|----------|----------|---------------------|
| | Value | q | Value | r | Value | Value |
| ML | 5.426393 | 0 | 308.0000000 | 0 | 5.733341 | |
| MM | 5.432231 | 0.2 | 114.7581233 | 0.25 | 5.646163 | |
| Jefferys | 5.430252 | 0.4 | 46.2232193 | 0.5 | 5.565309 | |
| Laplace | 5.434032 | 0.6 | 20.3808828 | 1 | 5.426393 | |
| SG | 5.426419 | 0.8 | 9.9555020 | 2 | 5.232437 | 0.183241 |
| Minimax | 5.430448 | 1 | 5.4263933 | 4 | 5.033098 | |
| CS | 5.426393 | 1.2 | 3.2950157 | 8 | 4.877461 | |
| Shrink | 5.438156 | 1.4 | 2.2043213 | 16 | 4.773391 | |
| | | 1.6 | 1.5972972 | 32 | 4.710785 | |
| | | 1.8 | 1.2314622 | 64 | 4.675161 | |
| | | 2 | 0.9946595 | Infinite | 4.623495 | |

Conclusion

In this research article, we studied the dynamics of Sars-Cov-2 for the daily reported data of Turkey. We have made volatility calculations using various entropy methods. In which, Tsallis Entropy, Approximate Entropy, Shannon Entropy, and Renyi Entropy have been used to explain this volatility. We acquired that given data sets of daily serious patients, the number of tests performed, healing number and, number of dying patients for Turkey's coronavirus cases series have great value of approximate entropy, respectively. We selected data series in Table 3-7 and Figure 1-5, for analyzing our results for the mentioned Turkey's corona pandemic situation of the number of daily seriously ill patients' volatility, number of tests performed when recovering from patient number and deaths number of high to lower order. We concluded that the given entropy approach is strong and effective to study the given epidemic structure. In the future,

the given algorithm can be further used to simulate the covid-19 data of any other particular country.

***Acknowledgments:** Thank you to the Republic of Turkey Ministry of health for our data set.*

REFERENCES

- [1] Ishizaki, R., & Inoue, M. (2018). Time-series analysis of multiple foreign exchange rates using time-dependent pattern entropy. *Physica A: Statistical Mechanics and its Applications*, 490, 967-974.
- [2] Khammar, A. H., & Jahanshahi, S. M. A. (2018). On weighted cumulative residual Tsallis entropy and its dynamic version. *Physica A: Statistical Mechanics and its Applications*, 491, 678-692.
- [3] Ponta, L., & Carbone, A. (2018). Information measure for financial time series: Quantifying short-term market heterogeneity. *Physica A: statistical mechanics and its applications*, 510, 132-144.
- [4] Ishizaki, R., & Inoue, M. (2020). Analysis of local and global instability in foreign exchange rates using short-term information entropy. *Physica A: Statistical Mechanics and its Applications*, 555, 124595.
- [5] Bhat, B. A., & Baig, M. A. K. Weighted Generalized Cumulative Residual Entropy and its Dynamic Version for Lifetime Distributions.
- [6] Sati, M. M., & Gupta, N. (2015). Some characterization results on dynamic cumulative residual Tsallis entropy. *Journal of probability and statistics*, 2015.
- [7] Krishnan, A. S., Sunoj, S. M., & Sankaran, P. G. (2019). Quantile-based reliability aspects of cumulative Tsallis entropy in past lifetime. *Metrika*, 82(1), 17-38.
- [8] Sheraz, M., & Preda, V. (2015). Entropy Measures in Finance and Risk Neutral Densities.
- [9] Mohamed, M. S. (2020). On cumulative Tsallis entropy and its dynamic past version. *Indian Journal of Pure and Applied Mathematics*, 51(4), 1903-1917.
- [10] Rajesh, G., & Sunoj, S. M. (2019). Some properties of cumulative Tsallis entropy of order α . *Statistical papers*, 60(3), 933-943.
- [11] Karakaş, A. M. (2019). Entropy approach for volatility of ethereum and bitcoin. *Asian Journal of Business and Management*, 7(1).
- [12] Karakaş, A. M., Doğan, M., & Çalik, S. (2021). The Impact of the SARS-CoV-2 Epidemic on World Indices: The Entropy Approach. *Mathematical Problems in Engineering*, 2021.
- [13] Pincus, S. M. (1991). Approximate entropy as a measure of system complexity. *Proceedings of the National Academy of Sciences*, 88(6), 2297-2301.

- [14] Pincus, S. M., & Goldberger, A. L. (1994). Physiological time-series analysis: what does regularity quantify?. *American Journal of Physiology-Heart and Circulatory Physiology*, 266(4), H1643-H1656.
- [15] Pincus, S. (1995). Approximate entropy (ApEn) as a complexity measure. *Chaos: An Interdisciplinary Journal of Nonlinear Science*, 5(1), 110-117.

“

Chapter 9

**BDELLOVIBRIO AND LIKE ORGANISMS
(BALOS): BRIEFLY LIFE**

Dilek ŐEKER¹

”

¹ Arař. Gör. Dr., Dilek ŐEKER, Manisa Celal Bayar Üniversitesi, Fen Edebiyat Fakültesi, Biyoloji Bölümü, Temel ve Endüstriyel Mikrobiyoloji Anabilim dalı

Introduction

Predation is a unique interaction in the ecosystem that predator organism takes energy and biosynthetic materials through its prey (Sinha et. al. 2014). The prey-predator relationship is one of the oldest and most important interactive relation(s) in nature. Predators are keystone species in ecosystems (Summers and Kreft, 2019) and they kill the prey during predation (Jurkevitch, 2006). Predatory prokaryotes, bacteriophage and protists are observed to prey upon bacteria. Predatory bacteria are living organism unlike viruses and phages, and small size and high swimming unlike protists (Sinha et. al., 2014). Predatory bacteria are phylogenetically various and found in terrestrial and aquatic environments (Baer et. al., 2000) such as rivers, groundwater, estuaries, the open ocean, sewage, soils, plant roots, and animal feces (Jurkevitch, 2007).

The best studied bacterial predator is *Bdellovibrio* and like organisms (BALOs) of the δ -proteobacteria which discovered in 1962 by Stolp and Petzold while they are making isolation from soil bacteriophage (Stolp and Starr, 1963). This was followed by the research for physiology, ecology, taxonomy, interactions with the prey and cell cycle of these microorganisms in the 1960s, 1970s and 1980s. Recently, this research field is combined with the modern molecular biology, microbial ecology and genetics (Rotem et. al., 2014). *Bdellovibrio* and like organisms (BALOs) were found within the α -proteobacteria which forms the genus *Micavibrio* sp. and the δ -proteobacteria which forms three families of *Bdellovibrionaceae*, *Bacteriovoraceae* and *Halobacteriovoraceae* (Jurkevitch and Davidov, 2006).

Morphology of BALOs

BALOs (0.25-0.5x0.75-2 μm) are shows Gram negative properties in free-living phases have rod, small vibroid shape, and moves at high speed with a single sheathed flagellum (Figure 1) (Thomashow and Rittenberg, 1985). The predicted speed of *Bdellovibrio bacteriovorus*, one of the predatory microorganisms, is approximately 100 cells per second. This value is about 10 times of the speed of *E. coli* cells (Rittenberg, 1983). These microorganisms are aerobic and mesophilic bacteria. In addition to providing their energy from oxidation of amino acids and acetate, they can absorb nucleotides, fatty acids, peptides and even whole proteins directly from the host cell. The optimum growth temperature is 28-30°C (Madigan and Martinko, 2010). BALOs are obligat aerob and they can multiply under oxy conditions, but they can remain alive in anoxic periods as attack

phase cells or bdelloplasts (Schoeffield, 1991). BALOs activity is significantly reduced in the presence of certain chemicals, such as high concentrations of glucose or glycerol, and also at low pH (Dwidar et. al., 2012). However, the growth and proliferation of wild predators can only occur in the presence of host cells. Usually, they are able to utilize various Gram negative bacteria as host cells. Therefore BALOs are obligate predatory prokaryotes (Seidler and Starr, 1969). The host cells used to isolated and characterized the predator were nearly exclusively from the Proteobacteria phylum. In particular bacteria used as a host cell such as *Escherichia coli*, *Pseudomonas* spp. and *Erwinia* spp. for terrestrial and freshwater habitats and *Vibrio parahaemolyticus* for marine habitats (Jurkevitch and Davidov, 2006).



Figure 1. *Bdellovibrio bacteriovorus* 100, Electron Micrograph, 14,000 × (Stolp and Starr, 1963).

The life cycle of BALOs are a dimorphic life cycle. It is composed of two main phases, an attack phase (AP), and a growth and division phase (GP) (Sinha et. al. 2014; Jurkevitch and Davidov, 2006). The axenic cycle, which includes the growth and division of predator cells, do not require prey cells, meanwhile the intracellular cycle is characterized by prey cells (Sinha et. al. 2014; Eckhard et. al., 2007). Under laboratory conditions, there are mutants that independent of host cells and this mutant types requires rich medium for growth (Seidler and Starr, 1969). Facultatives can develop in both host cells and media. All strains are chemoorganotroph (Krieg and Holt 1984). BALOs are isolated in habitats such as bulk soil (Stolp and Starr, 1963), rhizosphere (Elsherif and Grossmann, 1996), paddy field (Uematsu,1980), sea (Pan et. al.,1997), gulf (Miyamoto and Kuroda, 1975), fresh and saltwater ponds (Richardson, 1990), river (Fry

and Staples, 1976), estuaries (Williams et. al., 1982), sea creatures (Kelley and Williams, 1992), sewage (Staples and Fry, 1973) the gut of humans and animals (Cao et. al., 2012), and crab gills (Kelley and Williams, 1992).

BALOs are isolated with similar methods like bacteriophages. The sample is mixed with a prey in melted soft agar and poured onto an agar plate. The predator forms transparent lytic plaques and they are differentiated from by protozoa and bacteriophages plaques. Disadvantages of this isolation method are, first of all BALOs vary in host range, no bacterial species can't support the growth of all isolates. Another one, the method originate from presence of a great number of non predatory bacteria in the sample that grows on the plate and blur the plaques (Rotem et. al., 2014).

The number of BALOs detected from environmental samples using the standard double layer isolation procedure is generally low in units of tens to tens of thousands of plaque-forming units per gram or milliliter of sample, thus the number of BALOs related 16S rRNA sequences in the databases that sourced from environmental studies is also low. The reason for the lack of these sequences in the databases originate from PCR biases when domainwide 16S rDNA primers used for amplifying environmental DNA, as the predatory bacteria do not form a dominant population (Davidov, 2006).

Taxonomy

The predatory bacteria are isolated by Stolp and Petzold in 1962 and have been identified as the new genus *Bdellovibrio*, species *bacteriovorus* (Stolp and Starr, 1963). Based on all genome DNA-DNA hybridization tests, G+C contents, rRNA homology, enzyme migration patterns and genome-predicted dimensions, the genus was divided into three types: *Bdellovibrio bacteriovorus*, *Bdellovibrio stolpii* and *Bdellovibrio starrii*. Although BALOs showed high variability in G+C rates, fatty acid profiles, serological reactions, partial 16S rRNA sequences and DNA-DNA hybridizations have been found to give very low values between them (Siedler, 1972). The classification changes are based on the 16S rRNA analysis: *Bdellovibrio stolpii* and *Bdellovibrio starrii* are classified as the new genus, *Bacteriovorax stolpii* (Beebe, 1941), *Peredibacter starrii* (Davidov and Jurkevitch 2004) and *Bacteriolyticum stolpii* (Pineiro et. al., 2008). In these studies, two new species, *Bacteriovorax marinus* and *Bacteriovorax litoralis* have been identified (Baer et. al., 2004). Established with phylogenetic analysis that based on 16S rRNA gene sequences,

Bdellovibrio exovorus has been identified (Koval et. al., 2013). *Bacteriovorax litoralis* has been reclassified to *Halobacteriovorax marinus* and *Halobacteriovorax litoralis* (Koval et. al., 2015). *Micavibrio* sp. was initially described as two species: *Micavibrio admirantus* and *Micavibrio aeruginosavorus* (Lambina et. al., 1982). In later studies, according to 16S rRNA gene sequences, only *Micavibrio aeruginosavorus* has been identified (Davidov et. al., 2016). BALOs are found in the α -proteobacteria class, which forms the genus *Micavibrio* and in the δ -proteobacteria class, which forms three families: *Bdellovibrionaceae*, *Bacteriovoracaceae* and *Halobacteriovoraceae*.

The *Bdellovibrionaceae* is located within the *Bdellovibrionales* that contains one genus in *Bdellovibrio* and two species *Bdellovibrio bacteriovorus* and *Bdellovibrio exovorus*. The family defined as encompassing eleven stable monophylic clusters (Jurkevitch and Davidov, 2006). *B. bacteriovorus* HD100T and *B. exovorus* JSST is differ in the 16S rRNA gene sequence in terms of % mol G+C content (50% and 41% respectively) and decompose by 7% (93% similar). The difference between *Bdellovibrio bacteriovorus* and *Bdellovibrio exovorus* is in the predation strategy: *B. bacteriovorus* is a periplasmic predator, however, *B. exovorus* is an epibiotic predator. They are other important differences between the two species, such as *B. exovorus* does not form bdelloplast and does not use *E. coli* as host cells (Koval et. al., 2013).

The *Bacteriovoracaceae* is located within the *Bacteriovoracales* contains two species, *Bacteriovorax stolpii* and *Peredibacter starii*. The family was consisted of ten phylogenetic clusters (Pineiro, 2007). These clusters are robust because the rpoB gene that protects these clusters is present in genome (Pineiro et. al., 2008). *Bacteriovorax stolpii* has % mol G+C content of 41-43.5, while *Peredibacter starii* has % mol G+C content of 43.5.

The *Halobacteriovoraceae* is located within the *Bacteriovoracales* that contains three species, *Halobacteriovorax marinus*, *Halobacteriovorax litoralis* and *Halobacteriovorax vibrionivorans* (Davidov and Jurkevitch 2004). The G+C content (<38 mol%) in this family is the lowest value of the other BALOs. This family is the only family that found in saltwater habitats, and isolates of this bacteria needs NaCl supplement to grow (Koval et. al., 2015).

Micavibrio sp. belongs to the class of α -proteobacteria. It was first described in 1982 as *Micavibrio admirantus* (% mol G+C content of

57.1) (Lambina et. al., 1982) and *Micavibrio aeruginosavorus* (% mol G+C content of 54.7) (Lambina et. al., 1983) Both species were isolated from sewage (Jurkevitch and Davidov, 2006). *Micavibrio* sp. and the other BALOs doesn't belong to the same proteobacteria class. Accordingly, although some morphological features are different, their similarities in biochemical level are the same. For example; in the early stages of interaction, originating from the host bacteria, absorb material increase in the wavelengths of 260 and 280 nm in both predators. There are also enzymes of the glycolytic pathways and enzymes of tricarboxylic acid cycle (Afi-nogenova et. al., 1986).

BALOs' life cycle

The life cycle of BALOs are accompanies the cell cycle and consists of two main and different stages, namely an attack phase, and a growth and division phase. The lower parts of these phases are the life stages of both periplasmic and epibiotic predators. Generally, BALOs are periplasmic predator and the definition of BALOs life cycle based on with the periplasmic stage predator strategies (Figure 2) (Rotem et. al., 2014).

1) Motility and finding host cell: Attack phase cells are small, vibroid, highly motile, non-recurring cells and have a single sheathed flagellum consisting of six different flagellin proteins (FliC1-6) (Rotem et. al., 2014).

Chemotaxis: BALOs have multiple methyl-accepting chemotaxis proteins (MCPs). They detect various ligands and create positive and negative chemotaxis against inorganic ions, organic acids, amino acids and oxygen (Straley et. al., 1979).

2) Attachment to host cell: Attachment of BALOs to the host cell depends on many factors. These are consists of the composition and pH of the medium, oxygen pressure and temperature. The first attachment is reversible. The Type IVa pili provides the attachment of the predator to the host cell and the invasion through the periplasm of the host cell. It is the presence of specific receptors and domains that mainly affects the attachment. For example; the predators attack gram negative bacteria, because they have the same LPS layer. However, in the absence of certain porins such as OmpF and OmpC (outer membrane proteins, Omps) in *E. coli*, the attachment has been shown to be decreased (Rotem et. al., 2014).

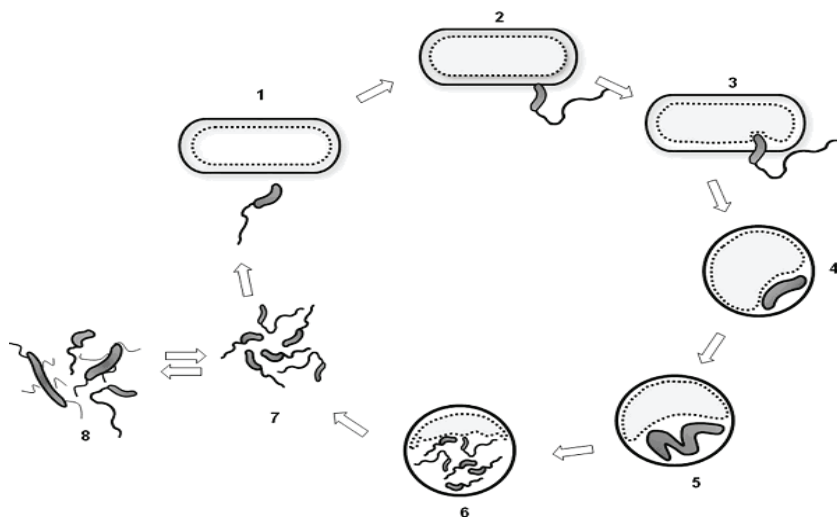


Figure 2. Life Cycle of *Bdellovibrio bacteriovorus* (In host-dependent) 1. Search for prey. 2. Attachment to prey. 3. Entry into periplasm. 4. Formation of bdelloplast. 5. Filamentous growth. 6. Segregation of *Bdellovibrio*. 7. Release of progenies. (In host-independent) 8. Attack phase like cells and long filamentous cells (Javaherdashti and Alasvand, 2019).

3) Host cell invasion and bdelloplast formation: Penetration of the periplasm is achieved by compressing the predator towards to the pore, which can be done using the pili (Evans et. al., 2007). Bdelloplast construction occurs by the activity of glycanases and the dissolution of 10-15% of the N-acetylglucosamine of the cell wall (Thomashow and Rittenberg, 1978c). However, according to studies, it has been shown that the peptidase penetrates into the host cell, not glycanase activity, and autolytic muramidases of the host cell are caused by the rounding of the bdelloplast (Tudor et. al., 1990).

4) Growth and division: The predator grows filamentously in width of the cytoplasmic content of the host cell (Rosson and Rittenberg, 1979). At the beginning of the growth phase, it synthesizes abundant hydrolytic enzymes to break down macromolecules of the host cell (Chanyi, 2014). Cell division is explained by the accumulation of a division factor (a small cyclic peptide) produced by the predator that triggers separation after reaching a certain level in the filament (Eksztejn and Varon, 1977). The transition from intracellular growth phase to the free-living attack phase is achieved by releasing the bdelloplast (Chanyi, 2014).

Bdellocysts

Bdellovibrio sp. strain W forms large, electron-dense resting organs called bdellocyst which they were occurred in an infected host cell (Hoeniger et. al., 1972; Rotem et. al., 2014). The predatory cell expands into a kidney-shaped cell surrounded by an unstructured, amorphous outer layer and a fine-grained inner layer surrounds their plasma membrane (Tudor and Conti, 1977). Bdellocysts are more resistant to dryness, high temperatures and sonication than vegetative cells and their germination is promoted by L-glutamate, K^+ and NH_4^+ (Tudor and Conti, 1977; Tudor and Conti, 1978).

Host independence BALOs

In laboratory conditions, it has been reported that there are spontaneous derivatives that can grow in rich environment in the absence of live host cells (Stolp and Starr, 1963). They have an archetypal dimorphic life cycle, therefore, they are facultative predators (Cotter and Thomashow, 1992). Host cell-independent (HI) isolates produce a protective yellowish pigment against photo-oxidative damage (Friedberg, 1977), use a wide carbon source (Ishiguro, 1974), synthesize different LPS structures (Schwudke et. al., 2003) and form sticky biofilms (Medina and Kadouri, 2003). “Type I” mutants are cell extract dependent, are saprophytic and results from a single mutation; “Type II” mutants, on the other hand, do not need cell extract, are axenic and are caused by an additional mutation, that is, double mutants (Seidler and Starr, 1969). Cotter and Thomashow (1992) showed that the saprophytic mutants have mutations in their short open reading frame (ORF) within a small genetic region (Cotter and Thomashow, 1992).

Physiology of BALOs

Energy Metabolism: BALOs don't go into the stationary phase in the culture. They constantly use high amounts of energy for both high-speed swimming and growth and replication. Endogenous and substrate respiration rates causes the satiety of the functional capacity of either the tricarboxylic acid cycle or the electron transport chain (Hespell et. al., 1973). BALOs can't do fermentation and use sugar actually (Seidler and Starr, 1969), so they procure energy (ATP) from amino acids, certain organic acids (acetate and α -ketoglutarate) and polyhydroxyalkanoates (PHA) (Hespell et. al., 1973). In a research, the ATP cycle in *B. bacteriovorus* during endogenous respiration is five times higher than *E. coli*

(Gadkari and Stolp, 1976). In another study, it was stated that the *Bdellovibrio* sp. can use nucleoside monophosphates and ATP as well as host cell-derived phospholipids directly from the substrate cell or an exogenous source (Ruby and McCabe 1986). Throughout the intraperiplasmic stage, the DNase of the predator disrupts the DNA of the substrate cell and providing most of the nucleosides necessary for growth (Rosson and Rittenberg, 1979). The ability of BALOs to recycle the host material have made the predator bacteria energy efficient. *B. bacteriovorus* that in the growth and division phase has been shown to elicit a Y_{ATP} (biomass per ATP consumed) of 26 compared to 10.5 for bacteria that has been grown in rich media (Rittenberg and Hespell, 1975).

In a study, it was observed that within 20 hours, *B. bacteriovorus* caused a 95% loss in viability of the cell suspension. This is partly due to the energetic swim of BALOs, which uses 20-40% of the total energy. So, the high breathing rates end up rapid energy consumption and a short half-life that specific for BALOs (Hespell et. al., 1974).

BALOs survival are realized by using respirable substrates such as amino acids, some organic acids, PHAs and in studies have shown that *B. bacteriovorus* can depolymerize PHA made by the host cell and use it to produce ATP (Hespell et. al., 1973).

Lytic-Enzymatic Activities: The host cell morphology varies considerably according to the penetration of *Bdellovibrio* sp: the host cell transforms into a generally round bdelloplast. The penetration of non-covalently linked outer membrane components is expounded by the influence of mechanical forces, besides covalent bonds must be cut by enzymes for pore formation and passage of peptidoglycan (Fackrell and Robinson, 1973). In one study, peptidoglycan dissolved rapidly during penetration as a result of glycanase and peptidase activities. This phenomenon is evidenced by free diaminopimelic acid (DAP) and amino sugar released into the extracellular medium (Thomashow and Rittenberg, 1978c). In the intraperiplasmic growth, free DAP was added to the peptidoglycan of the bdelloplast with a soluble enzyme activity (Araki and Ruby, 1988). The glycanase is ineffective by peptidoglycan deacetylation, during the bdelloplast stage, peptidase activity continues at a low rate (Thomashow and Rittenberg, 1978b). Inhibition of bdelloplast superinfection by *Bdellovibrio* sp. is the result of peptidoglycan deacetylation (Thomashow and Rittenberg, 1978c). It is acylated with long chain fatty acids of the peptidoglycan of the host cell, which stabilizes the outer membrane of the bdelloplast (Thomashow and Rittenberg, 1978a). In addition, with a second lytic activity,

the newly synthesized enzymes disrupted the remaining peptidoglycan (Thomashow and Rittenberg, 1978c).

Transport: The secretion secreted by BALOs includes the type I and type II (sec) systems and the twin arginine target protein translocation (TAT) system (Rendulic et. al., 2004), but type III and type IV secretion systems are not available. Protein secretion into the cytoplasm of the host bacterium is carried out by the release into the periplasm of the host bacterium and retranslocation into the cytoplasm of the host bacterium (Barabote et. al., 2007). Another special mechanism in predatory bacteria is belongs to that *B. Bacteriovorus*, OMPs are embedded in the cytoplasmic membrane of the host bacterium and permeabilize it to hydrophilic molecules (Beck et. al., 2004).

BALOs genome code inventories of large transport systems, such as *Bdellovibrionaceae* and *Bacteriovoraceae* carry a large number of uptake systems; in contrast, *Micavibrio* sp. doesn't carry this system (Barabote et. al., 2007; Hobley et. al., 2012). BALOs have a small amount of sugar transporters, for instance *B. bacteriovorus* has sugar permeases that allow the removal of ribose, glycosides, maltose and malto-oligosaccharides (Hespell et. al., 1973). There is no phosphoenolpyruvate-dependent sugar transport phosphotransferase system (PTS) (Barabote et. al., 2007).

Habitat and ecology

BALOs are commonly found in marine, freshwater and terrestrial ecosystems. The habitats from which these predatory bacteria are isolated has been divided into two part. One of these is marine or saltwater ecosystems (Shilo, 1966), and the other one is soil and freshwater ecosystems (Varon and Shilo, 1968). In the freshwater/terrestrial ecosystem, the microorganisms have been reported to be isolated from water, soil, sewage, rhizosphere, water distribution systems and intestinal remains of animals and people (Richardson, 1990). In the saltwater ecosystem the microorganisms have been reported to be isolated from ocean, sea, salt lakes, estuary and gills of blue crabs (Kelley and Williams, 1992). Also, another habitat that these microorganisms have been found are surface biofilms (Williams et. al., 1995).

In ecosystems, the abundance and diversity of BALOs are undervalued. In population the abundances of different BALOs clades were found to be 2.5 times larger than the existential (Van Essche et. al., 2009; Zheng et. al., 2008). In evaluation of abundance of BALOs, based on 16S rRNA

gene sequence, it has been reported that the predators form 0.2% of total bacteria (Rotem et. al., 2014). According to research, culture independent studies revealed that the BALOs diversity is much larger than they are determined by isolation studies (Davidov and Jurkevitch 2004).

In experiments related to the sensitivity of predators to the various bacteria were found to be the most sensitive to host bacteria, such as *Vibrio* sp. in saline environments, *E. coli* in freshwater and in terrestrial environments, *Pectobacterium carotovorum* subsp. *carotovorum* in soil and rhizosphere environments, *E. coli* and *Achromobacter* sp. in sewage and river environments.

According to the calculations based on the Lotka-Volterra prey-predator model (Varon and Zeigler, 1978), it has been showed that it needed at least 3×10^6 host cells to give the predator 50 % chance for survival. This calculation shows that the *Bdellovibrio* sp. can only live in special ecological niches. However, low-level and steady-state predatory bacterial populations have survived in continuous cultures at low host cell density (10^4 cfu/mL) for a long time. It also has been reported that a high host cell density is required for the survival of *Bdellovibrio* sp. such as host cell concentrations requirement in the soil is at least 10^5 - 10^6 cfu/g or mL minimum (Uematsu, 1980).

Applications

The characteristic lifestyle of BALOs have made them attractive candidates for a range of applications (Jurkevitch, 2006). BALOs have showed predation into very large and non specific host cells. The lytic properties of these bacteria plays an important role in the conservation of homeostasis in the ecological system (Edao, 2000). They can attack many Gram negative bacteria and some gram positive bacteria. It was reported that *Bdellovibrio bacteriovorus* 109J strain was attacked to the host bacteria; such as *Escherichia* sp., *Pseudomons* sp., *Chromatium* sp., *Spirillum* sp., *Acinetobacter* sp., *Aeromonas* sp., *Bordetella* sp., *Burkholderia* sp., *Citrobacter* sp., *Enterobacter* sp., *Klebsiella* sp., *Listonella* sp., *Morganella* sp., *Proteus* sp., *Serratia* sp., *Salmonella* sp., *Shigella* sp., *Vibrio* sp. and *Yersinia* sp. (Sinha et. al. 2014). These predatory bacteria are called 'living antibiotics' because of their ability to use many human, animal and plant pathogens as host bacteria (Socketk and Lambert, 2004).

Pathogenic bacteria that resistant to antibiotics causes serious diseases in humans. The predatory bacteria are used to combat bacterial infe-

ctions resistant to antimicrobial agents (Dashiff et. al., 2011). It has been reported that the antibiotics that contains β -lactamase inhibitor have no effect on BALOs species and so these antibiotics could be used together (Sinha et. al. 2014).

Most of the bacterial chronic inflammatory infections in humans involves biofilm formation. Most of the bacterial chronic inflammatory and infectious diseases in humans that including uropathogenic *E. coli* in urinary tract infections, and enterohemorrhagic *E. coli* in gastrointestinal infections and *P. aeruginosa* respiratory infections. Kadouri et al. (2005) showed that *Bdellovibrio* sp. invaded and effectively destroyed these biofilms.

Periodontitis is a polymicrobial infection that originates from complex biofilm embedded dental plaque that containing large number of Gram-negative pathogens (Stewart and Costerton, 2001). *Bdellovibrio* strains have been shown to be used successfully in the elimination of large number of gram-negative pathogens such as *Pseudomonas aeruginosa* embedded in a well-preserved complex biofilm embedded in dental plaque (Kadouri and O'toole, 2005). Van Essche et al. showed that in 2009, *Bdellovibrio bacteriovorus* HD100 was able to attack *Aggregatibacter actinomycetemcomitans* (one of the main species which contribute to periodontitis). It has been reported that the number of various periodontal pathogens rapidly decreases when BALOs strains has been inoculated into the oral microbiota (Sinha et. al. 2014).

BALOs did not show any pathogenic properties in high organisms. Nakamura reported in 1972 that keratoconjunctivitis caused by *Shigella flexneri* was effectively treated with *Bdellovibrio* sp. However, in rabbits, BALOs that used against pathogens in the intestinal tract of rabbits was proven unsuccessful (Westergaard and Kramer, 1977). *B. bacteriovorus* 109J strain infected with *Moraxella bovis*, which is the cause of bovine keratoconjunctivitis, has been applied and has been reported to be a potential agent for the treatment of *Moraxella bovis* infections (Boileau et. al., 2011).

Various studies have been conducted to investigate the potential of BALOs against phytopathogens. BALOs effectively eliminated *Xanthomonas oryzae* from rice paddy field water and caused rapid decline of *Pectobacterium carotovorum* subsp. *carotovorum* populations from the soil [20] and the predator bacteria isolated from the rhizosphere of soybean were used to control bacterial blight caused by *Pseudomonas glycinea*

(Scherff, 1973). It is reported that *Bdellovibrio* sp. has proven effective against rhizobacteria that promote plant growth (Germida, 1987).

Studies have suggested that *Bdellovibrio* sp. plays a role in the self-purification of natural water systems (Fry and Staples, 1976). *Bdellovibrio* sp. has been used as an indicator for compounds in water, as they are very sensitive to certain chemicals and metals (Varon and Shilo, 1981). In ecology, the physiological activities of these bacteria at various concentrations of dangerous pollutants have been investigated and it has been shown that they are not eliminated in the presence of pollutants (Markelova, 2002).

The most important problem in membrane bioreactors used in wastewater facilities were that microorganisms that forms biofilms on filters. It has been found that BALOs are destroyed the biofilm layer formed on the upper surface of membrane filters in wastewater facilities (Kim et. al., 2013) and reduced the number of Gram negative bacteria (Lambina et. al., 1982). Özkan and Yılmaz (2018) reported that *Bdellovibrio bacteriovorus* was cleaned the biofilm layer which formed in active sludge bacteria by 39% and these predatory bacteria could prevent unwanted biofilm formation.

By developing basic genetic parts, genetic manipulation experiments were carried out in predatory bacteria for practical applications. To control gene expression, *Bdellovibrio bacteriovorus* has been identified with theophylline-activated riboswitches during predation. It was stated that they placed riboswitches in *Escherichia coli* and the engineered strain showed faster swallowing kinetics (Dwidar and Yokobayashi, 2007).

Conclusions

Bdellovibrio and like organisms (BALOs) were first discovered randomly from soil in 1962. These predatory bacteria were isolated from various habitats after their initial discovery, and found to be common in aquatic and terrestrial environments. These bacteria, which have a different life cycle compared to other predatory bacteria, have become more remarkable with the possibility of being used as potential antimicrobial agents in industry, agriculture and medicine over time. In 1992, the hit locus was discovered in these bacteria related to the transition from a host-independent life. Thus, the studies on genetics related to these predatory bacteria have been started. In later studies, BALOs phylogenetic research that based on the 16S rDNA sequence studies were performed

and many predator species were identified. After the genetic studies, these predatory bacteria have been used in many areas today as alternative therapeutic agents. It has been showed that these bacteria, which are successful in predation against other bacteria, can be used for more productive purposes in many different fields.

REFERENCES

- Afinogenova, A.V., Markelova, N.Y. and Lambina, V.A. (1986). Detection of Enzyme-Activities of Some Metabolic Pathways in *Micavibrio admirandus* and *Bdellovibrio bacteriovorus*. *Zentralblatt für Mikrobiologie*, 141(6):471-475.
- Araki, Y. and Ruby, E.G. (1988). A Soluble Enzyme Activity that Attaches Free Diaminopimelic Acid Bdelloplast Peptidoglycan. *Biochemistry*, 27(7):2624-2629.
- Baer, M.L., Ravel, J., Chun, J., Hill, R.T. and Williams, H.N. (2000). A Proposal for the Reclassification of *Bdellovibrio stolpii* and *Bdellovibrio starrii* into a New Genus, *Bacteriovorax stolpii* comb. nov. and *Bacteriovorax starrii* comb. nov., respectively. *International Journal of Systematic and Evolutionary*, 50:219-224.
- Baer, M.L., Ravel, J., Pineiro, S.A., Guether-Borg, D. and Williams, H.N. (2004). Reclassification of Salt-water *Bdellovibrio* sp. as *Bacteriovorax marinus* sp. nov. and *Bacteriovorax litoralis* sp. nov.. *International Journal of Systematic and Evolutionary Microbiology*, 54(4):1011-1016.
- Barabote, R.D., Rendulic, S., Schuster, S.C. and Saier, M.H.Jr. (2007). Comprehensive Analysis of Transport Proteins Encoded within the Genome of *Bdellovibrio bacteriovorus*. *Genomics*, 90(4):424-446.
- Beck, S., Schwudke, D., Strauch, E., Appel, B. and Linscheid, M. (2004). *Bdellovibrio bacteriovorus* strains Produce a Novel Major Outer Membrane Protein During Predacious Growth in the Perioplasm of Prey Bacteria. *Journal of Bacteriology*, 186(9):2766-2773.
- Beebe, J.M. (1941). Studies on the Myxobacteria. 2. The Role of Myxobacteria as Bacterial Parasites. *Iowa State College Journal of Science*, 15:319-337.
- Boileau, M.J., Clinkenbeard, K.D. and Iandolo, J.J. (2011). Assessment of *Bdellovibrio bacteriovorus* 109J Killing of *Moraxella bovis* in an in vitro Model of Infectious Bovine Keratoconjunctivitis. *Canadian Journal of Veterinary Research*, 75(4):285-291.
- Cao, H., He, S., Wang, H., Hou, S., Lu, L. and Yang, X. (2012). *Bdellovibrios*, Potential Biocontrol Bacteria Against Pathogenic *Aeromonas hydrophila*. *Veterinary Microbiology*, 154(3-4):413-418.
- Chanyi, R.M. (2014). Cell Biology of the Entry of *Bdellovibrio* and Like Organisms, Electronic Thesis and Dissertation Repository, Graduate Program in Microbiology and Immunology, The University of Western Ontario.
- Cotter, T.W. and Thomashow, M.F. (1992). Identification of a *Bdellovibrio bacteriovorus* Genetic Locus, Hit, Associated with the Host-Independent Phenotype. *Journal of Bacteriology*, 174(19):6018-6024.

- Dashiff, A., Junka, R.A., Libera, M. and Kadouri, D.E. (2011). Predation of Human Pathogens by the Predatory Bacteria *Micavibrio aeruginosavorus* and *Bdellovibrio bacteriovorus*. *Journal of Applied Microbiology*, 110(2):431-444.
- Davidov, Y. and Jurkevitch, E. (2004). Diversity and Evolution of *Bdellovibrio*-and-like organisms (BALO), Reclassification of *Bacteriovorax starrii* as *Peredibacter starrii* gen. nov., comb. nov., and Description of the *Bacteriovorax-Peredibacter* Clade as *Bacteriovoracaceae* fam. nov.. *International Journal of Systematic and Evolutionary Microbiology*, 54(5):1439-1452.
- Davidov, Y., Huchon, D., Koval, S.F. and Jurkevitch, E. (2006). A New α -Proteobacterial Clade of *Bdellovibrio*-like Predators: Implications for the Mitochondrial Endosymbiotic Theory. *Environmental Microbiology*, 8(12), 2179-2188.
- Davidov, Y., Friedjung, A. and Jurkevitch, E. (2006). High Diversity of *Bdellovibrio*-and-like organisms (BALO) in Soil Revealed by Culture-Dependent and Culture-independent Methods. *Environmental Microbiology*, 8:1667-1673.
- Dwidar, M. and Yokobayashi, Y. (2007). Controlling *Bdellovibrio bacteriovorus* Gene Expression and Predation Using Synthetic Riboswitches, *ACS Synthetic Biology*, 6(11):2035-2041.
- Dwidar, M., Monnappa, A.K. and Mitchell, R.J. (2012). The Dual Probiotic and Antibiotic Nature of *Bdellovibrio bacteriovorus*. *BMB Reports*, 45(2):71-78.
- Eckhard, S., Dominik, S. and Michael, L. (2007). Predatory Mechanisms of *Bdellovibrio* and Like Organisms. *Future Microbiol*, 2(1), 63-73.
- Edao, A. (2000). Research on the Occurrence and Importance of *Bdellovibrio bacteriovorus* in the Gastrointestinal Tract of Humans, Animals as well as in the Natural Environment, Dissertation. University of Leipzig, Germany.
- Eksztejn, M. and Varon, M. (1977). Elongation and Cell Division in *Bdellovibrio bacteriovorus*. *Archives of Microbiology*, 114, 175-181.
- Elsherif, M. and Grossmann, F. (1996). Role of Biotic Factors in the Control of Soil-Borne Fungi by Fluorescent *Pseudomonads*. *Microbiological Research*, 151:351-357.
- Evans, K.J., Lambert, C. and Sockett, R.E. (2007). Predation by *Bdellovibrio bacteriovorus* HD100 Requires Type IV pili. *Journal of Bacteriology*, 189:4850-4859.

- Fackrell, H.B. and Robinson, J. (1973). Purification and Characterization of a Lytic Peptidase Produced by *Bdellovibrio bacteriovorus* 6-5-S. *Canadian Journal of Microbiology*, 19(5):659-666.
- Friedberg, D. (1977). Effect of Light on *Bdellovibrio bacteriovorus*. *Journal of Bacteriology*, 131(2):399-404.
- Fry, J.C. and Staples, D.G. (1976). Distribution of *Bdellovibrio bacteriovorus* in Sewage Works, River Water, and Sediments. *Applied and Environmental Microbiology*, 31(4):469-474.
- Gadkari, D. and Stolp, H. (1976). Energy Metabolism of *Bdellovibrio bacteriovorus*, II. P/O Ratio and ATP Pool Turnover Rate. *Archives of Microbiology*, 108(1):125-132.
- Germida, J.J. (1987). Isolation of *Bdellovibrio* spp. that Prey on *Azospirillum brasilense* in Soil. *Canadian Journal of Microbiology*, 33(5):459-461.
- Hespell, R.B., Rosson, R.A., Thomashow, M.F. and Rittenberg, S.C. (1973). Respiration of *Bdellovibrio bacteriovorus* strain 109J and its Energy Substrates for Intraperiplasmic Growth. *Journal of Bacteriology*, 113(3):1280-1288.
- Hespell, R.B., Thomashow, M.F. and Rittenberg, S.C. (1974). Changes in Cell Composition and Viability of *Bdellovibrio bacteriovorus* During Starvation. *Archives of Microbiology*, 97(1):313-327.
- Hobley, L., Fung, R.K., Lambert, C., Harris, M.A., Dabhi, J.M., King, S.S., Basford, S.M., Uchida, K., Till, R., Ahmad, R., Aizawa, S., Gomelsky, M. and Sockett, R.E. (2012). Discrete Cyclic di-GMP-dependent Control of Bacterial Predation Versus Axenic Growth in *Bdellovibrio bacteriovorus*. *PLoS Pathogens*, 8(2):e1002493.
- Hoener, J., Ladwig, R. and Moor, H. (1972). The Fine Structure of Resting Bodies of *Bdellovibrio* sp. strain W Developed in *Rhodospirillum rubrum*. *Canadian Journal of Microbiology*, 18: 87- 92.
- Ishiguro, E.E. (1974). Minimum Nutritional Requirements for Growth of Host Independent Derivatives of *Bdellovibrio bacteriovorus* strain 109 Davis. *Canadian Journal of Microbiology*, 20(2):263-264.
- Javaherdashti, R. and Alasvand, K. (2019). Biological Treatment of Microbial Corrosion. 101-144 s. doi: 10.1016/B978-0-12-816108-1.00005-7.
- Jurkevitch, E. (2006). A Brief History of Short Bacteria: A Chronicle of *Bdellovibrio* (and Like Organisms) Research. *Microbiology Monographs* (4), Jurkevitch, E. Predatory Prokaryotes. Berlin Heidelberg, 1-9 s.
- Jurkevitch, E. (2006). The genus *Bdellovibrio*, In *The Prokaryotes: a Handbook on the Biology of Bacteria*, Ed: Dworkin, M., Falkow, S., Rosenberg, E., Schleifer, K. H., Stackebrandt, E. New York: Springer. 3(7):12-30.

- Jurkevitch, E. and Davidov, Y. (2006). Phylogenetic Diversity and Evolution of Predatory Prokaryotes. *Microbiology Monographs* (4), Jurkevitch, E. Predatory Prokaryotes, Berlin Heidelberg, 11-56 s.
- Jurkevitch, E. (2007). Predatory Behaviors in Bacteria-Diversity and Transitions. *Microbe Magazine*, 2 (2): 67-73.
- Kadouri, D. and O'toole, G.A. (2005). Susceptibility of Biofilms to *Bdellovibrio bacteriovorus* Attack. *Applied and Environmental Microbiology*, 71(7):4044-4051.
- Kelley, J.I. and Williams, H.N. (1992). *Bdellovibrios* in *Callinectes sapidus*, the Blue Crab. *Applied and Environmental Microbiology*, 58(4):1408-1410.
- Kim, E.H., Dwidar, M., Mitchell, R.J. and Kwon, Y.N. (2013). Assessing the Effects of Bacterial Predation on Membrane Biofouling. *Water Research*, 47(16):6024-6032.
- Krieg, N.R. and Holt, J.G. (1984). *Bergey's Manual of Systematic Bacteriology*. Williams&Wilkins, Baltimore, 1:118-124.
- Koval, S.F., Hynes, S.H., Flannagan, R.S., Pasternak, Z., Davidov, Y. and Jurkevitch, E. (2013). *Bdellovibrio exovorax* sp. nov., a Novel Predator of *Caulobacter crescentus*. *International Journal of Systematic and Evolutionary Microbiology*, 63(1): 146-151.
- Koval, S.F., Williams, H.N. and Stine, O.C. (2015). Reclassification of *Bacteriovorax marinus* as *Halobacteriovorax marinus* gen. nov., comb. nov. and *Bacteriovorax litoralis* as *Halobacteriovorax litoralis* comb. nov.; Description of *Halobacteriovoraceae* fam. nov. in the class *Deltaproteobacteria*. *International Journal of Systematic and Evolutionary Microbiology*, 65(2):593-597.
- Lambina, V.A., Afinogenova, A.V., Romai, P. S., Konovalona, S.M. and Pushkareva, A.P. (1982). *Micavibrio admirandus* gen. et sp. nov.. *Mikrobiologiya*, 51(1):114-117.
- Lambina, V.A., Afinogenova, A.V., Romay, P.S., Konovalona, S.M. and Andreev, L.V. (1983). New Species of Exoparasitic Bacteria from the genus *Micavibrio* Infecting Gram-positive Bacteria. *Mikrobiologiya*, 52(5):777-780.
- Madigan, M.T. and Martinko, J.M. (2010). Brock Mikroorganizmaların Biyolojisi. Ed: Çökmüş, C. *Palme Yayınevi*, Ankara, 992 s.
- Markelova, N.Y. (2002). Effect of Toxic Pollutants on *Bdellovibrio*. *Process Biochemistry*, 37(10):1177-1181.
- Medina, A.A. and Kadouri, D.E. (2003). Biofilm Formation of *Bdellovibrio bacteriovorus* Host-independent Derivatives. *Research in Microbiology*, 160(3):224-231.

- Miyamoto, S. and Kuroda, K. (1975). Lethal Effect of Fresh Sea Water on *Vibrio parahaemolyticus* and Isolation of *Bdellovibrio* Parasitic Against the Organism. *Japanase Journal of Microbiology*, 19(4):309-317.
- Nakamura, M. (1972). Alteration of *Shigella* Pathogenicity by Other Bacteria. *The American Journal of Clinical Nutrition*, 25(12):1441-1451.
- Özkan, M. and Yılmaz, H. (2018). Avcı Bakteri *Bdellovibrio bacteriovorus* Hücre Özütünün Biyofilm Oluşumunu Engelleme Etkisi, *Türk Mikrobiyoloji Cemiyeti Dergisi*, 48(1):29-37.
- Pan, C.L., Hsu, Y.L., Tsai, G.J., Kuo, H.J., Chang, C.M., Wang, F.J. and Wu, C.S. (1997). Isolation and Identification of *Bdellovibrio* from Coastal Areas of Taiwan. *Fisheries Science*, 63(1):52-59.
- Pineiro, S., Stine, C.O., Chauhan, A., Steyert, S.R., Smith, R. and Williams, H.N. (2007). Global Survey of Diversity Among Environmental Saltwater *Bacteriovoraceae*. *Environmental Microbiology*, 9(10):2441-2450.
- Pineiro, S.A., Williams, H.N. and Stine, O.C. (2008). Phylogenetic Relationships Amongst the Saltwater Members of the Genus *Bacteriovorax* Using rpoB Sequences and Reclassification of *Bacteriovorax stolpii* as *Bacteriolyticum stolpii* gen. nov., comb. nov.. *International Journal of Systematic and Evolutionary Microbiology*, 58(5):1203-1209.
- Rendulic, S., Jagtap, P., Rosinus, A., Eppinger, M., Baar, C., Lanz, C., Keller, H., Lambert, C., Evans, K.J., Goesmann, A., Meyer, F., Sockett, E.R. and Schuster, S. (2004). A Predator Unmasked: Life Cycle of *Bdellovibrio bacteriovorus* from a Genomic Perspective. *Science*, 303(5658):689-692.
- Richardson, I.R. (1990). The Incidence of *Bdellovibrio* spp., in Man-made Water Systems: Coexistence with *Legionellas*. *The Journal of Applied Bacteriology*, 69(1):134-140.
- Rittenberg, S.C. and Hespell, R.B. (1975). Energy Efficiency of Intraperiplasmic Growth of *Bdellovibrio bacteriovorus*. *Journal of Bacteriology*, 121(3):1158-1165.
- Rittenberg, S.C. (1983). *Bdellovibrio*: Attack, Penetration and Growth on its Prey. *American Society for Microbiology*, 49:435-440.
- Rosson, R.A. and Rittenberg, S.C. (1979). Regulated Breakdown of *Escherichia coli* Deoxyribonucleic Acid During Intraperiplasmic Growth of *Bdellovibrio bacteriovorus* 109J. *Journal of Bacteriology*, 140(2):620-633.
- Rotem, O., Pasternak, Z. and Jurkevitch, E. (2014). The Genus *Bdellovibrio* and Like Organisms. *The Prokaryotes-Deltaproteobacteria and Epsilonproteobacteria*, 3-17 s.

- Ruby, E.G. and McCabe, J.B. (1986). An ATP Transport System in the Intracellular Bacterium, *Bdellovibrio bacteriovorus* 109J. *Journal of Bacteriology*, 167(3):1066-1070.
- Scherff, R.H. (1973). Control of Bacterial Blight of Soybean by *Bdellovibrio bacteriovorus*. *Phytopathology*, 63(3):400-402.
- Schoeffield, A.J., Falkler, Jr., W.A., Desai, D. and Williams, H.N. (1991). Serogrouping of Halophilic *Bdellovibrios* from Chesapeake Bay and Environs by Immunodiffusion and Immunoelectrophoresis. *Applied and Environmental Microbiology*, 57(12):3470-3475.
- Schwudke, D., Linscheid, M., Strauch, E., Appel, B., Zahringer, U., Moll, H., Müller, M., Brecker, L., Gronow, S. and Lindner, B. (2003). The Obligate Predatory *Bdellovibrio bacteriovorus* Possesses a Neutral Lipid A Containing Alpha-D-Mannoses that Replace Phosphate Residues: Similarities and Differences Between the Lipid As and the Lipopolysaccharides of the Wild Type Strain *B. bacteriovorus* HD100 and its Host-Independent Derivative HI100. *The Journal of Biological Chemistry*, 278(30):27502-27512.
- Seidler, R.J. and Starr, M.P. (1969). Factors Affecting the Intracellular Parasitic Growth of *Bdellovibrio bacteriovorus* Developing within *Escherichia coli*. *Journal of Bacteriology*, 97(2):912-923.
- Seidler, R. and Starr, M.P. (1969). Isolation and Characterization of Host-independent *Bdellovibrios*. *Journal of Bacteriology*, 100(2):769-785.
- Siedler, R.J., Mendel, M. and Baptist, J.N. (1972). Molecular Heterogeneity of the *Bdellovibrios*: Evidence for Two New Species. *Journal of Applied Bacteriology*, 109(1):209-217.
- Sinha, A., Hurakadli, M., Ravindra, S. and Agarwal, A. (2014). *Bdellovibrio* Like Organisms: The Predatory Assassin. *IOSR Journal of Dental and Medical Sciences*, 13(10), 32-36.
- Shilo, M. (1966). Predatory bacteria. *Science Journal*, 2:33-37.
- Sockett, R.E. and Lambert, C. (2004). *Bdellovibrio* as Therapeutic Agents: a Predatory Renaissance? *Nature Reviews Microbiology*, 2(8):669-675.
- Stanley, S.M. (1973). An Ecological Theory for the Sudden Origin of Multicellular Life in the Late Precambrian. *Proceedings of the National Academy of Sciences*, 70(5):1486-1489.
- Staples, D.G. and Fry, J.C. (1973). Factors which Influence the Enumeration of *Bdellovibrio bacteriovorus* in Sewage and River Water. *Journal of Applied Bacteriology*, 36(1):1-11.

- Stolp, H. and Starr, M.P. (1963). *Bdellovibrio bacteriovorus* gen. et.sp.n., a Predatory, Ectoparasitic, and Bacteriolytic Microorganism. *Antonie van Leeuwenhoek*, 29(1):217-248.
- Summers, J.K. and Kreft, J.U. (2019). Predation Strategies of the Bacterium *Bdellovibrio bacteriovorus* Result in Bottlenecks. Overexploitation, Minimal and Optimal Prey Sizes, *BioRxiv*, DOI: 10.1101/621490.
- Stewart, P.S. and Costerton, J.W. (2001). Antibiotic Resistance of Bacteria in Biofilms. *Lancet*, 358(9276):135-138.
- Straley, S.C., Lamarre, A.G., Lawrence, L.J. and Conti, S.F. (1979). Chemotaxis of *Bdellovibrio bacteriovorus* Toward Pure Compounds. *Journal of Bacteriology*, 140(2):634-642.
- Stolp, H. and Starr, M.P. (1963). *Bdellovibrio bacteriovorus* gen. et.sp.n., a predatory, ectoparasitic, and bacteriolytic microorganism. *Antonie van Leeuwenhoek*, 29(1):217-248.
- Thomashow, M.F. and Rittenberg, S.C. (1978a). Intraperiplasmic Growth of *Bdellovibrio bacteriovorus* 109J: Attachment of Long-Chain Fatty Acids to *Escherichia coli* peptidoglycan. *Journal of Bacteriology*, 135(3):1015-1023.
- Thomashow, M.F. and Rittenberg, S.C. (1978b). Intraperiplasmic Growth of *Bdellovibrio bacteriovorus* 109J: N-deacetylation of *Escherichia coli* Peptidoglycan Amino Sugars. *Journal of Bacteriology*, 135(3):1008-1014.
- Thomashow, M.F. and Rittenberg, S.C. (1978c). Intraperiplasmic Growth of *Bdellovibrio bacteriovorus* 109J: Solubilization of *Escherichia coli* Peptidoglycan. *Journal of Bacteriology*, 135:998-1007.
- Thomashow, L.S. and Rittenberg, S. (1985). Waveform Analysis and Structure of Flagella and Basal Complexes from *Bdellovibrio bacteriovorus* 109J. *Journal of Bacteriology*, 163(3):1038-1046.
- Tudor, J.J. and Conti, S.F. (1977). Characterization of Bdello cysts of *Bdellovibrio* sp. *Journal of Bacteriology*, 131(1):314-322.
- Tudor, J. and Conti, S.F. (1978). Characterization of Germination and Activation of *Bdellovibrio* Bdello cysts. *Journal of Bacteriology*, 133:130-138.
- Tudor, J.J., Mccann, M. and Acrich, I.A. (1990). A New Model for the Penetration of Prey Cells by *Bdellovibrios*. *Journal of Bacteriology*, 172(5):2421-2426.
- Uematsu, T. (1980). Ecology of *Bdellovibrio* Parasitic to Rice Bacterial Leaf Blight Pathogen *Xanthomonas oryzae*. *Review of Plant Protection Research*, 13:12-26.

- Van Essche, M., Sliepen, I., Loozen, G., Van Eldere, J., Quiryne, M., Davidov, Y., Jurkevitch, E., Boon, N. and Teughels, W. (2009). Development and Performance of a Quantitative PCR for the Enumeration of *Bdellovibrionaceae*. *Environmental Microbiology Reports*, 1(4):228-233.
- Varon, M. and Shilo, M. (1968). Interaction of *Bdellovibrio bacteriovorus* and Host Bacteria I. Kinetic Studies of Attachment and Invasion of *Escherichia coli* B by *Bdellovibrio bacteriovorus*. *Journal of Bacteriology*, 95(3):744-753.
- Varon, M. and Zeigler, B. (1978). Bacterial Predator-prey Interaction at Low Prey Density. *Applied and Environmental Microbiology*, 36(1):11-17.
- Varon, M. and Shilo, M. (1981). Inhibition of the Predatory Activity of *Bdellovibrio* by Various Environmental Pollutants. *Microbial Ecology*, 7(2):107-111.
- Westergaard, J.M. and Kramer, T.T. (1977). *Bdellovibrio* and the Intestinal Flora of Vertebrates. *Applied and Environmental Microbiology*, 34(5):506-511.
- Williams, H., Falkler, W. and Shay, D. (1982). Seasonal Distribution of *Bdellovibrions* at the Mouth of the Patuxent River in the Chesapeake Bay. *Canadian Journal of Microbiology*, 28(1):111-116.
- Williams, H.N., Schoeffied, H.N., Guether, D., Kelley, J., Shah, D. and Falkler, W.A. (1995). Recovery of *Bdellovibrions* from Submerged Surfaces and Other Aquatic Habitats. *Microbial Ecology*, 29(1):39-48.
- Zheng, G., Wang, C., Williams, H.N. and Pineiro, S.A. (2008). Development and Evaluation of a Quantitative Real-time PCR Assay for the Detection of Saltwater *Bacteriovorax*. *Environmental Microbiology*, 10:2515-2526.

“

Chapter 10

PLANE SYMMETRIC SCALAR FIELD IN LYRA THEORY

Doğukan TAŞER¹

Sertaç Serkan DOĞRU²

”

1 Assoc. Prof. Dr. Çanakkale Onsekiz Mart University, Çan Vocational School, Department of Electricity and Energy, Çanakkale, TURKEY dogukantaser@comu.edu.tr

2 Assist. Prof. Dr. Çanakkale Onsekiz Mart University, Çan Faculty of Applied Sciences, Department of Occupational Health and Safety. Çanakkale, TURKEY dogru@comu.edu.tr

INTRODUCTION

It can be said that foundations of gravitational theories begin with Newton's theory. Although Newton's theory was successful in studying motions of earth and determining orbits of planets and other celestial bodies, it failed to explain many issues. General Relativity, on the other hand, was the first theory that succeeded in explaining gravitational field geometrically (Einstein, 1916). In General Relativity, Lagrangian density of geometric part is theoretically defined by curvature scalar. However, progression of planet's perihelion is most valid theory of gravity, which provides tests such as gravitational deflection and redshift of light. Later, first geometric unified theory was proposed by Weyl (1918) to unify both gravity and electrodynamics. This theory has not received much attention due to failure of length conversions.

A modification of Riemannian geometry was proposed by Lyra (1951) by adding a gauge function to structureless manifold. In this theory, unlike Weyl theory, non-integrability of length transformation of a vector under parallel transformations is also eliminated. Sen (1957) and Sen and Dunn (1971) proposed a new scalar-tensor gravitational theory in this geometry and created an analogy of Einstein's field equations based on Lyra's geometry.

It is widely accepted that there were several phase transitions during evolution of very early phases of universe. During these phase transitions that occur in early universe, symmetry of universe is spontaneously broken. It is thought that matter forms called topological defects are formed as a result of symmetry deformations. These structures that emerge during symmetry deformation are called monopole, string, domain walls and texture (Vilenkin, 1953). Topological defects play an important role in transition of the initial energy of universe to first matter forms and cosmic forms we think exist in the universe today. It is also possible to express both the transitional stages and the common areas of the items as scalar fields. Shchigolev (2014) investigated exact solutions in Lyra geometry by considering scalar fields. Maurya and Zia (2019) investigated field equation solutions by considering Brans-Dicke type scalar fields within the scope of Lyra Geometry. Shchigolev (2015) examined tachyon fields and phantom energy in Lyra geometry with the superpotential method, taking into account scalar field. Rahaman et al. (2003) obtained and developed Lyra geometry field equations for topological defect and scalar field in Bianchi cosmologies. Doğru and Demirtaş (2018) discussed Lyra geometry black holes. Mahanta and Biswal (2012) examined LRS Bianc-

hi type-I space-time within the scope of Lyra geometry for the case where deceleration parameter is constant for both string and domain walls with quark matter attached. He obtained that created model is early universe model and that matter is invisible in the presence of quark matter. Patil et al. (2012) studied matter in the presence of electromagnetic field with viscous fluid domain walls for plane symmetric space-time in geometry. They found that the model created for fixed gauge function starts and expands with Big Bang. In addition, as a form of cosmic matter, the scalar field is frequently taken into account in many gravitational theories to reveal the relations of matter, geometry and field (Taşer and Ulu Dođru, 2020; Taşer et al., 2022; Aydın and Ulu Dođru, 2021; Türkođlu and Ulu Dođru, 2015).

Today's universe is homogeneous and isotropic on a large scale and is defined by Freidmann-Robertson-Walker metric. However, there is no evidence to support that universe was homogeneous and isotropic in its initial stages. From a cosmological point of view, it is quite common to use inhomogeneous or anisotropic models in initial phases of universe. One of these models is the non-static plane symmetric space-time. Non-static plane symmetric space-time is a homogeneous and anisotropic model. In this context, the aim of our study is to examine the matter distribution of scalar field, which were formed in the early period, in non-static plane symmetric space-time within the scope of Lyra geometry.

In the second part of this study, scalar gravity theory field equations based on Lyra geometry are given. Then, field equations of non-static plane symmetric space-time in the presence of scalar field are obtained. The solutions of field equations are obtained by considering relationship between metric potentials of plane symmetric space-time. Finally, obtained solutions are discussed both physically and geometrically.

This study includes investigation of scalar fields within the scope of Lyra Geometry, which is basis in one of the alternative gravity theories. We inform about an alternative gravitation theory based on Lyra Geometry in Section 2. The definition of scalar fields and plane symmetric space-time are revised. In Section 4, plane symmetric scalar field are given within the scope of Lyra geometry.

GRAVITATION DEPENT ON LYRA GEOMETRY

In recent years, there has been a significant development in alternative theories of gravity. Among these theories, the most important scalar tensor theories are Brans-Dicke (Brans and Dicke, 1961) theory and Lyra (Lyra, 1951) geometry-based scalar theory (Rahaman et al., 2006) can be counted as. A theory similar to Weyl geometry was put forward by Lyra in 1951. The deficiency in Weyl theory is that in Lyra theory, the cosmological constant is spontaneously derived from geometry. It emerges as an incoming quantity and lengths resolved by conservation under transformations, similar to Riemannian geometry,. Also, scalar curvature in Lyra theory concept was introduced (Pradhan and Chauhan, 2009). In General Relativity, Einstein, metric tensor to gravitational potentials while relating gravity and geometry connected defined. That's why he was successful. By making the fields have geometric meaning, Einstein's gravitation-geometry relationship achieved success (Rahaman et al., 2006).

In Lyra geometry, action is depending on n-dimensional space-time manifold M, gauge (gauge) function $\Phi\Phi$ and metric potentials $g_{ik}g_{ik}$ can be expressed. Coupling coefficients in this geometry are defined by

$$\Gamma_{ik}^l = \frac{1}{\phi} \{^l_{ik}\} + \frac{s+1}{\phi^2} g^{lm} (g_{km} \partial_i \phi - g_{ik} \partial_m \phi) \quad (1)$$

Here, $\{^l_{ik}\}$ is type II Christoffel symbols and s is an arbitrary constant. Non-zero torsion tensor of this theory is defined as follows.

$$T_{ik}^l = \frac{s}{\phi^2} (\delta_k^l \nabla_i \phi - \delta_i^l \nabla_k \phi) \quad (2)$$

where δ_{ik} is Kronecker-Delta function (Faraoni, 2004). Lyra geometry curvature tensor, depending on coupling coefficients and gauge function is

$$K_{ikl}^m = \frac{1}{\phi^2} [\partial_k (\phi \Gamma_{il}^m) - \partial_i (\phi \Gamma_{kl}^m) + \Gamma_{il}^n \Gamma_{kn}^m - \Gamma_{kl}^n \Gamma_{ni}^m] \quad (3)$$

Similar to Riemann geometry, one can obtained from contraction of the curvature tensor over two indices in Lyra geometry such as

and from contraction of metric tensor such as. The curvature tensor is depending on curvature scalar of Riemann geometry as follows:

$$K = \frac{R}{\phi^2} + \frac{2(s+1)}{\phi^3} (1-n) \square \phi + \frac{1}{\phi^4} [(s+1)^2(3n-n^2-2) - 2(s+1)(2-n)] \nabla^m \phi \nabla_m \phi \quad (4)$$

where \square signs d'Alambertian operator (Faraoni, 2004). The action function of the alternative gravity theory based on Lyra Geometry is defined as follows:

$$S = \int d^4x \sqrt{-g} (\phi^2 R - 4\omega g^{ik} \nabla_i \phi \nabla_k \phi) \quad (5)$$

where. By making use of variation of action function, the field equations in Lyra Geometry are given by

$$R_{ij} - \frac{1}{2} g_{ij} R + \frac{3}{2} \phi_i \phi_j - \frac{3}{4} g_{ij} \phi_k \phi^k = -\chi T_{ij} \quad (6)$$

where is called as displacement vector. The components of displacement vector are scalar functions that depend on the coordinates.

SCALAR FIELD AND PLANE SYMMETRIC SPACE-TIME

As it is known, one of the ways to understand gravitational interactions, relations between matter and geometry and also universe model is to benefit from equations of motion of chosen theory of gravity. The equations of motion, which clearly reveal contributions of matter-energy-field and geometry since General Relativity, are defined as field equations of related theory of gravity. For the general form of the field equations, components of field equations are determined by considering cosmic matter-energy-field to be considered with geometry that can confuse with its dynamic properties or represent any phase in universe. A geometry representing beginning or last periods of universe can be preferred, as well as spherical, cylindrical, plane or different symmetries suitable for the matter structure. In this context, plane symmetry can be chosen as a space-time geometry, both because it presents a time-dependent model evolution and because it is suitable for structure of scalar field and perfect fluid forms. Line element for non-static plane symmetric space-time is given by

$$ds^2 = -e^{2A} (dt^2 - dr^2 - r^2 d\theta^2 - S^2 dz^2) ds^2 = -e^{2A} (dt^2 - dr^2 - r^2 d\theta^2 - S^2 dz^2) \quad (7)$$

here A and S are the functions changed by radial coordinate. According to Big Bang theory, universe which has an inhomogeneous structure, had many phase transitions during rapid cooling and energy scattering. Phase transitions caused disruptions in original perfect symmetry of the universe. These symmetry breakings have led to the emergence of topological defects that form basis of matter. In this whole process, transformation, formation and diffusion of the energy and material forms that fill the universe cause universe to expand with different characteristics. The expansion during inflation period is associated with time-dependent scalar field in many gravitational studies. At the same time, scalar field is taken into account for tachyon contribution in last period expansion of the universe and therefore quintessence effect. In the literature, scalar field and perfect fluid conveniently draw attention. In detail, perfect fluid, which is a small-scale form of matter formed by particles that satisfy fluid laws, is more different with scalar field considered as average of small parts, fundamentally and completely. However, on a macroscopic scale, there is a duality described below between these two matter forms. It is widely known that perfect fluid energy-momentum tensor is given by

$$T_{ij} = (\rho + p)u_i u_j - p g_{ij}; T_{ij} = (\rho + p)u_i u_j - p g_{ij} \tag{8}$$

The fluid has energy density ($\rho\rho$) and equivalent radial and tangential pressure (pp). Scalar field and scalar potential are related with dynamical components of the perfect fluid as follows:

$$p = \frac{1}{2} \varepsilon \left(\frac{d\varphi}{dt} \right) - V(\varphi); p = \frac{1}{2} \varepsilon \left(\frac{d\varphi}{dt} \right) - V(\varphi) \tag{9}$$

$$\rho = \frac{1}{2} \varepsilon \left(\frac{d\varphi}{dt} \right) + V(\varphi); \rho = \frac{1}{2} \varepsilon \left(\frac{d\varphi}{dt} \right) + V(\varphi) \tag{10}$$

here $V(\varphi)$ signs potential energy. In this study, plane symmetric distributions are investigated by making use of the equivalence of two matter forms.

PLANE SYMMETRIC SCALAR FIELD IN LYRA GEOMETRY

From Eqs.(6)-(8), equation of motion for perfect fluid in non-static plane symmetric space time are obtained as

$$-\frac{A'^2}{e^{2A}} - \frac{3\beta^2}{4e^{2A}} - \frac{2S'A'}{Se^{2A}} - \frac{2A''}{e^{2A}} - \frac{S''}{Se^{2A}} = p; -\frac{A'^2}{e^{2A}} - \frac{3\beta^2}{4e^{2A}} - \frac{2S'A'}{Se^{2A}} - \frac{2A''}{e^{2A}} - \frac{S''}{Se^{2A}} = p \tag{11}$$

$$-\frac{A'^2}{e^{2A}} - \frac{3\beta^2}{4e^{2A}} - \frac{2A''}{e^{2A}} = p; -\frac{A'^2}{e^{2A}} - \frac{3\beta^2}{4e^{2A}} - \frac{2A''}{e^{2A}} = p \tag{12}$$

$$-\frac{3A'^2}{e^{2A}} + \frac{3\beta^2}{4e^{2A}} - \frac{2S'A'}{Se^{2A}} = \rho - \frac{3A'^2}{e^{2A}} + \frac{3\beta^2}{4e^{2A}} - \frac{2S'A'}{Se^{2A}} = \rho \quad (13)$$

here prime represents derivative of time coordinate. Also, $\beta\beta$ is component of displacement vector such as $\phi_l = (0, 0, 0, \beta(t))$ $\phi_l = (0, 0, 0, \beta(t))$. In field equations given by Eqs. (11)-(13), the conservation equation for left side is obtained as follows.

$$-3A'^2\beta^2 - \frac{3}{2}\beta\beta' - \frac{3\beta^2 S'}{2S} = 0 - 3A'^2\beta^2 - \frac{3}{2}\beta\beta' - \frac{3\beta^2 S'}{2S} = 0 \quad (14)$$

From Eqs.(9)-(10) and field equations given by Eqs.(11)-(13), we get field equations for plane symmetric scalar field in Lyra geometry as follows:

$$\begin{aligned} -\frac{A'^2}{e^{2A}} - \frac{3\beta^2}{4e^{2A}} - \frac{2S'A'}{Se^{2A}} - \frac{2A''}{e^{2A}} - \frac{S''}{Se^{2A}} &= \frac{1}{2}\epsilon\left(\frac{d\varphi}{dt}\right) - V(\varphi) \\ -\frac{A'^2}{e^{2A}} - \frac{3\beta^2}{4e^{2A}} - \frac{2S'A'}{Se^{2A}} - \frac{2A''}{e^{2A}} - \frac{S''}{Se^{2A}} &= \frac{1}{2}\epsilon\left(\frac{d\varphi}{dt}\right) - V(\varphi) \end{aligned} \quad (15)$$

$$\begin{aligned} -\frac{A'^2}{e^{2A}} - \frac{3\beta^2}{4e^{2A}} - \frac{2A''}{e^{2A}} &= \frac{1}{2}\epsilon\left(\frac{d\varphi}{dt}\right) - V(\varphi) \\ -\frac{A'^2}{e^{2A}} - \frac{3\beta^2}{4e^{2A}} - \frac{2A''}{e^{2A}} &= \frac{1}{2}\epsilon\left(\frac{d\varphi}{dt}\right) - V(\varphi) \end{aligned} \quad (16)$$

$$\begin{aligned} -\frac{3A'^2}{e^{2A}} + \frac{3\beta^2}{4e^{2A}} - \frac{2S'A'}{Se^{2A}} &= \frac{1}{2}\epsilon\left(\frac{d\varphi}{dt}\right) + V(\varphi) \\ -\frac{3A'^2}{e^{2A}} + \frac{3\beta^2}{4e^{2A}} - \frac{2S'A'}{Se^{2A}} &= \frac{1}{2}\epsilon\left(\frac{d\varphi}{dt}\right) + V(\varphi) \end{aligned} \quad (17)$$

Collins et al. (1980) noticed in their study that there is a relationship between Hubble parameter and shear parameter in homogeneous and isotropic universe. When this relationship is considered for non-static plane symmetric space-time, metric potentials are given by

$$A(t) = c_2 \ln(S(t)) \quad A(t) = c_2 \ln(S(t)) \quad (18)$$

here $c_2 c_2$ is an arbitrary constant. When the relationship between metric potentials is considered together with Eqs.(14)-(17), the following equations are obtained

$$\frac{c_2^2 S'^2}{S^{2c_2+2}} + \frac{3}{4} \frac{\beta^2}{S^{2c_2}} + \frac{S''(2c_2+1)}{S^{2c_2+2}} = -\frac{1}{2} \varepsilon \varphi' + V(\varphi)$$

$$\frac{c_2^2 S'^2}{S^{2c_2+2}} + \frac{3}{4} \frac{\beta^2}{S^{2c_2}} + \frac{S''(2c_2+1)}{S^{2c_2+2}} = -\frac{1}{2} \varepsilon \varphi' + V(\varphi) \tag{19}$$

$$\frac{c_2^2 S'^2}{S^{2c_2+2}} + \frac{3}{4} \frac{\beta^2}{S^{2c_2}} + \frac{2c_2 S''}{S^{2c_2+1}} - \frac{2c_2 S'^2}{S^{2c_2+2}} = -\frac{1}{2} \varepsilon \varphi' + V(\varphi)$$

$$\frac{c_2^2 S'^2}{S^{2c_2+2}} + \frac{3}{4} \frac{\beta^2}{S^{2c_2}} + \frac{2c_2 S''}{S^{2c_2+1}} - \frac{2c_2 S'^2}{S^{2c_2+2}} = -\frac{1}{2} \varepsilon \varphi' + V(\varphi) \tag{20}$$

$$\frac{3c_2^2 S'^2}{S^{2c_2+2}} - \frac{3}{4} \frac{\beta^2}{S^{2c_2}} + \frac{2c_2 S'^2}{S^{2c_2+2}} = \frac{1}{2} \varepsilon \varphi' + V(\varphi)$$

$$\frac{3c_2^2 S'^2}{S^{2c_2+2}} - \frac{3}{4} \frac{\beta^2}{S^{2c_2}} + \frac{2c_2 S'^2}{S^{2c_2+2}} = \frac{1}{2} \varepsilon \varphi' + V(\varphi) \tag{21}$$

$$c_2 \frac{\beta^2 S'}{S} + \frac{1}{2} \beta \beta' + \frac{1}{2} \frac{\beta^2 S'}{S} = 0 c_2 \frac{\beta^2 S'}{S} + \frac{1}{2} \beta \beta' + \frac{1}{2} \frac{\beta^2 S'}{S} = 0 \tag{22}$$

Eqs.(19)-(21) form a system of 2nd order non-linear ordinary differential equations. Scalar field, displacement vector component and metric potential as solution of the equation system are obtained as follows;

$$\varphi(t) = \frac{-(2c_2+1)(c_3 t + c_4)^{1-\frac{2(3c_2+1)}{2c_2+1}}}{c_3(4c_2+1)} + c_1$$

$$\varphi(t) = \frac{-(2c_2+1)(c_3 t + c_4)^{1-\frac{2(3c_2+1)}{2c_2+1}}}{c_3(4c_2+1)} + c_1 \tag{23}$$

$$S(t) = (2c_2 + 1)^{\frac{1}{2c_2+1}} (c_3 t + c_4)^{\frac{1}{2c_2+1}}$$

$$S(t) = (2c_2 + 1)^{\frac{1}{2c_2+1}} (c_3 t + c_4)^{\frac{1}{2c_2+1}} \tag{24}$$

$$\beta(t) = \frac{c_5 c_3^{\frac{2c_2+1}{2c_2}}}{(2c_2+1)(c_3 t + c_4)} \beta(t) = \frac{c_5 c_3^{\frac{2c_2+1}{2c_2}}}{(2c_2+1)(c_3 t + c_4)} \tag{25}$$

here $c_n c_n$ is arbitrary constant ($n=1,2,3,\dots$). The solutions have some singularity related with values of arbitrary constants. It is shown from Eqs.(23)-(25) that $c_2 \neq -\frac{1}{2}c_2 \neq -\frac{1}{2}$, $c_2 \neq -\frac{1}{4}c_2 \neq -\frac{1}{4}$, $c_2 \neq 0c_2 \neq 0$, $c_5 \neq 0c_5 \neq 0$ and $c_3 \neq 0c_3 \neq 0$ for finite values of obtained functions. It is clearly that Lyra Geometry allows time dependent displacement vector for plane symmetric scalar fields. In addition, it is seen that scalar field is obtained in a form that can be reduced to a time power series polynomial. When $t \rightarrow Ct \rightarrow C$ for the initial scalar field, $\varphi \rightarrow c_1\varphi \rightarrow c_1$ is obtained. Thus, it can be said that $c_1 c_1$ is the initial scalar field $\varphi_0 \varphi_0$. Variation of the scalar field in Eq.(23) with time for different constant selections is given in the Figures (1)-(7). If all constants are positive normalized, the scalar field is obtained as in Figure (1). It is seen from Figure (1) that the scalar field gives results within negative time intervals. Although a scalar field starting from $\varphi_0 \varphi_0$ in the case of $t \rightarrow Ct \rightarrow C$ is as expected, an unfavorable situation in time indicates that there is no correct adjustment on the constants.

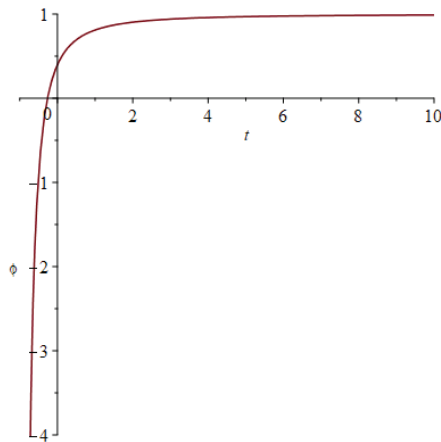


Figure 1. Change of Scalar Field with time ($c_1 = 1c_1 = 1$, $c_2 = 1c_2 = 1$, $c_3 = 1c_3 = 1$, $c_4 = 1c_4 = 1$).

Unlike Figure (1), when constant c_2c_2 is considered negative in Eq.(23), a reversible scalar field distribution around an axis is obtained, as seen in Figure (2). At this point, it is understood that the sign of the constant c_2c_2 plays a determining factor. However, inconsistency in time shows that different constant choices should also be taken into account.

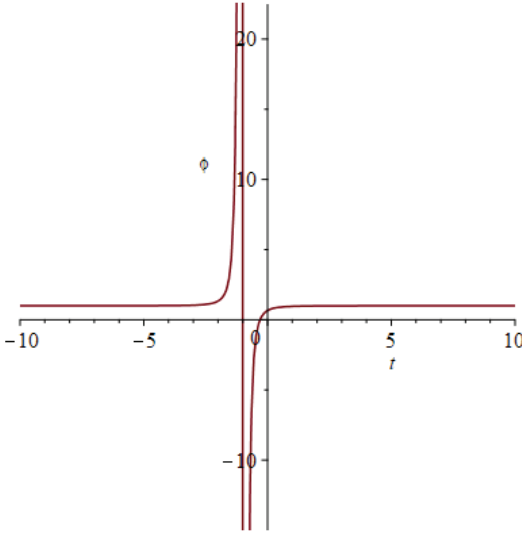


Figure 2. Change of Scalar Field with time ($c_1 = 1c_1 = 1$, $c_2 = -1$
 $c_2 = -1$, $c_3 = 1c_3 = 1$, $c_4 = 1c_4 = 1$).

Considering Figures (1) and (2) together, it is understood that it would be useful to examine case where constant c_3c_3 , which is factor of time, is negative. This situation is given in Figure (3).

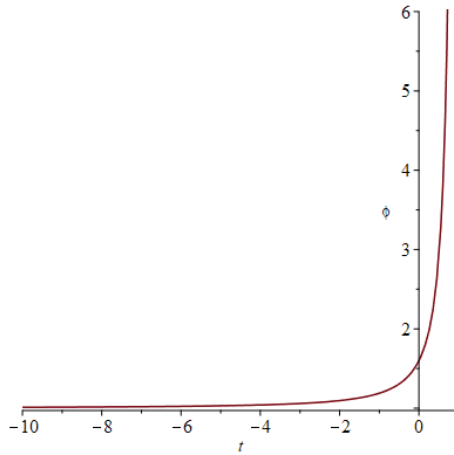


Figure 3. Change of Scalar Field with time ($c_1 = 1, c_2 = 1, c_3 = -1, c_4 = 1$).

It is seen from Figure (3) that only change in sign of constant c_3 causes an increasing scalar field with time acceleration. However, the initial-boundary values are not suitable due to existence of scalar field defined against negative time.

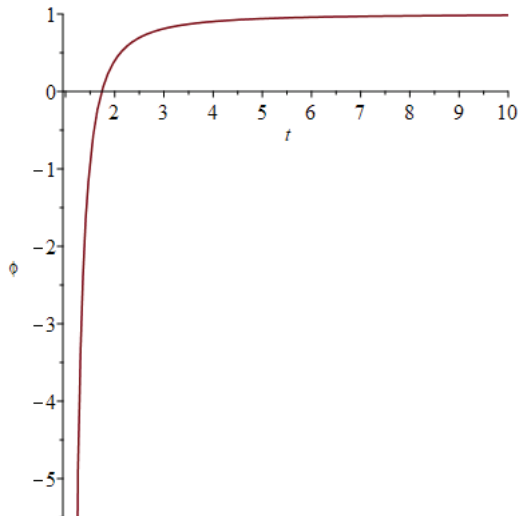


Figure 4. Change of Scalar Field with time ($c_1 = 1, c_2 = 1, c_3 = 1, c_4 = -1$).

In Figure (4), only constant c_4c_4 is chosen as negative. This gives an important result that all scalar field values correspond to positive time points. On the other hand, undefined result of the scalar field at time of $t = 0$ in terms of initial conditions is not suitable for the definition of initial scalar field φ_0 . In Figure (5), only constant c_1c_1 is chosen as negative. This gives that all scalar field values correspond to negative. Figures (6) and (7) show scalar field distributions provided by different constant selections.

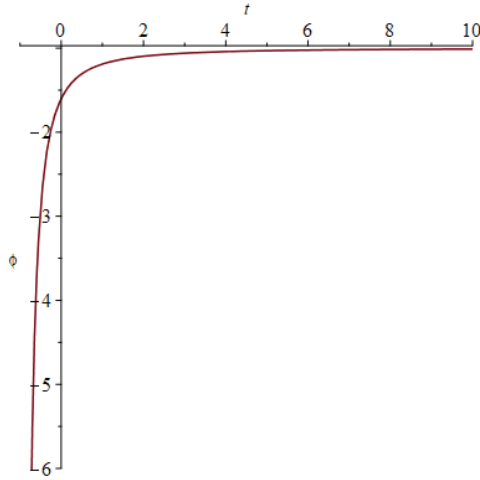


Figure 5. Change of Scalar Field with time ($c_1 = -1, c_1 = -1, c_2 = 1, c_2 = 1, c_3 = 1, c_3 = 1, c_4 = 1, c_4 = 1$).

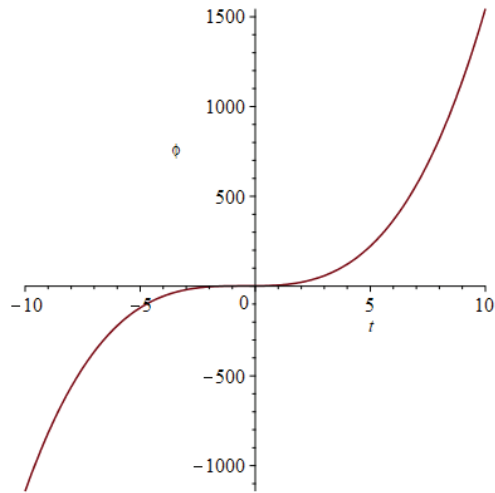


Figure 6. Change of Scalar Field with time ($c_1 = 1, c_2 = -2/5, c_3 = 2, c_4 = 1$).

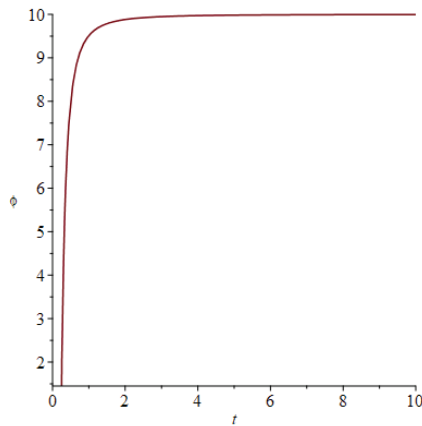


Figure 7. Change of Scalar Field with time ($c_1 = 10, c_2 = -10, c_3 = 1, c_4 = 0$).

5. CONCLUSION

In this study, it has been investigated whether a distribution can be obtained within scope of Lyra Geometry for scalar field that fills non-static plane symmetric space-time. It has been obtained that gravitational theory defined using Lyra Geometry allows a scalar field distribution dependent on time, such as a power series, such that exponent can take positive or negative values. Singular points of obtained scalar field and its distribution under different constant selections are examined. According to value ranges of the constants, it has been seen that scalar field can be parabolic increasing, parabolic decreasing, negative, positive and equal to or different from zero initial scalar fields are possible. In the literature, such scalar field distributions can be seen as sources of neutron stars, supernovae or early and late period expansion (Bo-Jun et al., 2013; Valentino, et al., 2019; Ikeda et al., 2021). Obtaining results consistent with literature and ability to define non-constant displacement vector are other results that can be counted.

REFERENCES

- Aydin, H. And Ulu Doğru, M. (2021) Cylindrically symmetric unimodular $f(R)$ black holes. International Journal of Geometric Methods in Modern Physics.
- Brans C. and Dicke R. H. (1961) Mach's principle and a relativistic theory of gravitation. *Phys. Rev.*, 124: 925.
- Bo-Jun, Z., Tian-Xi Z., Padmaja, G. and Mostafa, D. (2013) Neutron star mass-radius relation with gravitational field shielding by a scalar field *Res. Astron. Astrophys.* 13; 571.
- Collins, C.B., Glass, E. N. and Wilkinson, D. A. (1980) Exact spatially homogeneous cosmologies. *Gen. Relativ. Gravit.*, 12, 805-823.
- Einstein, A., and Rosen, N. (1935). The particle problem in the general theory of relativity. *Physical Review*, 48(1), 73.
- Faraoni V. (2004) *Cosmology in scalar-tensor gravity*, Fundamental theories of physics. Kluwer Academic Publishers, Netherland.
- Ikeda, T., Cardoso, V. and Zilhão, M. (2021) Instabilities of Scalar Fields around Oscillating Stars. *Phys. Rev. Lett.* 127, 191101.
- Lyra, G. (1951) über-eine Modifikation der Riemannschen Geometrie. *Math. Z.* 54, 52.
- Mahanta, K.L. and Biswal, A. K. (2012) String cloud and domain walls with quark matter in Lyra geometry. *Journal of Modern Physics*, 3(10), 1479.
- Maurya, D. C. and Zia, R. (2019) Brans-Dicke scalar field cosmological model in Lyra's geometry *Phys. Rev. D* 100, 023503 .
- Patil, V.R., Pawar, D.D. and Khapekar, G.U. (2012) Thick Domain Walls Coupled with Viscous Fluid and Electromagnetic Field in Lyra Geometry. *International Journal of Theoretical Physics*, 51(7), 2101-2108.
- Pradhan, A. and Chauhan, D.S. (2009) A New Class of LRS Bianchi Type-I Cosmological Model in Lyra Geometry. *RAPC*, 8: 179-190.
- Rahaman, F., Chakraborty, S., Begum, N., Hossain, M. and Kalam, M. (2003) Bianchi-IX string cosmological model in Lyra geometry. *PRAMANA c Indian Academy of Sciences* 60, 6, 1153–1159.
- Rahaman, F., Begum, N., Das, S., Hossain, M. and Kalam, M., (2006) Bianchi-I Cosmology with Magnetic Field in Lyra Geometry. eprint arXiv:gr-qc/0612126.
- Sen, D.K. (1957) A static cosmological model. *Z. Phys.* 149, 311.
- Sen, D.K. and Dunn, K.A. (1971) A scalar-tensor theory of gravitation in a modified Riemannian manifold. *J. Math. Phys.* 12, 578.

- Shchigolev, V. K. (2013) On Exact Cosmological Models of a Scalar Field in Lyra Geometry. **Universal Journal of Physics and Application**, **7(4)**, 408 – 413.
- Shchigolev, V. K. and Semenova, E. A. (2015) Scalar Field Cosmology in Lyra's Geometry. *International Journal of Advanced Astronomy*, 3(2), 117-122.
- Taşer, D. and Ulu Dođru, M. (2020) Scalar fields in $f(G)$ gravity. *International Journal of Geometric Methods in Modern Physics*, 17, 09, 2050132.
- Taşer, D., Ulu Dođru, M. and Aydın, H. (2022) Kantowski-Sachs model in non-minimally coupled scalar theory. *International Journal of Geometric Methods in Modern Physics*, 19, 9, 2250143-144.
- Türkođlu, M. M. and Ulu Dođru, M. (2015) Conformal cylindrically symmetric spacetimes in modified gravity. *Modern Physics Letters A*, 30, 37, 1550202.
- Ulu Dođru, M. and Demirtaş, M. (2018) Black Holes with Anisotropic Fluid in Lyra Scalar-Tensor Theory. *Süleyman Demirel University Journal of Natural and Applied Sciences*, 22, 1, 38 – 44.
- Valentino, E.D., Ferreira, R. Z. and Visinelli, L. and Danielsson, U. (2019) Late time transitions in the quintessence field and the H_0 tension. *Physics of the Dark Universe*, 26, 100385.
- Vilenkin, A. (1983) Gravitational field of vacuum domain walls. *Phys. Lett. B*, 133, 177.
- Weyl, H. (1918) Gravitation und Elektrizität. *Sitzungsberichte der Königlich Preussischen Akademie der Wissenschaften*, 465.

“

Chapter 11

**CHARGE CARRIER RECOMBINATION
KINETICS AND LIFETIME
MEASUREMENTS IN A-SI:H P-I-N SOLAR
CELLS WITH CR BACK CONTACT**

Bengü KAPLAN¹

”

¹ Prof. Dr., University of Mersin, Physics Division, Department of Mathematics and Science Education, Çiftlikköy Campus, 33343 Mersin, Turkey. bkaplan@mersin.edu.tr Orcid ID: 0000-0002-1334-6137

1. Introduction

There are many energy sources like coal, diesel, fission energy, etc., but they have side effects for humans and nature. Solar energy is the cleanest solution for emerging global warming and demanding energy resources. Silicon-based solar cells are efficient but are not cheap [1-2]. For exploring the more efficient and affordable materials, continuous efforts are going on. The different back contacts, like Al, Ag, Cr, ZnO/Ag, etc. are being searched for solar cells applications [3-4].

Photovoltaic cells utilize layered semiconductor materials as a p-I-n junction to convert light energy in the form of photons to electric current in the form of electrons. When the photon is absorbed by the intrinsic (I) layer type of semiconductor, a free electron-hole pair is generated. The negatively charged electron is attracted to the p-type material, and the positively charged hole is attracted to the n-type material. If a completed circuit is connected to the electrodes, the free electron will travel through the circuit, creating electric current and voltage, until it recombines with an electron-hole back in the material.

The efficiency of photovoltaic systems vary by the type of photovoltaic cell technology and the type of semiconductor material used. The first solar cells [5] were composed of inorganic polycrystalline and single-crystalline materials. Notable progress has been made in photovoltaic technology due to remarkable advancements in organic electronics and materials.

An organic solar cell is lightweight, flexible and can be produced at low cost with high-performance polymeric donors, fullerene, and non-fullerene acceptors through low-temperature solution processes on a transparent conductor, such as indium tin oxide (ITO) or fluorine-doped tin oxide (FTO). Organic hole-transport materials have enabled high-performance perovskite solar cells as an alternative, more efficient method for harvesting solar energy.

Perovskite solar cells typically use a hybrid inorganic-organic material as the light-harvesting active layer. They benefit from a high conversion efficiency, low cost, and simple manufacturing, making them the fastest advancing solar technologies for commercial applications [6-7]. Lead halide perovskites have the highest conversion efficiency and are the fastest growing solar cell technology.

Differences between the charge transport scale and optical absorption length can cause recombination losses in thin film photovoltaics, which lead to higher series resistances and lower fill factors [8]. Therefore, developing device architectures plays an important role in enhancing performance for thin film photovoltaics with active layers that are thinner than the optical absorption length [9]. Among all the strategies, light trapping is a necessary part in the design of thin film photovoltaics [4,10]. Effective light trapping promotes the effective absorption of the long-wavelength photons inside the thin absorb layer due to the extended path-length. Incorporation of textured surface with different nanostructures is the main strategy for light trapping in all kinds of thin film photovoltaic cells, such as amorphous/microcrystalline thin films [11], crystalline/heterojunction silicon technologies [12], recently promising perovskite photovoltaics [13] and high efficient tandem solar cells [14].

Over the last four decades, solar photovoltaic (PV) systems have seen a staggering cost reduction due to much reduced manufacturing costs and higher device efficiencies.

Illumination intensity and thus recombination, temperature and carrier lifetime are among the influential factors on the performance of solar cell devices, which mainly affect the voltage o/p and current o/p of such devices. Various kinds of photocurrent models and performance parameters of solar cells have been developed [15].

Hydrogenated amorphous silicon (a-Si:H) is a glassy semiconducting material that is not likely to occur in nature. The material is a disordered alloy of silicon and hydrogen whose composition may vary from about 1 at. % H to about 50 at. % H, depending on the method of formation [16]. Scientific interest in this material has increased enormously in the past few years so that today there are several hundred scientists worldwide investigating a-Si:H. The reason for this large research effort is that a-Si:H promises low-cost, nonpolluting electrical power via the photovoltaic effect. Solar cells are widely used application for p-I-n devices, especially when non-crystalline materials are employed [17].

Recombination [18] looks like a loss of current or a short circuit to the external electrical circuit. The grain boundaries look like an internal electrical resistance to the p-I-n solar cell circuit, which causes a loss of voltage from the p-I-n. The net effect of grain boundaries is to reduce the power output of a solar cell. Researchers [16] have found several ways to minimize the problems caused by grain boundaries: adjusting growth con-

ditions through treatments such as annealing (heating and then cooling) the semiconductor material so that grains are columnar and as large as possible; designing solar cell so that the charge carriers are generated within or very close to the built-in electric field; and filling broken bonds at grain edges with elements such as hydrogen. Although these methods are effective in increasing the output of amorphous solar cells, the processes that occur at the atomic level are not well understood.

In this work, we investigate the I-V characteristics, the intensity- and temperature-dependence of photocurrent, the photocarrier lifetime spectra, the capacitance, and the most important recombination process based on impurities and defects in a-Si:H p-I-n solar cells with Cr back contacts at room temperature (RT) and low temperature (LT). A knowledge of the photo-interaction in the p-I-n solar cells with Cr back contact is very important to understand the basic recombination kinetics and thus its technological applications. We also conclude with a discussion on the basic equations of solar cell device physics.

2. Samples And Experimental Details

The sample used in this study was obtained from the Institute of Energy Conversion (IEC), University of Delaware. It has 1x1 inch SnO₂ substrate of a-Si:H p-I-n device with Cr back contact. Its layer sequence is glass/ITO/p-I-n/Cr. The I-V results taken under 1 sun illumination (AM1.5 global light from an Oriel simulator) by using 4-terminal configuration (due to the high resistance) are: $V_{oc} = 0.84 V$ (open-circuit voltage), $J_{sc} = 13.22 \text{ mA/cm}^2$ (short-circuit current density), $V_{mp} = 0.64 V$ (voltage at maximum power point), $J_{mp} = 10.56 \text{ mA/cm}^2$ (current density at maximum power point), $FF = 60.4 \%$ (fill factor), $R_{oc} = 9.82 \Omega \cdot \text{cm}^2$ (resistance at open circuit), and $IQE = 12.90 \text{ mA/cm}^2$ (integrated quantum efficiency with the AM1.5 spectrum). The device cell area is 0.4 cm², and the substrate contact is along the side. The intrinsic layer thickness is about 0.5-0.6 μm.

A HeNe laser (632.8 nm, 0.65 mm beam diameter, 10 mW o/p max.) was used as the excitation light to obtain I-V characteristics, intensity- and frequency-dependences of photocurrent. Neutral density filters (NDF) were used to vary the intensity of light incident on the p-I-n solar cell. The

incident light was chopped at the frequencies between 10 Hz and about 4 kHz. The modulated signals were detected by pre- and lock-in amplifiers. For DC measurements, an electrometer (Model 6514) was used. The IQE was measured from 400 to 750 nm using the same lock-in detection system chopped at 70 Hz, illuminated through a monochromator having 12 nm width at half maximum. The system was calibrated using a filtered (Schott KG5) crystalline Si device as was used to calibrate the Oriel solar simulator.

3. Results And Discussion

Basically, a photovoltaic solar cell can be visualised as an equivalent electrical circuit. In operation, the solar cell can be represented by a photogenerated current source $I_{\lambda}I_{\lambda}$ feeding into an ideal p-I-n solar cell. The internal cell characteristics are better modeled by the introduction of a shunt resistor (R_{sh}), a shunt capacitor (C), and a series resistor (R_s). In the photovoltaic mode, an external high value of load resistor (R_L) is connected across the output and the voltage across this measured. In the photoconductive mode, an external bias (V_{app}) is applied in conjunction with a series load resistor (R_L). The current flowing through R_L is monitored by measuring the voltage across it. The effect of shunt and series resistances on I-V characteristics in solar cells is discussed in textbooks [19-20]. In order to determine the values of R_{sh} and R_s , some theoretical calculations were derived and their light intensity dependences reported in literature [19, 21]. Experimentally, it is also possible to find the values of R_{sh} and R_s from the I-V characteristics of p-I-n samples in dark and under illumination. In this work, we used the photoconductive mode.

Fig. 1 shows the I-V characteristics for various levels of illumination. As well known, the electrical characteristics of a solar cell is described by the relation between the current flowing through the solar cell and the potential V across it, while the solar cell is illuminated. Obviously, under increasing levels of illumination, the curve is progressively shifted downwards. We can explain this result in the light of a simple physical model of transport for p-I-n solar cells proposed by Crandal [22]. According to this model, for weakly absorbed light, the shape of photocurrent-voltage curve is completely specified by the electron and hole drift

lengths. Furthermore, it is the carrier with the longer drift length that determines the current-voltage curve and hence the solar cell fill factor.

A convenient way to characterize the electrical performance of a solar cell is to specify its open circuit voltage V_{oc} , its short-circuit current I_{sc} and its fill factor FF . The latter is a measure of the rectangularity of the I–V curve and is defined by

$$FF = \frac{V_m I_m}{(V_{oc} I_{sc})} \quad (1)$$

where V_m and I_m are the voltage and current density at the maximum power point respectively, and $(V_m I_m)$ is the maximum power per unit of area P_m . The graphical interpretation of P_m is the area of the largest rectangle below the I–V curve; $(V_{oc} I_{sc})$ is the area if the curve was a true rectangle. From the definition of FF , it follows that $P_m = FF(V_{oc} I_{sc})$. The efficiency of a solar cell η is in fact the efficiency at maximum power delivery, so that $\eta = P_m/P_{in}$, where P_{in} is the incident light intensity. It is clear that any loss in FF will reduce the efficiency of the solar cell. One must note that V_{oc} , I_{sc} and FF are not the fitting parameters and do not depend on any model describing the solar cell devices. From the fourth quadrant of Fig. 1, the calculated values of FF are also shown in the figure. The small value of FF may be due to the high excitation intensity used [23]. When compared with literature, Cr back contact gives low FF , but high short circuit current density (J_{sc}) ; while Al back contact gives high FF , but low J_{sc} under the same illumination condition. For the ZnO/Ag back contact, both FF and J_{sc} were found to be high and more stable [4].

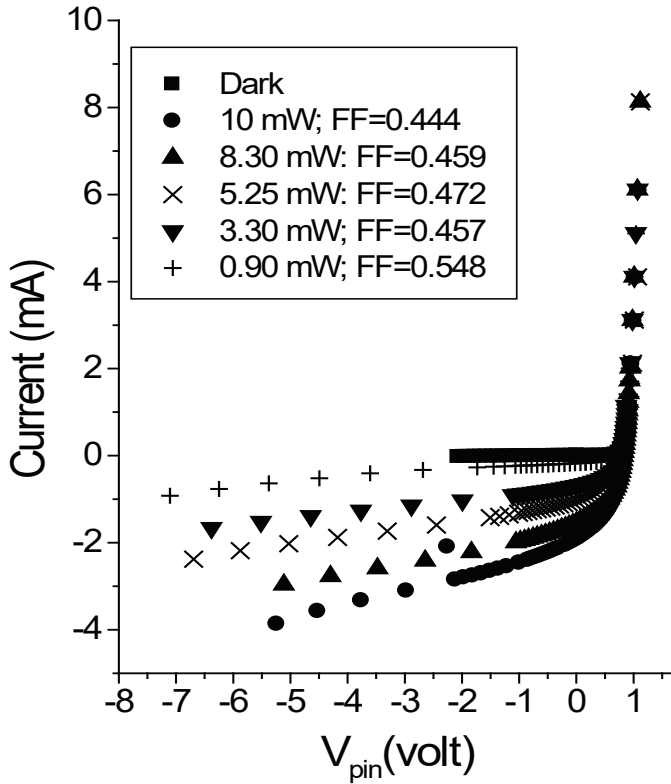


Figure 1. *I-V characteristics in dark and under different illumination intensity levels.*

The use of photocurrent is an attempt to describe the carrier lifetime, the intensity and temperature variations of photocurrent by a consistent recombination model involving nonlocalized and localized states, provided that such variations appear to be reliable indicators of solar cell properties. It is the fact that a consistent pattern of photocurrent behaviour is characteristic of a surprisingly large number of different types of amorphous semiconductors that makes this approach attractive.

An important feature of the transport properties of a-Si:H p-I-n solar cells is the recombination of photogenerated charge carriers via recombination centers. This affects the photocurrent, as well as being of importance for device application. The recombination usually occurs through the intermediary of the impurity or defect levels in the energy gap. In general, these levels correspond to localized electronic states and act as “traps” for

the electrons or holes in the band states. When a carrier makes a transition and is trapped at these localized levels, it no longer contributes to the conductivity. However, the carrier can be released and return to the band. If

the probability, for recombination, at the level, with a carrier of the opposite sign, is greater than the probability of release to the band, the level is called a recombination center. Conversely, if the probability for release is greater than recombination, the level is simply called a trap. The distinction is mainly based on the proximity of the level to the band edge. The recombination process comprises mainly two sequential steps in which electrons and holes can recombine so as to reestablish the equilibrium that has been distributed by photoexcitation. The excited electron or hole first loses energy by many transitions within the band, in which the energy decrements are small and frequent. This process is known as thermalization. The thermalization rate decreases as the electron moves into the localized band-tail states and the density of available states is lower. Eventually the electron completes the recombination by making a transition to a hole with the release of a large energy. Recombination lifetimes are generally much longer than the thermalization times, so that the two processes usually takes place on distinctly different time scales. Recombination at low temperatures mostly occurs by tunnelling, because there is not sufficient thermal energy to excite carriers from the band-tail states to the mobility edge. Thermal excitation becomes significant at higher temperatures and changes the recombination mechanisms.

Measurement of photocurrent as a function of excitation light intensity, temperature, modulation frequency, applied electric field, carrier lifetime and capacitance provides valuable information on the transport properties of photocarriers. The dependence of photocurrent $I_{p/h}$ on the photogeneration rate GG (which is linearly proportional to the incident light intensity) is given by the power-law,

$$I_{p/h} \sim G^{\nu} \quad (2)$$

where the exponent ν is differentially defined by

$$\nu = \frac{d[\ln(I_{p/h})]}{d[\ln(G)]} \quad (3)$$

It is now well-known that the value of $\nu\mathcal{V}$ differs in various materials. Mostly, a sublinear

dependence is found and the $\nu\mathcal{V}$ in Eq. (3) has quite complicated variation with light intensity, photon energy, modulation frequency, applied bias voltage and temperature [24]. Figs. 2 and 3 show the high and low excitation intensity dependence of photocurrent at different bias voltages and frequencies respectively.

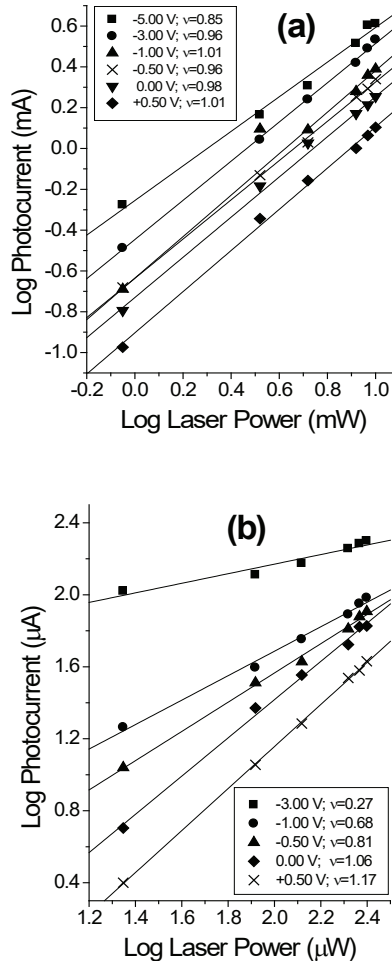


Figure 2. High (a) and low (b) excitation intensity dependence of photocurrent at different bias voltages.

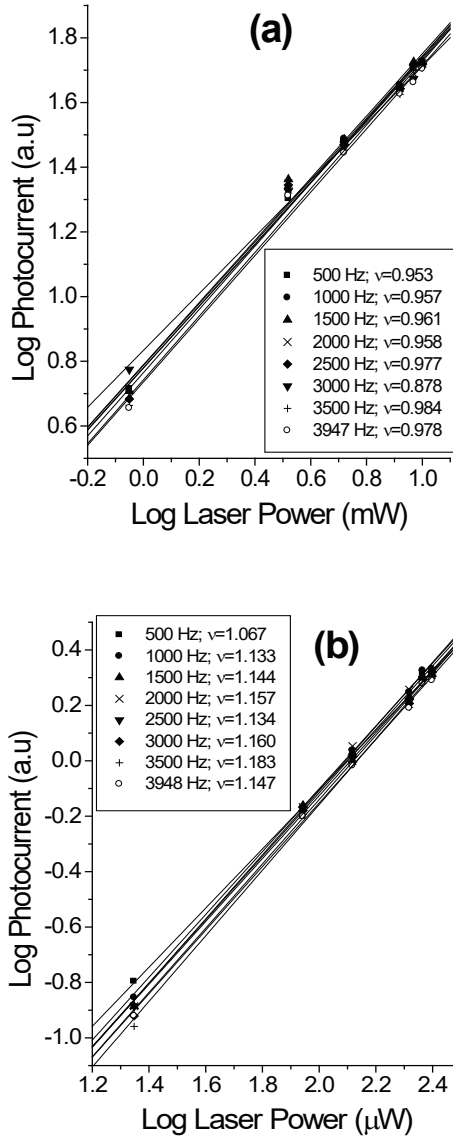


Figure 3. High (a) and low (b) excitation intensity dependence of photocurrent for different modulation frequencies. $V_{p-i-n} = -1$ V.

According to the classical kinetics model [25], $\nu = 1$ corresponds to monomolecular recombination and $\nu = 0.5$ to bimolecular recombination. But, in the case of continuous distribution of traps the value of ν may be anywhere between 0.5 and 1.0 depending on the light intensity, photon energy, bias voltage, frequency and temperature range [26].

As it is seen from Figs. 2 and 3, the log-log plots give straight lines. From the slopes of lines, the calculated values of exponent ν in $I_{ph} \sim G^\nu$ are also represented on the figures. The exponent ν for a p-I-n solar cell could qualitatively be associated with the amount of recombination centers located in the intrinsic layer; a higher value of ν , in general, implies a higher rate of carrier recombination.

In Figs. 2 and 3, the values of exponent ν lie between about 0.27 and 1.18, which indicate that its values are light intensity and frequency dependent. It is common practice to attribute ν between 0.5 and 1.0 to a mixture of two limiting recombination mechanisms [27]: a monomolecular recombination type occurring through recombination centers (dangling bonds, midgap, localized levels) which would correspond to $\nu=1.0$ and a bimolecular recombination process, in which the excess charge carriers recombine directly from the band tails ($\nu=0.5$). An alternative model proposed by Rose [26] considers an exponential distribution of density of states (DOS) whose states are increasingly converted from trapping to recombination states as the light intensity increased. Different ν values between 0.5 and 1.0 are obtained from this model, which depend upon the slope of DOS being swept by the steady state Fermi level, and on temperature. In past, the analytical work on photoconductivity in a-Si:H by Bube [28] demonstrated that a relative simple model for recombination via dangling bonds may produce superlinear photocurrent ($\nu > 1$) in undoped material. On the other hand, a sublinear characteristics with exponent ν as low as 0.3 has been observed by numerous groups [29-31]. However, a complete model covering the modulation frequency-dependence of ν has not emerged.

Fig. 6 shows the photocurrent, I_{ph} vs. $10^3/T$. In the thermally activated region, the I_{ph} increases almost linearly with increasing temperatures. It is produced by the thermal activation of photocarriers, following the exponential relation [32],

$$I_{ph} = I_0 \exp\left(-\frac{E_a}{k_B T}\right) \quad (4)$$

where I_0 is a prefactor, k_B is the Boltzmann's constant, and E_a is the thermal activation energy.

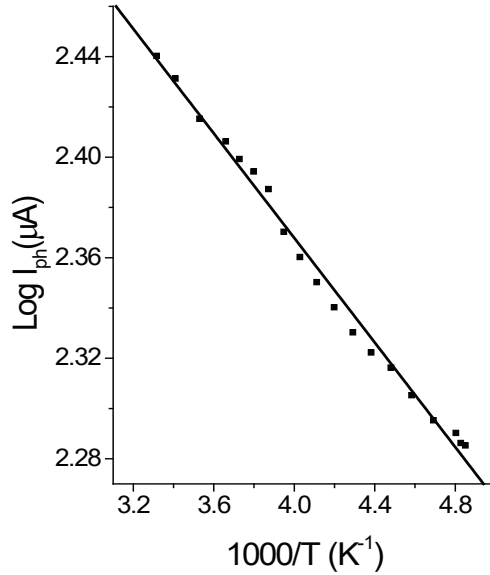


Figure 4. Photocurrent vs inverse temperature. $V_{p-i-n} = -0.5$ V. $E_a = 9$ meV.

The value of E_a can be calculated from the slope of a linear plot of $\ln(I_{ph})$ vs. $10^3/T$. From Fig. 4, an activation energy, E_a value of about 9 meV was calculated. At high temperatures, the transport of photocarriers can be described by the multiple trapping model [33-34], in which injected carriers thermalize in a broad distribution of localized band tail states, moving to deeper energies as a result of thermal activation to transport states and subsequent retrapping.

The frequency-resolved photocurrent (FRPC) spectroscopy technique has already been described [35-37]. The advantage of this frequency-locked AC measurements is that it rejects any stray light, dark current and any other unmodulated signals. In its simplest form, the optical excitation of a sample is modulated with a small amplitude sinusoid and

the sample response to this modulation is measured either in-phase (IP-) or in-quadrature (IQ-) to the phase of the excitation modulation, using a lock-in detection. Logarithmically sweeping the modulation frequency then generates a lifetime distribution directly.

In the mathematical analysis of frequency-resolved spectroscopy (FRS) method, the in-phase FRS gives the integral of lifetime distribution, between the limits $\tau \sim (2\pi\omega)^{-1}$ and ∞ , while the in-quadrature FRS gives the lifetime distribution directly. For a system with a single characteristic lifetime τ , the in-quadrature FRS spectrum is a symmetric band, of half width 0.7 decades peaked at the frequency

$$f_{peak} = \frac{1}{2\pi\tau} \quad (5)$$

Although the in-quadrature FRS is the most useful form, the in-phase version can also give important additional information on the existence of fast processes beyond the time domain of the in-quadrature measurements. It is worth remembering that if one knows the quadrature response from $\omega = 0 \rightarrow \infty$ (which one does not), a Kramers-Kronig transform will give the in-phase response. That is all the information is in either response, if complete in ω . Fig. 5 shows IQ-FRPC and IP-FRPC spectra for different excitation intensities of HeNe laser (632.8 nm). The data were taken under reverse bias voltage of - 1.00V.

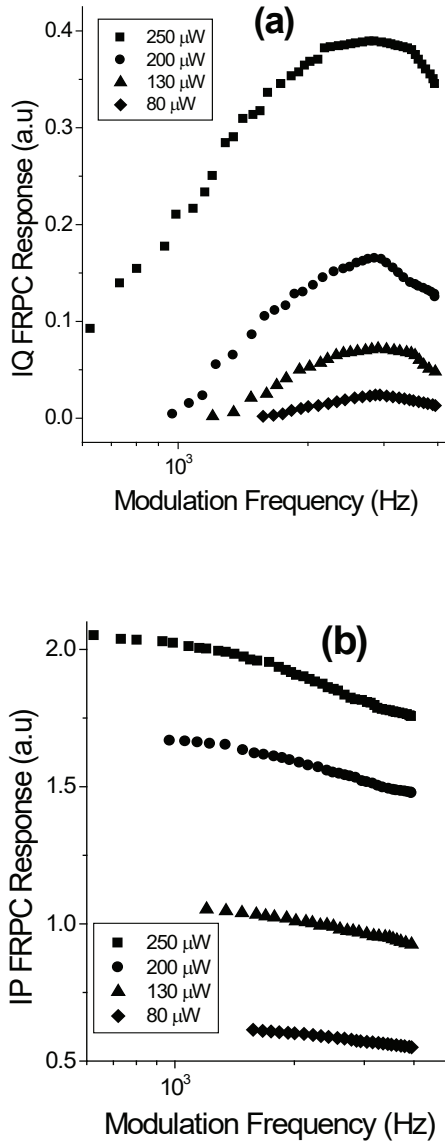


Figure 5. IQ (a) and IP (b) FRPC response for various light intensities. $V_{p-i-n} = -1.00$ V.

As seen from the IQ-FRPC spectra, there is only one single broad spectra in which the peak frequency is independent of excitation intensities. It means that there is only one characteristic lifetime. Using Eq. (5), a lifetime of about 54 μ s was calculated. This lifetime is also found to be

independent of applied voltage and thus electric field. At room temperature, the photocarriers may be thermally ionized from recombination or trapping states, in which only one recombination path is present. As well known, higher excitation light intensity and modulation frequency produce a larger fraction of photocarriers from deep trapping levels (defects) in the energy gap, and thus these contribute to the photocurrent.

The capacitance-voltage (C-V) measurement is widely used to determine a variety of semiconductor parameters, such as doping concentration and profiles, carrier lifetime, oxide thickness, interface trap density, and etc. Fig. 6 shows the capacitance as a function of frequency in dark. Unfortunately the illumination has no important effect on this result. Actually, the capacitance-voltage (C-V) measurements are made at AC frequencies. So, the capacitance for the device under work can be calculated with the following:

$$C = \frac{I_{pd}}{2\pi f V_{AC}} \quad (6)$$

where I_{pd} is the magnitude of the AC current through the p-I-n solar cell, f is the frequency, and V_{AC} is the magnitude and phase angle of the measured AC voltage. In other words, the basic test setup measures the AC impedance of the photodiode by applying an AC voltage and measuring the resulting AC current, AC voltage, and impedance phase angle between them. This measurement takes into account series and parallel resistance associated with the capacitance, as well as the dissipation factor (leakage).

In Figure 6, the magnitude of applied AC voltage is kept at 1.40 V. As seen, the capacitance sharply decreases with increasing frequency at low frequency range ($f < 2$ Hz). For about $f > 2$ Hz, it decreases slowly with increasing frequency. This result is in agreement with the Eq. (6). The magnitude of capacitance was found to be independent of AC and DC applied voltages.

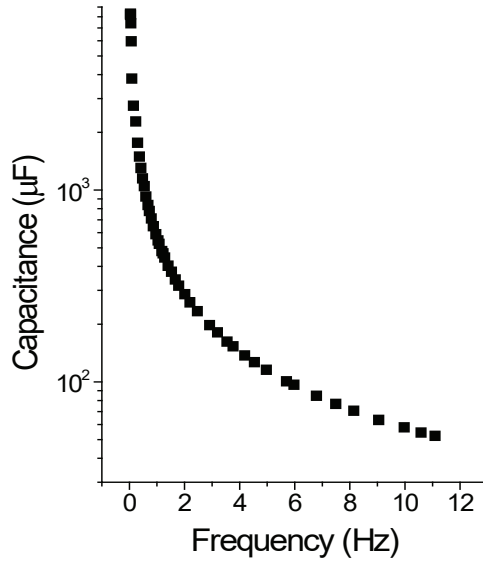


Figure 6. Capacitance versus frequency in dark. $V_{p-p} = 1.40 \text{ V (AC)}$.

4. Conclusion

It is well established that I-V, and thus $FFFF$, the exponent ν in the power-law $I_{ph} \sim G^\nu I_{ph} \sim G^\nu$, the carrier lifetime τ , the activation energy E_a , and the capacitance C are sensitive to the material of different back contacts which have influences on the p-I-n solar cell structure. These quantities can be improved on a-Si:H p-I-n devices by optimization of the back contact material which acts as a reflector allowing some of the passing light to reflect into the intrinsic layer.

From the photoconductive modes of I-V characteristics, we determined the fill factor values between 0.444 and 0.548 at room temperature (290 K). The low $FFFF$ can be due to the high excitation light intensity used.

Recombination process is a key point when describing carrier transport kinetics in solar cells because it strongly affects the photoresponse of these devices at all levels of external excitation.

The exponent ν , in the power-law relationship $I_{ph} \sim G^\nu I_{ph} \sim G^\nu$, is found to be between 0.27 and 1.18 depending on low and high excitation

intensities, bias voltages and frequencies. The intensity results were interpreted suitably, but there is no a complete theoretical model covering the modulation frequency dependence of $\nu\nu$ in literature. The high values of $\nu\nu$ (>1) at low light intensities may be due to the increase of photo-carrier release rate with frequency from deeper states, which is thermally activated at room temperatures.

From the temperature dependence of photocurrent measurements, the activation energy value of 9 meV was calculated.

A single broad lifetime distribution was observed to peak about 3000 Hz, which corresponds to the lifetime of about 54 μ s. This lifetime is found to be independent of excitation intensity and applied electric field at room temperature. High recombination rate means a low carrier lifetime, which is connected with a diffusion length that is small compared with the width of the space charge region.

Our results of the intensity and temperature-dependence of photocurrent, and also of the room temperature carrier lifetime show that the recombination occurs through the trap states in the higher temperature region. Thus the release rate from traps controls both the photocurrent and also the carrier lifetime.

The capacitance–frequency measurement in dark and also under illumination indicates that considerable photocarrier numbers of deep trap levels were not introduced by illumination in the intrinsic region of solar cell.

Acknowledgements

I would like to thank Dr. S. S. Hegedus for supplying a-Si:H p-I-n with Cr back contac samples.

REFERENCES

- [1] Kumar, M., Rani, S., Sing, Y., Mamta, Kumar, A., Sing, V. N., *Solar Energy* 232 (2022) 146.
- [2] Jyoti, Mohanty, B. C., *Solar Energy* 230 (2021) 986.
- [3] Louwen, A., Van Shark, W., Schropp, R., Faaij, A., *Solar Energy Mat. Solar Cells* 147 (2016) 295.
- [4] Hegedus, S. S., Kaplan, R., *Prog Photovolt: Res Appl* 10 (2002) 257.
- [5] Chapin, D. M., Fuller, C. S., Pearson, G. L., *J. Appl. Phys.* 25(5) (1954) 676.
- [6] Lang, F., Nickel, N. H., Bundersmann, J., Seidel, S., Denker, A., Albrecht, S., Brus, V. V., Rappich, J., Rech, B., Landi, G., Neitzert, H. G., *Adv. Mater.* 28 (2016) 8726.
- [7] Afshari, H., Durant, B. K., Brown, C. R., Hossain, K., Poplavskyy, D., Rout, B., Sellers, I. R., *Solar Energy Mat. Solar Cells* 212 (2020) 110571.
- [8] Huang, Q., Zhao, J., Chen, Y., Wang, J., Zhao, Y., Zhang, X., Hou, G., *Solar Energy Mat. Solar Cells* 225 (2021) 110997.
- [9] Lee, Y. H., Lee, T. K., Song, I., Yu, H., Lee, J., Ko, H., Kwak, S. K., Oh, J. H., *Adv. Mater.* 28 (2016) 4976.
- [10] Priola, F., Gregorkiewicz, T., Galli, M., Krauss, T. F., *Nat. Nanotechnol.* 9 (2014) 19.
- [11] Donie, Y. J., Smeets, M., Egel, A., Lentz, ., Preinfalk, J. B., Mertens, A., Smirnov, V., Lemmer, U., Bittkau, K., Gomard, G., *Nanoscale* 10 (2018) 6651.
- [12] Li, Y., Li, Y. K., Wang, X. X., Wang, Y., *Opt. Quant. Electron* 51 (2019) 138.
- [13] Wang, Y., Wang, P., Zhou, X., Li, G., Lee, H. Z., Hu, X. T., Lee, F. Y., Liu, X. P., Li, M. Z., Song, Y. L., *Adv. Energy Mater.* 8 (2018) 1702960.
- [14] Wang, D., Cui, H., Hou, G., Zhu, Z., Yan, Q., Su, G., *Sci. Rep.* 6 (2016) 18922.
- [15] Seapan, M., Hishikawa, Y., Yoshita, M., Okajima, K., *Solar Energy* 204 (2020) 459.
- [16] Carlson, D. E., Wronsky, C. R., *Amorphous Semiconductors-Topics in Applied Physics*, Brodsky, M. H., Ed., Vol. 36, Springer-Verlag, (1979).
- [17] Street, R. A., *Hydrogenated Amorphous Silicon*, Cambridge University Press, (1991).

- [18] Smith, A., *Semiconductors*, Cambridge University Press: Cambridge, UK (1986).
- [19] Fahrenbruch, A. L., Bube, R. H., *Fundamental of Solar Cells*, Academic Press, (1983).
- [20] Allison, J., *Electronic Engineering Semiconductors and Devices*, 2nd Ed., McGraw-Hill Book Company, (1990).
- [21] Takahashi, M., Konagai, M., *Amorphous Silicon Solar Cells*, translated by F. R.D. Apps., North Oxford Academic Publishers Ltd., (1986).
- [22] Crandal, R. S., *J. Appl. Phys.* 54 (1983) 7176.
- [23] McMahon, T. J., Von Roeder, B., *Proceedings of the 26th IEEE PVSC 1997*, p.375.
- [24] Kaplan, R., *Solar Energy Mat. Solar Cells* 85 (2005) 545.
- [25] Kaplan, R., Kaplan, B., *Turkish Journal of Physics* 22 (1998) 873.
- [26] Rose, A., *Concepts in Photoconductivity and Allied Problems*, Krieger, (1978).
- [27] Arene, E., Baixeras, J., *Phys Rev B* 30 (1984) 2016.
- [28] Bube, R. H., *J. Appl. Phys.* 74 (1993) 5138.
- [29] Hack, M., Guha, S., Shur, M., *Phys. Rev. B* 30 (1984) 6991.
- [30] Morgado, E., *J Non-Cryst Solids* 166 (1993) 627.
- [31] Bube, R. H., Redfield, D., *J. Appl. Phys.* 66 (1989) 3074.
- [32] Vomvas, A., Fritzsche, H., *J. Non-Cryst. Solids* 97-98 (1987) 823.
- [33] Huang, C. Y., Guha, S., Hudgens, S. J., *Phys. Rev. B* 27 (1983) 7460.
- [34] Hvam, J. M., Brodsky, M. H., *Phys. Rev. Lett.* 46 (1981) 371.
- [35] Depinna, S. D., Dunstan, D. J., *Phil. Mag. B* 50 (1984) 579.
- [36] Wagner, D., Irsigler, P., Dunstan, D. J., *J. Phys. C: Solid State Phys.* 17 (1984) 6793.
- [37] Kaplan, R., *Solar Energy* 84 (2010) 401.

“

Chapter 12

**USE OF DIFFERENTIAL SCANNING
CALORIMETRY IN MODEL MEMBRANE
RESEARCH**

Sevgi TÜRKER KAYA¹

”

¹ Dr.Öğr.Üyesi Sevgi Türker Kaya Kocaeli University Faculty of Arts and Sciences Department of Biology 41380 Kocaeli/Turkey ORCID ID: 0000-0002-5393-0207

Differential Scanning Calorimetry (DSC)

Differential scanning calorimetry (DSC) is a thermo-analytical invention for determining thermotropic features of different kinds of materials including biologically relevant systems. It directly measures variations in the heat energy uptake by a sample in corresponding to a reference during temperature change [1-3]. Its advantages are good data reproducibility, easy preparation of sample and analysis, and relatively need of low amount of sample. The method could be performed qualitative and quantitative characterization of transitions in association of specific parameters such as transition temperature, enthalpy and entropy, all of which can be correlated with alterations in biological properties of membranes [3-4]. The primary applications of DSC in membrane research are how hydration, pH, and solvent affect phase transition parameters of model and real membranes [5-7].

Instrumentation of DSC

Calorimetric measurements using DSC are performed based on the heat flux design. Figure 1 shows the representative diagram of DSC instrument. This system measures the molar heat capacity of samples depending on temperature [1,7-8]. In detail, a solution containing biological sample is loaded into a sample cell and a reference buffer place into the other holder. Both chambers are applied to heat at an identical scan rate. As the temperature increases and/or decreases, the heat is either being absorbed or released by sample, and subsequently transition of sample occurs. This leads to an unbalance between sample and reference. Such occurred imbalance is later compensated by heater. The recording of this covers a calorimetric measurement of sample transition. Thus, it monitors small heat changes between sample and reference in temperature and/or time dependent manner [9-10]. An exothermic or endothermic transition of the sample gives rise to a deviation in the difference between the two heat flows. The resultant is the DSC curve. Upon such convention, exothermic and endothermic processes represent as positive and negative peaks, respectively [11].

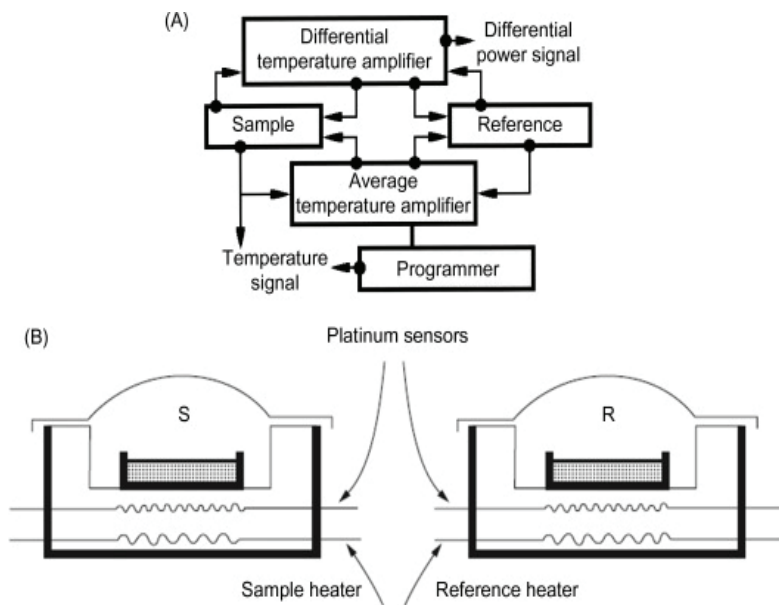


Figure 1. A representative diagram for operation of DSC [12].

Phase Transition of Lipids and Thermotropic Parameters

Lipids self-assemble with various phases with different structures and geometries in the presence of water [13]. In lipid water systems temperature and water are the main variables which are responsible for thermotropic and lyotropic phase behaviour. In addition, the physiologically important liquid crystal lamellar phase is of biological interest because it includes the gel to liquid crystalline phase, the lamellar and non-lamellar mesomorphic transitions. The lamellar to liquid crystalline phase transition ($L\beta - L\alpha$) is defined as melting of hydrocarbon tail, order-disorder, solid-liquid and principal transition. It is the fundamental energy phenomenon in lipid bilayers and occurs with an enthalpy alteration. This is related with disorder of hydrocarbon chains and risen head group hydration. The energy required to expand the hydrocarbon chain and to increase bilayer area against attractive van der Waals interactions contributes to enthalpy change of the transition. In gel to liquid phase transitions lipid surface area and specific volume are increased. In calorimetric measurements, these transitions occur in the enthalpy range of about 20-40 kJ/mol and appear as sharp, narrow heat capacity [13-15].

The gel phase differs from the liquid crystal phase. These differences can be listed as: In the gel phase, the acyl chains of phospholipids are

straight (trans configuration) and are positioned almost perpendicular to the bilayer plane. In this phase, the fatty acid chains have a closely ordered, side-by-side packed structure in a hexagonal arrangement. On the other hand, in the liquid crystalline phase, in addition to the hydrophobic interactions between the acyl chains, there is a long-range order in which the bilayer structure is preserved by electrostatic interactions between the polar head groups of lipids and water, and a short-range disorder in which the acyl chains are attached to the glycerol backbone [14-16].

Membrane lipids undergo three phase alterations in the temperature range of 5 °C-90 °C. The lowest temperature phase is the Lc phase, also called sub-gel, which transitions to the gel phase or $L\beta'$ phase with the increase in temperature. In both phases the hydrocarbon chains are bent relative to the bilayer normal while in the $L\beta'$ phase the head group is more hydrated. The transition from the Lc phase to the $L\beta'$ phase is called subtransition. An increment in temperature results in the formation of the wavy ($P\beta'$) phase. This transition is called the pretransition, and in this $P\beta'$ phase, the bilayer is inclined. Finally, the bilayer undergoes a liquid crystal ($L\alpha$) phase transition, called the principal transition or chain order/disorder transition. In this phase, the bilayer is such that the lipids move freely. The hydrocarbon tails become disordered and thus the transition to the $L\alpha$ phase is defined as the melting of the bilayer [14,17].

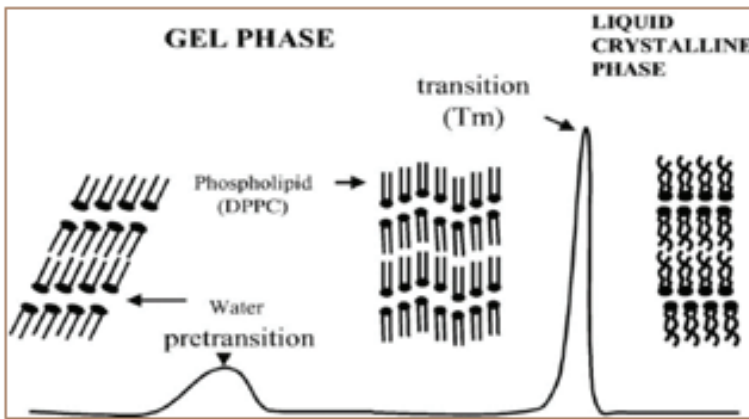


Figure 2. Schematic representation of the conformational changes in phospholipid bilayer during phase transition [17].

Calorimetric Measurement of Lipids

The calorimetric measurement of lipids involves scanning that gives a plot of heat energy versus temperature or time. The lipid transition can either be observed as endothermic or exothermic. These peaks occur at specific temperature values, reach maxima/minima, and end at specific final temperatures. These transitions include heat capacity or energy changes, which leads to the formation of DSC peak heat flow. Once a thermogram is obtained, the next procedure is the application of baseline. The usual procedure is to subtract a baseline from the overall curve to leave a profile of lipid transition relative to a zero baseline. It is generally user dependent process which determines the most appropriate baseline type. But it is usually worth mentioning that attemptation of several baseline procedures would be helpful to get an idea of the baseline fitting. Then, the area of the peak is evaluated from the onset temperature to completion of transition [7,9-10].

The curve is analyzed to determine thermotropic parameters listed below;

heat capacity (C_p) ($J g^{-1}$): value of excess heat capacity at the transition maximum, which is the areas within the corresponding peaks during scanning.

pre-transition (T_p) ($^{\circ}C$ and/or $^{\circ}K$): temperature value of pre-transition of lipids from gel to ripple phase

main transition (T_m) ($^{\circ}C$ and/or $^{\circ}K$): temperature value of main transition of lipids from gel to liquid phase

the half width of phase transition ($\Delta T_{1/2}$): the full width at half-maximum of DSC peak

calorimetric enthalpy (ΔH_{cal}) (Joule): the energy of transition of lipids, calculated from the area of the transition curve

the van't Hoff enthalpy (ΔH_{vH}): the amount of heat required for each cooperative unit to undergo the phase transition, calculated using following equation;

$$\Delta H_{vH} = 6.9 T_m^2 / \Delta T_{1/2}$$

cooperativity unit (CU): a measure of mean number of lipids undergoing transition, calculated using the following approach

$$CU = \Delta H_{v_H} / \Delta H_{cal}$$

entropy (ΔS): disorderness parameter of the transition

$$\Delta S = \Delta H_{cal} / T_m$$

Comparison of thermotropic values reveals the effect of a structural modification of lipids on the thermodynamics of the phase transition. However, it should be noted that the analysis of such parameters is easily obtained from the symmetrical DSC peaks utilized by software program. But, most of the time lipid bilayer phase transitions can contain more than two states [18-19]. This leads to asymmetric shape of DSC curve. Such peak shape reflects a non-two-state transition. In such cases, the adequate baseline fitting is required [20-21].

Limitations of DSC

Even though DSC is a valuable analytical tool with high sensitivity [11], it has some drawbacks. For instance, the baseline subtraction may lead to inconsistency in raw data; thus, variations in data analysis may be observed. Moreover, DSC has concentration limits at low level which might create difficulty in order for achievement at bulk manufacturing scale. And, the method works the most efficiently for purified samples. Impurities in samples may cause a shift in T_m values or may result in new thermal transitions. In any case, this may lead to difficulties in the interpretation of the results [23]. Furthermore, since some thermograms is composed of complex transition curves resulted from overlapping weak peaks, it is difficult to identify each individual peak contributing to whole transition [24]. To resolve such overlapping weak curves, the resolution may be enhanced by lowering the scan rate and sample capacity. Conversely, the identification of a weak transition needs higher sensitivity, which can may be achieved by rising the heating rate [8,25].

Lipids & Model Membranes

Plasma/biological/cell membranes have very complex and dynamic structures since they are mainly composed of a variety of lipid types in which different kinds of proteins are embedded. Because of such complexity systematic studies on cell membranes are impractical [26-28]. To overcome this, a variety of simplified model systems have been developed to offer an alternative easily accessible platform [29-32]. Moreover, such models serve to examine the alterations in the properties of lipids and environmental factors such as acidity and salt on the structure and function

natural membranes [31-32]. In order to reflect the lipid diversity in natural membranes, lipids isolated from biological sources with different chemical structures are used to create model membranes. Such lipid features can be listed as follows; quantity of lipids, saturation levels, length of the lipid hydrocarbon tail, polar head charge. While preparing model membrane type all these properties must be taken into consideration to represent as much as possible real membrane systems [30]. For example, eukaryotic cell membranes are mostly simplified by zwitterionic phospholipids such as phosphatidylcholines (PCs). The main used PCs are dioleoylphosphatidylcholine (DOPC), dipalmitoylphosphatidylcholine (DPPC) and dimiristoylphosphatidylcholine (DMPC). In addition, sphingomyelin (SM) and cholesterol (CHO) are also used. On the other hand, by using charged phospholipids it is possible to mimic prokaryotic cell membranes [33]. For this purpose, PGs are generally used. These PGs are namely dipalmitoylphosphatidylglycerol (DPPG) and dioleoylphosphatidylglycerol (DOPG). Other charged lipids like palmitoyl-oleoyl-phosphatidylethanolamine (POPE) and tetraoleoyl-cardiolipin (TOCL) are also used. In addition, charged lipids, CHO and phosphatidylethanolamin (PE) are also mixed to simulate the bacterial membranes [34].

The widely utilized model membranes involves lipid vesicles (liposomes), Langmuir monolayers, black lipid membranes (BLM), and micelles [30, 35]. Figure 3 represents schematic of some model membranes types.

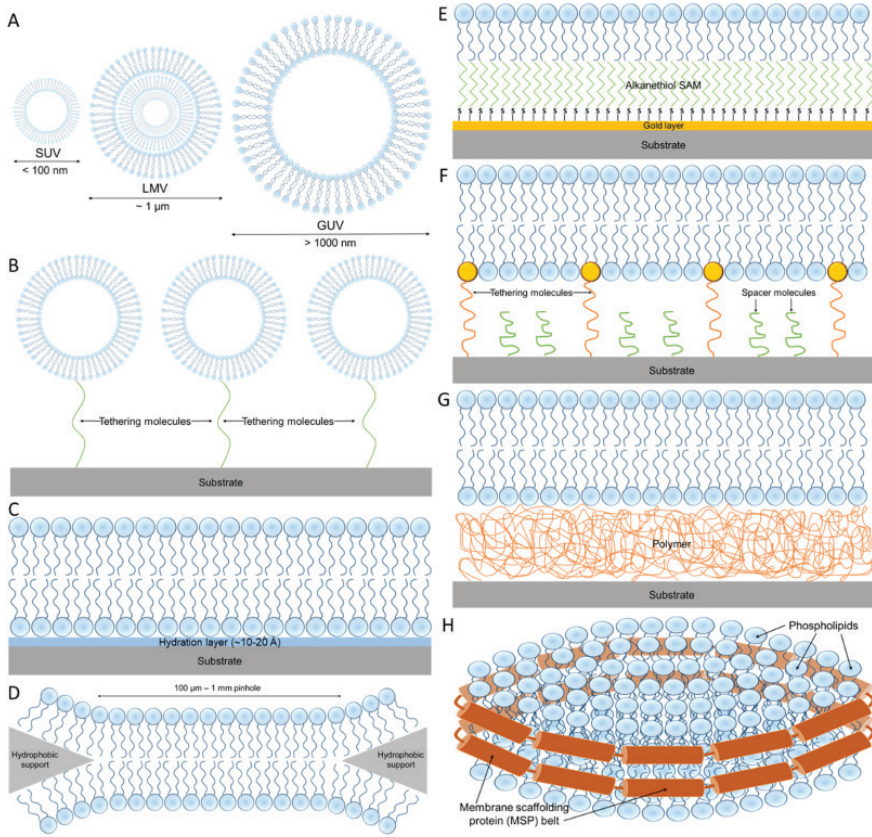


Figure 3. The most common used model membranes (cross-section) [36].

Liposomes are the simplest models of biological membranes. The size of liposomes can be from $0.025\ \mu\text{m}$ to large $2.5\ \mu\text{m}$ diameter. They can be composed of one or several bilayers. Depending on the size and bilayer number, these are divided as multilamellar vesicles (MLVs) and unilamellar vesicles. Unilamellar vesicles can also be classified into categories: large unilamellar vesicles (LUVs), small unilamellar vesicles (SUVs) and giant unilamellar vesicles (GUVs) [37-38]. In liposome systems MLVs are the most used ones in model membrane research. Because they are easy to make with reproducible features. They can be made in large amounts with high concentration. They consist of many bilayers in a single particle which have large dimensions compared with the other ones. In MLVs, vesicles are like an onion structure [37-39]. To prepare such models, lipids are dissolved in an organic solvent, and then dried down to a film in glass vessel. Later, the film is hydrated by addition of buffer (PBS, phosphate) and vortexed to produce milk suspension of

liposomes. On the contrary, they have some drawbacks such as limited aqueous space for trapping materials, inhomogeneity in size and number of layers and incapability to access both sides of vesicles [40]. MLVs are composed of bilayers departed by aqueous solution in between. Their diameter scale covers a few hundred to thousands of nanometers.

When MLVs are processed further, for instance when they are sonicated or extruded to create liposomes with a single bilayer [41]. In unilamellar vesicles, the vesicle has a single bilayer. These unilamellar vesicles can be further classified into SUVs, LUVs and GUVs based on their size [41-42]. SUVs (20-50 nm in diameter) are made by subjecting liposomes to ultrasonic irradiation, and finally have a diameter inferior to 100 nm. They are homogenous with respect to size and surface of bilayer contains about 60-75 % of total lipids. One limitation of SUVs that they are very small in size with a small radius, which in turn results in limited internal aqueous space. On the other hand, for the preparation of LUVs phospholipids are dissolved in a detergent. The solution is subjected to dialysis to remove detergent. Later, freezing-thawing procedures are applied and extruded. And, LUVs are formed with a diameter superior to 100 nm [43]. They have an advantage that they are large enough to trap molecules. But, as having drawback, they have residual organic solvents. GUVs (10-100 μm in diameter) are the closest to the size of actual cells, and they are usually formed by using well-defined mixtures of lipids. However, it is indefinite how the behaviour of such models compares to biological membranes [40,43].

Langmuir monolayers, lipids exhibit different surface activity. By applying lateral pressure lipid hydrophobic chains are situated perpendicular to air-water interface. The head groups are place in solution. In this model, since amount of lipid applied to the surface is known, the total area of formed monolayer and the area of each lipid can be measured. Thus, they are model of half a membrane. For this reason, they are excellent to investigate interactions of foreign molecules with lipids in two-dimensional arrangements [40,45-46]. The main limitation of such systems is that they are monolayer not bilayer and they have obstacles in determining what lateral surface pressure correspond to biological membrane [39,40,46].

Black lipid membranes are unique system that offer opportunity to evaluate electrical conductivity parameter of lipids. A single bilayer membrane is formed in a solvent across a Teflon cup place in solution. Electrodes are placed inside and outside the cup for electrical measure-

ment. Thus, such systems offer to measure the electrical properties of membranes [40,47].

In micelles lipids contain only one hydrocarbon chain instead of two. Sizes of micelles can be varied from 2 nm to 20 nm based upon composition and concentration of lipids. The size of a micelle is smaller than that of a lipid bilayer. Lipids are arranged either with the polar heads out or with the polar head in. They are only formed when the concentration of surfactant is larger than the critical micelle concentration (CMC). In other words, CMC is the concentration above surfactant when micelles will form spontaneously. The higher CMC, the more micelles are formed. Furthermore, micelle formation is based on the Kraft temperature, which is when surfactants will be created as micelles. If the environment temperature is below the Kraft value, there will be no spontaneous micelles formation. Micelles have been taken a significant role in drug delivery and drug stabilizing research [48-50]. They are very suitable with small entities (sub-50 nm) to solubilize hydrophobic foreign molecules such as drugs and pharmacological substances that are not well dissolved in water [51]. However, there is a challenge with these models is that all conventional micelles [50-51] can disassemble into free surfactants. The foreign molecule entrapped in the hydrophobic part of a micelle may become insoluble because of the loss of micelle structures.

Selected Reports about Application of DSC on Model Membrane Research

This section provides some reports in which DSC method has been employed to investigate phase/state thermodynamic transitions including thermotropic parameters of lipids representing real membrane systems in the presence of a great variety of molecules. DSC is a very useful to study the thermotropic features of lipid membranes [1-2,7,52]. By monitoring the alterations in such properties of lipids DSC technique has been used to examine specific interactions between foreign molecules and lipids over both model and/or biological membranes.

Drug-lipid interactions

Drugs inevitably interact with membrane lipids in biological systems to reach their target location, and thus to elicit their mechanisms [47]. Therefore, the investigation of drug-lipid interaction works have great importance in order to obtain information about their pharmacological and pharmaco-kinetical properties. Related with this, numerous works concer-

ning this issue have been published during a long time. Upon drug-lipid interaction the alterations in response of lipid bilayer to heat energy corresponding to thermotropic features have been examined by DSC method [7-8,53-54]. The use of DSC on such purpose is concentrated on interactions of the drugs (pharmacological substances) with membrane lipids to assess their contact with model/real membranes and to get an idea about their potential toxicity [47]. The drugs bind to specific regions of lipids (head groups, hydrophobic chains, and/or both head groups and hydrophobic chains) [7,16].

Related with the investigation of drug-lipid interactions DSC method have been widely used technique. For instance, Türker-Kaya et al. (2021) [55] utilized DSC to study the interaction profile of carboplatin (CAR), a chemotherapeutic agent, with SM lipids by monitoring the changes in T_m , ΔH and CU values as a function of drug concentration. The findings revealed a decrease in these parameters with increasing concentration of CAR. By using DSC, the same group also investigated the interaction of different drugs such as gabapentin, levetiracetam [56], lacosamide [57] and armodafinil [58] with DPPC and cholesterol containing MLVs. Same approach was also done by Aleskndranyl and Sahin (2020) [59] to investigate the effects of levothyroxine, which is a synthetic thyroid hormone, on the structure and dynamics of DPPC liposomes. The other group, Issé et al. (2013) applied DSC with mixed monomolecular layers and fluorescence spectroscopy techniques to explore the alterations in the biophysical properties of model membranes by thyroid hormones, and they observed that these hormones actively contact with lipids in a spontaneous way [60]. In another study, the impact of bisoprolol or enalapril as antihypertensive drugs on the structural properties of model lipid membranes formed by DSPC. Based on the results, the authors proposed that enalapril or bisoprolol can actively interact with DSPC lipids and induce changes in their physical-chemical properties. Likewise, it was reported that the anti-inflammatory medicine ibuprofen causes to change thermotropic phase behaviour of DMPC bilayer in a concentration dependent manner [61]. DSC technique was also performed by Pérez-Isidoro and Costas (2020) to examine the effects of seven neuroleptics on biomembrane models composed of DPPC, SM and cholesterol at different pH values under changing drug concentration. Upon DSC measurements such monitoring gel to crystalline phase transition, the authors concluded that fluidization and disordering effect of neuroleptics under investigation is directly related with insertion of the drug through the lipid bilayer under the influence of the size and geometry of the drugs. For instance, protonated forms of the

drug have stronger effects on these parameters than that of non-protonated ones [62]. Furthermore, Le-Deygen et al. (2020) intended to clarify corporation of moxifloxacin (Mox), an antibacterial drug, with a model of cell membrane also contained charged form of lipids. They found that MLVs of DPPC/ CL^{2-} represent two microphases, and Mox contacts with both microphases, which in turn reveal different structure and T_m . This interaction resulted in more stabilize gel-state of the bilayer with rising T_m value up to 3–5 °C. On the other hand, in case of neutral DPPC MLVs, Mox led to some deficiency in formation and a fluidization effect by means of lowering T_m value by 2–4 °C [63]. In another study, with the aim of developing proliposomal formulations to increase bioavailability of simvastatin (SV), DSC was one of complementary method [64]. Within the scope of the work, the proliposomes were examined for entrapment efficacy, drug-polymer compatibility. Based on DSC data there was no drug-liposome interaction, which revealed SV was successfully entrapped in the proliposomes. With the similar purpose, Affram and co-workers (2020) published a report related with a chemotherapeutic agent named gemcitabine (GEM). They used DSC method to obtain thermodynamic information about GEM-loaded solid lipid nanoparticle. The DSC thermogram of loaded lipid nanoparticles showed a broad main transition observed at about 59.65 °C, which could be corresponded to the wide surface area of the dispersed nano-size particles [65]. In addition, this method was also utilized to obtain information about transdermal permeation profile of flurbiprofen enantiomers. And, the findings suggested that the rate of the permeation and retention of (S)-flurbiprofen was 1.5 times more than that of (R)-flurbiprofen [66]. In addition, DSC technique was also applied by Montenegro et al. (2018) to characterize comparatively idebenone (IDE)-loaded solid lipid nanoparticle (SLN) interactions with both MLVs and bio-membranes. DSC analyses examined the changes in both ΔH and T_m values over time. And, obtained differences in ΔH and T_m parameters revealed that SLN has ability to locate IDE in the epidermis and in the stratum corneum, respectively [67].

In the literature, most of the studies dealing with drug-lipid interactions have been performed under equilibrium conditions, however there are also some works implementing kinetic experiments on drug distribution in lipid membranes [68-69]. In such works, real time measurements are possible. Similarly, Kasian and co-workers (2019) utilized both equilibrium and kinetic experiments for dimethyl sulfoxide (DMSO) and tilorone, an antiviral and immunomodulatory substance, respectively. By analysing kinetics of DSC profiles, it was feasible to discriminate the processes such

as drug absorption into membranes and drug diffusion through stacks of lipid bilayers. Data showed that 0.1 mol% DMSO effectively improved tilorone penetration into DPPC membrane [70].

Lipid-protein interaction

Banigan and colleagues (2018) systematically determined how structure of lipids can affect protein/bilayer interactions by means of membrane drug transporter EmrE as the model system in the presence of proton or drug substrates. The authors used varied kinds of lipids such as ditridecanoylphosphocholine, diTetradecylphosphocholine, palmitoyloleoylphosphoethanolamine, palmitoyloleoylglycerophospho(1'-rac-glycerol), DMPC and DPPC. Calorimetric measurements exhibited a variation in CU of lipid main transition for drug-free EmrE protonated at glutamic acid 14 (proton-loaded form) and the tetraphenylphosphonium (TPP+) bound form of the protein (i.e., drug-loaded form). According to the results, it was obtained that the binding of TPP+ to EmrE enhanced CU of gel to liquid crystalline phase transition as a function of a chain length of lipids [71]. Furthermore, the molecular association of food derived angiotensin converting enzyme inhibitory tri-peptides, namely ADF, FGR, and MIR, with DPPC containing model membranes at molecular level was investigated by Ji et al. (2022) [72]. DSC method was used to determine the effects of tri-peptides on Tm of DPPC lipids. The DSC findings represented that tri-peptides changed the physical properties of DPPC membrane by diminishing T_p value and decreasing T_m parameter about 3–5 °C of DPPC bilayer. In addition, the DSC results also indicated tri-peptides interacted with the head groups and penetrated into hydrophobic regions of membrane.

Parkinson's disease is defined by the formation Lewy bodies consisted of alpha-synuclein. It has been shown that alpha-synuclein has ability to co-assemble with lipids [73] (Figure 4). Similarly, related with such issue Galvagnion et al. (2019) performed DSC together with other analytical techniques to determine how alpha-synuclein is formed in the presence of lipids like dimyristoylglycerophosphotidylserine and dilauroylglycerophosphotidylserine. According to the data, these lipids lipids have potential to co-assemble with alpha-synuclein molecules, which leads to a decrement in both T_m and enthalpy parameters of main transition of the lipids compared to those in the absence of protein [74].

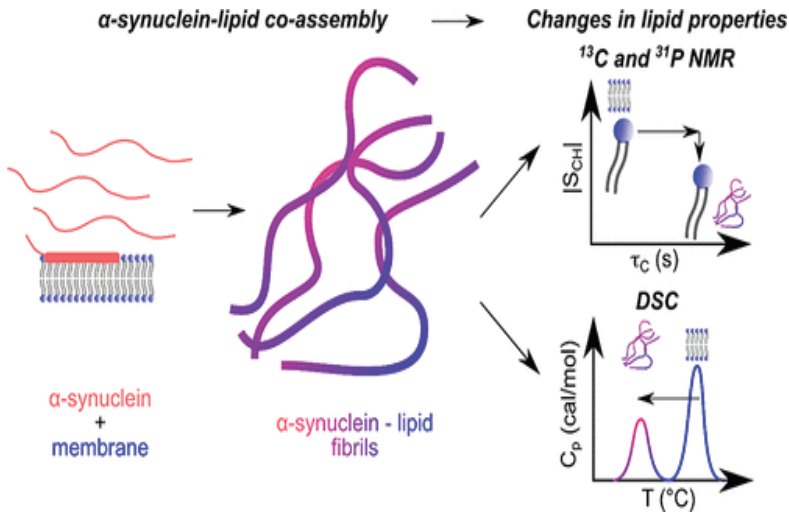


Figure 4. Demonstration of association of alpha-synuclein with model lipid membranes and the application of DSC study [74].

In another study, the absorption profiles of two different Micro Exon Gene (MEG) proteins (MEG-24 and MEG-27) from *Schistosoma mansoni* worms onto LUV of DMPC and erythrocyte ghost membranes were examined. With the use of DSC, it was obtained that these proteins led to alterations in T_m and ΔH values of erythrocyte ghost membrane with varied concentration. In addition, MEG-27 disrupts both the pre and main phase transition profile more effectively than MEG-24. Moreover, transition peak (at 24.0°C) of pure DMPC LUV became wider with the addition of 2 mol% MEG-27, whilst MEG-24 at the same concentration has less effect on such curve [75]. Moreover, under the investigation of protein-lipid interactions, Pérez-Isidoro and Ruiz-Suárez (2020) also performed a thermal study to explore membrane effects in a lipid-protein model made up of DMPC and albumin from chicken egg white (OVA) in the presence of varied neurotransmitters and anesthetics. Upon DSC studies, by monitoring thermotropic parameters, it was observed that ovalbumin, ovotransferrin, and lysozyme interact with DMPC model membrane, which gave rise to a lipid separation and an ordered lipid-protein formation. Such assembly were also induced in the addition of acetylcholine, γ -aminobutyric acid, tetracaine, and pentobarbital [76]. Furthermore, the corporation of Ageritin, a specific ribonuclease that irreversibly block protein synthesis. with some model systems of eukaryotic, cancer and bacterial cell membranes were determined by means of DSC. To mimic these membrane types, different combination of DPPC/CHO, DPPC/DPPE/CHO, DPPC/DPPG

lipids were used. The changes with the effect of Ageritin in ΔH , T_m and $\Delta T_{1/2}$ parameters revealed that the protein potentially perturbs each model membrane system [77].

Plant sourced-lipid interactions

Baicalein is a flavonoid in the roots of *Scutellaria baicalensis*. The association of baicalein and DPPC liposomes was evaluated by DSC together with some other techniques. The findings revealed that when the molar percentage of baicalein is under 5%, it initiates the hydration level of lipid head groups. At this concentration DPPC MLVs undergo $L_{\beta'}$ to L_{β} phase transition. Higher concentration (over 10 mol%) of baicalein caused to change the hydrogen bonding capacity of head groups [78]. In addition, Eliasson (1994) reported the thermal transition of the amylose—lipid complex is highly under the influence of number of C atoms in hydrocarbon chain, the head groups, water content and starch type [79]. Moreover, the formation of amylose/starch inclusion with lipid complex were also studied by different investigators [80-81]. In addition, specific interaction of (-)-Epigallocatechin-3-gallate (EGCG), a flavonoid, with DPPC formed membranes was published. In detail, according to the results, EGCG give rise to an increment in order parameter. Also, incorporation of EGCG does not have any effect on the zeta-potential and shape of the liposomes, but it may stimulate aggregation of lipids [82].

Conclusion

This short review addresses the use of DSC on model membrane research. It aims to present a general information about this method. The first part of the text introduces its principles with instrumentation, calorimetric measurement and analysis. In addition, this section describes the potentialities, advantages and limitations of DSC. The second section explain some model membrane systems widely used in such area with specific lipid molecules. The last part of the document gives some selected reports in the literature representing application of DSC to investigate drug-lipid, protein-lipid and plant sourced substances-lipid interactions on model membrane platform. In sum, it is anticipated that this can provide perspective and guidance regarding the choice of model cell membrane and DSC technique when performing new experiments.

REFERENCES

- [1] Gill, P., Moghadam, T.T., & Ranjbar, B. (2010). Differential scanning calorimetry techniques: applications in biology and nanoscience. *Journal of Biomolecular Technology*, 21(4), 167–193.
- [2] Melton, L. D., Fereidoon Shahidi, & Varelis, P. (2019). *Encyclopedia of food chemistry*. Amsterdam; Kidlington, Oxford; Cambridge Ma: Elsevier.
- [3] Ji, H., Zhao, W., & Yu, Z. (2022). Interaction mechanism of three egg protein derived ACE inhibitory tri-peptides and DPPC membrane using FS, FTIR, and DSC studies. *Food Chemistry: X*, 15, 100366.
- [4] Knopp, M. M., Löbmann, K., Elder, D. P., Rades, T., & Holm, R. (2016). Recent advances and potential applications of modulated differential scanning calorimetry (mDSC) in drug development. *European Journal of Pharmaceutical Sciences*, 87, 164–173.
- [5] Leyva-Porras, C., Cruz-Alcantar, P., Espinosa-Solís, V., Martínez-Guerra, E., Piñón-Balderrama, C. I., Compean Martínez, I., & Saavedra-Leos, M. Z. (2020). Application of Differential Scanning Calorimetry (DSC) and Modulated Differential Scanning Calorimetry (MDSC) in Food and Drug Industries. *Polymers*, 12(1), 5.
- [6] Hatta, I., Ichikawa, H., & Todoki, M. (1995). Application of dynamic differential scanning calorimetry to study of phase transitions. *Thermochimica Acta*, 267, 83–94.
- [7] Turker, S., Wassall, S., Stillwell, W., & Severcan, F. (2011). Convulsant agent pentylenetetrazol does not alter the structural and dynamical properties of dipalmitoylphosphatidylcholine model membranes. *Journal of Pharmaceutical and Biomedical Analysis*, 54(2), 379–386.
- [8] Durowoju, I. B., Bhandal, K. S., Hu, J., Carpick, B., & Kirkitadze, M. (2017). Differential Scanning Calorimetry — A Method for Assessing the Thermal Stability and Conformation of Protein Antigen. *Journal of Visualized Experiments : JoVE*, (121).
- [9] Redfern, J. P. (1983). Applications of thermal analysis. *Journal of Thermal Analysis*, 27(2), 427–438.
- [10] Danley, R. L. (2002). New heat flux DSC measurement technique. *Thermochimica Acta*, 395(1-2), 201–208.
- [11] Prenner, E., & Chiu, M. (2011). Differential scanning calorimetry: An invaluable tool for a detailed thermodynamic characterization of macromolecules and their interactions. *Journal of Pharmacy and Bioallied Sciences*, 3(1), 39.
- [12] Langier-Kuźniarowa, A. (1984). Standardization in thermal analysis. *Journal of Thermal Analysis*, 29(5), 913–918.

- [13] Ales Igljic, Rappolt, M., & Patricia Losada Perez. (2022). *Advances in Biomembranes and Lipid Self-Assembly*. Academic Press.
- [14] McElhaney, R. N. (1982). The use of differential scanning calorimetry and differential thermal analysis in studies of model and biological membranes. *Chemistry and Physics of Lipids*, 30(2-3), 229–259.
- [15] Tsogas, I., Tsiourvas, D., Paleos, C. M., Giatrellis, S., & Nounesis, G. (2005). Interaction of l-arginine with dihexadecylphosphate unilamellar liposomes: the effect of the lipid phase organization. *Chemistry and Physics of Lipids*, 134(1), 59–68.
- [16] M. Reza Mozafari. (2006). *Nanocarrier Technologies*. Springer Science & Business Media. pp. 207–220.
- [17] Rolland, A., Brzokewicz, A., Shroot, B., & Jamouille, J.-C. (1991). Effect of penetration enhancers on the phase transition of multilamellar liposomes of dipalmitoylphosphatidylcholine. A study by differential scanning calorimetry. *International Journal of Pharmaceutics*, 76(3), 217–224.
- [18] Gabbott, P. (2008). *Principles and Applications of Thermal Analysis*. John Wiley & Sons.
- [19] Günther Höhne, Hemminger, W. F., & H.-J. Flammersheim. (2013). *Differential Scanning Calorimetry*. Springer Science & Business Media.
- [20] Raleigh, D. P. (1996). Protein Stability and Folding: Theory and Practice. Bret A. Shirley. *The Quarterly Review of Biology*, 71(4), 564–564.
- [21] Saboury, A., & Moosavi-Movahedi, A. (1994). Clarification of calorimetric and van 't hoff enthalpies for evaluation of protein transition states. *Biochemical Education*, 22(4), 210–211.
- [22] Prenner, E., & Chiu, M. (2011). Differential scanning calorimetry: An invaluable tool for a detailed thermodynamic characterization of macromolecules and their interactions. *Journal of Pharmacy and Bioallied Sciences*, 3(1), 39.
- [23] Freire, E., Schön, A., Hutchins, B. M., & Brown, R. K. (2013). Chemical denaturation as a tool in the formulation optimization of biologics. *Drug Discovery Today*, 18(19-20), 1007–1013.
- [24] Reading, M., Luget, A., & Wilson, R. (1994). Modulated differential scanning calorimetry. *Thermochimica Acta*, 238, 295–307.
- [25] Verdonck, E., Schaap, K., & Thomas, L. C. (1999). A discussion of the principles and applications of Modulated Temperature DSC (MTDSC). *International Journal of Pharmaceutics*, 192(1), 3–20.
- [26] Mezzenga, R., Seddon, J. M., Drummond, C. J., Boyd, B. J., Schröder-Turk, G. E., & Sagalowicz, L. (2019). Nature-Inspired Design and Application of Lipidic Lyotropic Liquid Crystals. *Advanced Materials*, 31(35), 1900818.

- [27] Fenz, S. F., & Sengupta, K. (2012). Giant vesicles as cell models. *Integrative Biology*, 4(9), 982.
- [28] David, R. (2013). Getting into the membrane. *Nature Reviews Molecular Cell Biology*, 14(10), 612–612.
- [29] Yuan, W., Piao, J., & Dong, Y. (2021). Advancements in the preparation methods of artificial cell membranes with lipids. *Materials Chemistry Frontiers*, 5(14), 5233–5246.
- [30] Munusamy, S., Conde, R., Bertrand, B., & Munoz-Garay, C. (2020). Biophysical approaches for exploring lipopeptide-lipid interactions. *Biochimie*, 170, 173–202.
- [31] Jackman, J. A., & Cho, N.-J. (2012). Model Membrane Platforms for Biomedicine: Case Study on Antiviral Drug Development. *Biointerphases*, 7(1), 18.
- [32] George, A. (2011). *Advances in Biomimetics*. BoD – Books on Demand.
- [33] Selvaraj, S., Krishnaswamy, S., Devashya, V., Sethuraman, S., & Krishnan, U. M. (2015). Influence of membrane lipid composition on flavonoid–membrane interactions: Implications on their biological activity. *Progress in Lipid Research*, 58, 1–13.
- [34] Marx, L., Semeraro, E., Lohner, K., & Pabst, G. (2019). Structural Properties of Inner and Outer Membrane Mimics of Gram-Negative Bacteria. *Biophysical Journal*, 116(3), 87a.
- [35] Peetla, C., Stine, A., & Labhasetwar, V. (2009). Biophysical Interactions with Model Lipid Membranes: Applications in Drug Discovery and Drug Delivery. *Molecular Pharmaceutics*, 6(5), 1264–1276.
- [36] Bunea, A.-I., Harloff-Helleberg, S., Taboryski, R., & Nielsen, H. M. (2020). Membrane interactions in drug delivery: Model cell membranes and orthogonal techniques. *Advances in Colloid and Interface Science*, 281, 102177.
- [37] Sharma, A., & Sharma, U. S. (1997). Liposomes in drug delivery: Progress and limitations. *International Journal of Pharmaceutics*, 154(2), 123–140.
- [38] Akbarzadeh, A., Rezaei-Sadabady, R., Davaran, S., Joo, S. W., Zarghami, N., Hanifehpour, Y., & Nejati-Koshki, K. (2013). Liposome: classification, preparation, and applications. *Nanoscale Research Letters*, 8(1), 102–110.
- [39] Harashima, H., & Ishida, T. (2020). Editorial: Advanced Liposome Research. *Advanced Drug Delivery Reviews*, 154–155, 1.
- [40] Yeagle, P. (2012). *The structure of biological membranes*. Boca Raton: Crc Press.
- [41] Schroeder, A., Kost, J., & Barenholz, Y. (2009). Ultrasound, liposomes, and drug delivery: principles for using ultrasound to control the release of drugs from liposomes. *Chemistry and Physics of Lipids*, 162(1-2), 1–16.

- [42] Zhang, L., Pornpattananankul, D., Hu, C.-M., & Huang, C.-M. (2010). Development of Nanoparticles for Antimicrobial Drug Delivery. *Current Medicinal Chemistry*, 17(6), 585–594.
- [43] Plemper van Balen, G., Martinet, C. a M., Caron, G., Bouchard, G., Reist, M., Carrupt, P.-A., ... Testa, B. (2004). Liposome/Water Lipophilicity: Methods, Information Content, and Pharmaceutical Applications. *Chem-Inform*, 35(28).
- [44] Svetina, S., & Zek, B. (2002). Shape behavior of lipid vesicles as the basis of some cellular processes. *The Anatomical Record*, 268(3), 215–225.
- [45] Suresh, K. A., & Bhattacharyya, A. (1999). Phase transitions in Langmuir monolayers. *Pramana*, 53(1), 93–106.
- [46] Brezesinski, G., & Möhwald, H. (2003). Langmuir monolayers to study interactions at model membrane surfaces. *Advances in Colloid and Interface Science*, 100-102, 563–584.
- [47] Mouritsen, O. G. (2011). *Model Answers to Lipid Membrane Questions*. Cold Spring Harbor Perspectives in Biology, 3(9), a004622–a004622.
- [48] Lu, Y., Yue, Z., Xie, J., Wang, W., Zhu, H., Zhang, E., & Cao, Z. (2018). Micelles with ultralow critical micelle concentration as carriers for drug delivery. *Nature Biomedical Engineering*, 2(5), 318–325.
- [49] Ahmad, Z., Shah, A., Siddiq, M., & Kraatz, H.-B. (2014). Polymeric micelles as drug delivery vehicles. *RSC Adv.*, 4(33), 17028–17038.
- [50] Kim, S., Shi, Y., Kim, J. Y., Park, K., & Cheng, J.-X. (2009). Overcoming the barriers in micellar drug delivery: loading efficiency, in vivo stability, and micelle–cell interaction. *Expert Opinion on Drug Delivery*, 7(1), 49–62.
- [51] Yoo, J.-W., Irvine, D. J., Discher, D. E., & Mitragotri, S. (2011). Bio-inspired, bioengineered and biomimetic drug delivery carriers. *Nature Reviews Drug Discovery*, 10(7), 521–535.
- [52] Aleš Iglič, Chandrashekhar Kulkarni, & Rappolt, M. (2016). *Advances in biomembranes and lipid self-assembly*. Volume 23. Amsterdam Etc.: Elsevier.
- [53] Lucio, M., Lima, J. L. F. C., & Reis, S. (2010). Drug-Membrane Interactions: Significance for Medicinal Chemistry. *Current Medicinal Chemistry*, 17(17), 1795–1809.
- [54] Kasian, N. A., Vashchenko, O. V., Budianska, L. V., Brodskii, R. Ye., & Lisetski, L. N. (2019). Thermodynamics and kinetics of joint action of antiviral agent tilorone and DMSO on model lipid membranes. *Biochimica et Biophysica Acta (BBA) - Biomembranes*, 1861(1), 123–129.
- [55] Türker-Kaya, S., & Kına, A. (2021). Calorimetric and spectroscopic investigation of the interaction of chemotherapeutic agent carboplatin with sphingomyelin lipids. *Journal of Thermal Analysis and Calorimetry*, 146, 2515 - 2522.

- [56] Türker-Kaya, S., Kına, A., & Alın, S. (2017). Divergent interaction profiles of gabapentin and levetiracetam with dipalmitoylphosphatidylcholine lipids. *International Journal of Epilepsy*, 04(02), 150–158.
- [57] Yağış, B., & Türker Kaya, S. (2018). Binding Ability of Lacosamide to Phosphatidylcholine Lipids and Cholesterol Effects. *Medeniyet Medical Journal*, 33(3), 218-226.
- [58] Kırkoçoğlu, H., & Türker Kaya, S. (2019). The investigation of the interaction of Armodafinil with membrane lipids by using DPPC model membrane system. *Turkish Bulletin of Hygiene and Experimental Biology*, 76(1), 41–52.
- [59] Aleskndrany, A., & Sahin, I. (2020). The effects of Levothyroxine on the structure and dynamics of DPPC liposome: FTIR and DSC studies. *Biochimica et Biophysica Acta (BBA) - Biomembranes*, 1862(6), 183245.
- [60] Issé, B. A., Yunes Quartino, P., Fidelio, G. D., & Farias, R. N. (2013). Thyroid hormones-membrane interaction: Reversible association of hormones with organized phospholipids with changes in fluidity and dipole potential. *Chemistry and Physics of Lipids*, 175-176, 131–137.
- [61] Sreij, R., Prévost, S., Dargel, C., Dattani, R., Hertle, Y., Wrede, O., & Hellweg, T. (2018). Interaction of the Saponin Aescin with Ibuprofen in DMPC Model Membranes. *Molecular Pharmaceutics*, 15(10), 4446–4461.
- [62] Pérez-Isidoro, R., & Costas, M. (2020). The effect of neuroleptic drugs on DPPC/sphingomyelin/cholesterol membranes. *Chemistry and Physics of Lipids*, 229, 104913.
- [63] Le-Deygen, I. M., Skuredina, A. A., Safronova, A. S., Yakimov, I. D., Kolmogorov, I. M., Deygen, D. M., ... Kudryashova, E. V. (2020). Moxifloxacin interacts with lipid bilayer, causing dramatic changes in its structure and phase transitions. *Chemistry and Physics of Lipids*, 228, 104891.
- [64] Rahamathulla, M., H.V, G., Veerapu, G., Hani, U., Alhamhoom, Y., Alqahatani, A., & Moin, A. (2020). Characterization, Optimization, In Vitro and In Vivo Evaluation of Simvastatin Proliposomes, as a Drug Delivery. *AAPS PharmSciTech*, 21(4), 129.
- [65] Affram, K. O., Smith, T., Ofori, E., Krishnan, S., Underwood, P., Trevino, J. G., & Agyare, E. (2020). Cytotoxic effects of gemcitabine-loaded solid lipid nanoparticles in pancreatic cancer cells. *Journal of Drug Delivery Science and Technology*, 55, 101374.
- [66] Zhang, Y., Liu, C., Xu, W., Quan, P., Luo, Z., Yang, D., & Fang, L. (2021). An investigation on percutaneous permeation of flurbiprofen enantiomers: The role of molecular interaction between drug and skin components. *International Journal of Pharmaceutics*, 601, 120503.
- [67] Montenegro, L., Castelli, F., & Sarpietro, M. (2018). Differential Scanning Calorimetry Analyses of Idebenone-Loaded Solid Lipid Nanoparticles In-

- teractions with a Model of Bio-Membrane: A Comparison with In Vitro Skin Permeation Data. *Pharmaceuticals*, 11(4), 138.
- [68] Castelli, F., Caruso, S., & Uccella, N. (2003). Biomimesis of Linolenic Acid Transport through Model Lipidic Membranes by Differential Scanning Calorimetry. *Journal of Agricultural and Food Chemistry*, 51(4), 851–855.
- [69] Castelli, F., Micieli, D., Ottimo, S., Minniti, Z., Sarpietro, M. G., & Librando, V. (2008). Absorption of nitro-polycyclic aromatic hydrocarbons by biomembrane models: Effect of the medium lipophilicity. *Chemosphere*, 73(7), 1108–1114.
- [70] Kasian, N. A., Vashchenko, O. V., Budianska, L. V., Brodskii, R. Ye., & Lisetski, L. N. (2019). Thermodynamics and kinetics of joint action of antiviral agent tilorone and DMSO on model lipid membranes. *Biochimica et Biophysica Acta (BBA) - Biomembranes*, 1861(1), 123–129.
- [71] Banigan, J. R., Leninger, M., Her, A. S., & Traaseth, N. J. (2018). Assessing Interactions Between a Polytopic Membrane Protein and Lipid Bilayers Using Differential Scanning Calorimetry and Solid-State NMR. *The Journal of Physical Chemistry B*, 122(8), 2314–2322.
- [72] Ji, H., Zhao, W., & Yu, Z. (2022). Interaction mechanism of three egg protein derived ACE inhibitory tri-peptides and DPPC membrane using FS, FTIR, and DSC studies. *Food Chemistry: X*, 15, 100366.
- [73] Gilmozzi, V., Gentile, G., Castelo Rueda, M. P., Hicks, A. A., Pramstaller, P. P., Zanon, A., & Pichler, I. (2020). Interaction of Alpha-Synuclein With Lipids: Mitochondrial Cardiolipin as a Critical Player in the Pathogenesis of Parkinson's Disease. *Frontiers in Neuroscience*, 14.
- [74] Galvagnion, C., Topgaard, D., Makasewicz, K., Buell, A. K., Linse, S., Sparr, E., & Dobson, C. M. (2019). Lipid Dynamics and Phase Transition within α -Synuclein Amyloid Fibrils. *The Journal of Physical Chemistry Letters*, 10(24), 7872–7877.
- [75] Felizatti, A. P., Zeraik, A. E., Basso, L. G. M., Kumagai, P. S., Lopes, J. L. S., Wallace, B. A., & DeMarco, R. (2020). Interactions of amphipathic α -helical MEG proteins from *Schistosoma mansoni* with membranes. *Biochimica et Biophysica Acta (BBA) - Biomembranes*, 1862(3), 183173.
- [76] Pérez-Isidoro, R., & Ruiz-Suárez, J. C. (2020). Thermal behavior of a lipid-protein membrane model and the effects produced by anesthetics and neurotransmitters. *Biochimica et Biophysica Acta (BBA) - Biomembranes*, 1862(2), 183099.
- [77] Lampitella, E., Landi, N., Oliva, R., Gaglione, R., Bosso, A., De Lise, F., & Di Maro, A. (2021). Toxicity and membrane perturbation properties of the ribotoxin-like protein Ageritin. *The Journal of Biochemistry*, 170(4), 473–482.
- [78] Wei, T.-T., Cao, B.-B., Hao, X.-L., Gu, J.-Y., & Wu, R.-G. (2021). The Interaction of Baicalein with Dipalmitoylphosphatidylcholine Liposomes:

Differential Scanning Calorimetry, Synchrotron X-ray Diffraction, and Fourier Transform Infrared Studies. *Thermochimica Acta*, 703, 178993.

- [79] Eliasson, A.-C. (1994). Interactions between starch and lipids studied by DSC. *Thermochimica Acta*, 246(2), 343–356.
- [80] Lay Ma, U. V., Floros, J. D., & Ziegler, G. R. (2011). Formation of inclusion complexes of starch with fatty acid esters of bioactive compounds. *Carbohydrate Polymers*, 83(4), 1869–1878.
- [81] Kong, L., & Ziegler, G. R. (2014). Molecular encapsulation of ascorbyl palmitate in preformed V-type starch and amylose. *Carbohydrate Polymers*, 111, 256–263.
- [82] Šturm, L., Prislán, I., González-Ortega, R., Mrak, P., Snoj, T., Anderluh, G., & Poklar Ulrih, N. (2022). Interactions of (–)-epigallocatechin-3-gallate with model lipid membranes. *Biochimica et Biophysica Acta (BBA) - Biomembranes*, 1864(10), 183999.

“

Chapter 13

**USING MACHINE LEARNING
ALGORITHMS IN THE CLASSIFICATION
OF PRICES ON MOBILE PHONES**

Serpil AYDIN¹

”

¹ Asst.Prof.Dr.Serpil Aydın, Ondokuz Mayıs University, ORCID: 0000-0001-6985-6120

1. Introduction

Machine learning is a system from the past that uses algorithms to train data and make predictions without explicit coding to make predictions using certain data. The difference between machine learning and standard programming is that in programming, data and program are required for output, whereas in machine learning, data and output are required for the program. Machine learning; is defined as programming a computer to make descriptive or predictive inferences by using sample data or making use of past experiences (Alpaydın, 2004). Today, machine learning is needed to keep the increasing data volume under control. Machine learning has two main purposes. The first is to classify the data according to the trained model, and the second is to make predictions for future results based on these models.

Price is the most effective feature of marketing and sales (Asim & Khan, 2018). The first thing that the consumer pays attention to is usually the price of the products. Consumers think about whether they can buy something with the specified features or not. So, making price estimations in the background is the main purpose of the business. Cell phones are now one of the best-selling and purchased devices. New mobile phones with new versions and more features are released every day. It is therefore very important to consider many features to estimate the price. For example, the processor of the mobile phone is very important in the busy work schedule of people today. The size and thickness of the mobile phone are also important decision factors. Internal memory, camera pixels, and video quality must be considered. Internet browsing is also one of the most important constraints in this technological age in the 21st century. And the list of many features based on them also affects the price of the mobile phone. Therefore, many of the above-mentioned features must be used to classify whether the mobile phone will be very economical, economical, expensive, or very expensive.

Using machine learning techniques, mobile price prediction forms the background of interesting research due to the recent launch and availability of phones. Sakib et al. (2022) used different classification techniques to estimate the mobile phone price range. First, they made performance evaluations using a decision tree, then random forest machine learning algorithms. Pipalia and Bhadja (2020) investigated the accuracy of the algorithms in classifying the mobile phone price range by using different classification algorithms used in supervised machine learning. Pramanik et al. (2021) examined the different features of mobile phones and compa-

red various machine-learning models to categorize the price range. In the study based on performance metrics, support vector machines were the best classifier. The continuous release of new mobile phone models and features and the differences in mobile phone features used in each study makes the studies unique.

In this chapter, the classification of the price range of mobile phones according to their features was carried out using machine learning algorithms. The study aims to find the classification algorithm that makes the most successful price classification among 20 features.

2. Machine Learning

Machine learning is divided into two clients (supervised) learning and unsupervised (supervised) learning. In supervised learning, the label information is available, and trained data is used. Input and output are known in advance. These allow the computer to learn the model. According to this learning structure, the machine can perform classification by making predictions that may be opposed to new input data (Uzun, 2007). The most used supervised learning algorithms are Nearest Neighborhood (KNN), Support Vector Machines (SVM), Artificial Neural Networks, Decision Trees, linear regression and logistic regression. In the unsupervised learning method, there is no label information. It is aimed to reveal hidden relationships or groups based on the components in the data set. The most used unsupervised learning algorithms are Clustering, Association Rules, and Principal Component Analysis. Classification in machine learning is a supervised learning approach where the computer program learns from the given data input and then uses this learning to classify new observations. It is an estimator, or in other words, a predictive method (Han & Kamber, 2012). The classification algorithm is used to classify similar data in the data set into certain classes. There are different algorithms used for this. Major classification algorithms, entropy-based classification (C4.5 algorithm, C5.0 algorithm), Regression and Decision Trees (Gini algorithm, Towing algorithm), Memory Based Algorithms (k-nearest neighbor algorithm), Bayesian Classifiers, Regression Trees, Random can be listed as forest (Özkan and Erol, 2015).

Logistic Regression

Logistic regression can be used when the target variable is divided into binary, triple, or more categorical variables. In logistic regression analysis, the number of groups is known, a discrimination model is obta-

ined using the existing data, and it is possible to assign new observations added to the data set to the groups with the help of this established model (Tatlıdil, 1992).

Random Forest

The random forest algorithm is an ensemble learning method. Over-learning can occur when learning with a single tree. While trees learn the training data very well, they can give bad results in the data they see for the first time. Because trees are very sensitive to small changes in learning data. Therefore, in the random forest method, decision trees are created independently of each other and the information from the trees is combined in new ways. The random forest algorithm can be used for both classification and regression problems (Silahtaroglu, 2020).

K – Nearest Neighbor (KNN)

The K-NN algorithm is a classification method in which the class of the sample data point and the nearest neighbor are determined according to the k value (Cover and Hart, 1967). The method is the closest city, station, etc. to a determined point. Determining the k-nearest neighbor algorithm forms the basis of the algorithm (Beyer et al., 1999). The KNN algorithm is ineffective in multidimensional data sets, has high memory requirements, and is sensitive to parameters such as the number of neighbors and distance criteria (Duda et al., 2000). In this method, the user chooses the k value himself. If the value is selected high, different points can be gathered together, or if the value is selected low, the same points can fall into separate classes. When we enter new information, its distance to k is calculated and according to this distance, it is decided which cluster to include it.

Support Vector Machines

Support vector machines are a machine learning method built on strong statistical theories. It was first proposed by Vapnik in 1995 for classification and regression-type problem-solving (Vapnik, 1995). Its main purpose is to obtain the best hyperplane to separate the classes in the dataset. It is necessary to find this plane mathematically. In classical machine learning applications, the desire to have a large number of training data, low convergence rate, local minima, and overfitting/underfitting problems are encountered (Lu et al., 2002).

Naive Bayes Algorithm

The naive Bayes algorithm determines which class the samples belong to and with what probability (Rish, 2001). This method calculates the probability of a new entry entering any of the existing and classified data.

Naive Bayes is a form of Bayesian Network classifier based on Bayes's rule together with an assumption that the attributes are conditionally independent given the class.

$$P(y|x) = P(y)P(x|y)/P(x)$$

$$P(y|x) = P(y)P(x|y)/P(x) \quad (1)$$

For attribute–value data, this assumption entitles

$$the P(x|y) = \prod_{i=1}^n P(x_i|y) the P(x|y) = \prod_{i=1}^n P(x_i|y) \quad (2)$$

where x_i is the value of the i^{th} attribute in x , and n is the number of attributes.

$$P(x) = \prod_{i=1}^k P(c_i)P(x|c_i) P(x) = \prod_{i=1}^k P(c_i)P(x|c_i) \quad (3)$$

where k is the number of classes and c_i is the i^{th} class. Thus, (1) can be calculated by normalizing the numerators of the right-hand side of the equation. The resulting classifier uses a linear model, equivalent to that used by logistic regression, differing only in the manner in which the parameters are chosen. For categorical attributes, the required probabilities $P(y)$ and $P(x_i | y)$ are normally derived from frequency counts stored in arrays whose values are calculated by a single pass through the training data at training time. These arrays can be updated as new data are acquired, supporting incremental learning. For numeric attributes, either the data are discretized, or probability density estimation is employed.

Decision Tree Algorithm

The decision tree algorithm is a classification method that creates a tree-like structure consisting of decision and leaf nodes according to the target and independent variables. In this method, a tree is created for classification, then each entry in the dataset is applied to this tree and this entry is classified according to the result. There are many algorithms developed based on decision trees. These algorithms differ from each other in terms of the path they follow in the selection of root, node, and branching criteria (Brijain et al., 2014). Generally, ID.3, ID.5, C5.0, and CART algorithms are used to create a decision tree.

Gradient Descent Algorithm

The gradient descent algorithm in machine learning tries to adjust the input weights of neurons in artificial neurons and find the local minimum or global minimum to optimize a problem (Ruder, 2016). In this method, a few random points are chosen at the beginning and this is called the learning coefficient. Selecting the learning coefficient small may cause slow convergence, and choosing large may cause back-and-forth convergence problems. It takes several trials to choose a good learning coefficient. Starting from a randomly chosen value of x_0 in gradient descent, step by step, $x_{k+1} = x_k + \eta_k d_k$ is tried to converge the function $\nabla f(x_k)$ to zero. Here η_k indicates the step length and d_k indicates the descent direction.

Ensemble Learning

Ensemble learning is a method of classification. This learning algorithm is aimed to increase the performance of the model by using different classifiers together and running them simultaneously. Thanks to community learning, overfitting, and underfitting problems can be overcome, and high variance and bias problems can be reduced (Mahesh, 2020). There are different ensemble learning algorithms. Some of these are the bagging, boosting, voting, and stacking methods.

The bagging ensemble learning method, which is expressed as a bootstrap aggregating abbreviation, is based on the bootstrap sampling method. The method developed by Breiman is based on training different subsets of the training data set with bootstrap sampling (Breiman, 2001). In this method, classifiers are trained in parallel with different subsets randomly selected from the training data set. It combines the predictions of the classifiers using the majority vote technique. In this technique, majority estimation is accepted as the classification estimation of the ensemble method (Polikar, 2012).

The boosting method is a technique used to solve classification and regression problems. It combines several models whose individual performance may be considered poor, and when the individual predictions are combined, a highly accurate model is obtained. The boosting method trains weak learners in turn, with each learner trying to fix the previous one. We start by estimating the data set and each observation is given equal weight. In the next iterations, more weight is given to the observations that were predicted incorrectly in the previous observation, and learning

from the mistakes of the previous iterations is done. Thus, it aims to correctly classify those who are classified incorrectly by focusing on their education. In each iterative process, a strong classifier is obtained with the boosting method to prevent the same errors from occurring by taking into account the errors in the previous estimation (Zhou, 2012). As an iterative process, adding students is continued until a limit on the number of models or accuracy is reached. Each classifier produces predictions, and the predictions of the classifier that receives the majority vote are accepted as the ensemble estimate (Rokach, 2010).

Stacking was developed by Wolpert. To produce a higher performance estimation, the predictions of different types of classifiers are accepted as input for the meta-classifier (Wolpert, 1992). Meta classifier means the creation of a new classifier that learns from classes. Stacking the ensemble learning method consists of a two-stage learning process. In the first stage, predictions are obtained from the same training dataset with different types of classifiers. In the second stage, the predictions obtained from the first stage are processed in the meta classifier and the prediction of the ensemble learning model is obtained.

Voting is an ensemble method that creates multiple models and then combines them to generate better results. The variation in estimates is an element that improves accuracy performance in the ensemble method. For this reason, high-performance predictions can be obtained in the case of diversity in voting ensemble methods (Polikar, 2012). For the Voting method; There are two main approaches: hard voting and soft voting. Probabilistic voting; each classifier provides a probability value that a particular data point belongs to a particular target class. Estimates are weighted and aggregated by the importance of the classifier. The target tag with the most weighted probability sum wins the vote. In majority voting; each model votes for each test sample, and it is the final output estimate that gets more than half of the votes. If none of the forecasts receive more than half of the votes, it can be assumed that the ensemble approach cannot provide a stable forecast for this situation. Instead of building individual models and finding accuracy for each, a single model is built that trains on a set of multiple models and predict output based on the total voting majority for each output class. In case the performances of individual classifiers in the Voting ensemble learning method are not equal, it is more appropriate to use the weighted voting technique, which combines according to the performance weights of the classifiers.

3. Results

In this chapter, it has tried to create a model that can most accurately predict the price range of mobile phones according to their features. Machine learning algorithms were implemented using the Python programming language. The dataset used in the study consists of 2000 rows and 20 variables. The variable descriptions and basic statistics of the features in the data set are shown in Table 1.

Table 1. *Explanatory information and basic statistics of variables*

| Variables | Description | Min. | Max. | Mean | Standard Deviation |
|---------------|--|------|------|------|--------------------|
| Battery_power | Total energy a battery can store in one time measured in mAh. | 500 | 1999 | 1250 | 432 |
| Blue | Has bluetooth or not | 0 | 1 | 0,52 | 0,5 |
| clock_speed | Speed at which microprocessor executes instructions | 0,5 | 3 | 1,54 | 0,83 |
| dual_sim | Has dual sim support or not | 0 | 1 | 0,52 | 0,5 |
| fc | Front camera mega pixels | 0 | 19 | 4,59 | 4,46 |
| Four_g | Has 4G or not | 0 | 1 | 0,49 | 0,5 |
| int_memory | Internal memory in gigabytes | 2 | 64 | 33,7 | 18,1 |
| M_dep | Mobile depth in cm | 0,1 | 1 | 0,52 | 0,28 |
| Mobile_wt | Weight of mobile phone | 80 | 200 | 140 | 34,8 |
| N_cores | Number of cores of processor | 1 | 8 | 4,33 | 2,29 |
| pc | Primary camera megapixels | 0 | 20 | 10,1 | 6,09 |
| Px_height | Pixel resolution height | 0 | 1907 | 627 | 433 |
| Px_width | Pixel resolution width | 501 | 1998 | 1240 | 439 |
| ram | Random Access memory in megabytes | 263 | 3989 | 2140 | 1090 |
| Sc_h | Screen height of mobile in cm | 5 | 19 | 12 | 4,32 |
| Sc_w | Screen width of mobile in cm | 0 | 18 | 5,32 | 4,24 |
| Talk_time | Longest time that a single battery charge will last when you are | 2 | 20 | 11,1 | 5,49 |
| Three_g | Has 3G or not | 0 | 1 | 0,76 | 0,43 |
| Touch_screen | Has touch screen or not | 0 | 1 | 0,5 | 0,5 |
| Wifi | Has wifi or not | 0 | 1 | 0,51 | 0,5 |

To get the best efficiency, the data set was trained in three different categories: “70% train 30% test”, “80% train 20% test” and K-fold cross-validation. Here, it was aimed to determine which division would

yield higher yields and to compare the results with each other. The number of K subsets was set to 10 after several trials.

Mobile technology is a portable technology that moves with users. This portable technology consists of two-way communication, computing, and networking technology. While the number of mobile users in the world was approximately 3.2 billion in 2019, it will increase to approximately 3.5 billion in 2020. Mobile phones with new features and new versions are released in a short time. Many features should be considered in the price of a mobile phone, such as screen resolution, ram, camera, processor, and mobile phone thickness (Sakib et al., 2022). Therefore, it is a great advantage to know which features increase the cost in terms of decision-making. The best strategy is to find the most suitable product with minimum cost and maximum features. Thus, products can be compared in terms of their features and costs. As a result, a good product can be offered to the customer by determining the economic range (Asim and Khan, 2018). It is thought that even with little training data, gradient descent and support vector machines can classify very well and accuracy can be increased by using large data sets. The main reason for the low accuracy rate in some algorithms is the small number of samples in the data set (Pipalia and Bhadja, 2020). In the chapter, voting ensemble learning is applied and evaluated separately for each division. The results of the algorithms run with 70% train and 30% test division are shown in Figure 1.

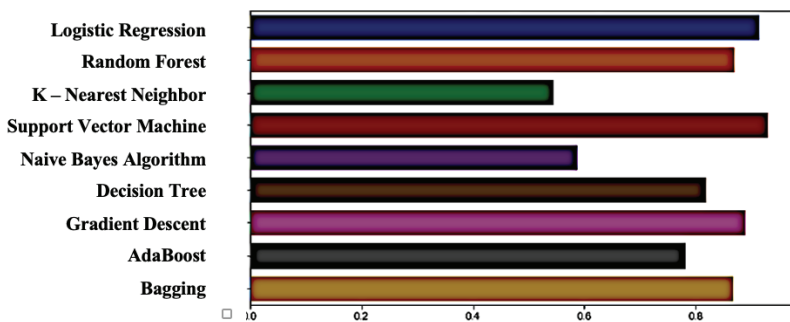


Figure 1. Analysis results (%30 splits)

Among the algorithms applied at a 30% split, the three best results were obtained from support vector machines (0.93), logistic regression (0.91), and gradient descent (0.88) algorithms. The results of the algorithms run with 80% training and 20% test division are shown in Figure 2.

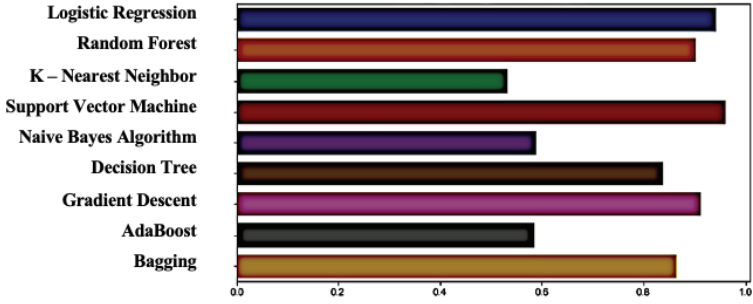


Figure 2. Analysis results (%20 splits)

Among the algorithms applied at a 20% split, the three best results were obtained from support vector machines (0.96), logistic regression (0.94), and gradient descent (0.91) algorithms. The results of the algorithms run with the K Fold test division are shown in Figure 3.

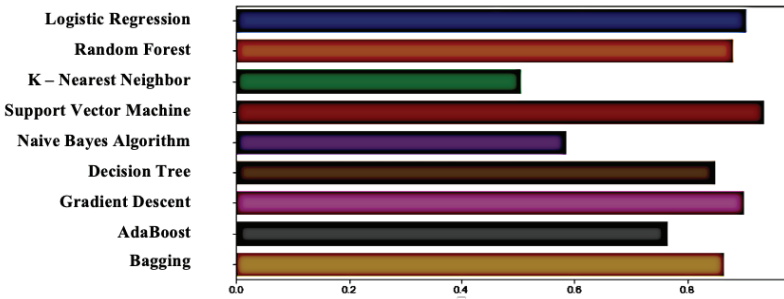


Figure 3. Analysis results (K – Fold)

Among the algorithms applied in the K Fold split, the three best results were obtained from support vector machines (0.93), logistic regression (0.90), and gradient descent (0.90) algorithms. The best model for the data set is decided by comparing the results of three different divisions. The voting ensemble learning algorithm results of each split are shown in Figure 4.

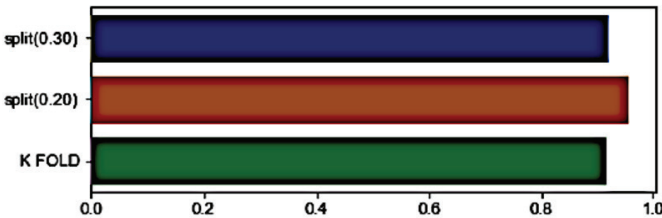


Figure 4. Split results

Accordingly, the best division is 20% and the most successful classification algorithm is support vector machines. The results of all algorithms applied to the splits are shown in Table 2.

Table 2. *General analysis results*

| | %70 Train - %30 Test | %80 Train - %20 Test | K - Fold |
|---------------------|----------------------|----------------------|----------|
| Logistic Regression | 0,91 | 0,94 | 0,91 |
| Random Forest | 0,87 | 0,90 | 0,88 |
| K - NN | 0,55 | 0,53 | 0,51 |
| SVM | 0,93 | 0,96 | 0,94 |
| Naive Bayes | 0,59 | 0,59 | 0,59 |
| Decision Tree | 0,81 | 0,84 | 0,85 |
| Gradient Descent | 0,89 | 0,91 | 0,90 |
| AdaBoost | 0,78 | 0,59 | 0,77 |
| Bagging | 0,87 | 0,87 | 0,85 |
| Voting | 0,92 | 0,95 | 0,91 |

In addition, considering that ensemble learning methods overcome the problems of overfitting or underfitting, it is possible to say that the voting method with a score of 0.9575 is a suitable model for this data set. Again, the best result was obtained from the data set, which was divided into 80% training and 20% testing.

4. Conclusions

Cost estimation is a very important factor in marketing and business. The best marketing strategy is to find the most suitable product (with minimum cost and maximum features). Thus, the products are divided into features, costs, a manufacturing company, etc. in terms of comparison. Only in this way can a good product be offered to the customer by determining the economic range. In this study, to obtain the most suitable model, the data set was divided into 30%, 20%, and K Fold divisions, and the most frequently used algorithms were tried on each division one by one. As a result, the best score was obtained from the model, which was

divided into 80% training and 20% testing, and the Support Vector Machines (SVM) algorithm was applied. The result obtained from this model is 0.96. In addition, considering that ensemble learning methods overcome the problems of overfitting or underfitting, it is possible to say that the voting method with a score of 0.9575 is a suitable model for this data set. RAM, battery, px height, px width, and internal memory had a positive effect on the classification of the inputs in the dataset as “very high cost” by the DVM classifier, respectively. The weight feature, on the other hand, had a negative effect. Other features did not contribute significantly. In future work, more sophisticated artificial intelligence techniques can be used to maximize accuracy and predict the correct price of products. A software or mobile application can be developed to estimate the market price of any newly released product.

REFERENCES

- Alpaydm E. Introduction to Machine Learning. The MIT Press; 2004.
- Asim M., Khan Z. Mobile price class prediction using machine learning techniques. International Journal of Computer Applications 2018; 179(29): 6-11.
- Beyer K., Goldstein J., Ramakrishnan R., Shaft U. When is “nearest neighbor” meaningful? International conference on database theory 1999; 217-235.
- Breiman, L. (2001). Random forests. *Machine learning*, 45(1), 5-32.
- Brijain M., Patel R., Kushik MR., Rana K. A survey on decision tree algorithm for classification. Penn State University Press; 2014.
- Cover TM., Hart PE. Nearest neighbor pattern classification. IEEE Transactions on Information Theory 1967; IT13(1): 21–27.
- Duda RO., Hart PE., Stork DG. Pattern classification. John Wiley & Sons, New Jersey; 2000.
- Han J., Kamber M. Data mining: Concepts and techniques, Elsevier Inc., Third Edition, USA; 2012.
- Lu W., Wang W., Leung A., Lo S., Yuen R., Xu Z., Fan. H. Air pollutant parameter forecasting using support vector machines. IJCNN Proceedings of the 2002 International Joint Conference on Neural Networks. 2002; 630-635.
- Mahesh B. Machine learning algorithms-a review. International Journal of Science and Research 2020; 9: 381-386.
- Özkan Y., Erol ÇS. Biyoenformatik DNA mikrodizi veri madenciliği. İstanbul: Papatya Yayıncılık; 2015.
- Pipalia K., Bhadja R. Performance evaluation of different supervised learning algorithms for mobile price classification. International Journal for Research in Applied Science and Engineering Technology 2020; 8: 1840-1848.
- Polikar, R. (2012). Ensemble learning. In *Ensemble machine learning* (pp. 1-34). Springer, Boston, MA.
- Pramanik R., Agrawal R., Gourisaria MK., Singh PK. Comparative analysis of mobile price classification using feature engineering techniques. 5th International Conference on Information Systems and Computer Networks 2021; pp.1-7.
- Rish I. An empirical study of the naive Bayes classifier. IJCAI 2001 workshop on empirical methods in artificial intelligence 2001; 3(22): 41-46.
- Rokach, L. (2010). Ensemble-based classifiers. *Artificial intelligence review*, 33(1), 1-39.

- Ruder S. An overview of gradient descent optimization algorithms 2016; arXiv preprint arXiv:1609.04747.
- Sakib AH., Shakir AK., Sutradhar S., Saleh MA., Akram W., Biplop KBMB. A hybrid model for predicting mobile price range using machine learning techniques. The 8th International Conference on Computing and Data Engineering 2022; pp. 86-91.
- Silahtaroglu G. Veri madenciliđi – Kavram ve algoritmaları. İstanbul: Papatya Yayıncılık; 2020.
- Tatlıdil H. Uygulamalı çok deđişkenli istatistiksel analiz. Ankara: Engin Yayınları; 1992.
- Uzun E. İnternet tabanlı bilgi erişimi destekli bir otomatik öğrenme sistemi, Doktora tezi, Trakya Üniversitesi; Edirne, Türkiye, 2007.
- Vapnik V. The nature of statistical learning theory. New York: Springer; 1995.
- Webb, G. I., Keogh, E., & Miikkulainen, R. (2010). Naïve Bayes. *Encyclopedia of machine learning*, 15, 713-714.
- Wolpert, D. H. (1992). Stacked generalization. *Neural networks*, 5(2), 241-259.
- Zhou, Z. H. (2012). *Ensemble methods: foundations and algorithms*. CRC press.

“

Chapter 14

**RECENT STUDIES ON THE
ANTIMICROBIAL AND ANTICANCER
ACTIVITIES OF HYDRAZIDE-
HYDRAZONES**

Belma HASDEMİR¹

”

¹ Istanbul University-Cerrahpaşa, Engineering Faculty, Chemistry Department, 34320 Avcılar, İstanbul/Türkiye <https://orcid.org/0000-0002-1071-1127>. E.mail: b.hasdemir@iuc.edu.tr

Hydrazide-hydrazones are condensation products of carboxylic acid hydrazides and aldehydes. These compounds are an important class of organic compounds of interest to medicinal chemists, as they contain the azomethine group (-NH-H=CH-), which is responsible for various pharmaceutical applications. When hydrazide-hydrazone derivatives, which are in the structure of many bioactive molecules, are evaluated in terms of medicinal chemistry, it is seen that they have a wide variety of pharmacological properties, including antimicrobial (Popiołek, 2017; Pham et al., 2019; Haiba et al., 2019), antifungal (Metwally et al., 2006; Musiol et al., 2006; Deep et al., 2010), anticancer (Nikolova-Mladenova et al., 2017; Patil et al., 2018; Mohareb et al., 2019), antiviral (Şenkardes et al., 2016; Gürsoy et al., 2020), antidepressant (Mohareb et al., 2010), antimalarial (Bekhit et al., 2019), anticonvulsant (Dehestani et al., 2018), antidiabetic (Sohrabi et al., 2022), antituberculosis (Koçyiğit-Kaymakçioğlu et al., 2006), anti-inflammatory (Abbas et al., 2015; Kumar Reddy and Kathale, 2017), antioxidant (Angelova et al., 2016) and analgesic activities (Navidpour et al., 2014). The biological effects of hydrazide-hydrazone compounds are depicted in Figure 1.

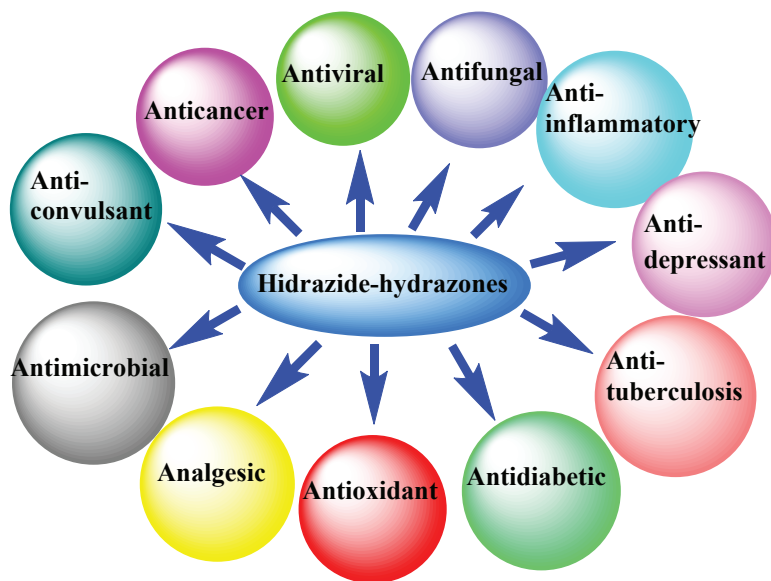


Figure 1. *Biological activities of hydrazide-hydrazone derivatives*

Small organic molecules play a critical role in drug design strategy by acting as bioactive scaffolds. The fundamental goal of medicinal chemistry is to discover novel compounds that are physiologically active. In

the light of these observations, the synthesis of biologically active new molecules was successfully carried out by our study group and biological activity studies of the synthesized compounds such as antifungal, anti-cancer and antioxidant were carried out (Hasdemir et al., 2018; Yıldız 2018; Yaşa 2018; Yaşa and Demir 2019; Hasdemir et al., 2019; Yaşa et al., 2019; Çelik Onar et al., 2020; Giray et al., 2020 ; Yıldız et al., 2021; Başpınar Küçük et al., 2022; Aydın et al., 2022).

In this review, it is aimed to guide researchers in the synthesis of new hydrazone hydrazone derivatives and the investigation of antibacterial and anticancer activities of these compounds by conducting a literature review of the years 2020-2022.

Biological activities of hydrazone-hydrazones

Antimicrobial activity

One of the pharmacological classes with the most rapid development during the past ten years is antibiotics (Beyer et al., 2018). However, with the increase in hospital infections caused by microorganisms resistant to antibiotics, the death rate due to these infections is increasing rapidly. Prolongation of the treatment due to hospital infections, the use of expensive drugs, or more than one antibiotic together increase the cost. As a result of this information, it is very important to develop new drug candidates that are expected to have better antibacterial effects and are less toxic. Some antibacterial drugs with hydrazone-hydrazone structure used in the clinic are given in Figure 2.

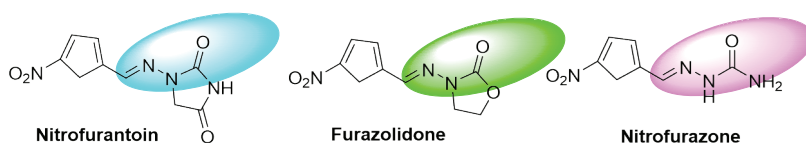
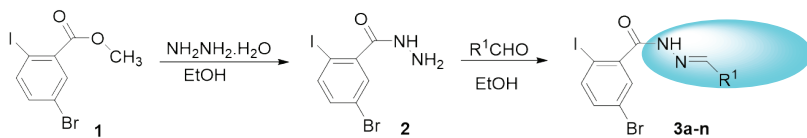


Figure 2. Some antibacterial agents with hydrazone-hydrazones scaffold

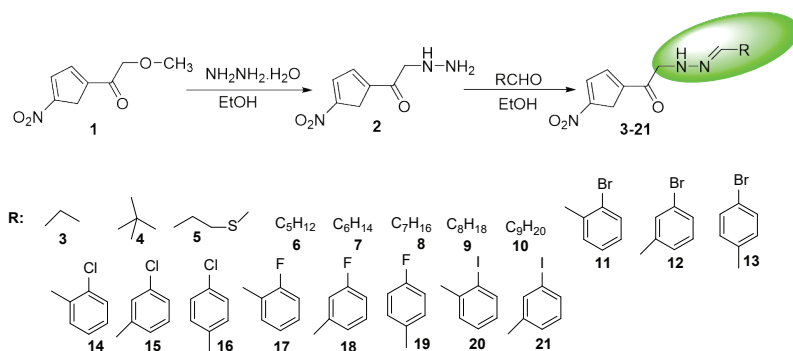
Popiołek et al. synthesized new hydrazone-hydrazone compounds by condensation reaction starting from compound **1** (Scheme 1). The obtained compounds were tested for antimicrobial activity against bacteria and fungi. The results of the tests for antimicrobial activity revealed that three of the compounds synthesized (**3j**, **3k**, and **3n**) displayed moderate antibacterial activity (Popiołek et al., 2020).



| Compound No | R ¹ | Compound No | R ¹ |
|-------------|--|-------------|--|
| 3a | ⁱ Pr(C ₃ H ₇) | 3h | 2,3-diOCH ₃ C ₆ H ₃ |
| 3b | C ₆ H ₅ | 3i | 3,4-diOCH ₃ C ₆ H ₃ |
| 3c | 2-ClC ₆ H ₄ | 3j | 2-OH-3-OC ₂ H ₅ C ₆ H ₃ |
| 3d | 2-Cl-5 NO ₂ C ₆ H ₃ | 3k | 4-OH-3-OC ₂ H ₅ C ₆ H ₃ |
| 3e | 2-NO ₂ C ₆ H ₄ | 3l | 4-[(OC ₂ H ₅) ₂ CH]C ₆ H ₄ |
| 3f | 3-NO ₂ C ₆ H ₄ | 3m | 4-(pyrrolidin-1-yl)phenyl |
| 3g | 4-NO ₂ C ₆ H ₄ | 3n | 1 <i>H</i> -indol-3-yl |

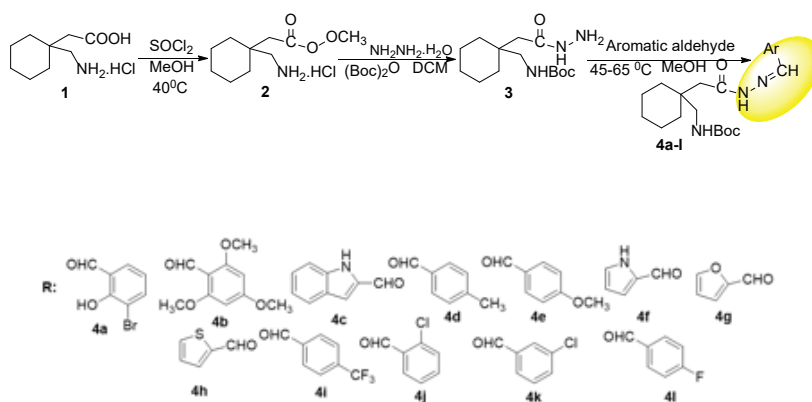
Scheme 1. Synthesis of novel hydrazone-hydrazone derivatives

Another study assessed the *in vitro* antibacterial efficacy of a new hydrazone-hydrazone series made from compound **2** (Scheme 2). The newly created compounds were found to exhibit strong antibacterial action, particularly against Gram-positive bacteria. Compounds **3-7** were the most active for Gram-negative bacteria. It was determined that hydrazone-hydrazone derivatives containing alkyl chains **3-10** (except heptilidene, octilidene, and nonylidene substituents) showed higher activity than aryl-substituted hydrazones (**11-21**) against Gram-negative bacteria (Popiołek et al., 2020).



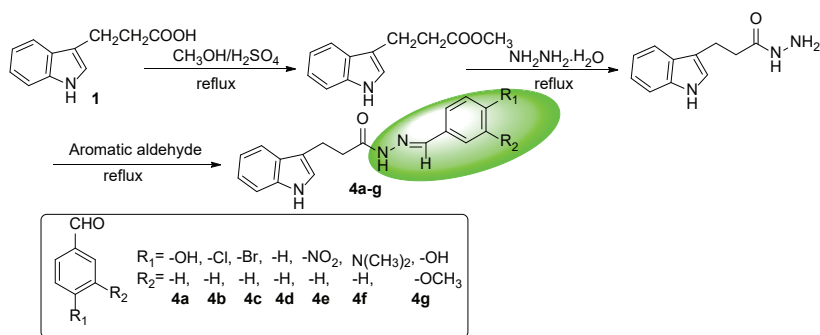
Scheme 2. Synthetic route for new hydrazide-hydrazones

In 2020, Pallapati et al. synthesized 12 new hydrazide-hydrazone derivatives from gabapentin scaffold in 66-82% yield (Scheme 3). They also looked into the antibacterial capabilities of the obtained compounds on three separate Gram-positive and Gram-negative bacterial strains. When the data were analyzed, it was revealed that compound **4g** had excellent antibacterial activity against all three Gram-positive bacteria tested, while compound **4c** had similar success against two of the three Gram-negative bacteria (*Salmonella enterica* and *Alcaligenes faecalis*) (Pallapati et al., 2020).



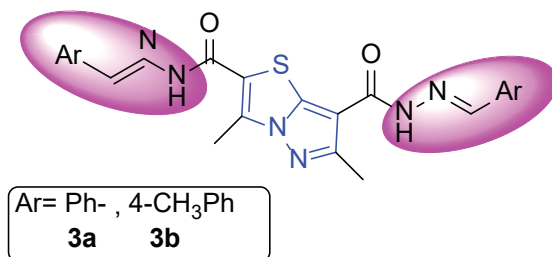
Scheme 3. Synthesis of targeted molecules

Sulaiman and Sarsam successfully synthesized a new series of N-acyl hydrazide-hydrazones, starting with indole-3-propionic acid (Scheme 4). They then carried out tests to determine the compounds' in vitro antibacterial effectiveness against six different microbe species. Results of the testing revealed that, with the exception of compound **4e**, all N-acyl hydrazones (**4a-g**) had modest activity against Gram-negative *E. coli* that was comparable to that of amoxicillin. Furthermore, it was found that compounds **4a**, **4c**, **4e**, **4f**, and **4g** shown moderate activity specifically against other Gram-negative bacteria, but compounds **4b** and **4d** demonstrated moderate action against Gram-positive *B. subtilis*. Additionally, none of the investigated compounds had antibacterial action against Gram-positive *S. aureus*, while all produced compounds showed preferentially decreased antibacterial activity compared to Ciprofloxacin. (Sulaiman and Sarsam, 2020).



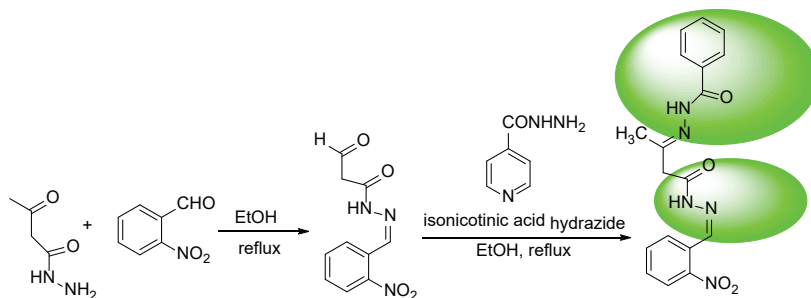
Scheme 4. Synthesis of *N*-acyl hydrazide-hydrazones

In 2021, Alsayari et al. synthesized new hydrazide-hydrazones based on pyrazolothiazole and evaluated them for antimicrobial activity (Scheme 5). Six bacterial species were used for the synthesized compounds' antibacterial properties. *Staphylococcus aureus* was found to be more sensitive to compound **3b** (Alsayari et al., 2021).



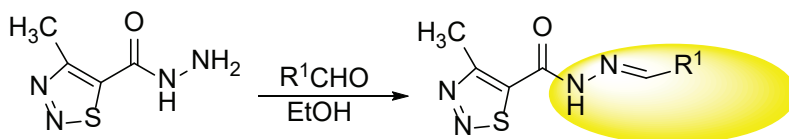
Scheme 5. Novel hydrazide-hydrazones based on pyrazolothiazole

In a study by Tolan et al. various metal complexes of the novel hydrazide-hydrazone ligand derived from the condensation of isonicotinic acid hydrazide with (*Z*)-*N*-(2-nitrobenzylidene)-3-oxobutanohydrazide were generated (Scheme 6). They found that the Hg(II) complex displayed significantly greater antibacterial and antifungal activity than the other complexes when the antibacterial and antifungal properties of these complexes were tested against various bacterial and fungal strains (Tolan et al., 2021).



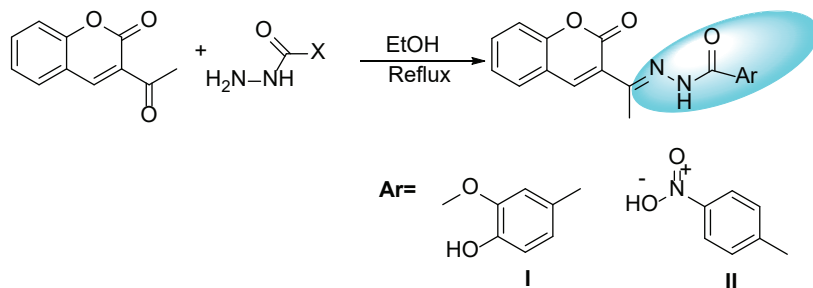
Scheme 6. Synthesis of hydrazide-hydrazone ligand

Paruch et al. synthesized 15 new hydrazide-hydrazone derivative compounds starting from 4-methyl-1,2,3-thiadiazol-5-carboxylic acid and investigated their in vitro antibacterial properties (Scheme 7). The novel hydrazide-hydrazone compounds showed promising antibacterial activity mostly against Gram-positive bacteria. The compound with the 5-nitro-2-furyl moiety had the most bioactivity among these compounds (Paruch et al., 2021).



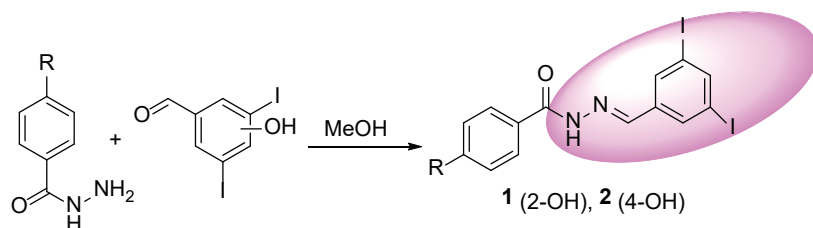
Scheme 7. Novel hydrazide-hydrazone derivatives

Abduljabbar and Hadi synthesized new coumarin hydrazide-hydrazone derivatives in 2021 and performed the structural analysis of the compounds (Scheme 8). Then, antibacterial activity tests of the synthesized molecules were performed against Gram-positive (*Staphylococcus aureus* and *Streptococcus pneumonia*) and Gram-negative bacteria (*E.coli* and *Pseudomonas aeruginosa*). It was determined that the highest activity was against *Pseudomonas aeruginosa* with compound **II** derivatives (Abduljabbar and Hadi, 2021).



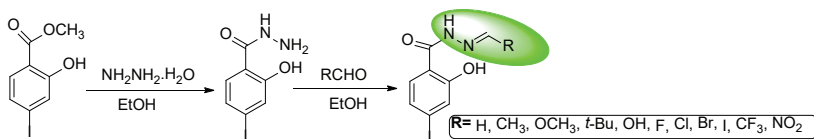
Scheme 8. Synthesis of novel coumarin hydrazide-hydrazone derivatives

Krátký et al. prepared a series of hydrazide-hydrazone compounds from 4-substituted benzohydrazides and investigated the antibacterial activities of these compounds against eight bacteria and eight fungal strains *in vitro* (Scheme 9). According to the results of the activity examination, the molecules were found to have strong antibacterial activity against Gram-positive cocci, including *Staphylococcus aureus*. In addition, four compounds were also found to inhibit human pathogenic fungi (MIC $\geq 1.95 \mu\text{M}$) (Krátký et al., 2021).



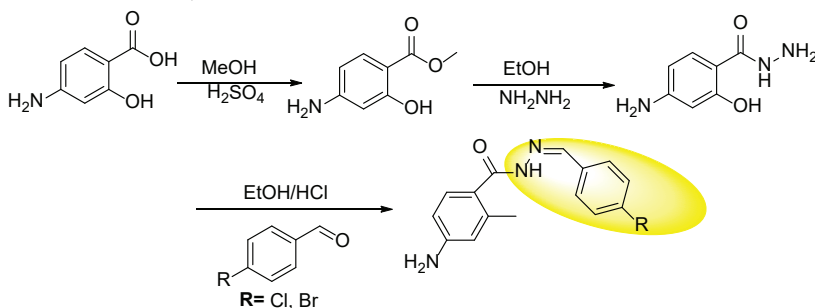
Scheme 9. Synthesis of new hydrazide-hydrazones

In another study by Popiołek et al., the synthesis of new hydrazide-hydrazones was carried out starting from 4-iodosalicylic acid and their *in vitro* antimicrobial properties were investigated (Scheme 10). The synthesized compounds showed considerable antibacterial efficacy against reference Gram-positive bacteria and *Candida spp* fungi, according to *in vitro* antimicrobial activity screening data (Popiołek et al., 2022).



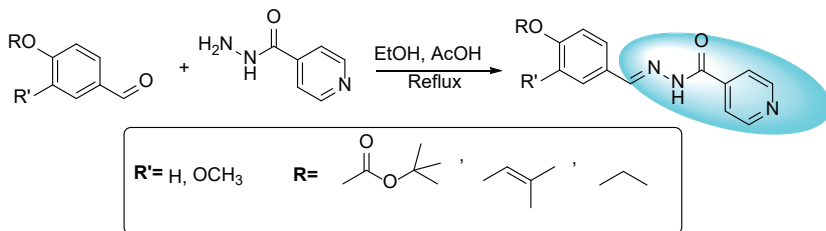
Scheme 10. Synthesis of new hydrazide-hydrazone

Coşkun et al. reported that they designed and synthesized the structures of new hydrazide-hydrazone compounds and hydrazide-hydrazone/amide hybrid compounds as drug candidates (Scheme 11). The obtained compounds' antibacterial and antifungal effects were tested against several strains, and their antibacterial activity was shown to be promising (Coşkun et al., 2022).



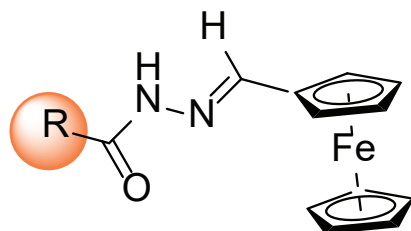
Scheme 11. Synthetic route to hydrazide-hydrazone compounds

In 2022, Shah et al. performed the synthesis of isonicotinic hydrazide-hydrazone derivatives with good yield and elucidated their structures (Scheme 12). *Escherichia coli*, *Bacillus subtilis*, and *Staphylococcus aureus* were used as test organisms to determine the antibacterial activity of the substances obtained. The findings demonstrated that the synthesized compounds had remarkable promise because of their antibacterial qualities (Shah et al., 2022).



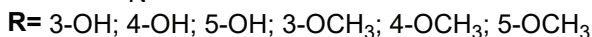
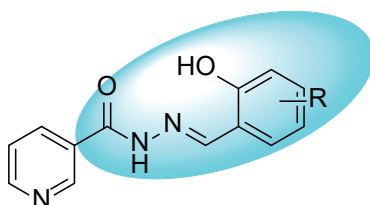
Scheme 12. Synthesis of alkylated isoniazid derivatives

In a different study, Filho and Castro were successful in creating a variety of novel ferrocenyl-*N*-acyl hydrazones (Fc-NAH) (Scheme 13). Studies on the synthesized compounds' *in vitro* antimicrobial activity demonstrated that all Fc-NAHs had antibacterial action, particularly against the Gram-positive bacterial strains *B. subtilis* and *S. aureus*. It was determined from the activity analysis results that electron-withdrawing substituents and the formation of hydrogen bonds have an important role in biological effects. In addition, it was found that derivatives containing non-polar substituents tend to have low activity or even inactivity (Filho and Castro 2022).



Scheme 13. *Ferrocenyl- N -acyl hydrazone derivatives*

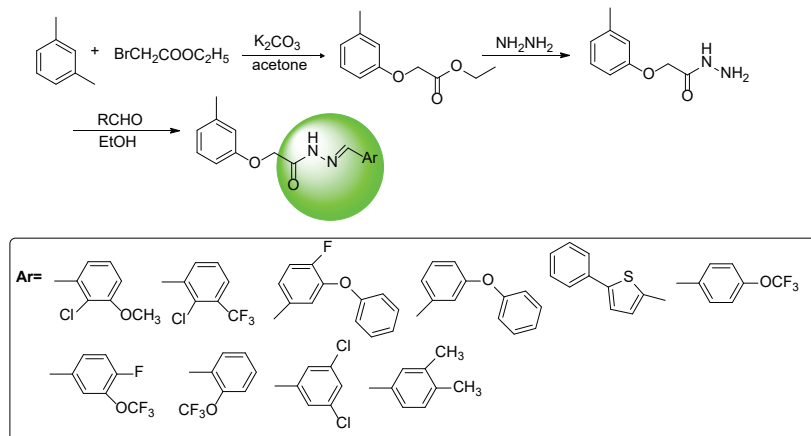
Klarić et al. reported that they prepared Fe(III) and Ga(III) complexes of aroyl hydrazones derived from nicotinic acid hydrazide (Scheme 14). They investigated *in vitro* antimicrobial activity of these compounds against several Gram-positive bacterial strains, a Gram-negative bacterial strain and, a yeast. According to the antimicrobial activity data, Ga(III) complexes with methoxy derivatives were more efficient than complexes with dihydroxy derivatives against the tested bacterial species, however Fe(III) complexes had no antibacterial activity (Klarić et al., 2022).



Scheme 14. *Structures of aroylhydrazide-hydrazone derivatives*

Şenkardeş and his work group synthesized twenty new hydrazide-hydrazone derivatives starting from *m*-cresol (Scheme 15). They tested the obtained compounds' antimicrobial efficacy against two Gram-po-

sitive bacteria, two Gram-negative bacteria, and three pathogenic fungi. Some substances were discovered to have substantial antibacterial activity against the examined microorganisms, particularly *E. coli*. (Şenkardeş et al., 2022).



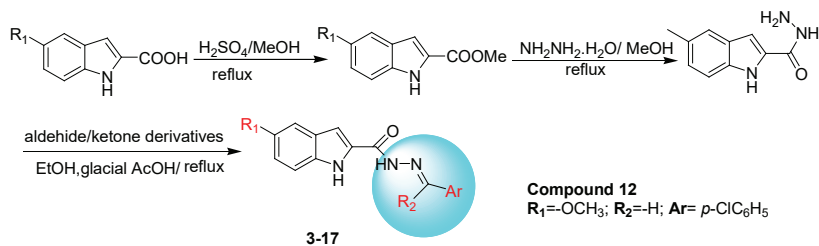
Scheme 15. Synthesis of hydrazone-hydrazone derivatives from *m*-cresol

Anticancer activity

Cancer is a disease that results in the body's growth of abnormal cells brought on by gene mutation and unchecked cell proliferation. According to the World Health Organization-International Agency for Research on Cancer (IARC), 10.3 million cancer deaths and 19.3 million new cancer cases occurred worldwide in 2020. Female breast cancer is the most common cancer type diagnosed, according to data from 2020. Breast cancer accounts for an estimated 2.3 million new instances of cancer worldwide (11.7%), followed by lung cancer (11.4%), colorectal cancer (10.0%), prostate cancer (7.3%), and stomach cancer (5.6%). Therefore, intensive work is carried out around the world to develop new drugs that can affect cancer, especially breast cancer (Sung et al., 2021). In recent years, many hydrazone-hydrazone compounds with anticancer activity have been synthesized through various targets.

Zühal Kilic-Kurt et al. in 2020, have been synthesized indole-2-carbohydrazone-hydrazone derivatives and tested their anticancer activities (Scheme 16). On MCF-7, HepG2, and PC3 cell lines, the antiproliferative potential of every synthesized molecule was examined. The most potent

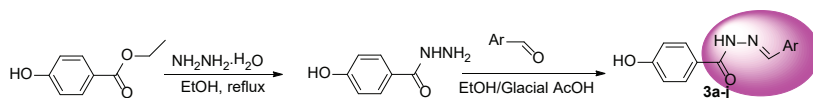
cytotoxic effect against breast cancer cell (MCF-7) was demonstrated by compound **12** ($IC_{50}=3.01 \mu M$) (Kilic-Kurt et al., 2020).



Scheme 16. Synthesis of indole-2-carbohydrazone-hydrazone derivatives

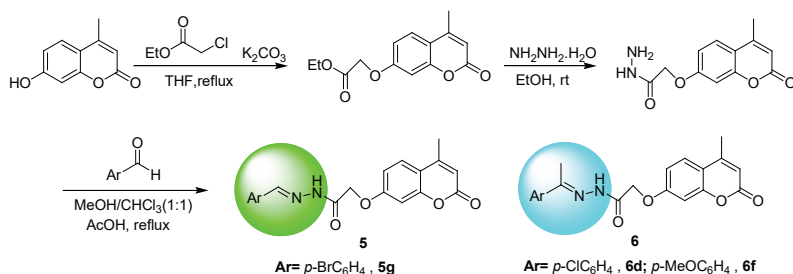
Popiołek and his colleagues performed *in vitro* cytotoxicity tests as well as antimicrobial activities of new hydrazone-hydrazone derivatives synthesized from 5-bromo-2-iodobenzoic acid. The synthesis of novel molecules is shown in Scheme 1. It was shown that compound **3c** has a significant level of selectivity against cancer cell lines. Compounds with a nitro group on the phenyl ring, such as **3e** and **3g**, exhibited a considerable inhibitory effect and were incredibly selective on the tumor cells. Additionally, it was discovered that compound **3k** has potent antiproliferative properties and good selectivity against the cancer cell lines 769-P and HepG2. The results of research on cytotoxic activity highlight the significance of certain substituents on the phenyl ring in the obtained hydrazone-hydrazone derivatives (Popiołek et al., 2020).

Based on ethyl paraben, a new series of hydrazone-hydrazone derivatives was synthesized in 2020 by Han et al (Scheme 17). To determine the anticancer activity of the synthesized molecules, they evaluated their *in vitro* cytotoxic activity on the liver cancer cell line (HepG2). Researchers reported that N' -{[4-phenylthiophen-2-yl] methylidene}-4-hydroxy benzo hydrazide and N' -{[4-fluoro-3(phenoxy)phenyl] methylidene}-4-hydroxybenzo hydrazide compounds have anticancer activity ($IC_{50}=37.4$ ve $42.4 \mu M$, respectively) against HepG2 cell line. Doxorubicin was used as a positive susceptibility reference standard for cell lines (Han et al., 2020).



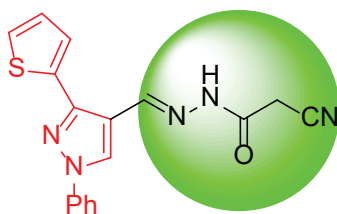
Scheme 17. Synthesis of hydrazone-hydrazone derivatives from ethyl paraben

A number of coumarin hydrazone-hydrazone compounds were developed and synthesized by Duangdee and colleagues (Scheme 18). Additionally, they assessed the obtained compounds' *in vitro* anti-proliferative activities against human colon cancer (Caco-2) cells, breast cancer (SKBR-3) cells, and liver cancer (HepG2 cells). Three of these substances, **5g**, **6d**, and **6f**, were discovered to have powerful effects on the Hep-G2 and SKBR-3 cell lines. The best cytotoxic activity against the Hep-G2 cell line was discovered to be compound **6d**, with an IC_{50} (2.84 0.48 $\mu\text{g/mL}$) comparable to regular doxorubicin (Duangdee et al. 2020).



Scheme 18. *Synthesis of coumarin hydrazone-hydrazone*

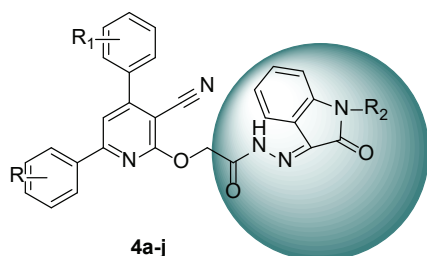
Compound **I** was obtained by El-Helw and El-Badawy in 2020 (Scheme 19) then, other N-heterocycle compounds that have biologically active were synthesized starting from this substance **I**. Two different human tumor cell lines (HepG2 and MCF7) were used to test the obtained compounds' *in vitro* anticancer activities. It was determined that compound **I** showed the strongest effect against both tumors (El-Helw and El-Badawy, 2020).



Scheme 19. *Structure of compound I*

Zebbiche et al. another group of researchers, successfully obtained nine novel hydrazone compounds in 2021 that had pyridine and isatin moieties (Scheme 20). The synthesized novel molecules were examined for

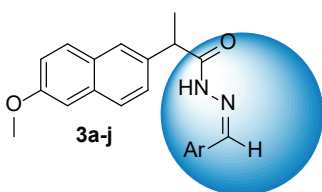
their anticancer potential on A-2780 and MCF-7 cancer cell lines. While three of these compounds (**4b**, **4d**, and **4i**) demonstrated superior anticancer activity to the standard drug against the MCF-7 cancer cell line at a concentration of 0.1 M, seven compounds (**4b**, **4c**, **4d**, **4e**, **4g**, **4h**, and **4i**) demonstrated better anticancer activity to docetaxel (standard drug) against the A-2780 cell lines at the same concentration (Zebbiche et al., 2021).



- 4a**= R=H, R₁=H, R₂=H
4b= R=H, R₁=H, R₂=Bz
4c= R=H, R₁=H, R₂=4-BrBz
4d= R=H, R₁=4OMe, R₂=H
4e= R=H, R₁=4OMe, R₂=4-BrBz
4f= R=4OMe, R₁=4OMe, R₂=H
4g= R=4OMe, R₁=4OMe, R₂=Bz
4h= R=3NO₂, R₁=4OMe, R₂=H
4i= R=3NO₂, R₁=H, R₂=H

Scheme 20. Structure of novel hydrazone-hydrazone molecules

A variety of new (S)-Naproxen derivatives with the hydrazone-hydrazone moiety were synthesized in another work by Han et al. (Scheme 21) and their anticancer properties were evaluated against MDA-MB-231 and MCF-7 cell lines (human breast cancer). Among the compounds tested, It was determined that compound **3a** exhibited the strongest cytotoxic activity with good selectivity against both cancer cell lines (Han et al., 2021).

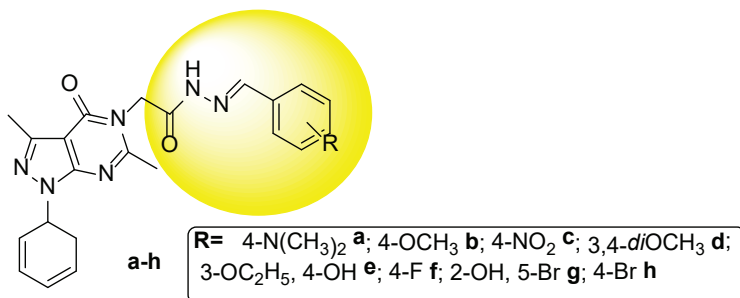


- Ar**= -C₆H₄-OCF₃ (**3a,b,c**)
 -C₆H₄-CF₃ (**3d,e,f**)
 -C₆H₄-CN (**3g**)
 -C₅H₂-NO₂ (**3h**)
 -C₅H₂-O-C₂H₅ (**3i**)
 -C₆H₄-F (**3j**)
 -C₅H₂-N-CH₃ (**3k**)
 -C₅H₂-S-Br (**3l**)

Scheme 21. Synthesized Naproxen derivatives

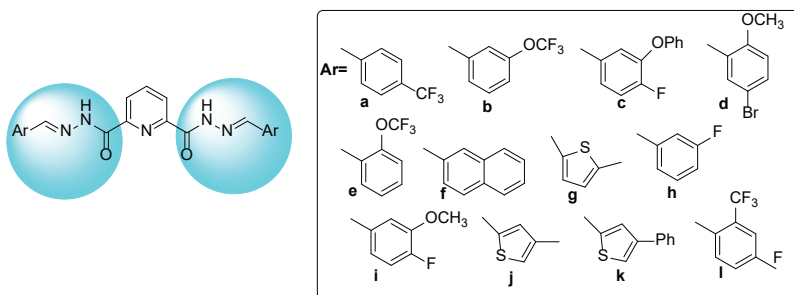
In 2021, Horchani and her team synthesized a hybrid pyrazolo [3,4-d] pyrimidin-4 (5H) -one compounds as a potential cytotoxic agent and evaluated their in vitro antiproliferative effects against MCF-7 cells (breast cancer). Among the compounds tested, the **a**, **e**, **g** and **h** series (Scheme

22) were found to exhibit very high cytotoxic activity against MCF-7 cells (Horchani et al., 2021).



Scheme 22. Compounds with high cytotoxic activity (**a**, **e**, **g** and **h**)

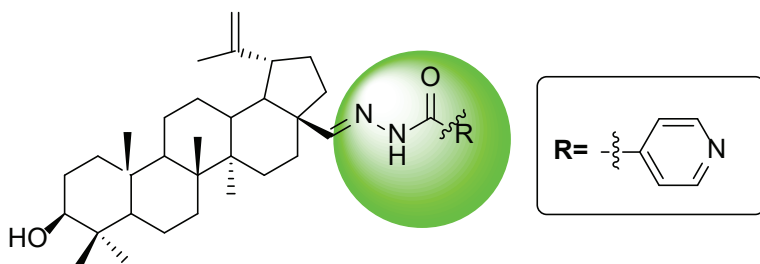
In another study by Şenkardeş and his working group, a series of new pyridine-based dihydrazone derivatives were synthesized with the condensation reaction between pyridine-2,6-dicarbohydrazone and suitable aldehydes (Scheme 23). The synthesized compounds were tested for their cytotoxic effects on the human endometrial cancer cell line (ISH) and the HT-29 colon cancer cell line and the Ishikawa human endometrial cancer cell line (ISH), and also molecular modeling studies were performed. Among the examined substances, compounds **f** and **k** had notable cytotoxic action (Şenkardeş et al., 2021).



Scheme 23. Structure of new pyridine-based dihydrazone derivatives

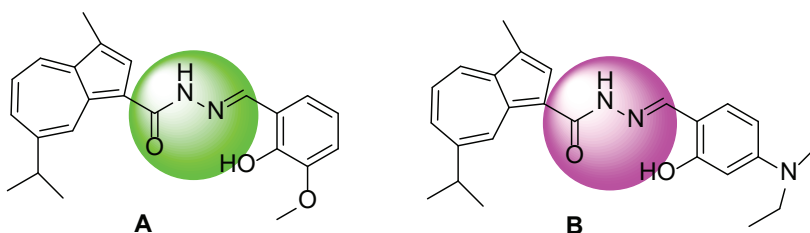
In another study, nine novel betulin derivatives containing hydrazone-hydrazone moieties were synthesized by Wu et al. All synthesized compounds were examined for their cytotoxicity against HepG2, A549, MCF-7 and HCT-116 cancer cell lines and GES-1 cell line (normal human gastric epithelial cell). When the activity results were evaluated, it was determined that the compound shown in scheme 24 had the strongest

activity (IC_{50} =9.27 and 8.87 μ M, respectively) against HepG2 and MCF-7 cell lines (Wu et al., 2021).



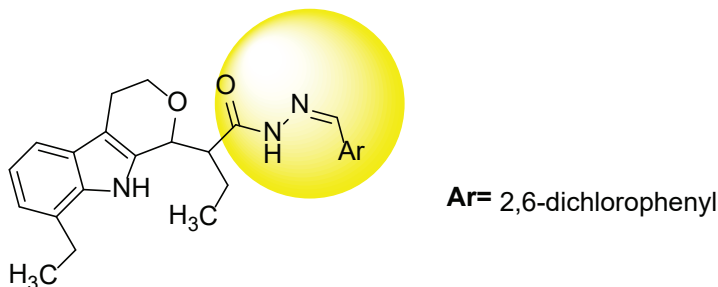
Scheme 24. *Betulin derivative containing hydrazide-hydrazone*

In 2022, Brogányi et al. produced three novel chelators based on substituted zulene carbohydrazide in high yield. The anticancer efficacy of the created chelators was examined using three pancreatic cancer cell lines (MIA PaCa-2, PANC-1, and AsPC-1) and a healthy cell line (human fibroblast BJh-TERT). The investigated substances were found to have strong cytotoxic action against MIA PaCa-2, PANC-1, and AsPC-1 cell lines. Compounds **A** and **B** in particular show greater selectivity for all pancreatic cancer cell types (Scheme 25) (Brogányi et al., 2022).



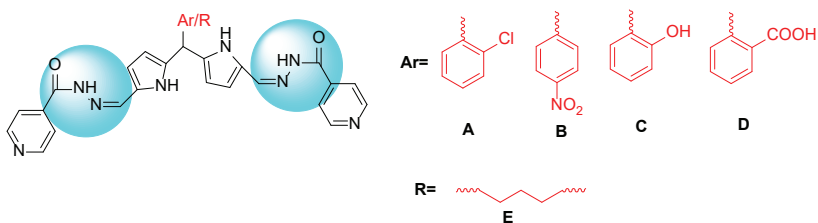
Scheme 25. *Structure of compounds A and B*

Koç et al. synthesized 12 novels (*R, S*)-Etodolac derivatives containing the hydrazide-hydrazone moiety and examined their anticancer activity against PC-3, DU-145, and LNCaP cell lines (prostate cancer) *in vitro*. As a result of the examination, it was found that only compound **A** (Scheme 26) showed a better cytotoxic effect on three prostate cancer cell lines with IC_{50} values of 10.36 μ M, 5.24 μ M and 15.53 μ M, respectively (Koç et al., 2022).



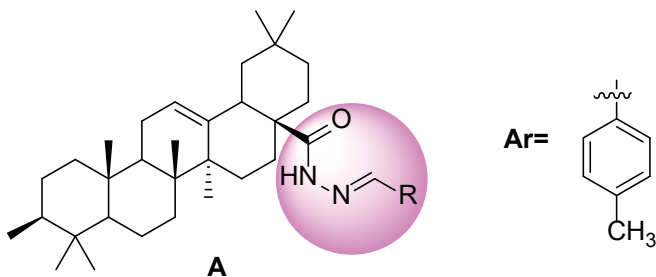
Scheme 26. Structure of compound A

In another study by Gautam et al., dipyrromethane hydrazide-hydrazone derivatives were obtained through a condensation reaction in the presence of a catalyst and then evaluated against leukemia (HL-60) and colon (HCT-116) cancer cells. Compounds **A**, **B**, **C**, **D**, and **E** showed moderate to extremely high cytotoxic effects against HL-60 and HCT-116 (Scheme 27) (Gautam et al., 2022).



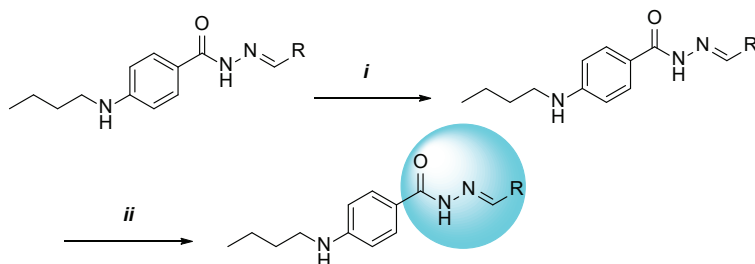
Scheme 27. Structure of dipyrromethane having hydrazide-hydrazone derivatives

13 novel triterpene/hydrazide-hydrazone molecules were obtained from oleanolic acid, biologically active natural product, by Şenol and his team. In vitro cytotoxic activities of these compounds on lung cancer cell lines (A549) and human healthy bronchial epithelial cell (BEAS-2B) lines were investigated. Doxorubicin was used as a standard in biological activity studies. On A549 cells. Compound A was shown to have cytotoxic activity comparable to that of Doxorubicin, nevertheless on BEAS-2B cells, it had activity that was roughly 32 times less potent (Scheme 28) (Şenol et al., 2022).



Scheme 28. Structure of compound *A*

Han et al. synthesized novel tetracaine hydrazide-hydrazones (Scheme 29) and evaluated the anticancer activity of these compounds against HepG2 and A549 cancer cell lines. Among the compounds tested, 4-(Butylamino)-N'-[(2,4-dichlorophenyl) methylidene] benzohydrazide showed the strongest anticancer activity with good selectivity against both cancer cells (Han et al., 2022).



Scheme 29. Synthetic route of Tetracaine derivatives. (i) $\text{NH}_2\text{NH}_2 \cdot \text{H}_2\text{O} / \text{C}_2\text{H}_5\text{OH}$, (ii) $\text{C}_2\text{H}_5\text{OH} / \text{glacial } \text{CH}_3\text{COOH} / \text{Ar-CHO}$.

REFERENCES

- Abbas, A.H., Elias, A.N., Fadhil, A.A. (2015) Synthesis, characterization and biological evaluation of new potentially active hydrazones of naproxen hydrazide, *Der Pharma Chemica*, 7(10), 93-101. ISSN 0975-413X
- Abduljabbar, T.T., Hadi, M.K., (2021) Synthesis, Characterization and Antibacterial Evaluation of Some Coumarin Derivatives, *Iraqi J. Pharm. Sci.*, 30(1), 249-257. Doi:10.31351/vol 30iss1 pp249-257
- Alsayari, A., Muhsinah, A.B., Asiri, Y.I., Al-aizari, F.A., Kheder, N.A., Almarhoun, Z.M., Ghabbour, H.A., Mabkhot, Y.N. (2021) Synthesis, Characterization, and Biological Evaluation of Some Novel Pyrazolo[5,1-b]thiazole Derivatives as Potential Antimicrobial and Anticancer Agents, *Molecules*, 26, 5383. Doi:10.3390/molecules26175383
- Angelova, V.T., Vassilev, N.G., Nikolova-Mladenova, B., Vitas, J., Malbaša, R., Momekov, G., Djukic, M., Saso, L. (2016) Antiproliferative and antioxidative effects of novel hydrazone derivatives bearing coumarin and chromene moiety, *Med. Chem. Res.*, 25, 2082–2092. Doi:10.1007/s00044-016-1661-4
- Aydın, E., Sentürk, A.M., Başpınar Küçük, H., Güzel, M. (2022) Cytotoxic Activity and Docking Studies of 2-arenoxybenzaldehyde N-acyl Hydrazone and 1,3,4-Oxadiazole Derivatives against Various Cancer Cell Lines, *Molecules*, 27, 7309. Doi:10.3390/molecules27217309
- Başpınar Küçük, H., Alhonaish, A., Yıldız, T., Güzel, M. (2022) An efficient approach to access 2,5-disubstituted 1,3,4-oxadiazoles by oxidation of 2-arenoxybenzaldehyde N-acyl hydrazones with molecular iodine, *Chemistry-Select*, 7, e202201391. Doi:10.1002/slct. 202201391
- Bekhit, A.A., Saudi, M.N., Hassan, A.M.M., Fahmy, S.M., Ibrahim, T.M., Ghareeb, D, El-Seidy, A.M., Nasralla, S.N., Bekhit, A.E.-D.A. (2019) Synthesis, in silico experiments and biological evaluation of 1,3,4-trisubstituted pyrazole derivatives as antimalarial agents, *Eur. J. Med. Chem.*, 163, 353–366. Doi:10.1016/j.ejmech.2018.11.067
- Beyer, P., Moorthy, V., Paulin, S.; Hill, S.R., Sprenger, M., Garner, S., Simão, M., Guerra, R., Magrini, N., Swaminathan, S. (2018) The drugs don't work: WHO's role in advancing new antibiotics. *Lancet*, 392, 264–266. Doi: 10.1016/S0140-6736(18)31570-8
- Brogyányi, T., Robert KapláneK, R., Kejik, Z., Hosnedlová, B., et al., (2022) Azulene hydrazide-hydrazones for selective targeting of pancreatic cancer cells, *Biomed. Pharmacother*, 155 (2022) 113736. Doi:10.1016/j.biopha.2022.113736

- Coşkun, G.P., Aklamuz, A., İnce, U., Ülgen, M. (2022) Synthesis, Structure Elucidation and Biological Activity of New Hybrid Hydrazone-Amide Compounds, *Cumhuriyet Sci. J.*, 43(3), 384-390. Doi: 10.17776/esj.1105811
- Çelik Onar, H., Yaşa, H., Sin, O. (2020) Comparison of Antioxidant Activities of Mono-, Di- and Tri-substituted Coumarins, *J. Turk. Chem. Soc. A: Chem.*, 7(1), 87–96. Doi:10.18596/jotcsa.624265.
- Deep, A., Jain, S., Sharma, P.C., Verma, P., Kumar, M., Dora, C.P. (2010) Design and Biological Evaluation Of Biphenyl-4-Carboxylic Acid Hydrazone-Hydrazone for Antimicrobial Activity, *Acta Poloniae Pharmaceutica-Drug Research*, 67 (3), 255-259. ISSN 0001-6837
- Dehestani, L., Ahangar, N., Hashemi, S.M. Irannejad, H., Masihi, P.H., Shakiba, A., Emami, S. (2018) Design, synthesis, in vivo and in silico evaluation of phenacyl triazole hydrazones as new anticonvulsant agents, *Bioorg. Chem.*, 78, 119–129. Doi:10.1016/j.bioorg.2018.03.001
- Duangdeea, N., Mahavorasirikula, W., Prateptongkum, S. (2020) Design synthesis and anti-proliferative activity of some new coumarin substituted hydrazide-hydrazone derivatives, *J. Chem. Sci.* 132, 66, 1-12. Doi:10.1007/s12039-020-01767
- El-Helw, E.A.E., El-Badawy, A.A. (2020) Synthesis of chromenone, pyrimidinone, thiazoline, and quinolone derivatives as prospective antitumor agents, *J. Heterocyclic Chem.*, 57, 2354–2364. Doi:10.1002/jhet.3948
- Filho, J.M.S., Castro, M.V.B.S. (2022) Synthesis, structural characterization, and antimicrobial activity of novel ferrocene- N -acyl hydrazones designed by means of molecular simplification strategy Celebrating the 100th anniversary of the birth of Professor Paulo Freire, *J. Organomet. Chem.*, 979, 122488. Doi:10.1016/j.jorganchem.2022.122488
- Gautam, A., Rawat, P., Singh, R.N., Holguin, N.R.F. (2022) Synthesis, spectroscopic and evaluation of anticancer activity of new hydrazone-containing dipyrromethane using experimental and theoretical approaches, *J. Mol. Struct.* 1260, 132781. Doi:10.1016/j.molstruc.2022.132781
- Giray, B., Karadağ, A.E., İpek, Ö.Ş., Pekel, H., Güzel, M., Başpınar Küçük, H. (2020) Design and synthesis of novel cyclopentapyrazoles bearing 1,2,3-thiadiazole moiety as potent antifungal agents, *Bioorg. Chem.*, 95, 103509. Doi:10.1016/j.bioorg.2019.103509
- Gürsoy, E., Dincel, E.D., Naesens, L., Güzeldemirci, N.U., (2020) Design and synthesis of novel imidazo[2,1-b]thiazole derivatives as potent antiviral and antimycobacterial agents, *Bioorg. Chem.*, 95, 103496. Doi:10.1016/j.bioorg.2019.103496.
- Haiba, N.S., Khalil, H.H., Moniem, M.A., El-Wakil, M.H., Bekhit, A.A., Khat-tab, S.N. (2019) Design, synthesis and molecular modeling studies of new

- series of s-triazine derivatives as antimicrobial agents against multi-drug resistant clinical isolates, *Bioorg. Chem.*, 89, 103013. Doi:10.1016/j.bioorg.2019.103013
- Han, M.İ., Atalay, P., İmamoğlu, N., Küçükgül, Ş.G. (2020) Synthesis, characterization and anticancer activity of novel hydrazide-hydrazones derived from ethyl paraben, *J. Res. Pharm.*, 24(3), 341-349. Doi:10.35333/jrp.2020.156
- Han, M.I., Atalay, P., Tunç, C.Ü., Ünal, G., Serkan Dayan, S., Aydın, Ö., Güniz Küçükgül, G. (2021) Design and synthesis of novel (S)-Naproxen hydrazide-hydrazones as potent VEGFR-2 inhibitors and their evaluation in vitro/in vivo breast cancer models, *Bioorganic & Medicinal Chemistry*, 37, 116097. Doi:10.1016/j.bmc.2021.116097
- Han, M.I., Yeşil Baysal, Ö.D., Başaran, G.S., Sezer, G., Telci, D., Küçükgül, Ş.G. (2022) Design, synthesis and anticancer activity studies of novel 4-butylaminophenyl hydrazide-hydrazones as apoptotic inducers, *Tetrahedron*, 115, 132797. Doi:10.1016/j.tet.2022.132797
- Hasdemir, B., Yaşa, H., Akkamış, Y. (2019) Synthesis and antioxidant activities of novel N-aryl (and N-alkyl) γ - and δ -imino esters and ketimines, *Journal of the Chinese Chemical Society* 66 (2), 197-204. Doi:10.1002/jccs.201800126
- Hasdemir, B., Sacan, O., Yasa, H., Kucuk, H.B., Yusufoglu, A.S., Yanardag, R. (2018) Synthesis and elastase inhibition activities of novel aryl, substituted aryl, and heteroaryl oxime ester derivatives, *Arch. Pharm. Chem. Life Sci.*, 351, e1700269. Doi:10.1002/ardp.201700269
- Horchani, M., Sala, G.D., Caso, A., D'Aria, F., et al., (2021) Molecular Docking and Biophysical Studies for Antiproliferative Assessment of Synthetic Pyrazolo-Pyrimidinones Tethered with Hydrazide-Hydrazones, *Int. J. Mol. Sci.*, 22, 2742-2762. Doi:10.3390/ijms 22052742
- Kilic-Kurt, Z., Acar, C., Ergul, M., Bakar-Ates, F., Altuntas, T.G. (2020) Novel indole hydrazide derivatives: Synthesis and their antiproliferative activities through inducing apoptosis and DNA damage, *Arch Pharm.*, 353, e2000059. Doi:10.1002/ardp.202000059
- Klarić, D., Pocrnić, M., Lež, D., Polović, S., Kontrec, D., Kosalec, I., Budimir, A., Galić, N. (2022) Search for new antimicrobials: spectroscopic, spectrometric, and in vitro antimicrobial activity investigation of Ga(III) and Fe(III) complexes with aroylhydrazones, *Journal of Biological Inorganic Chemistry*, 27, 715–729. Doi:10.1007/s00775-022-01967-y
- Koç, H.C., Atlıhan, İ., Mega-Tiber, P., Oya Orun, O., Küçükgül, Ş.G. (2022) Synthesis of some novel hydrazide-hydrazones derived from etodolac as potential anti-prostate cancer agents, *J Res Pharm.*, 26(1), 1-12. Doi:10.29228/jrp.97

- Koçyiğit-Kaymakçioğlu, B., Oruç, E., Unsalan, S., Kandemirli, F., Shvets N., Rollas, S., Anatholy, D. (2006) Synthesis and characterization of novel hydrazide-hydrazones and the study of their structure-antituberculosis activity, *European Journal of Medicinal Chemistry*, 14(11), 1253-1261. Doi: 10.1016/j.ejmech.2006.06.009
- Krátký, M., Konečn'á, K., Brablíková, :, Janoušek, J., Pflégr, V., Maixnerová, J., Trejtnar, F., Vin'sov'á, J. (2021) Iodinated 1,2-diacylhydrazines, benzohydrazide-hydrazones and their analogues as dual antimicrobial and cytotoxic agents, *Bioorganic & Medicinal Chemistry*, 41, 116209. Doi:10.1016/j.bmc.2021.116209
- Kumar Reddy, A.L.V., Kathale, N.E. (2017) Synthesis and anti-inflammatory activity of hydrazide-hydrazones bearing anacardic acid and 1,2,3-triazole ring based hybrids, *Orient. J. Chem.*, 33 (6), 2930–2936. Doi:10.13005/ojc/330628
- Metwally, K.A., Abdel-Aziz, L.M., Lashine, E.M., Hussein, M.I., Badawy, R.H. (2006) Hydrazones of 2-aryl-quinoline-4-carboxylic acid hydrazides: Synthesis and preliminary evaluation as antimicrobial agents, *Bioorganic & Medicinal Chemistry*, 14, 8675–8682. Doi:10.1016/j.bmc.2006.08.022
- Mohareb, R.M., El-Sharkawy, K.A., Hussein, M.M., El-Sehrawi, H.M. (2010) Synthesis of hydrazide-hydrazone derivatives and their evaluation of antidepressant, sedative and analgesic agents, *J. Pharmaceutical Sci. Res.*, 2 (4), 185-196.
- Mohareb, R.M., EL-Sharkawy, K.A., Al Farouk, F.O. (2019) Synthesis, cytotoxicity against cancer and normal cell lines of novel hydrazide-hydrazone derivatives bearing 5H chromen- 5-one, *Med. Chem. Res.*, 28, 1885–1900. Doi:10.1007/s00044-019-02421-6.
- Musiol, R., Jampilek, J., Buchta, V., Silva, L., Niedbala, H., Podeszwa, B., Palka, A., Majerz-Maniecka, K., Oleksyn, B., Polanski, J. (2006) Antifungal properties of new series of quinoline derivatives, *Bioorg. Med. Chem.*, 14, 3592-3598. Doi:10.1016/j.bmc.2006.01.016
- Navidpour, L., Shafaroodi, H., Saeedi-Motahar, G., Shafiee, A. (2014) Synthesis, anti-inflammatory and analgesic activities of arylidene-2-(3-chloroanilino) nicotinic acid hydrazides, *Med. Chem. Res.* 23, 2793–2802. Doi:10.1007/s00044-013-0860-5
- Nikolova-Mladenova, B., Momekov, G., Ivanov, D., Bakalovaa, A. (2017) Design and druglike properties of new 5-methoxysalicylaldehyde based hydrazones with anti-breast cancer activity, *J. Appl. Biomed.*, 15, 233–240. Doi:10.1016/j.jab.2017.04.004
- Pallapati, R.K., Mutchu, B.R., Khandapu, B.M.K., Umamaheswara Rao Vanga, U.R., Varala, R., Bollikolla, H.B.B. (2020) Synthesis of Novel Gabapentin Scaffold Derived Hydrazide-hydrazones for Potential Antimicrobial

- agents and Antioxidants, *Chemistry Africa*, 3, 881–888. Doi:10.1007/s42250-020-00184-x
- Paruch, K., Popiołek, L., Biernasiuk, A., Berecka-Rycerz, A., Malm, A., Gumieniczek, A., Wujec, M. (2021) Novel Derivatives of 4-Methyl-1,2,3-Thiadiazole-5-Carboxylic Acid Hydrazide: Synthesis, Lipophilicity, and in Vitro Antimicrobial Activity Screening, *Appl. Sci.* 11, 1180–1192. Doi:10.3390/app11031180
- Patil, S., Kuman, M.M., Palvai, S., Sengupta, P., Basu, S. (2018) Impairing powerhouse in colon cancer cells by hydrazide-hydrazone-based small molecule, *ACS Omega*, 3, 1470–1481, [Doi:10.1021/acsomega.7b01512](https://doi.org/10.1021/acsomega.7b01512)
- Pham, V.H., Phan, T.P.D., Phan, D.C., Vu, B.D. (2019) Synthesis and bioactivity of hydrazidehydrazones with the 1-adamantyl-carbonyl moiety, *Molecules*, 24, 4000–4011. Doi:10.3390/molecules24214000
- Popiołek, L. (2017) Hydrazide-hydrazones as potential antimicrobial agents: overview of the literature since 2010, *Med. Chem. Res.*, 26, 287–301. Doi: 10.1007/s00044-016-1756-y
- Popiołek, L., Rysz, B., Biernasiuk, A., Wujec, M. (2020) Synthesis of promising antimicrobial agents: hydrazidehydrazones of 5-nitrofurán-2-carboxylic acid, *Chem. Biol. Drug Des.*, 95, 260–269. Doi: 10.1111/cbdd.13639
- Popiołek, L., Patrejkoa, P., Gawrońska-Grzywacz, M., Biernasiuk, A., et al. (2020) Synthesis and in vitro bioactivity study of new hydrazide-hydrazones of 5-bromo-2-iodobenzoic acid, *Biomedicine & Pharmacotherapy* 130, 110526. Doi: 10.1016/j.biopha.2020.110526
- Popiołek, L., Tuszyńska, K., Biernasiuk, A. (2022) Searching for novel antimicrobial agents among hydrazide-hydrazones of 4-iodosalicylic acid, *Biomedicine & Pharmacotherapy* 153, 113302. Doi:10.1016/j.biopha.2022.113302
- Shah, M.A., Uddin, A., Shah, M.R., Ali, I., Ullah, R., Hannan, P.A., Hussain, H. (2022) Synthesis and Characterization of Novel Hydrazone Derivatives of Isonicotinic Hydrazide and Their Evaluation for Antibacterial and Cytotoxic Potential, *Molecules*, 27, 6770–6782. Doi:10.3390/molecules27196770
- Sohrabi, M., Binaeizadeh, M.R., Iraj, A., Larijani, B., Saedi, M., Mahdavi, M. (2022) A review on α -glucosidase inhibitory activity of first row transition metal complexes: a futuristic strategy for treatment of type 2 diabetes, *RSC Adv.*, 12, 12011–12052. Doi:10.1039/D2RA00067A
- Sulaiman, A.T. and Sarsam, S.W. (2020) Synthesis, Characterization and Antibacterial Activity Evaluation of New Indole-Based Derivatives, *Iraqi J Pharm Sci*, 29(1), 207–215. Doi:10.31351/vol29iss1pp207-2015

- Sung, H., Ferlay, J., Siegel, S.L., Laversanne, M., et al. (2021) Global Cancer Statistics 2020: GLOBOCAN Estimates of Incidence and Mortality Worldwide for 36 Cancers in 185 Countries CA, Cancer J. Clin. 71, 209-249. Doi:10.3322/caac.21660
- Şenkardes, S., Kaushik-Basu, N., Durmaz, I., Manvar, D., et al. (2016) Synthesis of novel diflunisal hydrazide-hydrazones as anti-hepatitis C virus agents and hepatocellular carcinoma inhibitors, Eur. J. Med. Chem., 108, 301–308. Doi: 10.1016/j.ejmech.2015.10.041
- Şenkardes, S., Kart, D., Bebek, B., Gündüz, M.G., Küçükgülzel, Ş.G. (2022) Synthesis, antimicrobial properties and in silico studies of aryloxyacetic acid derivatives with hydrazone or thiazolidine-4-one scaffold, J. Biomol. Struct. Dyn., 125, 1-12. Doi:10.1080/07391102.2022.2121761
- Şenkardes, S., Türe, A., Ekrek, S., Durak, A.T., et al., (2021) Novel 2,6-disubstituted pyridine hydrazones: Synthesis, anticancer activity, docking studies and effects on caspase-3-mediated apoptosis, J. Mol. Struct. 1223, 128962. Doi:10.1016/j.molstruc.2020.128962
- Şenol, H., Mercümeç, B., Şahin, R.B., Kapucu, H.B., Hacıosmanoğlu, E. (2022) Synthesis of oleanolic acid hydrazide-hydrazone hybrid derivatives and investigation of their cytotoxic effects on A549 human lung cancer cells, Results in Chemistry 4,100317. Doi:10.1016/j.rechem.2022.100317
- Tolan, D.A., Kashar, T.I., Kazunari Yoshizawa, K., El-Nahas, A.M. (2021) Synthesis, spectral characterization, density functional theory studies, and biological screening of some transition metal complexes of a novel hydrazide-hydrazone ligand of isonicotinic acid Appl Organomet Chem., 35, e6205. Doi:10.1002/aoc.6205
- Wu, J., Wang, J., Han, Y., Lin, Y., Wang, J., Bu, M. (2021) Synthesis and Cytotoxic Activity of Novel Betulin Derivatives Containing Hydrazide-Hydrazone Moieties, Nat. Prod. Commun., 16(10), 1–7. Doi: 10.1177/1934578X211055345
- Yaşa, H., Demir, K. (2019) Bi(NO₃)₃·5H₂O-catalyzed Mannich Reaction: A Potent Catalyst for Synthesis of β-Aminocarbonyl Compounds, Journal of the Turkish Chemical Society Section A, 6(3), 433-438. Doi:10.18596/jotcsa.605641
- Yasa, H. (2018) Synthesis, characterization, and evaluation of antioxidant activity of new gamma- and delta-imino esters, Turkish Journal Of Chemistry , 42(4), 1105-1132. Doi:10.3906/kim-1801-8
- Yaşa, H., Hasdemir, B., Erken, Ö. (2019) beta-Amino Carbonyl Compounds from Iodine Catalyzed Three Component Mannich Reactions and Evaluation of Their Antioxidant Activity, Organic Preparations And Procedures International, 51(6), 537-546. Doi:10.1080/00304948.2019.1677443

- Yıldız, T., Baştaş, I., Başpınar Küçük, H. (2021) Transition-metal-free intramolecular Friedel-Crafts reaction by alkene activation: A method for the synthesis of some novel xanthene derivatives, *Beilstein Journal of Organic Chemistry*, 17, 2203-2208. Doi:10.3762/bjoc.17.142
- Yıldız, T. (2018) Synthesis of new thioxanthenes by organocatalytic intramolecular Friedel-Crafts reaction, *Synthetic Communication*, 48(17), 2177-2188. Doi:10.1080/00397911.2018.1482351
- Zebbiche, Z., Tekin, S., Küçükbay, H., Furkan Yüksel, F., Boumoud, B. (2021) Synthesis and anticancer properties of novel hydrazone derivatives incorporating pyridine and isatin moieties, *Arch. Pharm.*, 354, e2000377. Doi:10.1002/ardp.202000377